Microwave Reflectometry on the Advanced Toroidal Facility to Measure Density Fluctuations and Their Radial Correlation Lengths

A Dissertation

Presented to

The Academic Faculty

by

Gregory Richard Hanson

In Partial Fulfillment

of the Requirements for the Degree of

DOCTOR OF PHILOSOPHY

Georgia Institute of Technology

September 1991

Microwave Reflectometry on the Advanced Toroidal Facility to Measure Density Fluctuations and Their Radial Correlation Lengths

APPROVED:

_____ 6/9/

C. E. Thomas, Chairman   Date

_____

W. M. Stacey

_____ /6/9/

J. N. Davidson

_____

J. H. Harris

_____

J. B. Wilgen

Acknowledgments

First, I would like to express my gratitude to my advisor and Committee Chairman, Dr. C. E. (Tommy) Thomas, for his support, guidance, and patience throughout this project and throughout all my years of graduate study at Georgia Tech. I would also like to thank my other committee members, Drs. Jeffrey H. Harris and John B. Wilgen of ORNL for their guidance and support throughout this project, and Drs. W. M. Stacey and J. N. Davidson of Georgia Tech.

I am indebted to the ORNL Fusion Energy Division for the opportunity to do this research and their support during this project. I would like to thank everyone on the Advanced Toroidal Facility (ATF) project team for operating ATF and the diagnostics, and providing experimental time and support to perform the reflectometer experiments. Special thanks must be given to Dr. John Wilgen for his invaluable support in designing and building the reflectometer system; John Bell for providing the data acquisition system, fluctuation data analysis codes, and many educational discussions on fluctuation data analysis and interpretation; and Dr. Jeffrey Harris for his time and support in developing better ways to analyze the reflectometer fluctuation data and interpreting the results. I would like to thank Dr. Masanori Murakami for being the driving force behind the successful operation of ATF and for his support in performing the reflectometer experiments on ATF, and Dr. Julian Dunlap for his support and encouragement. Drs. David Rasmussen, Alan

Table of Contents

List of Tables

List of Figures

xiii

Summary

A two-frequency correlation reflectometer has been designed, built, and operated on the Advanced Toroidal Facility (ATF) to measure plasma density fluctuations. This reflectometer uses quadrature phase detection to allow true phase measurement of the reflected microwave signal (probing beam). By measuring the phase fluctuations in the reflected probing beam, it is possible to estimate the amplitude of the density fluctuations. Simultaneous two-frequency operation makes it possible to measure the coherence between fluctuations at two radially separated cutoff layers, from which the radial correlation lengths and wave numbers can be estimated.

This reflectometer has been used to study the density fluctuations in the edge density gradient region in low-density ATF plasmas with electron cyclotron heating (ECH). These studies have revealed globally coherent turbulence having a radial correlation length ~ 5 cm, a radial wave number $k_r \sim 0$ cm^{-1}, and a poloidal wave number $k_\theta \sim 1$ cm^{-1}. The fluctuation rms amplitude reaches a maximum ($\sim 5\%$) at the plasma edge and decreases with radius to a level of $\lesssim 1\%$. Simultaneous measurements with the reflectometer, heavy ion beam probe and fast reciprocating Langmuir probe, provided verification of the measured fluctuation amplitude.

A comparison of the results of these measurements with theoretical models shows that the pressure-gradient-driven resistive interchange instabilities are a likely cause of the observed turbulence.

CHAPTER I

INTRODUCTION

The goal of magnetic fusion energy research is to produce a safer, cost-effective energy source. Net energy is produced when high-energy isotopes of hydrogen fuse to form helium. The realization of this goal will require the solutions to many technical obstacles. The technical problems stem from the high temperatures and pressures required to make the nuclei in the plasma fuse. These problems can be classified as engineering and physics problems. The engineering problems include such things as what structural materials to use in a fusion reactor and how to maintain the reactor after activation by the neutrons released by the fusion process. The physics problems are more basic to the whole fusion process. Mainly, the plasma is not as well confined by the magnetic field as neoclassical or diffusion theory predicts. The lack of particle and energy confinement is a common area of research in the fusion community. Some sources of particle and energy loss have been explained, but the majority of the losses have not yet been successfully explained and are categorized as resulting from anomalous transport.

Fluctuations in the plasma parameters — density, temperature, magnetic field, potential, etc. — are thought to be one source of the anomalous transport in toroidal plasmas.[1] Measurements of these fluctuations can provide the information necessary to identify the instability or instabilities, and may make it possible to avoid the instabilities through better plasma control or a change in the magnetic configuration. One technique for measuring density fluctuations inside a plasma is

1

microwave reflectometry.[2,3,4]

The advantage of a microwave reflectometer as a density fluctuation diagnostic is its ability to internally probe the plasma without disturbing it. Since the phase information in the reflected signal is localized to the cutoff layer, localized measurements of the density fluctuations can be made, and by scanning the reflectometer in frequency, a radial profile of the fluctuations can be obtained. These fluctuation data can be combined with other fluctuation data to develop a more complete picture of the plasma fluctuations and the instabilities driving them.

The Advanced Toroidal Facility (ATF) is a magnetic plasma confinement device with the mission of studying the plasma confinement in a steady-state magnetic configuration known as a stellarator. This is an important mission because the more common devices — tokamaks — are not steady state and are not likely to achieve reactor-relevant plasma pulse lengths much longer than one day. This could greatly limit their use as energy-producing reactors. An important part of any plasma confinement experiment is the measurement of the plasma parameters and their fluctuations. In ATF, reflectometry can provide important information on density fluctuations in the plasma interior to help determine their importance or relevance to the plasma confinement or lack of confinement.

Fluctuations and Instabilities

The fluctuations observed in toroidally confined plasmas are thought to be driven by saturated states of fast-growing instabilities.[5] Most low-frequency instabilities are thought to be magnetohydrodynamic (MHD) instabilities and drift wave instabilities. MHD instabilities are large-scale disturbances, while drift waves are small-scale toroidal microinstabilities; both are thought to enhance transport

2

over that predicted by neoclassical theory. Both types of instabilities are driven by plasma currents or gradients in the plasma parameters, such as pressure, temperature, density, potential, etc.; however, the instability mechanisms are different. MHD instabilities are caused by the fluid-like behavior of the plasma, while drift wave instabilities are caused by particle effects.[5]

The purpose of fluctuation diagnostics is to determine the spatial structure of the fluctuations and their wave propagation properties (wave vector, phase, amplitude, frequency, and velocity). This information can be compared with the theoretically predicted characteristics of MHD and drift wave instabilities to try to describe what instabilities are being observed experimentally in the plasma in hopes of finding a way to reduce or eliminate them.

Introduction to Reflectometry

Reflectometry is a microwave plasma diagnostic technique that can be used to measure localized density fluctuations or density profiles. This diagnostic relies on the principle of complete reflection of an electromagnetic wave at a cutoff layer, i.e., when the local refractive index goes to zero. The simplest case is for the ordinary-mode (O-mode) wave where the wave electric field $\vec{E}$ is parallel to the plasma magnetic field $\vec{B}$. For this mode, cutoff occurs when the wave frequency ω equals the electron plasma frequency ω_{pe}. For example, a 35 GHz wave is reflected when it reaches a position where the electron density is 1.5×10^{19} m^{-3}.

A reflectometer is simply a reflex interferometer. An electromagnetic wave of generally microwave or millimeter wave frequencies is split into two parts, with one part being sent to the plasma and the other part being used as a reference. The part of the signal that is sent to the plasma is reflected at the cutoff layer, collected,

and compared to the reference signal to determine the phase delay experienced by the plasma signal. Any changes in the phase delay are due to propagation path length changes resulting from the movement of the cutoff layer. Localization to the cutoff layer, i.e., spatial resolution, is achieved since the wave refractive index is much more sensitive to variations in the density at the cutoff layer. This means that the phase delay due to density fluctuations becomes strongly enhanced when the fluctuations are at the reflecting layer. The line-integrated effect of fluctuations when the local cutoff frequency is below the probing frequency is small.[6] Thus, by following this phase difference in time, the movement of the cutoff layer can be followed to measure density fluctuations and/or the position of the cutoff layer.

The Advanced Toroidal Facility

Toroidal plasma confinement systems, such as stellarators, torsatrons, and tokamaks, rely on a helical magnetic field to produce the closed flux surfaces that confine the plasma. This helical magnetic field is generated by a poloidal component of the magnetic field B_θ and a toroidal component B_ϕ. B_θ goes around the torus the short way, while B_ϕ goes around the torus the long way. The average amount of poloidal rotation of a helical field line during one complete toroidal rotation is called the rotational transform ι and when defined in radians is given by

$$\iota = \frac{\iota}{2\pi} = \left\langle \frac{d\theta}{d\phi} \right\rangle \tag{1.1}$$

where the angle brackets $\langle\ \rangle$ indicate an average over a magnetic flux surface. The rotational transform ι can be related to the safety factor q by

$$\iota = \frac{1}{q} = \left\langle \frac{RB_\theta}{rB_\phi} \right\rangle \tag{1.2}$$

where R is the major radius, and r is the minor radius of the plasma. The safety factor q gets its name from the role that it plays in the suppression of instabilities.

4

In typical stellarators, torsatrons, and tokamaks, $B_\theta \ll B_\phi$, $0 < \iota < 1$, and $1 < q < 10$.[5,7]

The helical field lines are not parallel across the minor radius r of the toroidal plasma. In fact, since ι is a measure of the average poloidal angle mapped out by a field line during one toroidal rotation and is a function of the magnetic flux surface and r, a radial profile of ι will show that the lines of magnetic force are sheared with a change in r. The amount of shearing of the magnetic field at a given radial location in the torus is given by the shear parameter[8]

$$\Theta = \frac{r^2}{2\pi R_0} \frac{d\iota}{dr} \tag{1.3}$$

where $2\pi R_0$ is the circumference of the magnetic axis. Like the rotational transform (or the safety factor), the amount of shear plays an important role in the stability of the confined plasma.[8]

The closed flux surfaces ψ generated by the helical magnetic field enclose a volume V. The specific volume V' of the flux surface ψ is then given by[8]

$$V' = \frac{dV}{d\Phi} = \oint \frac{d\ell}{B} \tag{1.4}$$

where Φ is the magnetic flux in the toroidal direction ϕ inside the magnetic surface ψ and the integration of $d\ell$ is taken along the field line over the entire magnetic flux surface. V' is proportional to an average of $|B|^{-1}$, so if V' is decreasing with increasing r, then $|B|_{\mathrm{avg}}$ must be increasing with increasing r. The central region where $|B|_{\mathrm{avg}}$ is increasing with radius is called the average minimum-B region (magnetic well) and is important for plasma stability. A measure of the depth of this magnetic well is given by the ratio of the specific volume at a radial position r to the value at the magnetic axis; that is, the magnetic well depth is $V'(r)/V'(0)$, where $V'(0)$ is the specific volume of the flux surface on the magnetic axis.[8,9]

In stellarators, the closed flux surfaces are produced entirely by means of external magnetic coils, as opposed to tokamaks, which require a toroidal plasma

current to produce a poloidal magnetic field to form the closed flux surfaces. A classical stellarator has l helical conductors with alternately antiparallel current flow that produces a poloidal field in the plasma.[10] The net toroidal field in the plasma from these helical conductors is nulled, so a set of toroidal field coils is also required to produce a net toroidal field.

The torsatron device is a subclass of the stellarator. It has l helical windings with parallel current flow so that the helical windings produce not only a poloidal field but a net toroidal field. This eliminates the need for toroidal field coils; however, separate vertical field coils are required to provide positioning and stabilization of the plasma. The distinct advantage of a torsatron, and of stellarators in general, is the intrinsic ability to run in a steady state and the absence of disruptive terminations (an instability in tokamaks due to the plasma current) of the discharge. In present tokamaks, a continuous transformer action is required to drive the plasma current that produces the poloidal magnetic field. Since this transformer action can only be sustained for a finite period of time, the discharge must eventually be terminated. This termination can only be avoided if some other reactor-relevant method of current drive is found. Since stellarators produce their complete magnetic configuration in external field coils, no transformer action is required, so the magnetic fields and plasma can be run steady state.

The ATF device at Oak Ridge National Laboratory, shown in Fig. 1.1, is an $l = 2$, 12-field-period torsatron with a rotational transform $\ell = 1/q$ between 0.3 and 1.0, shown in Fig. 1.2. Also shown in Fig. 1.2 is a radial profile of the magnetic well depth $-V'(r)/V'(0)$ in ATF, created by an outward displacement of the vacuum magnetic axis relative to the center of the last closed flux surface. This magnetic well has a stabilizing effect on interchange modes for $\ell \leq 0.5$, while the magnetic shear, indicated by the rapid rise in ℓ, has a stabilizing effect for $\ell > 0.5$. The plasma size in ATF is characterized by the average radius $\bar{a}$ of the last closed flux

7

INNER VF COILS

MID VF COILS

STRUCTURAL SHELL

VACUUM VESSEL

OUTER VF COILS

VACUUM VESSEL PORTS

SUPPORT COLUMNS

HF COILS

BASE

DIAGNOSTIC AND UTILITY PENETRATIONS

ATF
Advanced Toroidal Facility
Oak Ridge National Laboratory
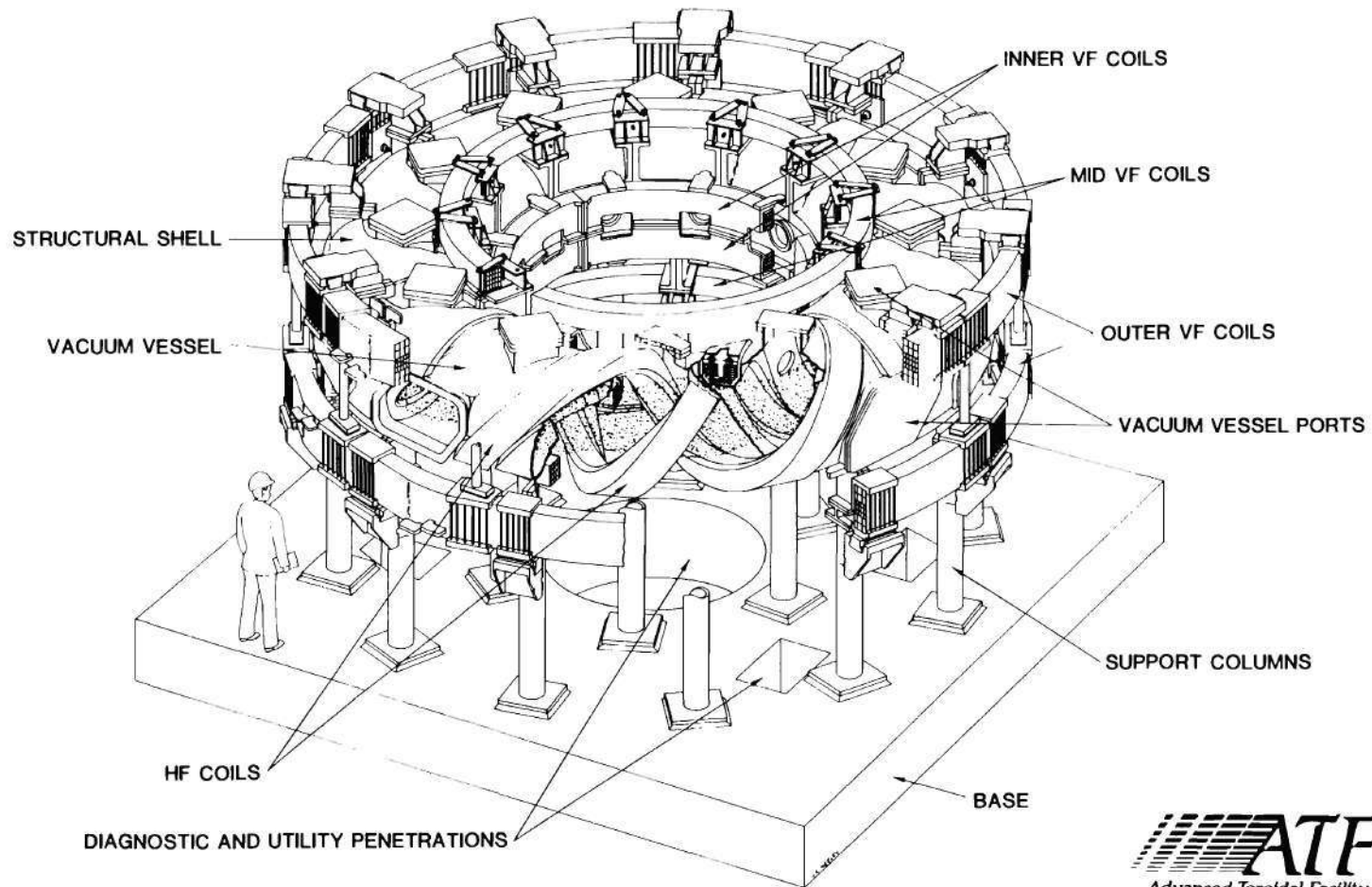
Figure 1.1: An artist's sketch of ATF vacuum and magnetic field coil systems.
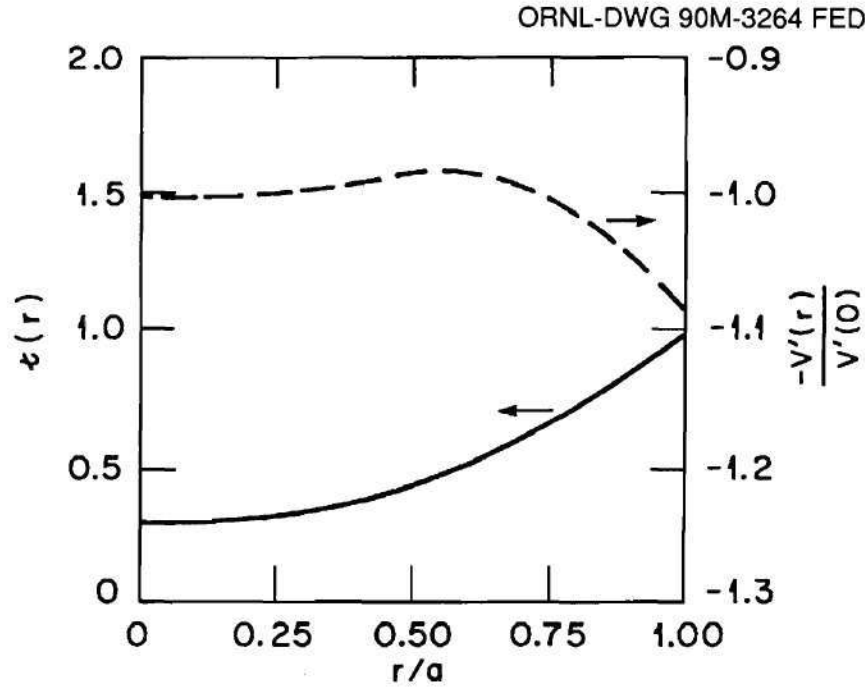
Figure 1.2: The rotational transform ι vs minor radius in ATF shown with a profile of the magnetic well depth.

surface, beyond which the magnetic field is ergodic (a magnetic limiter) or displays a separatrix (a magnetic divertor). The plasma aspect ratio for ATF, $R_0/\bar{a} = 7.7$, is defined using this average radius. The ATF device parameters are listed in Table 1.1.[9]

Although the ATF aspect ratio is smaller than that of most stellarators, it is larger than that of most tokamaks. This configuration was chosen after study of a large number of stellarator configurations and was specifically optimized for high-beta operation in the second stability region and for configuration flexibility.[9] Figure 1.3 shows the magnetic flux surfaces and the magnetic field contours $|B|$ for a poloidal cut through ATF at toroidal angles of $\phi = 0°$ and $15°$, while in Fig. 1.4 the flux surfaces and $|B|$ contours are shown for a toroidal cut through ATF. Note that $\phi = 0°$ is defined as the point where the two helical field coils cross the horizontal

Table 1.1. ATF device parameters (1990)

Magnetic Configuration

Poloidal multipolarity, l	2
Number of field periods, M	12
Standard central transform, $\iota(0)$	0.3
Standard edge transform, $\iota(a)$	1.0

Size

Major radius, R_0 (m)	2.1
Average minor radius, a (m)	0.27
Plasma volume, V_p (m^3)	3.0
Vacuum vessel volume (m^3)	10.5

Magnetic Field

Maximum field on axis, B_0 (T)	1.9
Field flattop time at 1.9 T (s)	5
Field flattop time at .95 T (s)	20

Plasma Heating

ECH	0.4 MW, 53 GHz, steady state
NBI	2 MW, 30 kV, 0.3 s
ICH	0.1 MW, 29 MHz, 0.1 s

midplane. One field period begins where the helical field coils cross the midplane and ends when they cross it again (i.e., when they undergo 180° of poloidal rotation).

Outline of Dissertation

In the following chapters, the theory and application of reflectometry are reviewed, and then the ATF reflectometer and the results obtained with it are discussed. In Chap. II, the basic theory of wave propagation and reflection is presented with special attention paid to the calculation of the phase delay experienced by the wave. A geometrical optics approximation is sufficient to model the wave propagation in the plasma, except near a cutoff where an exact solution of the full wave equation is required. The assumptions or conditions necessary for the applicability of the theoretical treatment of the wave propagation are not always satisfied in all plasmas. The failure of these assumptions and conditions and their possible implications for reflectometry on ATF are discussed.

In Chap. III, the application of reflectometry as a density diagnostic on toroidal devices is discussed. Reflectometer experiments have two basic operational schemes. The first is fixed-frequency operation for measurement of the phase delay due to movement or fluctuations of the cutoff layer. In the second scheme, the reflectometer probing beam frequency is swept, and the density profile is determined from the measured phase delay. The basic theory used on existing experiments to interpret these reflectometer fixed- or swept-frequency data is reviewed in the first part of this chapter. In the next section of Chap. III, the experimental techniques and microwave hardware used on existing microwave reflectometer experiments are reviewed. In the remainder of Chap. III, reflectometer experiments are discussed,

10
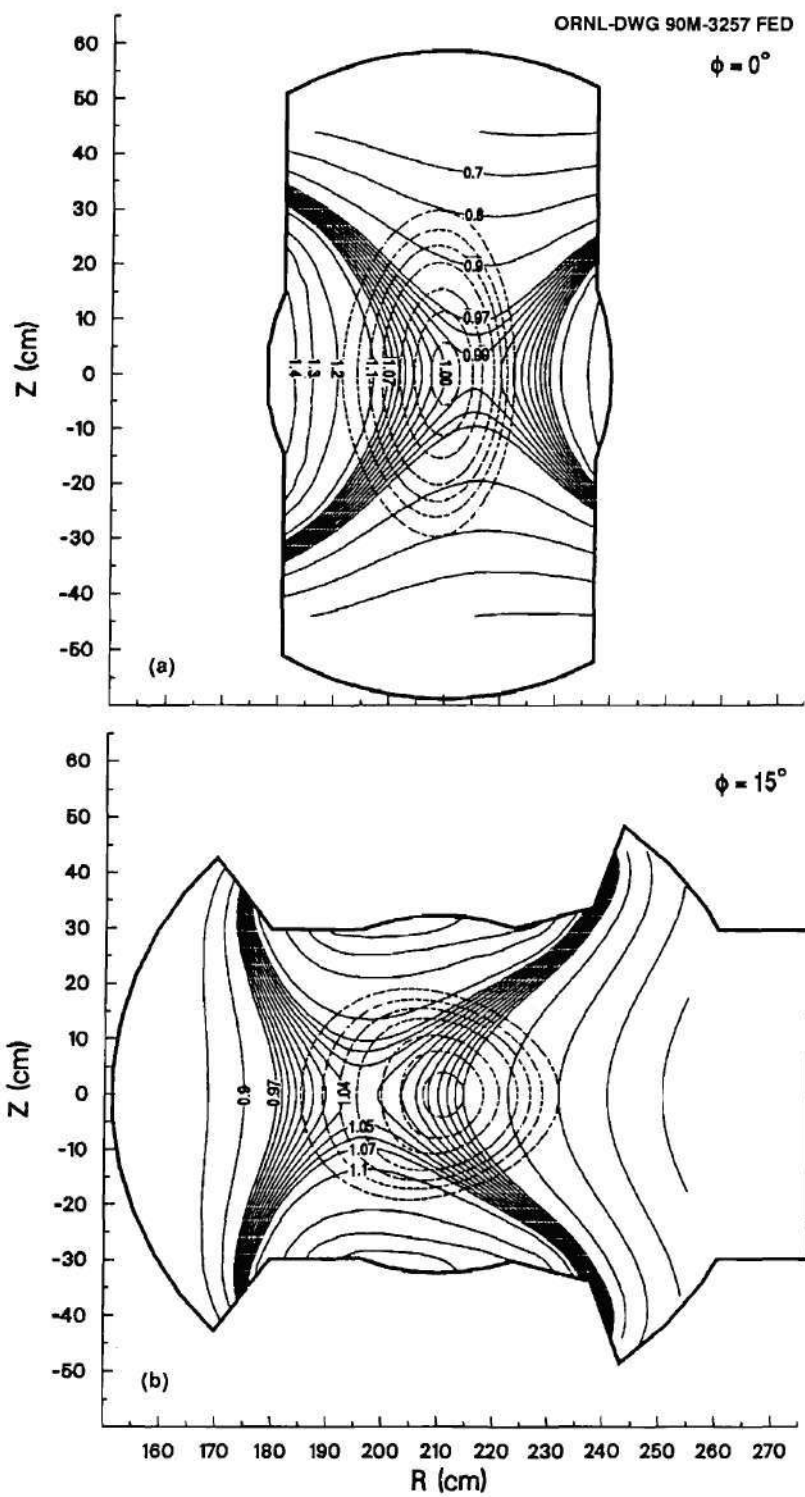
Figure 1.3: The flux surfaces and the magnetic field $|B|$ contours for two poloidal cuts through ATF at the beginning of ($\phi = 0°$) and halfway through a field period ($\phi = 15°$).

11
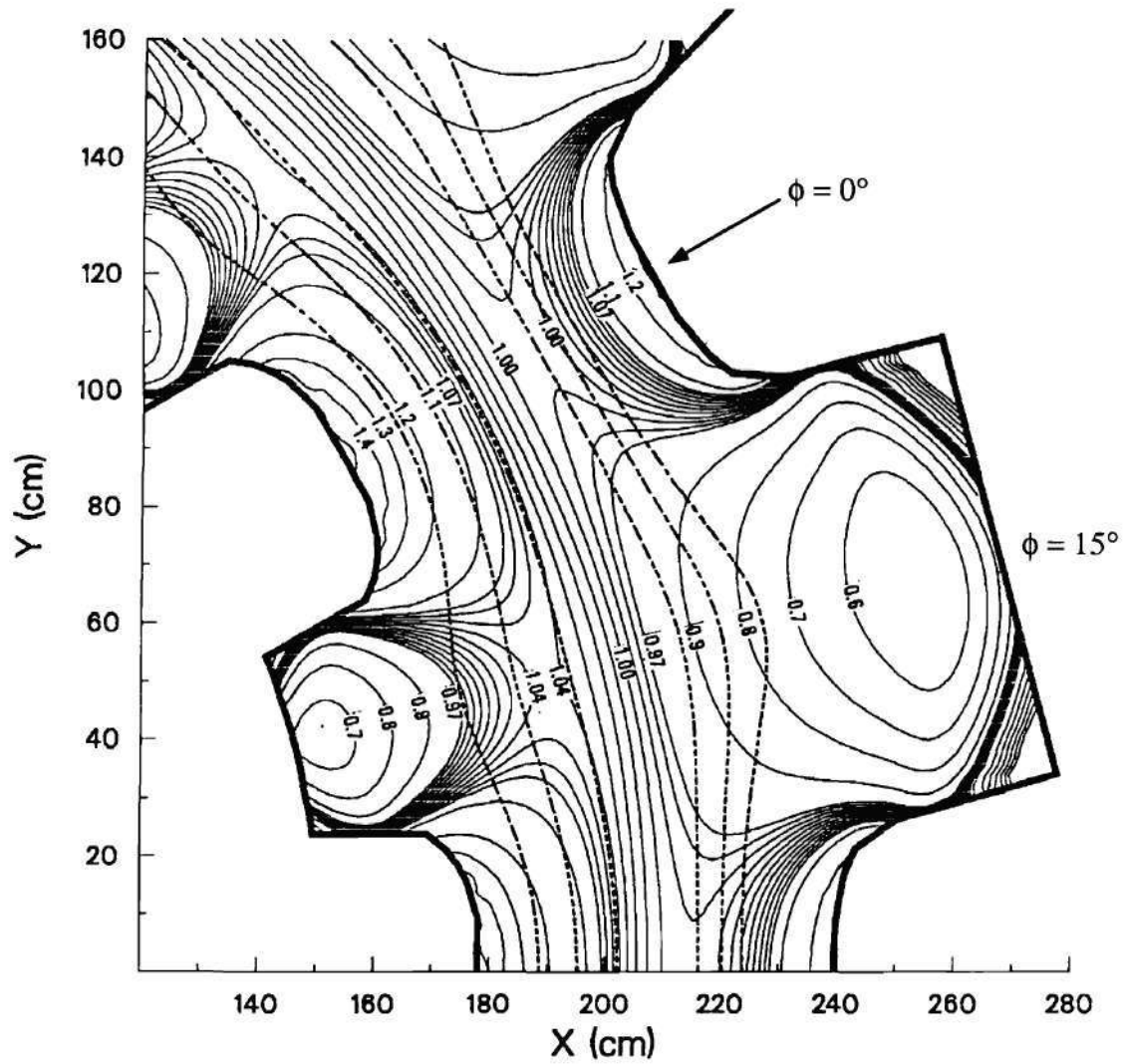
Figure 1.4: The flux surfaces and $|B|$ contours for a cut through ATF in the horizontal midplane showing one full field period.

12

concentrating on experiments in toroidal devices. A summary of present and past reflectometer experiments is given.

A review of instability theory with application to ATF is given in Chap. IV. This chapter begins with a discussion of the importance of fluctuations to transport in toroidal devices. Next, the basic concepts of instability analysis and the characterization of instabilities are discussed. Finally, the major categories of instabilities presently predicted by theory are reviewed, with consideration given to the ability of a reflectometer to observe their presence in ATF. As discussed in Chap. III, reflectometry can measure the amplitude, radial width, and correlation length of the density fluctuations. In the discussion of each instability, equations are given to allow estimates of the fluctuation rms amplitude produced by an instability. Also given are estimates of instability mode frequencies and radial widths. The chapter concludes with a summary of the instabilities and gives estimates of their fluctuation rms amplitudes, mode frequencies, and radial widths.

Chapter V reviews fluctuation data analysis with application to reflectometry on ATF. The primary tools of fluctuation data analysis, the Fourier transform and the cross-correlation function, are reviewed and discussed. Attention is given to the common mistakes made in fluctuation data acquisition and analysis.

After this review of theory and techniques applicable to reflectometry on ATF, a thorough discussion of the ATF two-frequency reflectometer is given in Chap. VI. The basic design criteria are discussed, and the final reflectometer system as installed and operated on ATF is described. The important elements of this reflectometer, i.e., the antennas, quadrature phase detectors, and differential amplifiers, are discussed in detail. The significance of the helical magnetic structure of ATF with respect to the alignment of the dual antennas is summarized, and the problems with mode selection in moderate- or high-shear devices such as ATF are reviewed. Also discussed are the estimates of the spatial resolution of the probing

13

beam and the system noise limitations. Finally, the phase detection technique that makes two-frequency operation possible and minimizes the potential for cross talk is discussed.

Because the ATF reflectometer made substantial gains in readily providing the phase fluctuation data from the probing beam and radial coherence data, new data analysis techniques were necessary. In Chap. VII, the techniques used and the problems with obtaining the phase data from fringe counting of the quadrature phase signals are discussed. Equations for converting these phase data to an estimate of the density fluctuation amplitude are derived, as are equations for estimating the uncertainty in these amplitudes. The determination of the cutoff location and its uncertainty due to random errors are discussed. The use of two probing beam frequencies simultaneously provides the signals necessary for radial coherence measurements. The technique used to estimate the radial correlation lengths from these coherence measurements is given, as is an estimate of the uncertainty for the calculated correlation lengths. Finally, estimation of the radial and poloidal wave numbers from the reflectometer phase signals is discussed.

Chapter VIII presents two sequences of electron cyclotron heated (ECH) discharges in ATF. (The reflectometer data from these discharges are analyzed in detail in Chap. IX.) First, the sequences are described and their parameters given. Examples of the reflectometer data for these sequences are shown and key features discussed. Similarities in the fluctuation spectra with measurements made simultaneously with the fast reciprocating Langmuir probe (FRLP) and the heavy ion beam probe (HIBP) are shown and their significance discussed. Further comparisons of the measurements made by all three diagnostics are given in Chap. IX.

Chapter IX includes the detailed analysis of the reflectometer data for the two sequences described in Chap. VIII. The data analysis methods presented in Chap. VII are used to quantify the measured fluctuations as completely as possible.

14

The density fluctuation profile and its uncertainty are calculated and compared to the HIBP and FRLP measurements. The radial coherence data are used to calculate the radial correlation lengths and the radial wave numbers. Also calculated are the poloidal wave numbers, which show good agreement with those values measured at the plasma edge by the FRLP. Finally, the instability models expected to be important in ATF, as discussed in Chap. IV, are analyzed for these sequences. The density fluctuation amplitude profile calculated for the resistive interchange instability is found to show good agreement with the reflectometer measurements. The importance of this instability and its consequences are discussed.

A summary of the material presented in this dissertation and the results of the ATF reflectometer is given in Chap. X. The advances of the ATF reflectometer in providing quantifiable fluctuation measurements are summarized, and the limitations of the diagnostic are discussed. The significant unknowns that still exist in the theory of reflectometry lead to the potential for systematic errors in the data presented in this dissertation. Suggestions for future reflectometer experiments with the ATF reflectometer and/or reflectometers of similar design are given.

CHAPTER II

REFLECTOMETRY THEORY

Wave Propagation and Reflection

Cold Plasma Dispersion Relations

At present, most plasmas under study in fusion experiments have electron temperatures below 5 keV. In this case the electron thermal velocity v_{Te} is much less than the speed of light, $v_{Te}/c \ll 1$, and the cold plasma approximation is used to study the propagation of most electromagnetic waves, as long as absorption can be neglected. Another simplification made in studying high-frequency ($\omega \gg \omega_{ci}$) electromagnetic wave propagation is to neglect the ion motion since $m_i/m_e \ll 1$, where m_i is the ion mass, m_e is the electron mass, and ω_{ci} is the ion cyclotron frequency. Finally, it is assumed that there is no collisional damping on the time scale of the plasma electrons (ω_{pe}, ω_{ce}), as required for a cold plasma approximation to hold. This assumption is valid since the natural electron frequencies are $\geq 10^{10}$ s^{-1}, while the electron-ion collision frequency is $\sim 10^{-5}$ s^{-1}. These assumptions greatly simplify the electromagnetic wave propagation problem; however, they do not remain valid near the electron cyclotron resonance. Wave propagation and interaction near resonances are discussed later. Miyamoto[8] gives a derivation of the cold plasma dispersion relations beginning with Maxwell's equations and the electron equation of motion. The rest of this section is based on Miyamoto's development.

In reflectometry experiments in toroidal plasmas, the electromagnetic waves

are usually launched and received with the wave vector $\vec{k}$ perpendicular to the local magnetic field $\vec{B}$. In this case, two types of wave modes are possible. In the simplest mode the wave's electric field $\vec{E}$ is parallel to $\vec{B}$ so that the wave propagates as if it were in an unmagnetized plasma. This "ordinary" wave is referred to as the "O-mode." If the wave propagates with $\vec{E}$ perpendicular to $\vec{B}$, it is called an "extraordinary" wave and is said to be propagating in the "X-mode."

The refractive index N of a wave determines whether the wave will propagate, be reflected, or be absorbed. N is related to the wave number k by $N = ck/\omega$. For the O-mode, the index of refraction is

$$N^2 = 1 - \frac{\omega_{pe}^2}{\omega^2} \qquad (2.1)$$

where ω is the wave frequency, and

$$\omega_{pe} = \sqrt{\frac{n_e e^2}{\epsilon_0 m_e}} \qquad (2.2)$$

is the electron plasma frequency. In this equation n_e is the electron density, e is the electron charge, m_e is the electron mass, and ϵ_0 is the permittivity of free space. If absorption is neglected, the relative permittivity of the plasma ϵ_r can be written as $\epsilon_r = N^2$. When N becomes purely imaginary, the wave is evanescent and is totally reflected. Thus the wave is cut off at $N = 0$, i.e., when the wavelength becomes infinite. For an incoming O-mode wave, cutoff occurs when $\omega = \omega_{pe}$. The reflecting point or cutoff layer is then defined as the density layer at which $\omega = \omega_{pe}$. We can solve for the density at the cutoff layer by letting $N = 0$ in Eq. (2.1). The cutoff density is then

$$n_c = \frac{\epsilon_0 m_e \omega^2}{e^2} \qquad (2.3)$$

For the X-mode, the index of refraction is

$$N^2 = 1 - \frac{\omega_{pe}^2}{\omega^2} \frac{\omega^2 - \omega_{pe}^2}{\omega^2 - \omega_{pe}^2 - \omega_{ce}^2} \qquad (2.4)$$

18

where $\omega_{ce} = eB/m_e$ is the electron cyclotron frequency. If we solve Eq. (2.4) for $N = 0$, two separate cutoff frequencies are obtained:

$$\omega_L = \frac{1}{2}\left[-\omega_{ce} + \left(\omega_{ce}^2 + 4\omega_{pe}^2\right)^{1/2}\right] \qquad (2.5)$$

and

$$\omega_R = \frac{1}{2}\left[\omega_{ce} + \left(\omega_{ce}^2 + 4\omega_{pe}^2\right)^{1/2}\right] \qquad (2.6)$$

where ω_L is the left-hand cutoff and ω_R is the right-hand cutoff. Thus, an incoming extraordinary wave will be reflected when it approaches a region in the plasma where $\omega = \omega_L$ or $\omega = \omega_R$. The left- and right-hand nomenclature is derived from the direction of rotation of the wave polarization. Note that the left-hand cutoff occurs at a much lower frequency than either the right-hand cutoff or the O-mode cutoff and is usually of no interest in present reflectometry experiments. It may be of interest in high magnetic field experiments.

Resonances occur when $N \to \infty$, i.e., when the wavelength becomes zero. From Eq. (2.1), it is seen that an O-mode wave has no resonance. From Eq. (2.4), an X-mode wave will have a resonance at

$$\omega_{uh} = \left(\omega_{pe}^2 + \omega_{ce}^2\right)^{1/2} \qquad (2.7)$$

where ω_{uh} is the upper hybrid resonance. The lower hybrid resonance can be obtained by including the ion motions in deriving the cold plasma dispersion relations.

For reflectometry experiments, any of the three wave cutoffs given above can be used to reflect a transmitted wave. Figure 2.1 shows these three reflecting layers vs the plasma minor radius in ATF at a toroidal position of $\phi = 15°$. This toroidal location is shown because this is the center of the large vacuum vessel ports where access for a reflectometry system is available on ATF. Also shown are the electron cyclotron frequency and its first harmonic and the upper hybrid resonance.

19
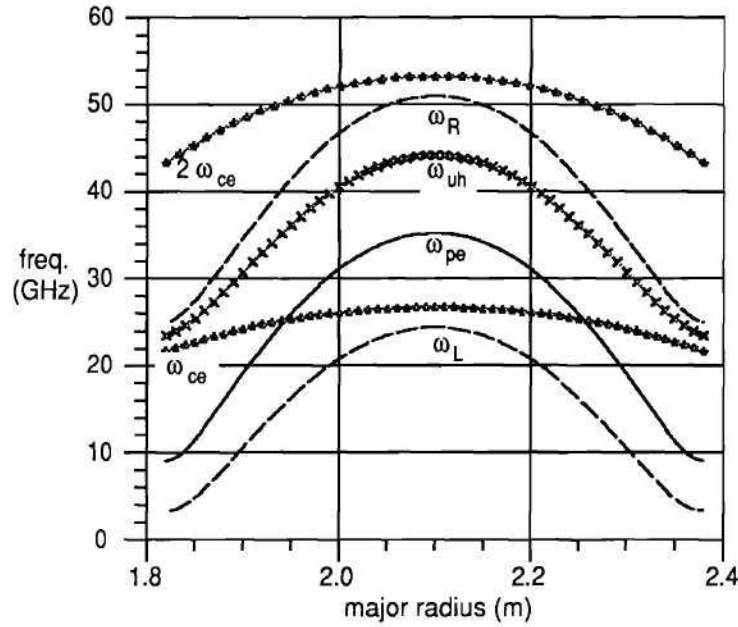
Figure 2.1: A plot of the O-mode (ω_{pe}) and X-mode (ω_R and ω_L) cutoff layers in ATF for $n_e(r) = 1.5 \times 10^{13}[1 - (r/a)^2]^2$ cm^{-3}, $B_0 = 0.95$ T, and $\phi = 15°$. Also shown are the fundamental (ω_{ce}) and first harmonic ($2\omega_{ce}$) electron cyclotron resonances and the upper hybrid resonance (ω_{uh}).

Phase Delay in Plasmas

Geometrical Optics Approximation

The geometrical optics approximation can be used to calculate the phase delay of an electromagnetic wave in an isotropic inhomogeneous plasma. In general, this approximation is good for toroidal devices, since the effects of the toroidal curvature can be neglected if the wave is launched along a minor radius and the beam width at the reflecting layer is much less than the major radius at that point. It is assumed that n_e and B have only a radial dependence, which is a good approximation for the horizontal midplane (symmetry plane at $\phi = 15°$) of the plasma and for the central rays of the beam. Note that this neglects the magnetic shear present in ATF, which is discussed later in this chapter in the section "Effects of Magnetic Shear." Any rays not propagating along a minor axis will be refracted away and are not likely to be picked up by the

20

receiving antenna. Thus, the wave equation can be reduced to just a dependence on the minor radius r and can be written as[11]

$$\frac{d^2 E(r)}{dr^2} + \frac{\omega^2}{c^2} \epsilon_r(\omega, r) E(r) = 0 \tag{2.8}$$

where $\epsilon_r = N^2$ is the relative permittivity of the plasma, absorption is neglected for simplicity, and an $e^{i\omega t}$ time dependence is assumed.

In a homogeneous plasma where ϵ_r has no radial dependence, the solution to Eq. (2.8) is

$$E(r) = A_0 \exp\left(\pm i \frac{\omega}{c} N r\right) \tag{2.9}$$

where A_0 is an amplitude constant and $\omega N r / c = \phi$ is the phase change. However, in an inhomogeneous plasma ϵ_r has a radial dependence, and the solution to Eq. (2.8) is not so straightforward. If ϵ_r changes slowly with r, it is reasonable to replace N in Eq. (2.9) with the average of $N(r)$ over the path of propagation. The phase can then be written as

$$\phi = \frac{\omega}{c} \int_{r_1}^{r_2} N(r) dr \tag{2.10}$$

where r_1 and r_2 are two positions along the same radius. This is the basic approximation of geometrical optics and is valid when ϵ_r varies only slightly over the length of an electromagnetic wave, that is, when

$$\lambda \frac{d\epsilon_r}{dr} \ll \epsilon_r \tag{2.11}$$

where λ is the wavelength of the electromagnetic wave at a position r in the plasma. Physically, this condition can be interpreted as $\lambda/L_n \ll 1$ for the O-mode and $(\lambda/L_n, \lambda/L_B) \ll 1$ for the X-mode. Here, $L_n = n_e(dn_e/dr)^{-1}$ is the density gradient scale length and $L_B = B(dB/dr)^{-1}$ is the magnetic field gradient scale length.

Ginzburg[11] seeks the same solution more precisely by obtaining a solution to Eq. (2.8) in the form of the series

$$E(r) = \left[E_0(r) + \frac{c}{\omega}E_1(r) + \frac{c^2}{\omega^2}E_2(r) + \cdots\right] \exp\left[\pm i\frac{\omega}{c}\psi(r)\right] \tag{2.12}$$

21

where ψ, E_0, E_1, etc., are unknown functions of r. Substituting Eq. (2.12) into Eq. (2.8) and setting the coefficients of the successive powers of ω/c equal to zero gives rise to a series of conditions:

$$
\begin{array}{ll}
1) & \psi(r) = \pm \int_{r_1}^{r_2} N(r)dr \\[2mm]
2) & E_0(r) = A_0[N(r)]^{-1/2} \\[2mm]
3) & E_1(r) = [N(r)]^{-1/2} \int_{r_1}^{r_2} \frac{1}{2i}\frac{d^2 E_0}{dr^2}[N(r)]^{-1/2}dr
\end{array}
\qquad (2.13)
$$

Now assuming that only the first term in the series solution, Eq. (2.12), is significant, i.e., $|E_0| \gg (c/\omega)|E_1|$, and using conditions 1 and 2 from Eq. (2.13), the more exact solution for the first approximation of geometrical optics is obtained,

$$
E(r) = A_0[N(r)]^{-1/2} \exp\left[\pm i\frac{\omega}{c}\int_{r_1}^{r_2} N(r)dr\right] \qquad (2.14)
$$

where if $N(r)$ is monotonic then a sufficient condition for Eq. (2.14) to be valid is

$$
\frac{\omega}{c}\frac{N^2}{|dN/dr|} = \frac{2\pi L_N}{\lambda} \gg 1 \qquad (2.15)
$$

where $L_N = N(dN/dr)^{-1}$ is the refractive index scale length and λ is the local wavelength of the electromagnetic wave in the plasma. The physical interpretation of this equation is that the local wavelength of the electromagnetic wave must be small compared to the scale length of the variations in the refractive index. If a function γ_g is defined to be

$$
\gamma_g \equiv \frac{\omega}{c}\frac{N^2}{|dN/dr|} \qquad (2.16)
$$

then condition (2.15) can be written as $\gamma_g \gg 1$. Figure 2.2 shows γ_g vs the minor radius for an O-mode wave at 35 GHz in ATF. Also shown are the electron plasma frequency ω_{pe} and the index of refraction N. Note that the geometrical optics approximation is good, i.e., $\gamma_g \gg 1$, except for a small region near the reflecting layer. A more precise treatment for this region is given below.

22
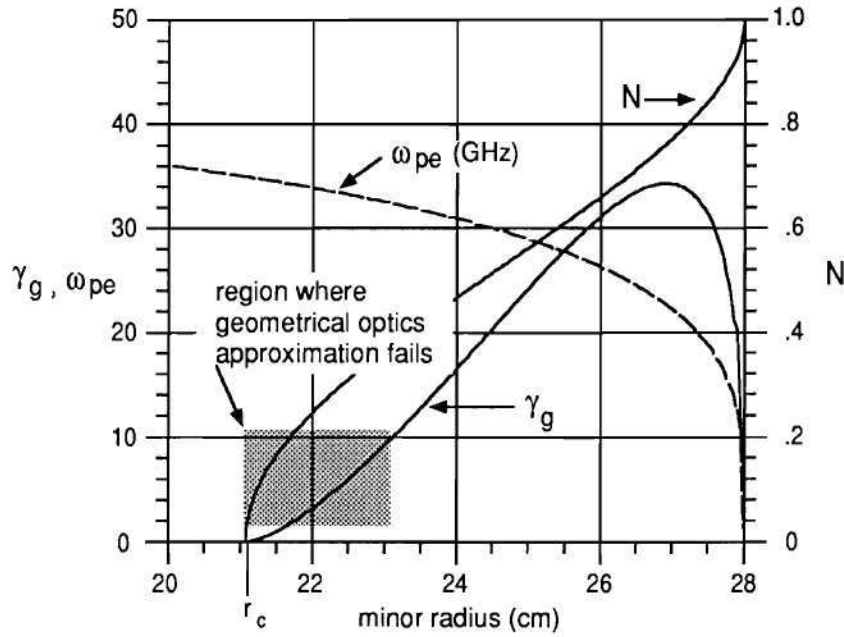
Figure 2.2: The geometrical optics condition for validity, $\gamma_g \gg 1$, for a 35 GHz wave propagating in the O-mode in ATF which is cut off at a radius r_c. The assumed density profile is $n_e(r) = 2.3 \times 10^{13}[1 - (r/a)^2]^{1/2}$ cm^{-3}.

Exact Solution of the Wave Equation   The exact solution of the wave equation near the reflecting layer has been derived for radio waves in the ionosphere by Budden.[12] The conditions necessary to use Budden's solution are that the plasma density increases continuously and monotonically with decreasing minor radius r, the plasma is collisionless, and $n_e(r)$ varies linearly in a small region including the reflecting layer. Applying the condition of Eq. (2.16) to the small region where $n_e(r)$ varies linearly, we find that $\gamma_g \to 1$, so the geometrical optics approximation is not valid here, and the exact solution of the wave equation must be found.

If r_c is the plasma radius at the cutoff layer, then as we proceed away from the cutoff layer, $n_e(r)$ remains linear until $|r - r_c|$ is large enough for asymptotic (geometrical optics) approximations to be used and departure from linear $n_e(r)$ does not matter. However, exact linearity of $n_e(r)$ is not necessary. A sufficient condition

23

on $n_e(r)$ near the reflecting layer is that[12]

$$\frac{d^2 n_e(r)}{dr^2}|r - r_c| \ll \frac{dn_e}{dr} \tag{2.17}$$

Then in this region of linear $n_e(r)$, the permittivity of the plasma can be written as

$$\epsilon_r = a_o(r - r_c) \tag{2.18}$$

where a_o is an unknown constant. Then the wave equation [Eq. (2.8)] can be written as

$$\frac{d^2 E(r)}{dr^2} + \frac{\omega^2}{c^2} a_o(r - r_c)E(r) = 0 \tag{2.19}$$

This is in the form of a Stokes' differential equation, and its solutions are found in terms of Airy integrals.[13] The physical condition that the amplitude of the wave must decrease as the path length increases (spherical expansion) is used to obtain the final solution.

Finally, Budden shows that for a wave reflected at the cutoff layer,[12] the full wave solution matches the geometrical optics solution exactly except for a phase advance of $\frac{\pi}{2}$ associated with the reflection. Thus, the geometrical optics solution in Eq. (2.14) is correct except that the phase term must be written as

$$\phi = \frac{2\omega}{c} \int_{r_c}^{r_1} N(r)dr - \frac{\pi}{2} \tag{2.20}$$

where r_1 is some arbitrary reference point outside the plasma. The factor of 2 comes from assuming symmetrical paths to and from the cutoff layer, i.e., reflection back to the transmitter/receiver along the path of propagation, so that only half of the total path need be calculated.

Cutoff Layer Depth

Once the propagating wave reaches the cutoff layer, it becomes evanescent; i.e., its amplitude decays exponentially with radius on the high-density side of the

layer. The scale length of this exponential decay defines the cutoff layer depth and is given by[11]

$$W_c = \left(\frac{\omega^2}{c^2} \left| \frac{d\epsilon_r}{dr} \right|_{\epsilon_r=0} \right)^{-1/3} \tag{2.21}$$

where the derivative of the permittivity is taken at the cutoff layer, i.e., where $\epsilon_r = 0$. For the O-mode, $\epsilon_r = N^2$ is simply defined in terms of the density [Eq. (2.1)], and its derivative is

$$\left. \frac{d\epsilon_r}{dr} \right|_{\epsilon_r=0} = \left. \frac{-2\omega_{pe}}{\omega^2} \frac{d\omega_{pe}}{dr} \right|_{\epsilon_r=0} = \left. \frac{-1}{L_n} \right|_{\epsilon_r=0} \tag{2.22}$$

The cutoff layer depth for the O-mode can now be written as

$$W_c = \left(\frac{L_n}{k_0^2} \right)^{1/3} \tag{2.23}$$

where $k_0 = \frac{2\pi}{\lambda_0}$ is the vacuum wave number of the probing beam and L_n is evaluated at the cutoff layer. For the X-mode, the permittivity is given by Eq. (2.4) and has the derivative

$$\left. \frac{d\epsilon_r}{dr} \right|_{\epsilon_r=0} = \left. \frac{-2}{L_n} \right|_{\epsilon_r=0} - \left. \frac{2}{L_B} \left(\frac{\omega^2}{\omega_{pe}^2} - 1 \right) \right|_{\epsilon_r=0} \tag{2.24}$$

where all parameters are evaluated at the cutoff layer. The cutoff layer depth is obtained by substituting this equation into Eq. (2.21). The effect of this region of exponential decay is to spread out the radial resolution; i.e., the phase information in the reflected signal is a result of the sum of many small reflections occurring over a region of thickness W_c.

Problems with Reflectometry Theory

The analysis of reflectometry data is limited by the approximations made in deriving the equations that define the phase delay due to propagation through the plasma and reflection at a cutoff layer.[14] The first assumption made is in using the cold plasma dispersion relations to define the wave propagation in the plasma. The

cold plasma dispersion relations might fail when the wave frequency approaches the frequency of the local electron cyclotron resonance or its harmonics. In this region, strong absorption by the plasma electrons can prevent the launched wave from reaching a cutoff layer.

The second assumption made in deriving the governing equations of reflectometry is in using the geometrical optics approximation to describe the wave propagation in the plasma. The approximation of geometrical optics [Eq. (2.10)] is valid only when the permittivity ϵ_r varies slightly over the length of the electromagnetic wave [Eq. (2.15)]. This condition may be violated when steep edge density gradients are present. These gradients may lead to partial reflection of the wave before the wave reaches the cutoff layer. The geometrical optics approximation also assumes that the magnetic field has only a radial dependence. In machines with significant magnetic shear, such as stellarators and reversed-field pinches (RFPs), the magnetic field has an additional dependence on the vertical (or poloidal) coordinate. The changing direction of the magnetic field lines of force (the shear) causes the relationship between the wave polarization and the magnetic field to change continually. This causes part of the propagating wave mode to be converted to the other mode, i.e., there is coupling between the X- and O-modes. This mode coupling can change the measured phase of a wave after propagation through the plasma because the X- and O-modes have different phase velocities.[15]

Finally, the last assumption made is in deriving the exact solution of the wave equation near the reflecting layer. In this derivation, it is assumed that $n_e(r)$ increases continuously and monotonically with decreasing minor radius and that $n_e(r)$ varies linearly in a small region including the reflecting layer. These two conditions are met over most of the plasma radius except at or near the plasma center where the density profile flattens out or peaks. If the reflecting surface occurs in this region, the wave may only be partially reflected as some of the wave power

26

may tunnel through the cutoff layer. Tunneling can occur near the peak in the density profile where the electron density gradient scale length L_n reverses sign if $L_n \gg \lambda$.

Each of the problems mentioned above is discussed in more detail in the following sections. The conditions for each problem are applied to reflectometry in ATF and the results discussed.

Electron Cyclotron Resonance (ECR) Absorption

If the probing beam of the reflectometer encounters a location where the electrons are gyrating around the magnetic field lines at a frequency equal to the probing beam frequency ($\omega = \omega_{ce}$), the electrons and the electromagnetic waves interact and strong absorption of the wave power can occur. In general, reflectometers launch from a low-field side into a plasma with increasing magnetic field and electron density. In this case, three possible resonances may be reached. First, the fundamental electron cyclotron resonance may be reached by an O-mode propagating wave. An X-mode propagating wave will not reach the fundamental resonance because it will be reflected at the right-hand cutoff, which, from Eq. (2.6), always occurs on the low-field side of the fundamental resonance. Next, the second harmonic electron cyclotron resonance may be encountered by an X-mode propagating wave, and finally, an O-mode propagating wave may encounter the second harmonic resonance. Higher harmonic resonances may be reached; however, the absorption at these resonances is in general very weak.

Bornatici et al.[16] discuss in detail wave absorption at cyclotron resonances for the conditions encountered in reflectometry; that is, for wave propagation perpendicular (or nearly perpendicular) to the magnetic field in a finite-density plasma.

The condition for a finite-density plasma is

$$\left(\frac{\omega_{pe}}{\omega_{ce}}\right)^2 \gg \left(\frac{v_{Te}}{c}\right)^2 \tag{2.25}$$

where v_{Te} is the electron thermal velocity. This condition is always met for the regimes of interest in ATF. To quantify the absorption of the wave power at the resonance layer, an energy balance equation for an inhomogeneous medium is derived using Maxwell's equations and the Vlasov equation[17]

$$\nabla \cdot \vec{S} = -\alpha \, |\vec{S}| \tag{2.26}$$

where $\vec{S}$ is the total power flux density and α is the absorption coefficient, which has units of inverse length. The absorption coefficient is defined as

$$\alpha \equiv 2 \, \text{Im} \, \vec{k} \cdot \frac{\vec{S}}{|\vec{S}|} \tag{2.27}$$

where $\text{Im} \, \vec{k}$ is the imaginary part of the wave vector. In this description, both $\vec{S}$ and α refer to a specific fundamental wave mode, corresponding to one solution of the dispersion relation.

It is easier to get a feeling for the wave absorption if it is discussed in terms of the optical thickness of the plasma to a particular frequency wave. The optical thickness τ_{opt} is defined as[16]

$$\tau_{\text{opt}} = \int_{r_2}^{r_1} \alpha(s) ds \tag{2.28}$$

and is simply the integral of the absorption coefficient α defined in Eq. (2.27) for a particular wave along the path of propagation. If $\tau_{\text{opt}} \gg 1$, the plasma is optically thick, and the wave power is strongly absorbed by the plasma. If $\tau_{\text{opt}} \ll 1$, the plasma is optically thin, and the wave power is only weakly or negligibly absorbed.

The fundamental O-mode optical thickness τ_1^o, the second harmonic X-mode optical thickness τ_2^x, and the second harmonic O-mode optical thickness τ_2^o are given
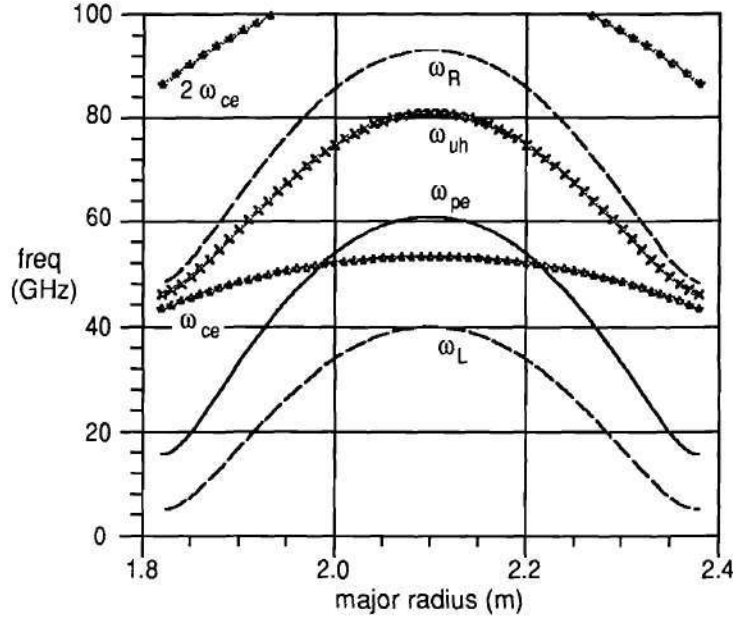
Figure 2.3: The cutoff and resonance layers in ATF at 1.9 T for $n_e(r) = 2.3 \times 10^{13}(1 - (r/a)^2)^2$ cm^{-3}. Note that an X-mode propagating wave cannot reach the fundamental resonance from the low-field side because the ω_R cutoff occurs between the resonance and the plasma edge.

by Bornatici et al.[16] as

$$\tau_1^o \simeq \pi^2 \left(1 - \frac{\omega_{pe}^2}{\omega_{ce}^2}\right)^{1/2} \left(\frac{\omega_{pe}}{\omega_{ce}}\right)^2 \left(\frac{v_{Te}}{c}\right)^2 \frac{|L_B|}{\lambda_0} \tag{2.29}$$

$$\tau_2^x \simeq 2\pi^2 \left(\frac{\omega_{pe}}{\omega_{ce}}\right)^2 \left(\frac{v_{Te}}{c}\right)^2 \frac{|L_B|}{\lambda_0} \tag{2.30}$$

$$\tau_2^o \simeq 2\pi^2 \left(1 - \frac{\omega_{pe}^2}{4\omega_{ce}^2}\right)^{3/2} \left(\frac{\omega_{pe}}{\omega_{ce}}\right)^2 \left(\frac{v_{Te}}{c}\right)^4 \frac{|L_B|}{\lambda_0} \tag{2.31}$$

where λ_0 is the free-space wavelength of the reflectometer probing beam.

For operation in ATF, absorption at all three of the above resonances can occur. Figure 2.1 shows the position of the O-mode cutoff ω_{pe} and the X-mode cutoffs ω_R and ω_L and the corresponding positions of the fundamental electron cyclotron resonance ω_{ce} and its first harmonic $2\omega_{ce}$ for 0.95 T. Figure 2.3 shows the same information as Fig. 2.1 for 1.9 T operation. For a reflectometer using the 30

29

to 40 GHz band, the fundamental resonance is encountered outside the last closed flux surface by the O-mode in 1.9 T operation, and both the X-mode and the O-mode encounter the second harmonic resonance outside the last closed flux surface in 0.95 T operation. Since the resonances are encountered outside the last closed flux surface, absorption at the resonance will depend on the electron density present at the absorption layer.

ECR Absorption Estimates in ATF   In this section, the effects of electron cyclotron resonances on a 30 to 40 GHz reflectometer system are discussed, and estimates of the optical thickness are given. Note that these estimates assume that the reflectometer will be located on the horizontal midplane with the antenna apertures at $R = 270$ cm. At 1.9 T operation, the fundamental resonance is located between $R \simeq 242$ cm (40 GHz resonance) and $R \simeq 260$ cm (30 GHz resonance) on a major axis on the horizontal midplane. The strongest absorption by this resonance will occur during high-density operation when the plasma densities outside the last closed flux surface are highest. On this axis, the last closed flux surface is at approximately $R = 238$ cm, and the edge density on this flux surface is about 2×10^{13} cm^{-3} with an e-folding length of approximately 2 cm as measured by the FRLP.[18] The electron temperature at this position is typically 40 eV, also measured by the FRLP. If it is assumed that the electron temperature stays constant in the edge region to maximize the absorption calculations, at $R = 242$ cm, $\omega_{ce} = 40$ GHz, and ω_{pe} and v_{Te} will be their largest in the edge region under consideration. From Fig. 7.11, the magnetic field gradient length L_B in this region ($r \simeq 30$ cm) is $|L_B| \simeq 65$ cm. From Eq. (2.29) the O-mode optical depth is found to be $\tau_1^o \simeq 0.02$. Since $\tau_1^o \ll 1$, the plasma is optically thin to a reflectometer probing beam at 40 GHz. Probing beams at frequencies below 40 GHz will be absorbed even less since the edge density and temperature fall off more rapidly than the magnetic field. A

30 to 40 GHz X-mode probing beam will not reach the fundamental resonance at 1.9 T because the upper hybrid resonance is always located between the resonant surface and the plasma edge.

For the case of 0.95 T operation, a 30 to 40 GHz reflectometer would use the X-mode during the low-density ECH discharges, but would use the O-mode during the higher density neutral-beam-heated discharges. For typical low-density ECH discharges $[n_e(r = 0) \simeq 6 \times 10^{12}$ cm$^{-3}]$, the density at the last closed flux surface has been measured by the FRLP[18] to be about 2.5×10^{12} cm^{-3}. If all other conditions are similar to those in the 1.9 T calculation except that ω_{ce} is now 20 GHz at $R = 242$ cm, it is found that $\tau_2^x \simeq 0.02$. Here again, the plasma is found to be optically thin to an X-mode probing beam in the 30 to 40 GHz band.

If the O-mode 1.9 T case above is repeated for 0.95 T neutral beam discharges, the density and temperature parameters will be the same and only ω_{ce} need be changed. As Bornatici notes, the second harmonic absorption of O-mode is much weaker than the fundamental absorption, and so in this case it is not important since the fundamental absorption is very weak. These calculations show that a 30 to 40 GHz reflectometer can operate in the typical ATF plasma regimes with little or no absorption from the cyclotron resonances.

Possible Reflection at Edge Gradients

Earlier in this chapter, the geometrical optics approximation was discussed. The final condition for the validity of this approximation was that the local wavelength of the electromagnetic wave being launched must be small compared to the scale length of the variations in the refractive index. This condition, given in Eq. (2.15), can be written as

$$1 \gg \frac{c}{\omega} \frac{\left| \frac{dN}{dr} \right|}{|N^2|} \equiv \gamma_g^{-1} \tag{2.32}$$

where all terms have been previously defined. Under most conditions encountered with microwave reflectometry this condition is easily met. However, if very low edge densities are to be probed using low frequencies, then this condition may eventually be violated. The edge gradient lengths measured by the FRLP[18] in ATF are longer than those attained with the assumed profile shape used in Fig. 2.2, so Eq. (2.32) is not violated.

Effects of Magnetic Shear

In ATF, the components of the toroidal and poloidal (or vertical) fields are of comparable magnitude across most of the minor radius. Also, the magnetic shear (the rotation of the magnetic field as a function of radius) is large. In the geometrical optics approximation, it is assumed that the X- and O-modes propagate independently through the isotropic inhomogeneous plasma. The magnetic shear, however, causes the two modes to couple together; that is, if purely one mode is launched, the propagation through a region with shear will cause some of the wave power in the launched mode to couple over or convert to the other mode. Although mode mixing could, in principle, be used to measure the density and magnetic field profiles or fluctuations simultaneously, the resulting loss in control over the wave polarization would make the analysis of any reflected signal more difficult.[15,19]

Brambilla and Moresco[15,20] showed numerically that a nonnegligible mixing between the two plasma modes occurs when the shear length is short (high shear) compared to the wavelength of the plasma wave. Their conclusion was that mode conversion does not make reflectometry impossible in high-shear machines as long as the direction of the magnetic field at the plasma edge is known sufficiently accurately, so that the unwanted component of the unwanted mode can be filtered out. Filtering out the unwanted mode allows only the desired mode to reach the microwave detectors so that the coupled mode has no effect on the probing beam

phase. The point of their argument was that if the electric field in the launching and receiving waveguide systems can be made to align with the desired plasma mode polarization, then the converted mode will be filtered out by the waveguide system since rectangular waveguide is an excellent polarization filter. Because the magnetic field is rotating and the plasma density does not go to zero rapidly, the location in the plasma edge where the plasma mode polarization is determined for a wave launched towards the plasma, i.e., where plasma propagation begins for the launched wave, is not simply defined.

Fidone and Granata[21] have described the propagation of radiation in a plane-layered inhomogeneous plasma, treating the case where the wave vector is parallel to the density gradient and perpendicular to the plane in which the magnetic field is sheared. They give two limiting cases for the polarization rotation. The first is propagation in high-density plasmas where the plasma modes are weakly coupled by the shear and so the wave polarization rotates with the shear; the second is propagation in low-density plasmas where the plasma modes are nearly undefined (degenerate) and easily coupled by the shear (free-space propagation). The boundary between free-space propagation of the X- and O-modes and polarization rotation (plasma propagation) can be shown to be given by[22]

$$|N_o - N_x| = \frac{2c}{\omega}\frac{d\Psi}{dr} \qquad (2.33)$$

where N_o and N_x are the refractive indices for the O- and X-modes, respectively, ω is the wave frequency, and $d\Psi/dr$ is the local shear where Ψ is the angle that the magnetic field makes with respect to the horizontal midplane and is a function of radius r. The term $|N_o - N_x|$ is a measure of the anisotropy due to the electron density and the magnetic field, while the term $(2c/\omega)(d\Psi/dr)$ is a measure of the shear. If the anisotropy term dominates, then the wave polarization rotates with the applied magnetic field; if the shear term dominates, the wave propagates as if it

33

were in vacuum, and its polarization does not rotate with the magnetic field. Thus, a wave launched toward the plasma along a radius will propagate independently of the sheared magnetic field as long as the shear term dominates. Eventually, the wave reaches a region where the shear and anisotropy terms are of equal order. In this region, the wave polarization begins to rotate due to the magnetic shear but does not rotate as fast as the shear; that is, part of the wave is affected by the shear and part continues to propagate independent of the shear. In this region the plasma propagation begins and the plasma mode of the launched wave is determined. Eventually, the anisotropy term dominates and the entire wave rotates with the magnetic field.

Shear Effects in ATF   For a 30 to 40 GHz reflectometer in ATF, the effect of the shear is to prevent operation in purely one plasma mode. Bell[23] has discussed the effects of the shear in ATF with regard to the ATF electron cyclotron emission (ECE) diagnostic. From his work, it can be shown that the anisotropy and shear terms in Eq. (2.33) are of equal order for a wave frequency between 30 and 40 GHz over a significant region outside the plasma owing to the finite density in the ergodic divertor region through which a reflectometer would have to launch its probing beam. The selection of a plasma mode will thus require choosing some average polarization determined by the average angle of the magnetic field in some region between the plasma edge and the antenna apertures. Modeling of the mode selection problem resulting from the magnetic shear is given in Chap. VI

Possible Wave Tunneling

Earlier in this chapter the exact solution of the wave equation near a reflecting layer was discussed. The assumption of near linearity of $n_e(r)$ in a very small region including the reflecting layer was said to be satisfied if $\frac{d^2 n_e(r)}{dr^2}|r - r_c| \ll \frac{dn_e}{dr}$.

This condition is easily met except when the density profile begins to peak or flatten out. In this region, the density gradient becomes very small, and the width of the reflecting layer becomes very large. Here, the curvature of the profile becomes large and the assumption of linear $n_e(r)$ is invalid.

Normally, the reflectometer probing wave becomes evanescent in the cutoff layer and is completely reflected because it cannot propagate through an evanescent region. However, under the conditions discussed above, part of the evanescent wave may be able to propagate through the cutoff layer (before completely decaying) and come out the other side of the evanescent region. In this case, part of the probing wave is reflected and part is transmitted. Under these circumstances, interpreting the information contained in the reflected signal would be very difficult because of the large width of the reflecting layer (poor localization of the reflected signal) and the possible interference created if the transmitted wave is later reflected and then mixes with the reflected probing beam. This potential problem can be avoided by not operating under conditions that may permit wave tunneling to occur.

Implications for Reflectometry on ATF

This review of wave theory applied to reflectometry experiments is useful in understanding the limitations and complications of reflectometry. The X- and O-mode cutoff surfaces were obtained from the cold plasma dispersion relations, as were the cyclotron resonances. From calculations of the frequencies of the cutoff surfaces and resonances as a function of the density and magnetic field profiles in ATF (Figs. 2.1 and 2.3), the possible frequencies for reflectometry experiments are obtained. For ATF, the 30 to 40 GHz band is of primary interest because of its usefulness at lower densities and the availability of the hardware to build such a

reflectometer. The major complications of a system in this frequency band include absorption at the electron cyclotron resonance in the plasma edge region and the difficulty of wave plasma mode selection due to the magnetic shear. Other minor problems that might occur under special operating conditions include reflection at the edge density gradient and wave tunneling through the cutoff layer near the peak in the density profile. The absorption at cyclotron resonances should be small under most conditions. A possible exception would be O-mode operation in very high density 1.9 T discharges. In these discharges, the fundamental resonance is located outside the last closed flux surface in the ergodic divertor region. The density in the divertor might be sufficiently large that the absorption is nonnegligible. This would result in lost signal amplitude of the reflected signal; however, as long as some reflected signal is returned, the reflected signal can be detected. The problem of plasma mode selection of the launched microwave signal is far more difficult. Because of the magnetic shear and the finite density outside the plasma, the region where plasma propagation begins is approximately the entire path between the antenna and the plasma edge (last closed flux surface). This requires the use of an average polarization determined from the average magnetic field orientation over this range.

CHAPTER III

REFLECTOMETER DIAGNOSTICS

Reflectometry Techniques and Data Interpretation

Two techniques are available to obtain density information from the phase of a reflected wave.[14,24] The simplest technique is to operate the reflectometer at a single frequency; the other is to modulate or sweep the reflectometer microwave frequency. Each of these techniques has advantages; which one to use will depend on the density information that is to be measured.

Fixed Frequency

Cutoff Layer Position/Movement Measurements   A fixed frequency reflectometer may be able to provide information on the inception of cutoff, i.e. cutoff density achieved in the plasma, movement of the cutoff layer, and fluctuations of the cutoff layer. In principle, using a reflectometer to monitor the plasma for the inception of cutoff and movement of the cutoff layer is straight forward; however, strong refractive effects as the density approaches the cutoff density and poor reflection when the portion of the plasma above the cutoff density is small make it difficult to determine the exact time when the cutoff density is achieved. Then after cutoff is achieved, trying to count the fringes (2π phase shifts) due to the movement of the cutoff layer is complicated by the very small signal level near the time of cutoff and by large density fluctuations which can obscure the fringe resets.[25]

37

Density Fluctuation Measurements   A more reliable measurement for fixed-frequency reflectometers is to measure fluctuations in the cutoff layer. This technique can provide measurements of local density fluctuation amplitudes at the cutoff layer. Other techniques for measuring localized density fluctuations exist, but they have limitations.[26] Langmuir probes can measure the mean and fluctuating parts (including the frequency, amplitude, average wave number, and cross-coherence) of the density, temperature and potential.[27] These measurements can suffer from the disturbance of the plasma due to the presence of the probe and the inability to survive, except in the edge, in plasmas of the densities and temperatures obtained in the larger toroidal devices. Therefore, Langmuir probe fluctuation measurements are confined to the edge region of the plasma.[26] Heavy ion beam probes (HIBPs) can measure density fluctuations throughout much of the plasma for moderate density and magnetic field values.[28] HIBPs are often much more expensive than reflectometers, require significantly more access to the plasma, and are technically more complicated; however, they can simultaneously measure the density and potential fluctuations at the same location in the plasma. Far-infrared (FIR), CO_2 and microwave scattering diagnostics are nonperturbative and can measure the frequencies, wave vectors, and amplitudes of the density fluctuations. The primary limitation of scattering diagnostics is the poor spatial resolution of the measurement due to the large scattering volumes.[29,30] A reflectometer density fluctuation measurement can be made anywhere that a cutoff layer can be achieved, and the measurement can be radially localized to the cutoff layer. However, the major limitation of reflectometry is the difficulty in obtaining quantitative results.

Data Interpretation   Analysis of fluctuation data is performed in the frequency domain. Discrete Fourier transforms are performed to transform the data into the frequency domain for analysis. The section "Fourier Transform" in

38

Chap. V discusses the transformation of data signals to the frequency domain and their analysis in more detail. The two primary fixed-frequency measurements are the density fluctuation amplitude and the radial coherence of the density fluctuations. A lower limit estimate of the amplitude of the density fluctuations for O-mode operation is given by the expression[6]

$$\frac{\bar{n}_e}{n_e} \simeq \frac{\tilde{\zeta}\lambda_0}{2L_n} \tag{3.1}$$

where $\tilde{\zeta}$ is the phase fluctuations in the reflected microwave signal in fringe units, λ_0 is the vacuum wavelength of the probing beam, and $L_n = n_e(dn_e/dr)^{-1}$ is the density gradient scale length. The actual probing beam wavelength in the plasma is greater than λ_0, thus resulting in this estimate being a lower limit. This equation is obtained by performing a perturbation expansion on the equation for the O-mode cutoff density [Eq. (2.3)] and transforming the change in the location of the cutoff surface to an equivalent change in the probing frequency. The approximation $\bar{n}_e/n_e = \delta r_c/L_n$ is used to relate the movement of the cutoff layer $\delta r_c \simeq \tilde{\zeta}\lambda_0/2$ to the amplitude of the density perturbation. The estimation of $\bar{n}_e/n_e$ from the phase fluctuations is discussed in detail in Chap. VII.

If the frequency of the probing beam can be changed during or between discharges, a radial profile of the fluctuation amplitudes can be developed and used to understand the possible instabilities producing the fluctuations. A major limitation of reflectometry fluctuation measurements is the need to have accurate density profiles to determine where in the plasma the measurement is being made and the density gradient scale length at that location.

Radial Coherence Measurements   If two probing beam frequencies are used simultaneously in the same antenna system, the fluctuations at two radially separated points can be measured simultaneously. The application of cross-correlation

39

techniques (see the section "Cross-Correlation Analysis" in Chap. V for an explanation of cross-correlation analysis) can be applied to the data to determine the cross-power spectral density (CPSD), normalized coherence γ, and cross-phase of the fluctuations. This analysis can be used to determine the radial width of a coherent perturbation, and if several coherence measurements are made for several different radial separations, the radial correlation length of the fluctuations can be inferred. The radial correlation length L_c is obtained from

$$\gamma = \gamma_0 e^{-\Delta r/L_c} \tag{3.2}$$

where γ_0 is the coherence for zero radial separation and Δr is the radial separation between the cutoff layers for the two probing beams. This equation assumes that the phase fluctuations in the reflected microwave beam are being used in the cross-correlation analysis. If the sine signals from the microwave detectors are being used in the cross-correlation analysis, Eq. 3.2 must be modified to allow for the phase difference between the two signals due to the path length differences.[31] Radial coherence measurements are discussed in detail in Chap. VII.

Swept Frequency

Swept-frequency reflectometers can be of two types: modulated frequency and broadband swept frequency. Frequency-modulated (FM) or narrow-band swept-frequency reflectometers can be used to measure the approximate position of the cutoff layer, movement of the cutoff layer, and density profiles if multiple frequencies are used. A broadband swept-frequency reflectometer can provide a complete density profile for the density region corresponding to the swept frequency.

The basis for the usefulness of a swept-frequency measurement is seen in Eq. (2.20). This equation for the phase change of the reflected wave shows that the phase change can result from three possible sources:

40

1. Movement of the cutoff layer r_c,

2. Changes in the refractive index $N(r)$,

3. Changes in the probing frequency ω.

Thus, if the probing frequency of the reflectometer is swept at a rate df/dt, where df/dt is much faster than the rate of change of the position of the density profile or of the refractive index, the resulting phase shift $\zeta(t)$ can be related to the rate of the frequency sweep to obtain $d\zeta/df$.[14,32,33,34]

The Meaning of $d\zeta/df$ As shown in Eq. (2.20), the phase change that a wave will undergo in propagating through a plasma to a cutoff layer, being reflected at the cutoff layer, and propagating back out of the plasma is given by

$$\zeta = \frac{2\omega}{c} \int_{r_c}^{r_1} N(r)dr - \frac{\pi}{2} \qquad (3.3)$$

As shown by Hubbard[14] and others,[35,36,37] this equation can be Abel inverted to obtain an equation for the position of the cutoff layer in terms of $d\zeta/df$. Equation (3.3) can be differentiated with respect to f at an input frequency f_o to obtain

$$\frac{1}{2\pi}\frac{d\zeta}{df}\bigg|_{f=f_o} = \frac{d}{df}\left\{ \frac{2f}{c} \int_{r_c}^{r_1} N(r,f)dr - \frac{\pi}{2} \right\}\bigg|_{f=f_o}$$

$$= \frac{2}{c}\left\{ \int_{r_c}^{r_1} \frac{d}{df}[fN(r,f)]_{f=f_o}dr \right.$$

$$\left. -f_oN(r_c,f_o)\frac{dr_c}{df}\bigg|_{f=f_o} \right\} \qquad (3.4)$$

Since $N(r_c, f_o)$ is the refractive index at the f_o cutoff layer, it is identically zero, and the second term on the right vanishes as long as dr_c/df is bounded, i.e. the slope of the cutoff layer in the plasma must not go to zero. For the O-mode, this means that the density gradient must not be zero.

41

Equation (3.4) can then be written as

$$\frac{1}{2\pi}\frac{d\zeta}{df}\bigg|_{f=f_o} = \frac{2}{c}\int_{r_c}^{r_1}\frac{d}{df}[fN(r,f)]_{f=f_o}dr \tag{3.5}$$

Budden[12] shows that a packet of waves of frequency f_o travels with velocity V_z parallel to the density gradient, where V_z is given by

$$\frac{c}{V_z} = \frac{d}{df}(fN)\bigg|_{f=f_o} \tag{3.6}$$

He then states that V_z is the component of the group velocity V_g parallel to the density gradient. By analogy to the wave refractive index $N(r)$, $d(fN(r))/df = N'(r)$ is known as the group refractive index. The round-trip delay time τ is then given by[11]

$$\tau = \frac{1}{2\pi}\frac{d\zeta(f)}{df}\bigg|_{f=f_o} \tag{3.7}$$

so that Eq. (3.5) can now be written as[14]

$$\tau = \frac{2}{c}\int_{r_c(f_o)}^{r_1} N'(r_c, f_o)dr \tag{3.8}$$

Abel Inversion for the O-mode   For the case of O-mode waves, the refractive index given in Eq. (2.1) can be rewritten using Eqs. (2.2) and (2.3) as

$$N(r) = \left[1 - \frac{n_e(r)}{n_c}\right]^{1/2} \tag{3.9}$$

where $n_e(r)$ is the local electron density and n_c is the cutoff density for the wave of frequency f_o. For the O-mode, the group velocity $V_g = d\omega/dk$ is obtained from the dispersion relation

$$\omega^2 = \omega_{pe}^2 + c^2k^2 \tag{3.10}$$

Differentiating this equation with respect to the wave number k and using the definition $N(r) \equiv kc/\omega$, the group velocity is found to be $V_g = cN(r)$. Then from

42

the previous definition of the group refractive index, the O-mode group refractive index can be written as

$$N'(r) = \frac{c}{V_g} = \left[1 - \frac{n_e(r)}{n_c}\right]^{-1/2} \tag{3.11}$$

Using Eq. (3.11) in Eq. (3.8), the group delay can now be written as

$$
\begin{aligned}
\tau &= \frac{2}{c} \int_{r_c(f_o)}^{r_1} \left(1 - \frac{n_e(r)}{n_c(f_o)}\right)^{-1/2} dr \\
&= \frac{2}{c} \int_{r_c(f_o)}^{r_1} \frac{[n_c(f_o)]^{1/2}}{[n_c(f_o) - n_e(r)]^{1/2}} dr
\end{aligned} \tag{3.12}
$$

This equation can be rewritten into the form of Abel's integral equation[14]

$$\frac{\tau}{[n_c(f_o)]^{1/2}} = \frac{-2}{c} \int_0^{n_c(f_o)} \frac{dr/dn_e}{(n_c(f_o) - n_e(r))^{1/2}} dn_e \tag{3.13}$$

where the left-hand side can be determined experimentally, and dr/dn_e on the right-hand side is the unknown function determining the density profile. The standard solution, given by Arfken,[38] to this equation is

$$\frac{dr_c}{dn_c} = -\frac{c}{2\pi} \frac{d}{dn_c} \int_0^{n_c} \frac{\tau}{n_e^{1/2}(n_c - n_e)^{1/2}} dn_e \tag{3.14}$$

Integrating and applying the condition that $r_c = r_1$ when $n_e = 0$ gives

$$r_c = r_1 - \frac{c}{2\pi} \int_0^{n_c} \frac{\tau(n_e)}{n_e^{1/2}(n_c - n_e)^{1/2}} dn_e \tag{3.15}$$

Finally, using Eq. (3.7) for the definition of $\tau(n_e)$, Eq. (3.15) can be written in the more usual form[14]

$$r_c = r_1 - \frac{c}{2\pi^2} \int_0^{f_o} \frac{d\zeta/df}{(f_o^2 - f^2)^{1/2}} df \tag{3.16}$$

Therefore, measurement of $d\zeta/df$ over the entire frequency range from 0 to f_o will give sufficient information to obtain the density profile up to $n_c(f_o)$.[14] This is the basis of density profile measurements using broadband swept-frequency

reflectometers. Note that this equation requires the frequency sweep to begin at 0 GHz or that the density profile up to the cutoff density of the lowest probing frequency be known since the integration in Eq. (3.16) is over the phase delay up to the cutoff density $n_c(f_o)$. Since the frequency sweep cannot be started at 0 GHz, the usual approach is to assume an edge density profile up to the lowest frequency and calculate $d\zeta/df$ for this region. The experimental determination of $d\zeta/df$ is accomplished by measuring the phase shift as a function of the frequency change during the frequency sweep. This is often accomplished by measuring $d\zeta/dt$ and obtaining df/dt from a calibration measurement.[34]

For X-mode propagation, the Abel inversion can not be performed analytically because of the dependence of the refractive index on the density and magnetic fields, and the density profile must be determined numerically from the data. Since the X-mode refractive index also depends on the local magnetic field $|\vec{B}(r)|$, $|\vec{B}(r)|$ will have to be measured or calculated for the inversion.[39,40,41] An advantage of the broadband swept frequency-reflectometer over a multichord interferometer in obtaining density profiles is that the Abel inversion is carried out along the propagation path. Thus the density profile may be determined with only one viewing chord and no assumptions regarding the plasma symmetry need be made.

In narrow-band swept reflectometers, $d\zeta/df$ is measured for a small modulated frequency sweep. From Eq. (3.7) it is seen that $d\zeta/df$, through the group refractive index, depends on the whole density profile between r_1 outside the plasma and r_c. The information derived on the position of r_c is therefore limited in accuracy because of the unknown density profile. If multiple modulated frequency reflectometers are used, $d\zeta/df$ can be obtained at multiple points along the profile, and by interpolating between the measured values of $d\zeta/df$ the density profile can be obtained using a modified version of the broadband-swept frequency inversion equation [Eq. (3.16)].

44
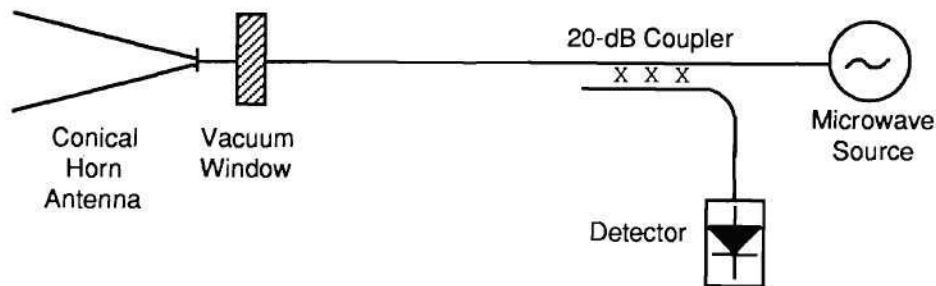
Figure 3.1: Basic fixed-frequency, single-antenna, homodyne reflectometer.[6] (Note that the reference signal comes from reflection at the vacuum window.)

Reflectometry Hardware Techniques

In this section, the different experimental techniques used in most reflectometer experiments are reviewed. The basic schemes or microwave system designs used for reflectometry are discussed along with the microwave hardware necessary to build the microwave system.

Basic Experimental Schemes

In the previous section two different types of reflectometers were discussed: the fixed-frequency system used to measure the absolute movement or fluctuations of the cutoff layer and the swept-frequency system that measures the position of the cutoff layer as a function of frequency. Swept-frequency systems can be broken into two subtypes: broad-frequency sweep systems and narrow-frequency sweep systems.

Fixed-Frequency Systems   Figure 3.1 shows the scheme or layout of the most basic type of fixed-frequency reflectometer.[6,42,25,34] In this scheme, the microwave signal is sent to the plasma via a waveguide run. A window is located at the

vacuum interface to allow the microwaves to pass into the vacuum chamber. This window may be located in the waveguide, so that the antenna can be located nearer to the plasma (inside the vacuum vessel), or mounted on the vacuum vessel independent of the microwave system. In the latter case, the antenna will be mounted outside the vacuum vessel and will launch the microwave beam through the window. In either window configuration, a portion of the microwave beam incident on the window will be reflected (up to $\approx 10\%$). This reflected signal is used as the reference signal. The portion of the signal not reflected by the window is launched into the plasma, where it propagates until it reaches a cutoff and is reflected. After reflection, this plasma signal propagates back out of the plasma and is partially collected by the antenna. The reference signal and the plasma signal propagate back down the waveguide and are directed into a microwave detector by a coupler or power divider. At the detector, the reference signal mixes with the plasma signal, and the resulting combination is converted into a voltage signal at the detector output. Fluctuations in the voltage are then a result of the phase and amplitude fluctuations in the plasma signal. Since the desired signal is the phase fluctuations, the effects of the the amplitude fluctuations are neglected because they cannot be separated from the phase fluctuations.

This simplest type of reflectometer has several limitations. First, internal reflections in the microwave system mix with the reference reflections from the vacuum window to cause distortion of the microwave signal at the detector. An improvement to the system that eliminates this problem is to use two antennas.[39,43] In this case, one antenna is a launcher and the other is a receiver (Fig. 3.2). The reference signal is taken from the transmitting side of the microwave circuit by a coupler and mixed with the plasma signal at the detector by another coupler or single-ended mixer. Since the reference signal is taken directly from the microwave source by a coupler, internal reflections in the transmitting system can have little
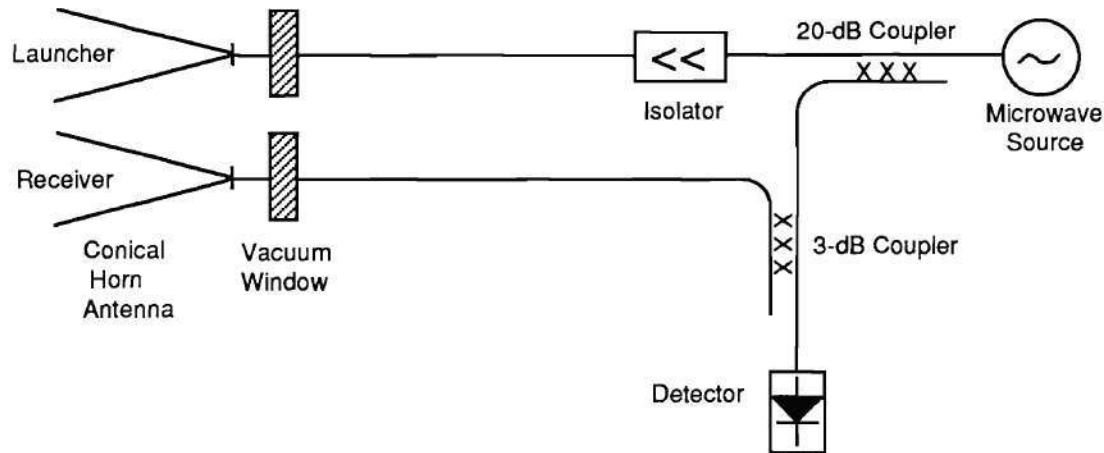
Figure 3.2: Dual-antenna, fixed-frequency, homodyne reflectometer.[39] The advantage of dual antennas is the minimization of errors resulting from spurious reflections in the waveguide system because the reference signal is taken directly from the source by the 20 dB coupler in this figure.

or no effect on the detected signal because the isolator prevents reflections in the launcher circuit from traveling back to the reference coupler, and reflections in the receiving circuit are at such a low power level, since the reference signal is normally at least 10 dB above the plasma signal, that they also have little effect. Using two antennas imposes the physical limitation of requiring two vacuum interfaces and mounting structures.

Another problem with simple homodyne reflectometers is the effect of amplitude fluctuations in the plasma signal resulting from propagation and reflection in the plasma. The simple homodyne system does not allow for absolute phase detection, but rather only the sine of the phase fluctuations times the amplitude fluctuations. Two methods are available to measure the phase fluctuations or decouple the phase fluctuations from the amplitude fluctuations. The simplest method is to use a sine-cosine detection scheme of either the dual homodyne[44,45] or the quadrature phase detection[31] type, both of which rely on two detectors arranged with

47

a 90° phase relation to allow the phase change to be tracked via fringe counting. Quadrature phase detection and dual-homodyne detection are discussed in more detail later in this chapter. The second method of measuring the phase fluctuation is to use a heterodyne receiver.[24] In a heterodyne system, a second microwave source, known as the local oscillator (LO), provides the reference signal. The second source is at a slightly different frequency, where the difference frequency is called the intermediate frequency or IF, so that the phase fluctuations in the plasma signal will be seen as phase fluctuations in the IF signal which is at a low enough frequency to be measured directly. Phase fluctuations show up as fluctuations in the amplitude of the IF signal. The heterodyne scheme suffers from the complexity and expense of using two separate microwave sources and an IF system. Heterodyne detection is discussed later in this chapter.

Frequency Modulated Systems   A block diagram of the FM reflectometer designed for DIII-D is shown in Fig. 3.3.[32,46] Discussions on the Joint European Torus (JET) FM reflectometer are given by Hubbard[14] and Hugenholtz.[24] FM or narrow-band swept-frequency reflectometers are basically narrow-band FM radars[47] with one or more FM microwave sources. The frequency modulation is usually driven by a sawtooth waveform to obtain the small frequency sweep. The system in Fig. 3.3 uses simple homodyne detection with the reference signal coming from reflections at the vacuum window. The plasma signal is collected by the antenna and directed along with the reference signal to the balanced mixer by the directional coupler. The reference signal and the plasma signal combine in the mixer to give a voltage signal proportional to their phase difference. This voltage signal is then amplified and high-pass filtered. The high-pass filtering removes the phase fluctuations resulting from the fluctuating plasma density while allowing the very fast phase changes due to the frequency modulation to be seen. A fringe counting circuit

48
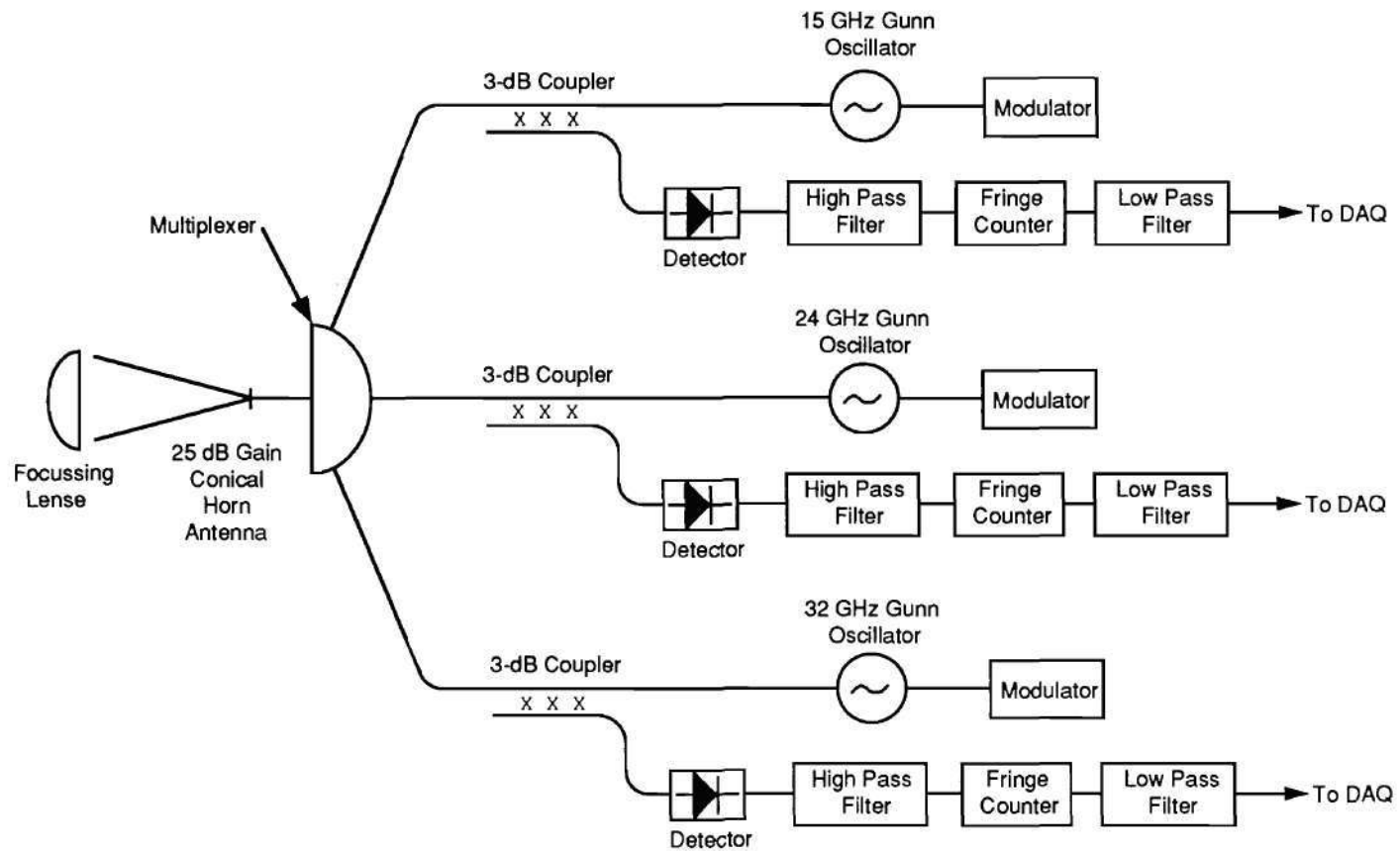
Figure 3.3: Block diagram of the DIII-D FM reflectometer.[32]

49

is then used to count the phase shift as a function of time. The frequency change as a function of time is either measured at the source or calibrated beforehand so that $d\zeta/df$ can be determined, i.e. $d\zeta/df = (d\zeta/dt)(dt/df)$. See the section "The Meaning of $d\zeta/df$" earlier in this chapter for a discussion of the meaning of $d\zeta/df$. Two components contribute to $d\zeta/df$; the first is due to the change in the position of the cutoff layer as the probing frequency is changed, while the second is due to the unequal path lengths traveled by the reference and plasma signals before mixing at the detector. This unequal path length contribution is removed from $d\zeta/df$ by measuring the phase shift as a function of frequency with a fixed reflector in front of the antenna. This phase shift can then be subtracted from the total measured $d\zeta/df$ obtained with plasma.

To go to multiple sources, the DIII-D system uses a special stripline filter circuit to multiplex the multiple frequencies into one system for launching and receiving.[32] Since a single antenna is used, the same stripline filter circuit is used to separate the different frequencies for detection. Additional IF filters are required to ensure that the signal to be fringe counted consists only of the zero IF signal, i.e. to ensure that signals from two different sources do not mix together to form an IF signal.

Broadband Swept-Frequency Systems   These systems have been used in many experiments for density profile measurements.[14,39,37,48,32,33,49,50] Figure 3.4 shows a block diagram of the DIII-D broadband swept-frequency reflectometer. This system is basically the same as an FM system except that the source must be able to sweep over the entire frequency band at a very fast rate to minimize the phase distortion due to fluctuations of the cutoff layer. A two-antenna system is used, so the reference signal is taken from the source output by a coupler and mixed with the reflected signal in a microwave mixer/detector. Overmoded waveguide is used to
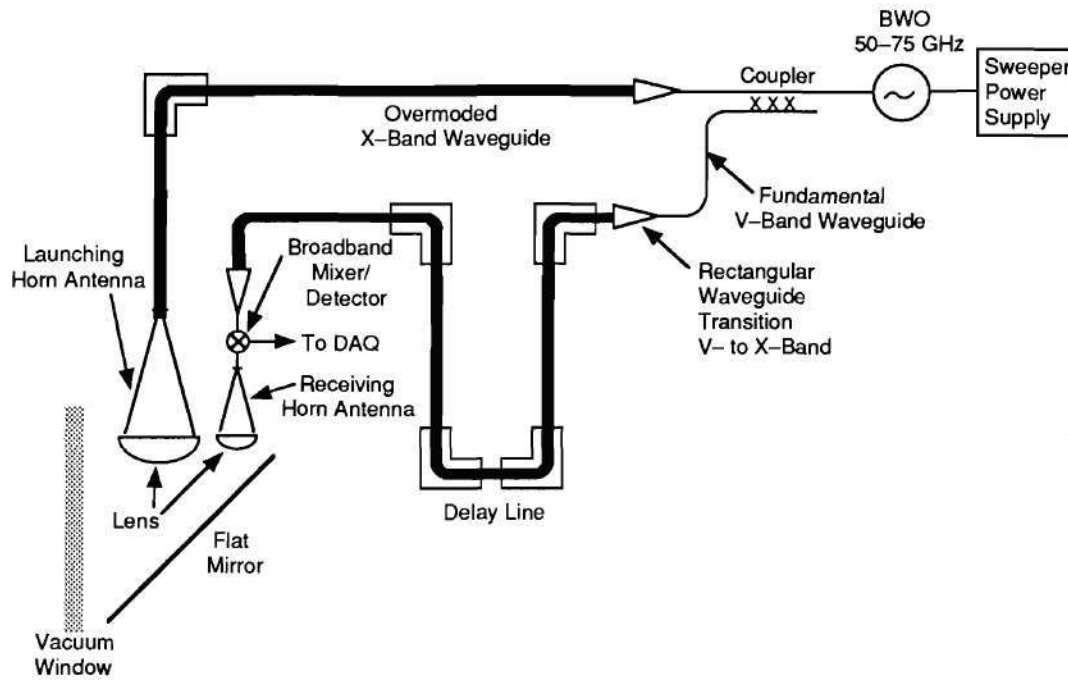
Figure 3.4: Block diagram of the DIII-D broadband swept-frequency reflectometer.[32]

minimize the signal losses in the long waveguide run. The purpose of the delay line is to equalize the plasma and reference arm lengths. A flat mirror aims the launching and receiving antenna beams through the flat vacuum window. Simple homodyne detection is used at the mixer with a zero crossing detector to determine the amount of phase shift as a function of time. The frequency change with respect to time is then combined with the fringe count to determine the time resolved $d\zeta/df$.[41]

Review of the Microwave Hardware

This section is a review of the basic microwave hardware used in reflectometry. In general, a simple description of the component and how it functions is given. Where a mathematical description of the operation of a component is beneficial to the understanding of how it functions in reflectometry, such a description is given.

51

<u>Sources</u>   Several different types of microwave sources can be used for reflectometry; however, Gunn diode oscillators and backward-wave oscillators (BWOs) are the most common.

Gunn Diode Oscillators   Gunn oscillators are semiconductor devices with a limited power-bandwidth product.[51] Because of this power-bandwidth product, Gunn oscillators are normally tunable over less than 1% of their center frequency with power levels exceeding 30 mW; however, their frequency can be modulated or swept over this narrow band by changing the bias voltage to the semiconductor. The ability to electrically modulate the frequency of Gunn oscillators makes them an extremely useful source for FM systems. They are also used in fixed-frequency systems; however, the ability to tune a fixed-frequency source over a large frequency range between discharges is very useful to measure fluctuations at different radial positions in the plasma. Some Gunn oscillators are now being built with a bandwidth approaching 10 GHz with a center frequency between 60 and 80 GHz and a minimum power level of 30 mW.[52] These broadband sources are mechanically tuned, so they are not useful for swept-frequency systems, but their broadband operation is very useful for tunable fixed-frequency systems. Generally, the bandwidth and output power decrease significantly in Gunn oscillators designed for electrical frequency control.[52]

Backward-Wave Oscillators   A BWO produces a microwave signal by injecting electrons along a slow wave structure, which reduces the rf phase velocity to the level of the electron velocity of a traveling-wave tube.[51] The slow wave structure is generated by a helix, and the velocity of the electrons is determined by the potential between the helix and the electron source. As the electrons travel down the helix, they interact with electromagnetic waves having a phase velocity equal

52

to their kinetic velocity. In this interaction, the electrons are slowed down as their kinetic energy is coupled to the energy of the electromagnetic wave. The frequency of these electromagnetic waves is then proportional to the velocity of the electrons. Since the helix voltage controls the velocity of the electrons, the frequency of the electromagnetic waves can be changed by changing the voltage applied to the helix. A power supply can then be designed to sweep or modulate the helix voltage over the range necessary to produce the desired frequency sweep. BWOs are inherently broadband devices with the potential to do very fast full band sweeps. This makes them the primary source for broadband swept-frequency systems. They are also used in FM systems and tunable fixed-frequency systems.

Microwave Detection   A microwave detector is a semiconductor diode that is designed to convert the incident microwave power to a voltage output. These detectors are normally operated in the square law regime where, ideally, the voltage out varies as the square of the power of the input signal.[53] For example, consider homodyne detection with S_1 being the reference signal power and S_2 being the plasma signal. These two signals are mixed at the detector to obtain

$$V = k_d \left| S_1 + S_2 \right|^2 \tag{3.17}$$

where V is the detector output voltage and k_d is the detector response constant or sensitivity. S_1 and S_2 are both complex quantities consisting of an amplitude A and a phase ψ so they can be written as

$$S_1 = A_1 \left(\cos \psi_1 - i \sin \psi_1 \right) \tag{3.18}$$

$$S_2 = A_2 \left(\cos \psi_2 - i \sin \psi_2 \right) \tag{3.19}$$

Here, the phase terms are defined to be

$$\psi_1 = \omega t + \phi_1 \tag{3.20}$$

$$\psi_2 = \omega t + \phi_2 \tag{3.21}$$

where ω is the wave frequency and ϕ is an arbitrary phase delay due to the path length difference. From Eq. (3.17), we then obtain, after the application of some basic trigonometric identities and noting that the detector only responds to the real part of the applied signal,

$$\frac{V}{k_d} = A_1^2 \cos^2(\psi_1) + A_2^2 \cos^2(\psi_2) + A_1 A_2 \left[\cos(\psi_1 - \psi_2) + \cos(\psi_1 + \psi_2)\right] \qquad (3.22)$$

Using the above definitions for ψ_1 and ψ_2, and noting that the detector time response is too slow to respond to signals at the microwave frequency ω so that the signals are rectified and averaged, the final equation for the output voltage of a square law detector is

$$V = \frac{k_d}{2} \left[A_1^2 + A_2^2 + 2A_1 A_2 \cos(\phi_1 - \phi_2)\right] \qquad (3.23)$$

where $\phi_1 - \phi_2$ is the phase difference between the reference signal and the plasma signal resulting from path length differences, i.e. changes in the position of the cutoff layer. The notation in this equation is often simplified by noting that $A_1^2 + A_2^2$ is the sum of the signal powers of S_1 and S_2 and so can be represented by a power term $p_o = p_1 + p_2$. The $2A_1 A_2$ is the cross power, which can be written in terms of the input signal powers, $2\sqrt{p_1 p_2}$. Finally, the detector output voltage can be written as[6]

$$V = \frac{k_d}{2} \left[p_o + 2\sqrt{p_1 p_2} \cos(\phi_1 - \phi_2)\right] \qquad (3.24)$$

Balanced Detectors A balanced detector is basically a combination of two single detectors with equal sensitivities k_d, a differential output, and a 180° phase delay between them. Thus at the balanced detector we have the two voltage signals

$$V_1 = \frac{k_d}{2} \left[p_o + 2\sqrt{p_1 p_2} \cos(\phi_1 - \phi_2)\right] \qquad (3.25)$$

$$V_2 = \frac{k_d}{2} \left[p_o + 2\sqrt{p_1 p_2} \cos(\phi_1 - \phi_2 - \pi)\right] \qquad (3.26)$$

54
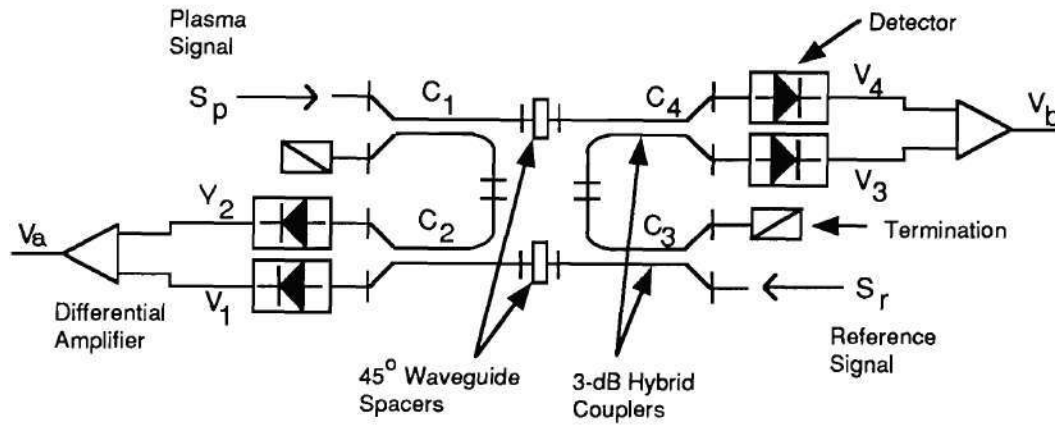
Figure 3.5: A basic quadrature phase detector using four square law detectors and four 3 dB hybrid couplers.[31]

The detector differential output voltage V_{bal} can then be written as

$$V_{\text{bal}} = V_1 - V_2 = 2k_d\sqrt{p_1 p_2}\cos(\phi_1 - \phi_2) \qquad (3.27)$$

The advantage of such a detector is the removal of the large offset voltage in the detector output resulting from p_o. This allows amplification of voltage due to the phase term without obtaining large dc offset voltages or requiring ac coupling.

A balanced detector can be made with a hybrid tee or with 3 dB couplers and two square law detectors. The outputs of the detectors are fed into a differential amplifier to obtain the balanced signal. Also, a balanced mixer can function as a balanced detector if the rf and LO signals are at the same frequency (homodyne), if the IF output can be dc coupled, and if the mixer diodes can operate in the square law regime.

Quadrature Phase Detection   Figure 3.5 shows a schematic of a quadrature phase detector consisting of four detectors and four 3 dB hybrid couplers.[54,31] This phase detector consists of two balanced detectors, produced by a 3 dB hybrid

55

coupler and two square law detectors, connected together by two additional 3 dB hybrid couplers. Each 3 dB hybrid coupler produces a 90° phase delay in the coupled signal, and 3 dB power division in the two output signals. Additionally, two 45° waveguide spacers are located between the two balanced detectors to produce a 90° phase relation between the two balanced signals. Consider the detector associated with voltage V_1 in Fig. 3.5, and define the two input signals as

$$S_p = A_p(t)e^{i\phi_p(t)} \tag{3.28}$$

$$S_r = A_r(t)e^{i\phi_r(t)} \tag{3.29}$$

where S_p is the plasma signal and S_r is the reference signal. S_p couples through couplers C_1 and C_2 to reach this detector. This produces a phase delay of 180° in S_p and a 6 dB drop in the signal power. S_r must go through couplers C_2 and C_3, but it does not experience any coupling phase delay. S_r is delayed by 45° in the waveguide spacer. Using the same technique used in deriving Eq. (3.24), the voltage V_1 out of this detector can be written as

$$V_1(t) = \frac{P_o}{4} + \frac{\sqrt{P_r P_p}}{2} \cos[(\phi_p(t) - 180°) - (\phi_r(t) - 45°)] \tag{3.30}$$

where the constant $k_d/2$ in front of the equation is implicit. Using the same technique to track the phase through the quadrature phase detector for the other three detectors gives the following voltages:

$$V_2(t) = \frac{P_o}{4} + \frac{\sqrt{P_r P_p}}{2} \cos[(\phi_p(t) - 90°) - (\phi_r(t) - 135°)] \tag{3.31}$$

$$V_3(t) = \frac{P_o}{4} + \frac{\sqrt{P_r P_p}}{2} \cos[(\phi_p(t) - 135°) - (\phi_r(t) - 90°)] \tag{3.32}$$

$$V_4(t) = \frac{P_o}{4} + \frac{\sqrt{P_r P_p}}{2} \cos[(\phi_p(t) - 45°) - (\phi_r(t) - 180°)] \tag{3.33}$$

where it is assumed that all four detectors are matched so that they have equal sensitivities k_d. Since each set of detectors forms a balanced detector, the balanced

56

outputs can be written as

$$V_a(t) \;=\; V_1(t) - V_2(t) = \sqrt{p_r\, p_p}\, \cos(\phi_p - \phi_r - 135°) \qquad (3.34)$$

$$V_b(t) \;=\; V_3(t) - V_4(t) = \sqrt{p_r\, p_p}\, \cos(\phi_p - \phi_r - 45°) \qquad (3.35)$$

and again the sensitivity term is neglected. Since V_a and V_b have a 90° phase relation, quadrature phase detection obtains the sine and cosine of the phase delay. With sine and cosine, the absolute phase delay can be determined by tracking the phase from the arc tangent of the two signals (fringe counting). Since the phase is the desired information, the detector sensitivity k_d is not important as long as all detectors have equal sensitivities.

Dual Homodyne Detection   Dual homodyne detection is similar to quadrature phase detection in that it provides the sine and cosine of the phase; however, each signal also contains a large voltage offset.[55] Dual homodyne detection is achieved in the same manner as quadrature phase detection, i.e. a 90° phase delay is inserted between the two detectors, except that unbalanced detection is used. The unbalanced detection is achieved by replacing the balanced detectors with single square law detectors. The voltage offset in the output signal is removed electronically (ac coupling) or digitally (in software). Since dual homodyne and quadrature phase detection function very similarly, quadrature phase detection is sometimes referred to as balanced dual homodyne detection.

Heterodyne Detection   Heterodyne detection mixes the rf signal to be detected with the signal from a local oscillator (LO) operating at a slightly different frequency.[24] The mixer output is then proportional to the rf signal with an IF. The IF is the difference frequency of the rf signal and the LO. A mixer functions in a similar fashion to a detector, except that it is normally strongly biased so that it

57

operates with a linear response rather than a square law response, and the output signal can have frequencies up to the rf range. The mixer output voltage can be written as

$$V_{\mathrm{mix}} = \sqrt{p_o} + \sqrt{p}\cos\left(\omega_{IF}t + \phi_{rf} - \phi_{LO}\right) \qquad (3.36)$$

where the power p is dependent on the response of the mixer diode and the power of the input signals. Mixers can be operated as balanced mixers or ac coupled to eliminate dc offsets. Additionally, high-pass filtering can be used to eliminate any undesired frequency harmonics below the IF, and low-pass filtering can be used to eliminate the undesired harmonics above the IF.

The advantage of heterodyne detection is that the phase information can be obtained by direct phase tracking (fringe counting) of the IF signal because the phase information is now at a much lower frequency. The disadvantages of heterodyne detection are the requirement of the second microwave source and the need to phase lock the LO and the rf source so that the phase difference in the output mixer IF is proportional only to the phase of the rf signal.[24] Phase detection is accomplished by taking the mixer output signal, splitting it into two parts, and delaying one part by 90°. This generates the sine and cosine of the phase information so that fringe counting techniques can be used to track the phase.[24,26]

Antennas Antennas for reflectometer experiments should be of a high gain type that provides good directivity to the probing beam. The object of the antenna is to convert the electromagnetic radiation propagating in the waveguide to free-space propagation and to direct this radiation in a narrow beam to maximize the wave power that is reflected at the cutoff layer back into the antenna. Additionally, narrow beam antenna patterns have a small 3 dB spot size, which improves the poloidal and toroidal localization of the information contained in the reflected signal. Several types of antennas can provide this capability. The antennas most commonly

58

used in reflectometry are the pyramidal and conical horns. An improvement on the conical horn antenna is to put a dielectric lens at the horn aperture to collimate the diverging rays coming out of the horn. Finally, reflector-type antennas such as the Cassegrain and hoghorn parabolic reflector antennas provide a means of collimating the launched rays without the use of a dielectric lens. Heald and Wharton[56] provide a good discussion on the application of these various antennas to plasma physics experiments, while an antenna engineering handbook (e.g., Johnson and Jasik[57]) provides a detailed discussion of the performance of these antennas and how to design one for a specific application.

Vacuum Windows   The vacuum interface for the microwave system normally consists of a vacuum window. The vacuum window may be located in the waveguide so that the probing beam can be launched by an antenna mounted inside the vacuum vessel, or the window may be mounted on the vacuum vessel with the antenna mounted so that the probing beam is launched through the window.[56] Waveguide vacuum windows are usually very thin ($\sim$0.001–0.005 in.) disks of Teflon, Mylar, or mica. They are usually sealed with an O-ring or epoxy at the waveguide flange nearest to the vacuum waveguide feedthrough. For example, such a disk can be clamped against an O-ring between a choke-and-cover flange assembly to form a window adequate for fundamental waveguide systems for frequencies ranging from 26.5 GHz to 140 GHz. The standing-wave ratio for a window of this design is normally smaller than 1.2, and the losses are about 0.5 dB.[56] O-ring sealed windows as described above are easily made for both rectangular and circular waveguide by machining the O-ring groove into the vacuum-side flange.

Windows mounted on the vacuum vessel are standard items obtainable from many vacuum component manufacturers, e.g. Varian, or they can be machined to a desired specification and sealed with an O-ring. Because of their large circumference,

Table 3.1. Rectangular waveguide parameters

Band	Frequency (in GHz)	Inner Dimensions (mm)	Losses (dB/m)	Waveguide Number	Flange Number
X	8.2–12.5	22.860x10.160	0.11	WR-90	UG-39/U
Ku	11.9–18.0	15.799x7.899	0.176	WR-62	UG-419/U
K	18–26.5	10.668x4.318	0.37	WR-42	UG-595/U
Ka (A)	26.5–40	7.112x3.556	0.58	WR-28	UG-599/U
U	40–60	4.775x2.388	1.06	WR-19	UG-383/U
V	50–75	3.759x1.880	1.52	WR-15	UG-385/U
E	60–90	3.099x1.549	2.03	WR-12	UG-387/U
W	75–110	2.540x1.270	2.74	WR-10	UG-387/U
F	90–140	2.032x1.016	3.82	WR-8	UG-387/U
D	110–170	1.651x0.826	5.21	WR-6	UG-387/U
G	140–220	1.295x0.648	7.50	WR-5	UG-387/U
R	220–330	0.864x0.432	13.76	WR-3	UG-357/U

they are usually much thicker than a waveguide window. The presence of the window in the near field of the antenna may distort the radiation pattern, lead to frequency sensitivity due to multiple internal reflections, and cause severe propagation losses. This can be avoided by designing the window to be a multiple of a half-wavelength thick or to have a wedge-shaped cross section. Canting the antenna so that the antenna beam does not have normal incidence on the window can also avoid heavy losses due to Fabry-Perot reflection in the window and help minimize the amount of reflected energy from the window that is received by the antenna.

Waveguide Components A wide assortment of waveguide components are needed to assemble a reflectometer. Table 3.1 lists the standard waveguide bands and gives their frequency range, theoretical propagation losses assuming the conductivity of copper, and flange designator.[58] Such items as couplers or power

dividers, bends, twists, tapered transitions, mode transitions, variable attenuators, phase shifters, and matched terminations will generally be required in building a reflectometer. There are many sources of information on these waveguide components such as textbooks, manufacturers' catalogs, and trade magazines. Gandhi[51] and Adam[53] provide good descriptions of the function and theory of these basic waveguide components.

Previous Reflectometry Experiments

So far in this chapter, the basic theory and techniques of reflectometry have been reviewed, and the basic hardware used in reflectometry systems has been discussed. In this section, previous reflectometry experiments on laboratory plasmas are discussed. In designing a reflectometer, the desired information to be measured must be determined, i.e. absolute density information (profiles or monitoring of the cutoff density) or density fluctuations (inferred from the phase fluctuations in the reflected signal). Once the type of information desired is determined, the type of reflectometer best suited for this measurement can be determined with consideration of the plasma density and magnetic field. As previously discussed, the three basic types of reflectometers and their possible measurements are:

1. Fixed-frequency

   - detect the presence of a cutoff density

   - track the movement of the cutoff layer

   - measure density fluctuations

   - measure radial coherence of density fluctuations if multiple sources are used

2. FM

- measure position of the cutoff layer

- measure movement (and direction) of cutoff layer

- measure density profile if multiple sources are used

3. Broadband swept-frequency

- measure the density profile over the region covered by the frequency sweep

The initial reflectometry experiments on laboratory plasmas involved fixed frequency measurements of the cutoff density and were basically an extension of interferometry. Heald and Wharton[56] discuss an experiment in which both the transmitted and reflected signals were monitored. When the transmitted signal dropped drastically and the reflected signal increased, the maximum plasma density had reached the cutoff density of the microwave signal. Phase measurements of the reflected signal were not made. In 1960, Anisimov[59] reported a more advanced reflectometer experiment in which three separate frequency signals were launched and received by three individual systems. The phase delay of each signal was measured, and the radial profile of the electron density was inferred by computing the predicted phase shift for each of these frequencies assuming a linear or trapezoidal density profile. A similar technique using two frequencies was conducted on the Alpha toroidal device the same year.[60]

The first application of reflectometry to the larger magnetically confined plasma physics devices of the 1970's was the fixed-frequency system operated on the Oak Ridge Tokamak (ORMAK) by Colchin in 1973.[42] This proof-of-principle experiment (the results of which are unpublished) showed that a wave could be launched into the plasma and the phase of the reflected signal measured. This system used a klystron at 34.9 GHz and a single antenna launching waves radially into the plasma in the O-mode. Homodyne detection was used with the reference

62

signal being taken from the source by a 20 dB coupler. The total number of fringes of phase shift before (for reflection off the vacuum vessel) and after cutoff was measured and compared to the predicted phase shift using a numerical model and the line-averaged density obtained from an interferometer. Good agreement between the predicted and measured phase shift was obtained. Fluctuations correlated to MHD instabilities were also observed.[42] After this initial experiment, the klystron source was replaced with a 26.5 to 40 GHz BWO.[61] Swept-frequency measurements were performed, but strong internal reflections in the waveguide system prevented profile measurements. ORMAK used a double vacuum system, i.e. an inner vacuum liner and an outer vacuum vessel enclosing the entire magnet system and inner liner. This required two vacuum windows, one at the liner and one at the outer vessel wall. The beating of the reflections from the two windows and between other reflections made it impossible to determine the phase shift due to the reflection off the plasma. This internal reflection problem led to the design and installation of a dual antenna system using IMPATT diode sources.[61] Each source was sweepable over a 10 GHz range with center frequencies of 45 and 55 GHz, respectively. Unfortunately, the IMPATTs had a very nonlinear frequency sweep, and it was not possible to use them to perform profile measurements.[42,61] The results of these experiments were not published.

In Table 3.2, the previous and present reflectometry experiments on toroidal plasma confinement devices (tokamaks and stellarators) are summarized. In the following sections, most of these experiments are briefly discussed, but since many of the experiments are quite similar they are not all discussed.

Fixed-Frequency Reflectometers

After Colchin's unpublished experiment, two years went by before any further reflectometry experiments were performed. Then in 1975 on the Adiabatic

Table 3.2. Previous reflectometry experiments

Technique	Experiments	Date[†]	Mode	F(GHz)[#]	Measured[¥]
1. Single Fixed Frequency	ORMAK	1973	O	35, 26-40	n_c, $\tilde{n}$
	ATC	1975	O	27-38	$\tilde{n}$
	TFR	1983	O	75-110	$\tilde{n}$
	JET	1984-?	X	29-38	n_c, $\tilde{n}$
	Petula	1985-86	X	60-110	n_c
	T-10	1986	O	36	n_c, $\tilde{n}$
	TJ-1	1988-p	O, X	33-50	$\tilde{n}$
	Wendelstein VII-AS	1989-p	X	47-80	$\tilde{n}$
	Versator-II	1989-p	O	20	$\tilde{n}$
	ATF	1989	O	30-40	$\tilde{n}$
2. Mulitple Fixed Frequencies	TORSO	1976	O	10,27(2)	$\tilde{n}$
	ASDEX	1987	O, X	18-60(3)	$\tilde{n}$
	JET	1988-p	O	18-80(12)	n_c, $\tilde{n}$
	DIII-D	1988-p	O	15-75(7)	n_c, $\tilde{n}$
	JET	1989-p	X	49-57(2)	$\tilde{n},\gamma,L_c$[*]
	ATF	1990-p	O, X	30-40(2)	$\tilde{n},\gamma,L_c$
	DIII-D	1990-p	X	50-75(2)	$\tilde{n},\gamma,L_c$
	TJ-1	1990-p	O, X	33-50(2)	$\tilde{n},\gamma,L_c$
	TFTR	1990-p	X	110-170(4)	$\tilde{n},\gamma,L_c$
3. Single Modulated Frequency	TFR	1978	O	36, 106	n_c
	PLT	1980	O	34	n_c
	Versator II	1990-p	O	20	n_c
4. Mulitple Modulated Frequencies	JET	1988-p	O	18-80(12)	$n_c, n_e(r)$
	DIII-D	1988-p	O	15-75(7)	$n_c, n_e(r)$
5. Broad-Band Frequency Sweep	TFR	1983-85	O	75-110	$n_e(r)$
	Petula-B	1985-86	X	75-110	$n_e(r)$
	TJ-1	1987-p	O, X	33-40	$n_e(r)$
	DIII-D	1988-p	X	50-110(2)	$n_e(r)$
	Tore Supra	1988-p	O, X	25-110(5)	$n_e(r)$

[†]Experiments still operating in the summer of 1991 are indicated by a 'p'.

[#]When more than one microwave source is used, the number of sources used at one time (but not necessarily in one waveguide system) is enclosed in parenthesis.

[¥]n_c – measurement of the position and/or movement of the cutoff layer. The density profile may be deduced from this measurement if the total phase shift during the density rise can be followed.

$\tilde{n}$ – density fluctuation measurement.

$n_e(r)$ – density profile measurement.

[*]γ is the coherence from the cross-correlation of two reflectometer signals reflected from two positions radially separated by δr, and Lc is the radial correlation length estimated from $\gamma(\delta r)$.

64

Toroidal Compressor(ATC) tokamak and in 1976 on the TORSO stellarator, fixed-frequency reflectometers were operated primarily as density fluctuation diagnostics. The ATC reflectometer operated at a single frequency, adjustable from 27 to 38 GHz, in the O-mode using homodyne detection.[4] The magnitude of large-scale MHD oscillations was derived from the phase shift of the reflected signal, and the spectrum of the density fluctuations was measured up to 300 kHz. The TORSO reflectometer operated two fixed frequencies, 10 GHz and 27.3 GHz, in the O-mode with each frequency signal having its own waveguide system.[62] Apparently, this reflectometer used individual antennas for each signal, rather than launching and receiving in the same antenna system. The fluctuations were observed and nominally identified as drift waves. The authors concluded that the amplitude and spectra of these drift waves could explain the observed anomalous particle loss.

In 1983, a reflectometer operating in the 75 to 110 GHz frequency range was installed on the Tokamak Fontenay-aux-Roses (TFR) with two operational modes: fixed frequency or broadband sweep.[63] (It is a common practice for FM and swept-frequency systems to also operate at a fixed frequency to do density fluctuation measurements.) This system used the O-mode with two antennas and homodyne detection. The results of these fluctuation measurements were in agreement with drift wave theory in that the amplitude of the fluctuation spectrum decreased as the cutoff layer was scanned further into the plasma. Large MHD instabilities localized to resonant magnetic surfaces were observed only when the cutoff layer and the resonant magnetic surface overlapped.[2] Similar fixed-frequency fluctuation measurements were made on Petula-B using the X-mode and a sine-cosine detection scheme to give the sign and magnitude of the phase fluctuations in the reflected signal.[40]

In 1984, JET started operating a single-frequency reflectometer, tunable between 29 and 38 GHz, using X-mode and homodyne detection.[25] This system

65

had two unique features: the first use of a Gunn oscillator microwave source for magnetic fusion reflectometry experiments, and the reference signal for the homodyne detection was not taken directly from the source signal but rather from the power reflected from the vacuum window and other waveguide components. This reflectometer utilized an existing ECE waveguide system rather than a separate system for reflectometry. The first JET density profiles were obtained using this reflectometer.[64] The total phase shift after cutoff of the reflectometer signal was measured for several different frequencies and then combined to deduce a profile. This experiment led to the JET multichannel FM reflectometer (discussed later). The JET team also developed a new measurement that relies on measuring the movement of the cutoff layer. By monitoring the collapse of the central density during sawtooth oscillations and comparing the data with computer models, the particle diffusion coefficient was estimated.[65] JET was also the first experiment to use reflectometry, in conjunction with other fluctuation diagnostics, to study fluctuations during H-mode (an improved energy confinement regime) and the transition to H-mode.[66]

Fluctuation measurements were performed on the T-10 tokamak at 36.6 GHz in the O-mode in 1986.[43] This experiment appears to be the first use of heterodyne phase detection in reflectometry. The main thrust of this experiment was to test the possibility of using radio range finder techniques to measure the distance to the cutoff layer. In radio range finders, amplitude modulation of the microwave signal is used to measure the time of flight to the cutoff layer and back. The conclusions were that this technique was possible, and a proposal to use an array of radio range finders with two microwave interferometers to continuously monitor the development of the density profile was made.

The Axially Symmetric Divertor Experiment (ASDEX) tokamak reflectometer appears to be the first reflectometer to launch and receive multiple frequency

signals in the same antenna system, although it is not clear if the experimenters operated multiple frequencies simultaneously.[67] This reflectometer system operated in the 18 to 60 GHz band using three BWOs (18–26.5 GHz, 26.5–40 GHz, and 40–60 GHz) and homodyne detection with the reference taken directly from the source signal. The system consisted of two separate reflectometers mounted 180° poloidally apart, each using a single antenna designed to operate anywhere in the 18 to 60 GHz range. Fixed- and swept-frequency operation was planned, but it is not clear whether the system was designed to allow simultaneous use of more than one frequency in each reflectometer. No other reports on this experiment were found.

In 1988, both JET and DIII-D operated with multiple FM systems in the fixed-frequency mode to monitor fluctuations.[68,32,46,69] The JET system has 12 frequencies between 18 and 80 GHz and uses heterodyne detection with an existing ECE waveguide system. The DIII-D system has seven frequencies between 15 and 75 GHz using homodyne detection and a dual antenna arrangement with the antenna mounted outside the vacuum vessel looking through a flat vacuum window. Both of these experiments monitored the fluctuations simultaneously at multiple radial positions. Special attention was paid to the changes in the fluctuation spectra observed during the transition to H-mode, during H-mode, and during ELMs.[68,70,69] The JET team also refined their particle diffusion coefficient measurements with better radial resolution of the central density collapse and radial propagation of the resulting density pulse.[71,72]

The Wendelstein VII-AS stellarator's reflectometer has provided good fluctuation data. This system operates in the 47–80 GHz range at one frequency in the X-mode using homodyne detection and a single antenna.[6,3] Enhanced fluctuations were observed in currentless neutral beam injection (NBI) plasmas with pellet injection to peak the profile and an edge iota of 0.52. These enhanced fluctuations are thought to be associated with the rational $q = 2$ ($\iota = 0.5$) surface. Analysis of the

broadband fluctuation spectra and comparison with a known 300 Hz modulation are used to analyze the evolution of the iota profile inside the plasma.

Correlation Reflectometry   In 1988, correlation reflectometry was first attempted.[73] This experiment was conducted on JET and was first conceived by Costley during a questions session following an oral presentation on reflectometry in 1986.[64] The basic technique is to launch two or more frequencies simultaneously from the same antenna system and detect each signal separately. If the cutoff layers for each frequency are close enough together, the coherence of the density fluctuations can be calculated using standard cross-correlation techniques.[73] If the coherence is obtained for multiple radial separations, the radial correlation length can be estimated. The JET experiment used a fixed frequency at 49 GHz and a second frequency stepped between 51.3 GHz and 53 Ghz. Homodyne detection was used with a diplexer to separate the two frequency signals to provide > 20 dB isolation between the two detection systems. The results of the experiments were not conclusive. Although researchers did find coherence for their smaller Δf pair, the larger Δf pair showed no coherence. They thus concluded that the radial coherence measurements were possible and that the radial correlation lengths in JET were less than the radial separation corresponding to the larger Δf pair of signals. Correlation reflectometry has since been done on several other machines, including ATF, DIII-D, and TJ-I.

FM Reflectometers

The development of FM reflectometry to determine the position and motion of the cutoff layer was an attempt to overcome the two main limitations of fixed-frequency homodyne reflectometry for monitoring the cutoff layer motion: the inability to tell which direction the motion was in, and the effect of fluctuations

68

on the phase measurement. The technique involves sweeping or modulating the frequency over a small Δf and was first tried on TFR in 1978 to monitor changes in the plasma position for feedback control.[74] The ability to modulate the frequency very fast, i.e. faster than the density fluctuations, greatly reduces the interference in the phase determination resulting from fluctuations. In 1980, Doane et al.[47] operated a single-frequency FM system on PLT using a BWO with a 33.5 to 35.5 GHz sweep. A dual antenna arrangement with homodyne detection was used with the reference signal coming directly from the BWO output. The beat frequency, i.e. the frequency of the occurrence of fringe resets, is used to derive the round-trip delay time τ [Eq. (3.7)]. Measurements of the position of the cutoff layer were in agreement with the expected position deduced from other diagnostics.

In her thesis, Hubbard developed the analysis for and conceptual design of a multiple-frequency FM system.[14] This advancement of FM reflectometry provided a means of obtaining the density profile by determining the round-trip delay time at several points in the plasma. Interpolating between each position at which τ has been measured, the density profile can be obtained using an inversion equation for τ similar to that used for broadband swept-frequency measurements [Eq. (3.15)].

In 1988 (one year later), the JET multifrequency FM reflectometer system was operated.[68] This system had 12 frequencies between 18 and 80 GHz and operated in the O-mode with heterodyne detection. The same year, the DIII-D multifrequency FM system was operated.[32,46,69] This system had seven frequencies between 15 and 75 GHz and operated in the O-mode with homodyne detection. Both systems produced density profiles but apparently are now primarily operated as fluctuation diagnostics as discussed earlier.

Broadband Swept Frequency Reflectometers

In the 1973 experiment, Colchin et al. performed a proof of principle experiment for a broadband swept-frequency reflectometer that had been proposed in an earlier unpublished memo.[35,42,61] He derived the inversion equation for the swept-frequency data and performed a numerical simulation. Fixed- and swept-frequency measurements were attempted, but problems with the microwave system and sources prevented actual profile measurements.[42,61] In 1981, Doane et al.[47] proposed a broadband reflectometer for the Princeton Large Torus (PLT) based on the success of their FM system, and Cavallo and Cano[36] proposed a system for JET in 1982. Apparently, these two experiments also went undone, and so no other broadband swept-frequency reflectometers were built until 1983 when one was installed on TFR.[63]

The TFR broadband reflectometer[63] had a swept frequency between 75 and 110 GHz with a sweep time of 5 ms. A BWO was used as the microwave source. A dual antenna system launching the O-mode with homodyne detection and looking vertically down at the plasma was used. Simonet[63] reported that the density profile was successfully measured, but that several limitations did exist. First, the 5 ms sweep time of the BWO may have led to spurious profile information since the density profile in TFR may change on time scales faster than that, and second, reflectometry cannot provide the profile information for hollow density regions in the plasma.[39]

In 1985, an X-mode broadband reflectometer was operated on the Petula-B tokamak.[48,40] Again, a BWO was swept from 75 to 110 GHz but in 200 μs, and the plasma was viewed radially. The density profile was obtained by numerically inverting the measured phase change and using data on the magnetic field. The use of the X-mode and the upper cutoff layer [Eq. (2.6)] allowed probing of a wide range of densities and observation of the inner radius of the plasma since the magnetic

field in a tokamak increases monotonically as R decreases. A second BWO in the 60 to 90 GHz range allowed the extension of the profile measurements to the edge of the plasma.

A broadband reflectometer sweeping between 33 and 50 GHz was installed on TJ-I in 1987. This reflectometer used either the X- or O-mode depending on the expected density to be achieved in the machine. A BWO with an 850 μs sweep time was used with homodyne detection.[33] Anabitarte gives an excellent discussion on the calibration of a swept-frequency reflectometer and on the interpretation and analysis of the raw data to obtain the beat frequency or group delay.[34] Successful measurements of the density profile were obtained automatically via automated data analysis during plasma discharges in TJ-I. It was noted that faster sweep times ($\sim$ 10 μs) would allow for multiple sweeps during a shot and reduce the effect of fluctuations and density profile changes during the sweep.

The most recent and most successful broadband reflectometer is the one on DIII-D. As reported by Doyle et al.,[41,75] this reflectometer uses a BWO in the frequency band of 50 to 75 GHz. Homodyne detection is used with zero-crossing fringe counting electronics to automatically determine the phase shift during a sweep. The sweep rate is varied between 400 and 1000 μs, and allowing for the reset time of the BWO tube, a profile can be determined every 8 ms. This system operates in the X-mode with a dual antenna arrangement mounted outside the vacuum vessel looking radially into the plasma from the low-field side. The antennas are standard horns with polyethylene lenses for beam forming. A 45° flat mirror aims the antenna beams through the flat fused-silica window and into the plasma. This system has been very successful at determining the density profile in DIII-D, but several limitations are noted. Density fluctuations do produce false fringes during the frequency sweep, resulting in some error in the profile. With a minimum frequency of 50 GHz, the low-density part of the profile is never viewable, so a profile up to

71

the lowest cutoff density must be assumed for the inversion equation. Absorption at the cyclotron harmonic layers has resulted in very low received power levels at the detector during-low field operations. This decreases the signal-to-noise ratio, which can lead to false fringes due to noise in the system. Rapidly evolving profiles are observed in DIII-D during the transition from L-mode to H-mode and during edge-localized modes (ELMs). Since these profile evolutions happen on a time scale comparable to the BWO sweep time, the profile information obtained during the evolution is inaccurate. In spite of these limitations, the measured profiles agree well with profiles measured by Thomson scattering.

Summary

Reflectometry relies on the phase change in the reflected microwave beam resulting from the propagation path length to and from the reflecting layer to obtain information on the density at the reflecting layer. Two techniques are available to obtain this density information: (1) fixed probing beam frequency, and (2) swept probing beam frequency. Fixed-frequency operation can provide information on the inception of cutoff density in the plasma, movement of the cutoff layer, and fluctuations in the density at the cutoff layer. The first measurement is difficult because of the strong refractive effects as cutoff density is approached and because the small size of the reflecting surface immediately after cutoff is achieved makes it difficult to determine the time at which cutoff occurs. Tracking the movement of the cutoff layer after the inception of cutoff is also difficult because the phase of the reflected signal must be tracked over many 2π cycles as the cutoff layer moves. Tracking this phase is difficult because of the inability to tell exactly when cutoff occurred and the small signal level immediately after cutoff resulting from the physically small size of the cutoff layer. The most straightforward measurement for fixed fre-

quency reflectometry is the measurement of density fluctuations at the cutoff layer. In this measurement, the phase does not need to be tracked over many 2π cycles; rather, only the fluctuations in the phase need be measured. The phase fluctuations in the reflected signal are proportional to the magnitude of the density fluctuations localized to the cutoff layer. By using two microwave probing frequencies simultaneously, the cross-correlation between the fluctuations at two different locations in the plasma can be measured. If the frequencies are launched and received in the same waveguide system, the radial correlation length can be determined by performing coherence measurements at several different radial separations.

Swept-frequency reflectometers can be divided into two types: (1) FM, and (2) broadband swept-frequency. FM systems modulate or sweep the frequency over a narrowband, while broadband systems sweep the frequency over one or more waveguide bands. Sweeping the frequency allows the differential phase information $d\zeta/df$ to be determined, where $d\zeta$ is the differential phase change resulting from the differential frequency change df. This function is dependent on the density profile, and by Abel inversion, the density profile function dn_e/dr can be calculated. FM systems measure $d\zeta/df$ at multiple locations along the density gradient and interpolate between these points to obtain $d\zeta/dr$ for the entire profile, while broadband swept systems measure $d\zeta/dr$ in one complete sweep along most of the gradient. The major complication with swept-frequency measurements is the need to track the phase of the reflected signal over many 2π cycles or fringes. Fluctuations in the density at the cutoff layer or fast changes in the local density profile can cause the loss or gain of fringes during the phase tracking.

In implementing either a fixed-frequency or a swept-frequency reflectometer, several major aspects of the hardware system are generic. A reflectometer will use one or two antennas to launch and receive the microwave signal. In the single-antenna arrangement, simple homodyne detection is used to measure the amplitude

and phase of the reflected signal. In a two-antenna system, simple homodyne or more advanced sine-cosine homodyne detection can be used. If the signal level is very low, heterodyne detection can be used to obtain a better signal-to-noise ratio. For broad-band swept-frequency operation, the primary source in use is the BWO which can sweep the frequency over an entire waveguide band. For FM systems, voltage tunable Gunn oscillator sources are primarily used, although BWOs can also be used. For fixed-frequency experiments, both Gunn oscillators and BWOs are acceptable sources.

The initial reflectometry experiment on a laboratory plasma reported by Heald and Wharton[56] involved monitoring both the transmitted and reflected signals from a microwave interferometer. When the transmitted signal fell to zero and the reflected signal increased, they inferred that the cutoff density had been achieved in the plasma. More advanced reflectometry experiments were conducted in the Soviet Union in 1960.[59,60] These experiments involved using multiple fixed frequencies and determining the density profile from the phase delay of each signal. Colchin et al. first applied this technique to a tokamak in 1973 on ORMAK.[42,61] Since the ORMAK experiment, reflectometry experiments have been conducted on at least 15 different tokamaks and stellarators to measure both the density profile and the density fluctuation amplitudes.

CHAPTER IV

FLUCTUATIONS AND INSTABILITIES

Introduction

The phase of a microwave signal reflected from a cutoff layer in the plasma will fluctuate proportionally to the density fluctuations at the cutoff layer. Since the effect of the density fluctuations on the phase of the probing beam will be greatest in a thin layer near the cutoff point in the plasma, the fluctuation information obtained by reflectometry is localized to the cutoff layer. Using the techniques discussed in Chap. III, estimates of the normalized fluctuation amplitudes can be made, as well as the radial width, radial wave number, and radial correlation lengths of the fluctuations. This information, in conjunction with information from other diagnostics, can be used to describe the fluctuations in the plasma and their behavior with various plasma conditions. This information may help in determining the sources of these fluctuations and ways to control them.

It has long been known that the rate at which energy leaves a toroidally confined plasma is much faster than that predicted by neoclassical theory.[1,76] The losses that cannot be attributed to known classical processes are referred to as "anomalous" losses. Generally, the dominant anomalous energy loss is through enhanced electron thermal conduction, but anomalous ion thermal conduction and particle transport may also be important. This anomalous transport has generally been attributed to microscopic plasma turbulence, i.e. turbulence with radial wavelengths

much smaller than the plasma radius.

Small fluctuations in the electric field and magnetic field lead to small fluctuations in particle velocities and radial positions. This can lead to transport of both particles and energy across the confining magnetic field. For low-frequency fluctuations (e.g., $\omega \ll \omega_{ci}$, where $\omega_{ci} = q_i B/m_i$ is the ion cyclotron frequency), a particle's radial velocity can be written as[1]

$$\tilde{v}_r \cong \frac{\tilde{E}_\theta}{B} + \frac{v_\parallel \tilde{B}_r}{B} \tag{4.1}$$

where $\tilde{E}_\theta$ is the poloidal component of the fluctuating electric field, $\tilde{B}_r$ is the radial component of the fluctuating magnetic field, and $v_\parallel$ is the particle velocity along the unperturbed magnetic field $\vec{B}$. The fluctuations in the particle's radial motion can lead to "anomalous" transport of both particles and heat; however, the net transport depends not just on the level of the fluctuations, but also on the correlation between the various fluctuating quantities. Consider the radial particle flux, $\Gamma = n_e V_r$, where n_e is the electron density and V_r denotes the radial fluid velocity. For turbulent plasmas, each plasma quantity can be written with a time-averaged part and a fluctuating part, e.g., $n_e = \langle n_e \rangle + \tilde{n}_e$, where the brackets $\langle\ \rangle$ indicate a time average over many fluctuation cycles so that $\langle \tilde{n}_e \rangle = 0$ and $\langle n_e \rangle$ is the macroscopic density. The fluctuation terms have amplitude and phase, e.g., $\tilde{n}_e(\omega, k, t) = n_e(\omega, k) \exp[i(\vec{k} \cdot \vec{r} - \omega t)]$, where ω is the wave frequency and $\vec{k} \cdot \vec{r}$ is the relative phase. The net particle flux (as given by Liewer[1]) is then

$$
\begin{aligned}
\Gamma &= \langle (\langle n_e \rangle + \tilde{n}_e)(\langle V_r \rangle + \tilde{V}_r) \rangle \\
&= \langle n_e \rangle \langle V_r \rangle + \langle \tilde{n}_e \tilde{V}_r \rangle
\end{aligned} \tag{4.2}
$$

where $\langle \tilde{n}_e \tilde{V}_r \rangle$ denotes the radial particle flux due to turbulence and is defined as

$$\Gamma^t = \langle \tilde{n}_e \tilde{V}_r \rangle \cong \frac{1}{T} \int_{-T/2}^{T/2} \left[\int_{-\infty}^{\infty} \tilde{n}_e^*(\omega, k, t) \tilde{V}_r(\omega, k, t)\, d\omega \right] dt \tag{4.3}$$

and Γ^t represents the turbulence-induced flux due to the correlation between $\tilde{n}_e$ and $\tilde{V}_r$. Thus, to determine the fluctuation-induced transport experimentally, correlations of the fluctuations must be measured.[1]

Instability Analysis

The basic procedure to analyze instabilities in magnetically confined plasma is to expand about the equilibrium solution and assume that the perturbed quantities (density, temperature, magnetic field, etc.) can be represented in the form

$$
\begin{aligned}
&\xi(\vec{r})e^{i(\vec{k}\cdot\vec{r}-\omega t)} \qquad \text{MHD instabilities[77]} \\
&\xi(\vec{k},\omega)e^{i(\vec{k}\cdot\vec{r}-\omega t)} \quad \text{drift wave instabilities[78]}
\end{aligned}
\tag{4.4}
$$

where $\vec{r}$ is the spatial variable and $\vec{k}$ and ω are the complex wave vector and frequency, respectively. MHD and drift wave instabilities are discussed in more detail in the following sections. This representation makes the implicit assumption that the perturbations can be Fourier transformed in time and space. Using this form for a perturbation, the plasma equilibrium equations are linearized and an eigenvalue problem, in the form of the sum of a series of normal modes, is obtained.

For MHD analysis, the initial MHD equations define a static equilibrium, so any perturbation can be expressed as the sum of unique eigenfunctions for a given set of equilibrium and boundary conditions. All the eigenfunctions or eigenmodes have a simple exponential time dependence, which will indicate growth (instability) or decay (stability) of that mode. If the linearized equations are used to define the potential energy of the equilibrium, the energy principle states that any perturbation that decreases the potential energy, i.e. a growing eigenfunction, is unstable because the potential energy is converted to kinetic energy, causing the perturbation to grow.[7]

77

For drift instability analysis, some form of the linearized kinetic equilibrium equations are written in the form of a dispersion relation

$$D(w, \vec{k}) = 0 \qquad (4.5)$$

linking ω and $\vec{k}$ from which the eigenfunctions can be determined. Stability is determined by the complex eigenfunctions $I_m(\omega)$; that is, positive imaginary solutions $(I_m(\omega) > 0)$ have a growing amplitude and are unstable (instability), while negative solutions $(I_m(\omega) < 0)$ are evanescent (stability). Solutions with $I_m(\omega) = 0$ are not unstable, but since they do not grow or diminish in time, they can last indefinitely.[77,5]

It should be noted that the linearized solutions are only valid for small perturbations. In real plasmas, unstable perturbations only briefly remain small enough to be approximated as linear and generally saturate rapidly. Numerical techniques are needed to follow the nonlinear development and multimode interaction of instabilities. However, the linearized solution is still useful because it indicates which instabilities may be active and warrant further analysis.[5,7]

Toroidal instabilities are usually treated as a series of normal modes having the generalized form

$$\xi \, e^{i[(m\theta - n\phi) - \omega t]} \qquad (4.6)$$

where m and n are the poloidal and toroidal mode numbers, respectively. It is possible to return to the wave vector model by defining

$$\vec{k} = \left(\frac{m}{r} \hat{\theta} - \frac{n}{R} \hat{\phi} \right) \qquad (4.7)$$

where $\hat{\theta}$ and $\hat{\phi}$ are the poloidal and toroidal unit vectors, respectively. In this context, the safety factor q is defined as $q = m/n$, and the mode wavelengths are given by $\lambda_\theta = (2\pi r)/m$ and $\lambda_\phi = (2\pi R)/n = (2\pi q R)/m$. [5,7,77]

78

Instability Characterization

If an instability produces a radial displacement

$$\delta r \simeq \delta r_0 \, e^{\omega t} \tag{4.8}$$

where δr_0 is the displacement at $t = 0$, it then has a radial velocity

$$\delta v = \frac{\partial}{\partial t}(\delta r) \simeq \omega \, \delta r_0 \, e^{\omega t} \tag{4.9}$$

and a kinetic energy

$$\delta W \simeq (\rho_0 \Delta r)(\delta v)^2 \sim \rho_0 \, \omega^2 (\Delta r)^3 \tag{4.10}$$

where ρ_0 is the mass density at r_0 and the displacement scale length δr is assumed to be comparable to the density gradient relaxation scale length Δr.[77] The free energy ΔE released by the displacement must provide at least the kinetic energy δW of the displacement for an instability to exist. This is the basic tenet of the energy principle which holds that the potential energy that would be released by a perturbation must exceed the kinetic energy necessary to drive the perturbation for an instability to exist. The characteristic frequency range of such instabilities is then determined from the condition that $\Delta E > \delta W$ and is[77]

$$\omega < \left(\frac{1}{\rho}\frac{\partial \rho}{\partial r}\right)\sqrt{p/\rho} \simeq \left(\frac{1}{\rho}\frac{\partial \rho}{\partial r}\right) v_{Ti} = \frac{v_{Ti}}{L_n} = \frac{\rho_i \omega_{ci}}{L_n} \tag{4.11}$$

where $\rho_i = v_{Ti}/\omega_{ci}$ is the ion gyroradius, $L_n = n_e(dn_e/dr)^{-1}$ is the electron density gradient scale length, v_{Ti} is the ion thermal velocity, p is the plasma pressure, ρ is the mass density, ω_{ci} is the ion cyclotron frequency, and the plasma is treated as an ideal gas undergoing an adiabatic expansion. Note that $\rho_i/L_n \ll 1$, so Eq. 4.11 implies that the frequencies of such instabilities are much less than the ion cyclotron frequency ($\omega \ll \omega_{ci}$).[7,77] This characterization of the fluctuations is valid for those fluctuations driven by relaxation of spatial nonuniformities (gradients).

Fluctuations driven by relaxation of the velocity-space distribution primarily occur at frequencies near ω_{ci} and have wavelengths of the order of the ion gyroradius.[8] The spatial resolution of present reflectometry density fluctuation measurements (frequencies $\lesssim 100$ GHz) is greater than the wavelength of the probing microwave beam, and so the small wavelength fluctuations discussed above will average out over the spatial volume of the probing beam.

The most important low-frequency ($\omega \ll \omega_{ci}$) instabilities are believed to be MHD instabilities and drift wave instabilities. MHD instabilities are the dominant form of the large-scale, low-n perturbations of the plasma, while drift waves are the dominant form of the small-scale (or micro-) instabilities. Higher order n-number instabilities can also contribute to this turbulence. Both kinds of instabilities can be pressure-gradient-driven in stellarators.[1,5,7,77] The MHD instabilities are obtained from a fluid treatment of the plasma, while the drift wave instabilities most often come from a particle (kinetic theory) treatment of the plasma.

Once a perturbation initiates an instability, the growth of the instability has two distinct phases: the linear phase and the nonlinear phase. In the linear phase, the dominant mode, which is the most linearly unstable m,n-mode, grows at an approximately linear rate. As this mode grows, higher order modes also begin to grow at the expense of the dominant mode by taking energy from it. The loss of this energy eventually causes the dominant mode to stop growing or "saturate." The saturation level is the peak energy level of the dominant mode, while the growth rate is the rate of increase of the mode in the linear regime. When the mode has saturated, it is in the nonlinear regime.

The growth rate is often the primary parameter calculated in the theoretical development of most instabilities. Generally, the local instability with the fastest growth rate will dominate the turbulence in that region of the plasma by using up the available free energy before other instabilities driven by the same free energy

80

source can grow. The frequency of most instabilities is to first order the diamagnetic frequency, given in Eq. (4.17) and defined in the section "Drift Wave Instabilities," while the wavelengths are estimated from Eq. (4.7) and $q = m/n$. The saturation level of the dominant mode is generally estimated by assuming that transport occurs due to convection resulting from the fluctuation over the spatial width or amplitude of the fluctuation. This is the principle behind mixing length arguments.[79] From a mixing length argument, the saturation level is then estimated as

$$\frac{\tilde{n}_e}{n_e} \simeq \frac{\Delta}{L_n} \tag{4.12}$$

where Δ is the radial width of the eigenmode. The radial correlation length can be taken to first order to be the radial width Δ. The kinetic treatment used for the drift wave analysis generally assumes a slab model and then may apply a ballooning transformation to include toroidal effects.[79] In the case of stellarators, the parallel wave number $k_\parallel \sim k_\phi$ is not simply defined. It can range from a wavelength of approximately one field period to a wavelength of approximately the torus circumference; that is, $2\pi M/qR < k_\parallel < 2\pi/qR$, where M is the number of field periods.[80,81] The perpendicular wave number is more easily approximated by $k_\perp \simeq k_\theta = m/r$ for those instabilities that do not require the toroidal bad curvature to exist, such as the MHD interchange mode, and $k_\theta = nq/r$ for those instabilities that do require the toroidal bad curvature to exist, such as the MHD ballooning mode.[81,82] The MHD modes and the bad magnetic curvature are discussed in the following sections.

Table 4.1 at the end of this chapter lists the major instability modes, the required theoretical treatment to obtain the mode, and the free energy source. From the equations given in the following sections, the growth rate, frequency, poloidal mode number and $\tilde{n}_e/n_e$ are estimated for each instability mode for the $q = 3/2$ rational surface in ATF. The parameters used in making these calculations are listed in Table 4.2. The $q = 3/2$ rational surface has been chosen for these calculations

81

because it is the dominant rational surface occurring in the density gradient region viewable by microwave reflectometry. Table 4.3 contains a summary of the symbols used in this chapter.

Ideal and Resistive MHD Instabilities

Ideal MHD instabilities are not considered sources of micro-turbulence because if they exist, the plasma is rapidly lost, i.e. the time scale for ideal MHD modes is $\tau \sim a/v_{Ti} \simeq 1\ \mu s$.[82] Thus, a viable plasma confinement device must be ideal MHD stable. Here a is the minor radius and $v_{Ti} = \sqrt{2kT_i/m_i}$ is the ion thermal velocity. Resistive MHD instabilities are derived from the one-fluid MHD equations in which the plasma resistivity is included in Ohm's law.[1,7,77] The ideal MHD instability modes have resistive analogues, so this discussion will deal with the more applicable case of resistive MHD. Pressure-gradient-driven resistive MHD turbulence is often suggested as an important component in confinement in toroidal devices.[83,84,85] The addition of resistivity to the ideal equations would, at first glance, reduce the growth rate of the ideal instabilities because the resistivity dissipates electrical currents. However, the addition of resistivity can produce new instabilities by removing constraints from the ideal equations and, thereby, making states of lower potential energy accessible to the plasma. An MHD treatment of the plasma assumes a fluid model, which requires that the circulating particles be collisional. See the section "Electron Drift Wave Instabilities" in this chapter for an explanation of circulating particles and collisionality.

In the ideal MHD case the magnetic field lines are tied to the plasma, and so the plasma and field lines must move together. The addition of resistivity allows the magnetic field lines to move independently of the plasma or to break and reconnect so that they are no longer frozen into the fluid. This allows the magnetic surfaces to break up into a number of thin filaments called magnetic islands, which thread their

82

way through the plasma. A magnetic island is a filament of plasma with its own set of nested flux surfaces surrounding its own local magnetic axis.[7,77] MHD instabilities are driven by plasma currents or a combination of a pressure gradient and bad magnetic curvature. Bad magnetic curvature occurs in regions where the magnetic field lines are convex so that the magnetic pressure decreases with increasing minor radius. A pressure-gradient-driven instability can occur when a pressure gradient has a component in the direction of the radius of curvature of a field line.[82]

The resistive analogue of the ideal kink mode is the tearing mode for which resistivity allows the magnetic field lines to reconnect to achieve a lower energy state.[1] Since the kink mode is associated with axial plasma currents or plasmas confined by only a poloidal magnetic field (i.e., $q \leq 1$),[10] stellarators are, in general, stable to this class of instabilities. The resistive analogue of the ideal pressure-driven interchange (or flute) mode is the resistive interchange mode.[1] The resistive interchange mode is sometimes referred to as the resistive-g mode because a gravity-like force can be used in the MHD equations to model complicated geometric aspects of the magnetic field. The resistive ballooning mode is obtained from the same resistive MHD development as the interchange mode but is associated with the bad field line curvature region of the toroidal field.[86] In toroidal plasmas, there are two components of the field line curvature. The first is in the poloidal field and is associated with the interchange mode, while the second is in the toroidal field and is associated with the ballooning mode.[87] These modes have been proposed as a possible cause of anomalous thermal transport in stellarators.[84,88]

Interchange and ballooning instabilities are driven by the relaxation of a pressure gradient in an area with bad magnetic curvature.[77] The growth of these modes is tied to the rational surfaces because the field lines close upon themselves (enhancing the instability) and do not map out a flux surface when followed many times around the torus. Since charged particles are tied to the field lines, an inter-

83

change perturbation occurring on a rational surface will allow charge separation due to particle drifts. The resulting electric field produces an outward $\vec{E} \times \vec{B}$ force resulting in an outward particle drift that increases the perturbation. Field lines that don't close upon themselves, i.e. those that map out a flux surface when followed many times around the torus, do not allow charge separation to occur because of the rapid particle transport along the field lines. Plasma perturbations that conform to the field line pitch of a rational surface and cause two adjacent field lines to interchange their positions result in charge separation and growth of the interchange instability. The growth of the ideal interchange mode is inhibited by neighboring flux surfaces that have a different field line pitch, i.e. magnetic shear. This is known as 'shear stabilization.'[88] However, the resistive interchange mode is not stabilized by the shear because a small amount of resistivity allows a significant decoupling of the field line and plasma motion and because the growth of this mode goes as the resistivity to the one-third power. Thus, shear does not stabilize the resistive interchange mode, but the growth rate does decrease with increasing shear.[87]

A magnetic well, i.e., a region with an outwardly increasing magnetic field (as discussed in Chap. I in the section "The Advanced Toroidal Facility"), is stabilizing to the pressure-gradient-driven instabilities because the radius of curvature of the field lines is reversed with respect to the pressure gradient. The driving term in the MHD equations for the interchange mode is only unstable, i.e. positive, when no magnetic well is present. As soon as any amount of well is introduced, the driving term goes negative, and the mode becomes stable. The resistive ballooning mode is driven by a second term in the same MHD equation that involves the pressure gradient and the toroidal field curvature. In general, the ballooning mode is expected to be absent or much smaller than the interchange mode in stellarators.[88,89] This is primarily due to the stabilizing effect of the magnetic shear. However, where a magnetic well will stabilize the interchange mode, it can only reduce the growth

rate and saturation level of the ballooning mode.[86]

The growth rates of ideal and resistive MHD instabilities are very fast, and so they saturate on a time scale much shorter than the length of the plasma discharge.[82] Thus, measurements of the resistive MHD instabilities are made in the nonlinear regime, and the important characteristics to be measured include the fluctuation saturation level, the wavelength, the frequency, and the location in the plasma. Coherence between fluctuating parameters is also very important in determining the transport induced by the instability.[1] The exact saturation levels and frequencies are difficult to predict; however, the spatial locations of the instabilities are easier to predict. The interchange mode is tied to a resonant flux surface but will extend poloidally and toroidally on that flux surface throughout the plasma; however, it is localized in radius to rational flux surfaces in regions with a strong pressure gradient. The ballooning mode is localized to the middle of a field period along a major radius where the toroidal field curvature is worst in the outer half of the plasma and will not extend poloidally or toroidally around the torus.

Resistive MHD instabilities of the interchange type have been observed in several stellarator devices. During the initial operating period of the ATF torsatron, magnetic island formation resulting from magnetic field errors produced very peaked pressure profiles and a smaller plasma, allowing access to the second stability regime. Second stability is discussed in more detail in the following section. The observed fluctuation behavior was consistent with the theoretical predictions for the resistive interchange mode in the second stability regime.[90,91] In Heliotron-E, an $m = 1$ mode was observed and found to be consistent with pressure-gradient-driven MHD instabilities (interchange mode).[92] In the Proto-Cleo torsatron, the observed low-frequency turbulence was attributed to the rippling mode, which is driven by the unstable convection of current in a resistivity gradient.[5,93] This mode is usually localized to the plasma edge and is driven by a plasma current in a region with a

85

resistivity gradient.[94]

MHD in ATF and Second Stability The stability of the ATF plasma to ideal MHD instabilities was an important consideration in the device design.[9] ATF was designed with an ideal and resistive interchange mode stabilizing magnetic well at the plasma center and ideal interchange mode stabilizing shear in the plasma edge region. The MHD stability is determined by the pressure gradient, which is the main source of free energy, and the magnetic field line curvature (shear, magnetic well/hill).

The ATF plasma size is characterized by the average radius a of the last closed flux surface, beyond which the magnetic field is ergodic (magnetic limiter) or displays a separatrix (magnetic divertor). The plasma edge is defined by the $\iota = 1.0$ surface. The rotational transform profile for a standard configuration, shown in Fig. 1.2, is the result of MHD optimization studies. The $q = 1$ and $q = 3$ surfaces are excluded from the plasma, which minimizes the number of high-order rational surfaces in the plasma, since $\iota(r)$ varies from 0.35 at the center to 1.0 at the edge. The $\iota = 0.5$ surface falls within a magnetic well, as shown in Fig. 1.2, which is stabilizing to the interchange modes. The low-order resonances, $0.5 < \iota < 1.0$, fall in a region of high shear that is stabilizing to the ideal interchange and ideal ballooning modes but only slightly reduces the growth rates and saturation levels of the resistive interchange and resistive ballooning modes.[9]

The free energy available to drive the MHD instabilities increases as beta increases, but the accompanying outward magnetic axis (Shafranov) shift increases the magnetic well depth and changes the magnetic field line curvature. If the well depth increases fast enough with beta, there is a beta self-stabilization effect, and the MHD stability improves with beta. This results in stable access to the second stability regime, which is relevant only to the pressure-gradient-driven instabilities.

86

Self-stabilization with beta and second stability are discussed further by Shafranov,[88] Carreras et al.,[95,96] Hender et al.,[97] and Harris et al.[90]

In the second stability regime, resistive MHD instabilities can be, and usually are, unstable. In ATF, the shear in the plasma edge stabilizes the ideal interchange modes, but it only slightly reduces the linear growth rate of the resistive interchange modes. However, second stability does have an effect on the resistive interchange modes. As beta increases, the magnetic well broadens because of the magnetic axis shift, reducing the radial range of the resistive interchange instability. The saturation level of the resistive interchange is therefore reduced with increasing beta in the second stability regime. Thus, measurements of the rms fluctuation levels associated with this instability can give an indication of if and when second stability is achieved.[91]

Resistive Interchange Mode   The theoretical work on resistive MHD instabilities is extensive; for example, see the papers by Carreras et al.,[84,91] Charlton et al.,[89,98] Lee and Carreras,[99] and Shaing et al.[100] Additionally, the MHD equations have been extended to include such effects as compressibility,[86] to extend the equations to the low-temperature collisionality regime,[85] and to include electron temperature gradient effects.[101] The most likely resistive MHD instability mode in a stellarator is the pressure-gradient-driven interchange instability. Carreras et al.[83,84,91] give equations for the linear growth rate and radial width and for the nonlinear correction factor for the saturation density, potential, and magnetic field fluctuation levels in ATF for the resistive interchange mode. The linear growth rate in terms of local parameters is

$$\gamma_m = \frac{1}{S^{1/3}} \left(\frac{\beta}{2} \frac{r}{L_p} R_0^2 \kappa_n k_\theta \frac{q}{\hat{S}} \right)^{2/3} \tau_{hp}^{-1} \tag{4.13}$$

and the linear radial width is

$$\Delta_m = \left(\frac{q^2}{S\hat{S}^2 k_\theta r}\right)^{1/3} \left(\frac{\beta}{2} \frac{R_0^2 \kappa_n}{L_p}\right)^{1/6} r \qquad (4.14)$$

where $m = \langle m \rangle$ is the rms value of the poloidal mode number, $S \equiv \tau_R(r)/\tau_{hp}(r)$ is the local Lundquist number, $\tau_R(r) = r^2\mu_0/\eta(r)$ is the local resistive skin time, $\tau_{hp}(r) = R_0\sqrt{\mu_0\rho_m(r)}/B_0$ is the poloidal Alfvén time, $\eta(r)$ is the resistivity, $\rho_m(r)$ is the mass density, $\hat{S} = (r/q)(dq/dr)$ is the shear parameter, $\beta(r) = p(r)/(B_0^2/2\mu_0)$ is the local beta, $p(r)$ is the equilibrium plasma pressure, $L_p = p(r)/(dp/dr)$ is the pressure gradient scale length, $\kappa_n = 1/R_c = (1/B)(dB/dr)$ is the local value of the averaged normal curvature, R_c is the radius of curvature, and r is the plasma radius. For a stellarator, R_c for the interchange mode is determined from the helical curvature, while for the ballooning mode R_c is determined by the toroidal curvature. In Fig. 4.1 the helical curvature κ_n and the toroidal curvature are shown. Note that the helical curvature dominates the toroidal curvature for $r/a > 0.5$. The implication of this is that the resistive interchange mode will dominate the ballooning mode in this region of the plasma.

The nonlinear radial width of the pressure (and so density) fluctuations is given as

$$\Delta_m^{nl} \simeq \Delta_m \Lambda^{7/6} \qquad (4.15)$$

where Λ is the nonlinear enhancement factor, which depends weakly on the physics parameters and is the solution to the equation

$$\Lambda = \frac{2}{3\pi} \ln\left[\frac{256 S^2 L_p}{\beta R_0^2 \kappa_n} \left(\frac{\hat{S}}{r k_\theta q}\right)^4\right] - \frac{2}{\pi} \ln \Lambda \qquad (4.16)$$

The frequency of the instability mode is approximately the local electron diamagnetic frequency

$$\omega_{*e} = k_\theta v_D \qquad (4.17)$$

where v_D is the electron drift velocity and is defined in Eq. (4.20).

88
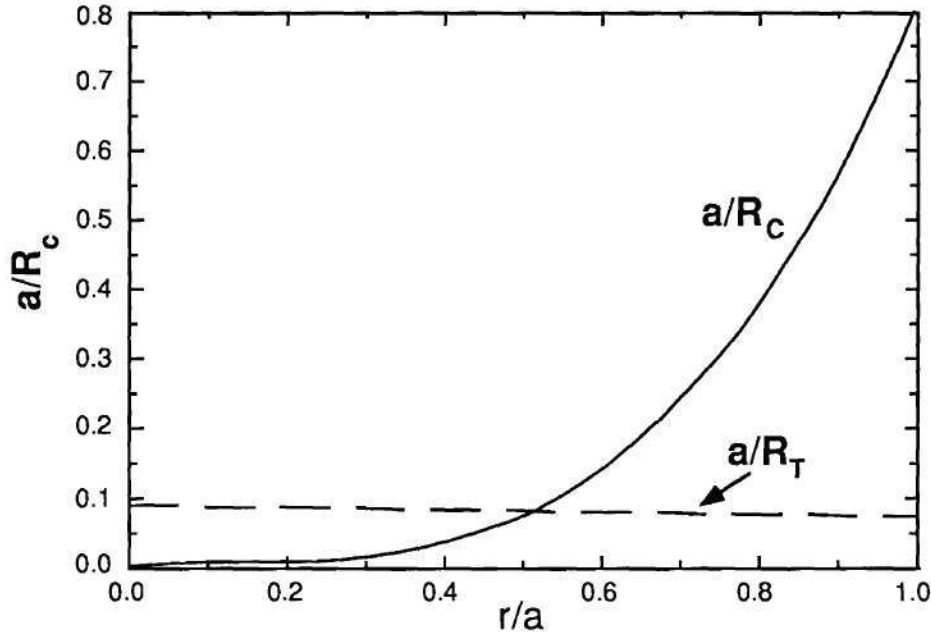
Figure 4.1: The helical and toroidal curvatures vs the minor radius. This plot demonstrates the dominance of the resistive interchange mode driving helical curvature over the resistive ballooning mode driving toroidal curvature.

Resistive Ballooning Mode The ballooning mode is only obtained if the MHD equations are developed for a full toroidal model, as opposed to a simple cylindrical model, and depends on the toroidal bad curvature. Since the ballooning mode is a toroidal mode, i.e., it requires toroidal geometry to exist, the poloidal wave number is defined in terms of the toroidal mode number n, $k_\theta = nq(r)/r$, and the modes are centered on the outside of the torus. The linear growth rate of the resistive ballooning mode in a stellarator is given by Carreras and Diamond[83] as

$$\gamma_n = \frac{1}{S^{1/3}} \left(\frac{\beta}{\sqrt{2}} \frac{rR_0}{L_p} k_\theta q \right)^{2/3} \tau_{hp}^{-1} \tag{4.18}$$

and the linear radial width is given as

$$\Delta_n = \left(\frac{\gamma_n \eta q^2}{k_\theta^2 \hat{S}^2 \mu_0} \tau_{hp}^2 \right)^{1/4} \tag{4.19}$$

89

where $n = \langle n \rangle$ is the rms value of the toroidal mode number, and all the parameters are again local and have been defined in the previous section. The nonlinear theory for the resistive ballooning modes is not given, but to first order, the same enhancement factor can be applied to obtain a nonlinear estimate.[102]

In the outer half of the ATF plasma, the resistive ballooning mode does not play a significant role in driving fluctuations because of the dominance of the helical curvature (which drives the resistive interchange mode) over the toroidal curvature (which drives the resistive ballooning mode), see Fig. 4.1. Charlton et al.[86,89,98] have shown that when compressibility is kept in the resistive MHD equations, the growth rate and thus the saturation level of all the resistive MHD modes (interchange and ballooning) in ATF are reduced to those of the resistive interchange mode outside of the magnetic well, and are small but finite inside the magnetic well, where the interchange mode is stabilized, if a strong pressure gradient exists in the well. The ballooning mode is not expected to be important in the standard ATF configurations.[102] Further discussions of the resistive ballooning mode and its theoretical development are given by Diamond et al.,[103] Hender et al.,[104] and Carreras et al.[105]

Other Resistive MHD Modes   Although the tearing mode should not be important in stellarators, conditions may be encountered in which these modes can become unstable. ATF normally operates in a currentless configuration; however, during magnetic configuration scans, bootstrap currents are produced. These currents are small compared to the currents in tokamaks, but they are large enough to modify the ℓ profile and so possibly change the stability.[106] Diamond et al.[107] and Bateman[7] discuss tearing modes for tokamaks. Garcia[94] discusses resistivity-gradient-driven interchange-like turbulence, which evolves from rippling instabilities in tokamaks. He states that the saturation level of the resulting temperature, po-

tential, and density fluctuations and their related correlation lengths and predicted anomalous diffusion coefficients are sufficiently consistent with experiments to provide a plausible explanation for edge turbulence.

Drift Wave Instabilities

The one-fluid MHD stability model does not include all the sources of free energy or inhomogeneities in the plasma. If a two-fluid or kinetic model is used, new effects, such as two species, finite ion gyroradius, resonant and trapped particles, electron motion along the magnetic field lines, and separate temperature and density gradients, are included. These new effects can alter the existing stability of MHD modes and give rise to new instabilities associated with the new sources of free energy.[1,108] These new instabilities are grouped together under the heading of drift waves because they are associated with particle drifts in the plasma.

Drift waves involve ion motion perpendicular to the magnetic field. The ion charge density set up by this perpendicular motion is then neutralized by electron motion along the field lines. In order for the electrons to be able to neutralize the ion density fluctuations, the electrons must travel many wavelengths along the field in one wave period.[77,87] This condition can be used with the electron momentum equation and the ion continuity equation to obtain an adiabatic equation for the plasma potential. From this equation, the electron drift speed can be inferred as[77,87]

$$v_D = \frac{1}{L_p} \frac{T_e}{e} \frac{}{B}$$ (4.20)

where T_e is the electron temperature and $L_p = p(dp/dr)^{-1}$ is the pressure gradient scale length. Note that this equation neglects other contributions to the drift velocity, such as the $\vec{E} \times \vec{B}$, ∇B, curvature, and polarization drifts. The corresponding diamagnetic drift frequency is

$$\omega_{*e} = k_\theta v_D$$ (4.21)

where k_θ is the perpendicular component of the wave vector. In obtaining this solution, quasi-neutrality ($n_e \simeq n_i$) is assumed, and for simplicity it is assumed that there is no temperature gradient. The important point of this derivation is that the drift wave propagates in the poloidal direction with velocity v_D and that perturbations at one radial position (on one flux surface) do not affect perturbations at another radial position (on another flux surface). This analysis is valid only if the drift waves do not couple to the ion acoustic modes propagating along the field; i.e., the ion cross-field motion must dominate the ion parallel motion. This requirement can be written as $|\omega_{*e}| \gg |k_\| v_s|$, where ω_{*e} is the electron drift frequency, v_s is the ion acoustic velocity, and $k_\|$ is the ion acoustic wave vector component along the field.[87]

The requirement for a drift wave to become unstable is that there be a phase shift between the density and potential fluctuations. Dissipation — for instance, diffusion, thermal conduction, or resonant particles — can cause a phase shift between the density and potential fluctuations for either the electrons or the ions. This phase shift induces a net particle flux that causes growth or damping of the wave. Any imbalance between the ion and electron fluxes caused by the dissipation must be compensated for by the growth or damping of the drift waves in order to maintain quasi-neutrality. Note that a dissipation mechanism that gives rise to equal ion and electron fluxes causes no wave damping or growth.[77,87] If the adiabatic plasma potential equation is modified to include a nonadiabatic term involving collisional effects on the trapped particle population, it is found that the untrapping of particles by collisions provides the necessary phase shift, i.e., dissipative effect, for a net particle flux. The net particle flux then causes the wave to grow.[77]

Electron Drift Wave Instabilities   Drift waves are the most frequently invoked cause of turbulence and anomalous transport.[109,110] These microscopic in-

92

stabilities are driven by the free energy in the density and temperature gradients individually or together. These are electrostatic modes because they exist when the perturbation in the magnetic field is removed. They do create a small magnetic component, which increases with plasma beta and may become important at high beta. The electron drift instabilities can be grouped by their scaling with the electron collisionality, which is included in the wave dispersion relation obtained by a two-fluid or kinetic treatment. The collisionality determines whether a particle can complete one or more trapped orbits before being untrapped by a collision. The electron collisionality operator ν_{*e} can be defined as the ratio of the frequency of untrapping collisions ν_{eff} and the electron trapped particle bounce frequency ω_{be}. This ratio is

$$\nu_{*e} = \frac{\nu_{\text{eff}}}{\omega_{be}} . \tag{4.22}$$

where $\nu_{\text{eff}} \equiv \nu_{ei}/\epsilon$, ω_{be} is the electron bounce frequency, ν_{ei} is the electron collision frequency for electrons with ions, and ϵ is the inverse aspect ratio applicable to the type of trapped particles. Stellarators have two classes of particles: those that are toroidally trapped and those that are helically trapped. Each of these classes of particles has its own bounce frequency, which depends on the scale length of the trapping magnetic well. For toroidally trapped particles, the bounce frequency is given by[111]

$$\omega_{be}^t \simeq \sqrt{\frac{\epsilon}{2}} \frac{v_{Te}}{qR_0} \tag{4.23}$$

and the inverse aspect ratio is simply $\epsilon = r/R_0$. For the helically trapped particles, the bounce frequency is[80]

$$\omega_{be}^h \simeq \frac{v_{Te}M}{R_0} \tag{4.24}$$

and the helical configuration inverse aspect ratio for stellarators is given by $\epsilon^h = \delta (r/a)^2$, where δ is the ratio of the helical magnetic field to the toroidal field. In Eqs. (4.23) and (4.24), $v_{Te} = \sqrt{2kT_e/m_e}$ is the electron thermal velocity and M is the number of field periods in the stellarator.[80] Using ω_{be}^t and ω_{be}^h in Eq. (4.22), the

93

toroidal ν_{*e}^t and helical ν_{*e}^h collision frequencies can be calculated. When $\nu_{*e}^t > \epsilon^{-3/2}$, the circulating electrons are in a collisional regime, and the time between collisions is less than the time for an electron to complete an untrapped orbit. In this regime, the collisions provide a drag-like dissipation that causes a drift wave to grow. For $1 < \nu_{*e}^t < \epsilon^{-3/2}$, the circulating electrons are in a low-collisionality regime, and the particles are marginally trapped. In this regime, a Landau (wave-particle) resonance between the electrons and the drift waves provides the destabilizing dissipation. For $\nu_{*e}^h < 1$, the helically trapped electrons can complete at least one orbit before being untrapped by a collision. The untrapping of the electrons by collisions then provides the destabilizing dissipative mechanism.[77,79]

Collisional or Dissipative Drift Instability   This instability mode is driven by collisions of the circulating electrons in a collisional plasma and is obtained by including electron heat flow along the magnetic field (finite $\chi_\parallel$), electron-ion collisional friction (resistivity), and a finite ion Larmor radius ρ_i in the Braginskii two-fluid equations. The results below were obtained by using a shearless slab geometry approximation for a tokamak with $k_\parallel = \vec{k} \cdot \vec{B}/B$. From this approach, the frequency of this instability is found to be[79,111]

$$\omega = \omega_{*e}\left[1 - k_\perp^2 \rho_i^2(1+\tau)\right] \tag{4.25}$$

where ω_{*e} is the diamagnetic frequency, ρ_i is the ion Larmor radius, $k_\perp \simeq k_\theta = m/r$, and $\tau \equiv T_e/T_i$. The growth rate γ for this mode is given by

$$\gamma = \frac{m_e \nu_{ei}}{k_\parallel^2 T_e} \omega_{*e}^2 k_\perp^2 \rho_i^2 (1+\tau) \tag{4.26}$$

where ν_{ei} is the electron collision frequency and $k_\parallel \simeq k_\phi = m/qR_0$. The radial width of this instability is obtained from the exponentially decaying eigenfunction in the eigenmode equation. The width, for a slab limit, can be approximated as[111]

$$\Delta \simeq \rho_i \left(2\frac{L_s}{L_n}\frac{\tau\omega}{\omega_{*e}}\right)^{1/2} \tag{4.27}$$

94

where $L_s = (R_0 q^2/r)(dq/dr)^{-1}$ is the shear length and in terms of the shear parameter $\hat{S}$ is given by $L_s = R_0 q/\hat{S}$. For low-m values, this mode is the macroscopic drift-dissipative instability. The inclusion of electron temperature gradients in the wave dispersion relation shows that these collisional drift waves smoothly transition to the resistive MHD rippling mode at low m and high collisionality.

Universal Drift Instability This instability is associated with circulating electrons in the low-collisionality regime. In this regime, the drift waves and the electrons have a Landau resonance (Landau dissipation), and so a kinetic description of the plasma is necessary.[1] The frequency of this mode for a shearless slab approximation in a tokamak is given by[79]

$$\omega = \frac{\omega_{*e} \Gamma_0(b)}{1 + \tau\left(1 - \Gamma_0(b)\right)} \qquad (4.28)$$

where $\Gamma_0(b) = I_0(b)e^{-b}$, $b = k_\perp^2 \rho_i^2$, and $\tau \equiv T_e/T_i$. I_0 is the zeroth-order modified Bessel function.[38] The growth rate of this mode is given by

$$\gamma = \frac{\sqrt{\pi}\tau(\tau - 1)\omega^2(1 - \Gamma_0(b))}{k_\parallel v_{Te} \Gamma_0(b)[1 + \tau(1 - \Gamma_0(b))]} \qquad (4.29)$$

where the drift wave scaling, $v_{Te} \gg \omega/k_\parallel \gg v_{Ti}$, has been used. The approximate radial width of this mode can be approximated by the equation for the dissipative drift instability, Eq. (4.27). The effect of an electron temperature gradient in the direction of the density gradient is to stabilize these modes.[1]

Trapped Electron Modes Electrons trapped in magnetic wells are more susceptible to destabilizing collisional effects than untrapped electrons. The dissipative contribution from the trapped electrons is obtained from a kinetic treatment of the plasma. Trapped electron modes (TEMs) are generally driven by temperature gradients with collisional dissipation and have a characteristic frequency of $\omega_{bi} < \omega_{\text{TEM}} < \omega_{be}$, where ω_{be} and ω_{bi} are the electron and ion bounce frequencies,

95

respectively.[77] For a stellarator, the helically trapped particle bounce frequency is given by $\omega_b^h = v_T M/R_0$, where v_T is the particle thermal velocity and M is the number of field periods.[80] The following discussion of the TEMs in stellarators is obtained from work in progress by Dominguez et al. for the ATF stellarator.[80]

In stellarators, the dissipative TEM (DTEM) can occur in the low electron collisionality regime where $\nu_{*e}^h < 1$, while the collisionless TEM (CTEM) can occur in the $\nu_{*e}^h \ll 1$ collisionless regime. The division of the two modes with respect to the collisionality is a result of the frequency scaling used in solving the dispersion relation for each mode. In stellarators, the helically trapped electrons become collisionless much sooner than the toroidally trapped electrons, and so TEMs in stellarators are associated with the helically trapped particles. For the DTEM in a stellarator satisfying the condition $M\Delta_\phi \ll 1$, where Δ_ϕ is the width of the mode in ballooning space,

$$\Delta_\phi = \frac{1}{k_\theta \rho_s} \sqrt{\frac{L_n \omega_{*e}}{M R_0 \omega}} \left(\frac{\delta}{2}\right)^{1/4} \tag{4.30}$$

the mode frequency is given by

$$\omega = \omega_{*e} \frac{1 + \frac{M L_n}{R_0}\sqrt{\frac{\delta}{2}} + \frac{\delta M^2 \rho L_n}{R_0}}{1 + k_\theta^2 \rho_s^2 (1+\delta)^2} \tag{4.31}$$

where L_n is the electron density gradient length, δ is the ratio of the helical magnetic field to the toroidal field, ρ is the normalized radius, and $\rho_s = \rho_i \sqrt{\tau}$. The rms density fluctuation level can then be approximated by $\tilde{n}_e/n_e \simeq \Delta/L_n$, where Δ is the radial width of the mode and is given by

$$\Delta = \left[\frac{M}{q^2}\left(\frac{\delta}{2}\right)^{1/2} \frac{L_s^2}{L_n R_0} \frac{\omega}{\omega_{*e}}\right]^{1/2} \rho_s \tag{4.32}$$

In their present work, Dominguez et al. do not give an expression for the growth rate of the DTEM, but Diamond[112] gives a general expression (not solved for the specific conditions assumed by Dominguez et al.) for the DTEM growth rate,

$$\gamma = \frac{\epsilon^{h 1/2}}{\nu_{\text{eff}}}\left(1 + \alpha\eta_e - \frac{L_n}{R_0}\right)\omega_{*e}^2 \tag{4.33}$$

96

where $\nu_{eff} = \nu_{ei}/\epsilon^h$, $\eta_e = (d \ln T_e)/(d \ln n_e) = L_n/L_T$, and $\alpha = 1.71$ is the thermal force factor. The equations for the CTEM in a stellarator have not been published and so are not given in this review; however, for a tokamak approximation, the papers by Adam et al.,[113] Kadomtsev and Pogutse,[114] and Liu et al.[111] can provide the desired equations for both the DTEM and CTEM.

Summary of Electron Drift Waves   All of the above-mentioned electron drift wave instabilities are more unstable when the effects of bad magnetic curvature are included, that is, when the modes are allowed to have a ballooning structure. The theoretical development of electron drift waves or trapped electron instabilities is extensive. For a review of these instabilities, see Tang[115] and Kadomtsev and Pogutse.[114] Additional references on the DTEM include Chen et al.,[116] Tsang et al.,[117,108] and Chu and Manheimer.[118] In recent drift wave studies on the helical-axis stellarator SHEILA, it was found that the experimentally observed fluctuation behavior was best explained by a collisional drift wave model.[119] Density fluctuation measurements on the L-2 stellarator have recently been reported, and the apparent source of these fluctuations is a collisional drift wave instability.[120]

Ion Drift Wave Instabilities   Ion drift waves have been invoked as the cause of ion anomalous thermal conduction and could be relevant in discharges with large ion temperature gradients. They propagate in the ion diamagnetic direction, which is opposite the MHD and electron drift waves, and have a characteristic frequency $\sim \omega_{*i}$, where

$$\omega_{*i} = \frac{k_\theta}{L_{pi}} \frac{T_i}{eB} \qquad (4.34)$$

is the ion diamagnetic frequency, L_{pi} is the ion pressure gradient length, and T_i is the ion thermal temperature.[121]

Ion Temperature-Gradient-Driven Mode   This mode, known as the η_i mode, is an electrostatic sound wave driven unstable by an ion pressure gradient and has a ballooning structure driven by the bad toroidal curvature. Its existence depends on satisfying some threshold condition in $\eta_i = (d \ln T_i)/(d \ln n_i) = L_{ni}/L_{Ti}$, where L_{ni} and L_{Ti} are the ion density and temperature gradient lengths, respectively. For instance, one threshold condition is $\eta_i > 2/3$.[122] Ion temperature-gradient-driven turbulence has received much attention over the last couple of years as a possible explanation for the anomalous transport in tokamaks.[115,123,124] The theoretical work on the η_i mode is extensive; for example see Mattor and Diamond,[125,126] Dominguez and Waltz,[127] Biglari et al.,[121] Romanelli,[128] Hahm and Tang,[129,130] Rewoldt and Tang,[131] Hassam et al.,[122] and Hamaguchi and Horton.[132]

Biglari et al.[121] have summarized the theoretically predicted physical quantities for the η_i mode and the trapped ion mode, which is discussed in the following section, in full toroidal geometry for a tokamak. Note that the expressions that they give are well behaved in the flat density gradient profile limit. These results can be used to compare experiment with theory in assessing the importance of the η_i mode.

The predicted poloidal wave number range for the η_i mode is $(1 + \eta_i)^{-1/2} > k_\theta \rho_i > \epsilon^{1/2}/q$. For this range of k_θ, the growth rate is given by[121]

$$\gamma_{\eta_i} \simeq \left(\frac{\omega_d}{\omega_{*e}} \frac{1 + \eta_i}{\tau} \right)^{1/2} \omega_{*e} \qquad (4.35)$$

and the radial width is given by

$$\Delta \simeq \left[\left(\frac{q}{\hat{S}} \right)^2 \frac{\omega_d}{\omega_{*e}} \frac{1 + \eta_i}{\tau} \right]^{1/4} \rho_s \qquad (4.36)$$

where $\omega_d = L_n \omega_{*e}/R_0$. An estimate for the rms density fluctuation level is

$$\frac{\tilde{n}_e}{n_e} \simeq \left(\frac{q}{\hat{S}} \right)^{1/2} \left(\frac{\omega_d}{\omega_{*e}} \right)^{1/4} \left(\frac{1 + \eta_i}{\tau} \right)^{3/4} \frac{\rho_s}{L_n} \qquad (4.37)$$

where all the parameters have been previously defined.

Trapped-Ion Modes   If both trapped electrons and ions are present in the plasma, a new class of electrostatic instabilities, generally referred to as the trapped-ion modes (TIMs), can be found. There are many regimes of these modes, and they can be associated with either the electron or ion drift waves. TIMs become important in the low ion collisionality regime given by[121]

$$\nu_{*i} = \frac{\nu_{\text{eff},i}}{\omega_{bi}} < 1 \tag{4.38}$$

where $\nu_{\text{eff},i} = \nu_i/\epsilon^h$ is the effective ion collision frequency with ν_i the ion collision frequency and ϵ^h the helically trapped particle inverse aspect ratio for a stellarator, as discussed in the section "Electron Drift Wave Instabilities." The ion bounce frequency for a stellarator is given by $\omega_{bi} = v_{Ti}M/R_0$. Note that the TIM theory has been developed for the toroidally trapped particles in tokamaks; however, stellarator estimates are made here by using the parameters defining helically trapped particles.

For TIMs, the expected poloidal wave number range is given by Biglari et al.[121] as $k_\theta \rho_i < \epsilon^{h3/4}/q$. The growth rate is given by

$$\gamma_{\text{TIM}} \simeq \left(\sqrt{2\epsilon^h} \, \frac{\bar{\omega}_{de}}{\omega_{*e}} \frac{1+\eta_i}{\tau} \right)^{1/2} \omega_{*e} \tag{4.39}$$

and the radial width is given by

$$\Delta \simeq \left(k_\theta \hat{S} \right)^{-1} \tag{4.40}$$

where $\bar{\omega}_d = \oint dl\tilde{\omega}_d$ is bounce averaged and $\omega_d = (L_n/R_0)\omega_{*e}$. The predicted rms density fluctuation level is

$$\frac{\tilde{n}_e}{n_e} \simeq \frac{(2\epsilon^h)^{1/4}}{k_\theta \hat{S} L_n} \left(\frac{\bar{\omega}_d}{\omega_{*e}} \frac{1+\eta_i}{\tau} \right)^{1/2} \tag{4.41}$$

TIMs are driven by density gradients with collisional dissipation and are further destabilized by temperature gradients. The characteristic frequency of TIMs is $\nu_{*i}/\epsilon^h < \omega_{\text{TIM}} < \omega_{bi}$. Additional information on these instabilities is given by Tang[115] and by Kadomtsev and Pogutse.[114]

99

Electromagnetic Drift Waves   The drift wave modes discussed above have characteristic wavelengths of $\sim \rho_i$. There is a short-wavelength analogue of the η_i mode with $k_\theta \rho_e \lesssim 1$ in which the ions and the electrons interchange their roles. Here, $\rho_e \simeq v_{Te}/\omega_{ce}$ is the electron Larmor radius. This mode becomes unstable when $\eta_e = L_n/L_T \simeq 1$ and contains a magnetic component when $\beta \gtrsim m_e/m_i$. The poloidal wavelength range is approximately $2\pi\rho_e \lesssim \lambda_\theta \lesssim 2\pi c/\omega_{pe}$.[79] Wavelengths in this range will be much less than the resolution of present reflectometer diagnostics.

Summary of Fluctuation Modes in ATF

Table 4.1 lists the major instability modes and their important characteristics for ATF at the $q = 3/2$ rational surface. This table is limited to modes with wavelengths large enough to be resolved by reflectometry, i.e., poloidal wavelengths of order the probing beam diameter at the cutoff layer, ~ 10 cm. The electromagnetic and the velocity space modes are, in general, high-frequency short-wavelength modes that cannot be resolved by reflectometry. The parameters used in making these calculations are listed in Table 4.2. Table 4.3 defines the symbols used in the equations given in this chapter. From Table 4.1 it appears that the resistive interchange and DTE modes will dominate the $\tilde{n}_e/n_e$ spectrum in the edge region of ATF for plasmas with conditions similar to those assumed here. This agrees with the results obtained by numerical studies of the expected turbulence modes on ATF.[80,91,98] Although the numbers listed for the resistive ballooning mode in Table 4.1 would imply that this mode could also be important, it was shown in Fig. 4.1 that the helical curvature, which drives the interchange mode, dominates the toroidal curvature, which drives the ballooning mode. The dissipative drift mode is shown to have a high saturation level for $\tilde{n}_e/n_e$, but its growth rate is so slow that other instabilities will use up the available free energy before this mode can

100

grow and saturate. For this reason, the dissipative drift mode is also not important. Finally, one difference between the resistive interchange and the DTE modes can be used experimentally to distinguish which of these two modes is being observed in the plasma. The resistive interchange mode will be a global mode extending toroidally and poloidally around the torus on a flux surface, while the DTEM will be localized to the outer half of the plasma in one field period. Thus, if coherence is found between fluctuation diagnostics separated toroidally and/or poloidally by one or more field periods, the resistive interchange mode is the likely source of the turbulence.

Table 4.1. Instability table for the edge region (q = 3/2) of ATF

(Parameters used in calculations are given in Table 4.2)

Instability Mode	Treatment	Free Energy Source	Growth Rate	Frequency[§]	<m>	ñ/n[¤]
interchange	resistive-MHD	∇p	1.3×10^4 s^{-1}	3.8 kHz	6	2%[(nl)]
ballooning	resistive-MHD	∇p	7.7×10^3 s^{-1}	2.9 kHz	4.5	2.6%[(nl)]
dissipative drift	two-fluid	$\nabla n_e, \nabla T_e, \nabla p_e$	8 s^{-1}	25 kHz	45[†]	6%
universal drift	kinetic	$\nabla n_e, \nabla T_e, \nabla p_e$	(low collisionality regime only)[*]			
DTEM	kinetic	$\nabla n_e, \nabla T_e, \nabla p_e$	1.6×10^4 s^{-1}	40 kHz	45[†]	4.5%
CTEM	kinetic	$\nabla n_e, \nabla T_e, \nabla p_e$	(collisionless regime only)[*]			
η_i modes	kinetic	$\nabla n_i, \nabla T_i, \nabla p_i$	4.5×10^4 s^{-1}	-9.5 kHz[#]	45[†]	0.4%
TIM	kinetic	$\nabla n_i, \nabla T_i, \nabla p_i$	2.8×10^4 s^{-1}	-8.3 kHz[#]	37[¥]	0.5%

[¤]Spectrum integrated (rms) value

[(nl)]Nonlinear estimate.

[§]The frequency listed for each instability simply gives the estimated frequency for the assumed set of plasma conditions. The actual instability frequencies will be spread out (and possibly shifted) around this frequency.

[*]For the assumed plasma conditions in these calculations, the electrons are collisional.

[#]A negative mode frequency indicates propagation in the ion diamagnetic direction.

[†]The value of <m> for these modes assumes $k_\perp \rho_s = 0.3$.

[¥]The value of <m> for this mode is estimated assuming $k_\perp \rho_s = 0.25$.

Table 4.2. Physical parameters used in estimating the density fluctuation level at the q = 3/2 surface in ATF

Plasma parameters	Assumed value
q	3/2
r	0.23 m
a	0.30 m
$n_e = n_i{}^*$	4×10^{18} m^{-3}
T_e	75 eV
$T_i{}^*$	25 eV
$L_{ne} = L_{ni}{}^*$	-0.2 m
$L_{Te} = L_{Ti}{}^*$	-0.2 m
B_0	0.95 T
$B(r)$	0.75 T
$\kappa_n = 1/R_c$	-1.4 m^{-1}
$\hat{S}$	-1.1
η	10^{-5} $\Omega \cdot$m
S	1.1×10^5
β_0	0.25 %
ν_{ei}	4×10^5 s^{-1}
v_D	1×10^3 m/s
δ	0.2
M	12

*Ion density and temperature profiles are not known, so these values are only estimates.

Table 4.3. Definitions of symbols used in Chap. IV

symbol	description
B	magnetic field
e	electron charge
$k_{\parallel}, k_{\perp}$	parallel and perpendicular wave vectors in slab geometry
k_{θ}, k_{ϕ}	poloidal and toroidal wave vectors in toroidal geometry
L_n, L_T, L_p	electron density, temperature and pressure gradient lengths
L_{ni}, L_{Ti}	ion density and temperature gradient lengths
L_s	shear length
m	poloidal mode number
M	number of field periods in stellarator
m_e, m_i	electron and ion mass
n	toroidal mode number
n_e, n_i	electron and ion density
q	safety factor
R_c	radius of curvature of the magnetic field
S	Lundquist number
$\hat{S}$	shear parameter
T_e, T_i	electron and ion temperature
v_D	electron drift velocity
v_{Te}, v_{Ti}	electron and ion thermal velocities
α	thermal force factor
β	plasma beta
γ	instability mode growth rate
δ	ratio of helical to toroidal magnetic field
Δ	radial width of instability eigen mode
ε	inverse aspect ratio
ε^h	helical configuration inverse aspect ratio for stellarators
η	resistivity
η_e, η_i	ratio of the density to temperature gradient lengths for electrons and ions
κ_n	averaged normal curvature of the magnetic field
ν_{ei}	electron-ion collision frequency
$\nu_{eff}, \nu_{eff,i}$	frequency of untrapping collisions for electrons and ions
ν_{*e}, ν_{*i}	electron and ion collisionality operators
ρ_e, ρ_i	electron and ion Larmor radii
ρ_s	modified ion Larmor radius
τ	ratio of electron to ion temperature
τ_R	resistive skin time
τ_{hp}	poloidal Alfvén time
ω	instability mode frequency
ω_{be}, ω_{bi}	electron and ion bounce frequencies
ω_d	electron drift frequency
ω_{ExB}	ExB drift velocity
ω_{*e}	diamagnetic frequency

CHAPTER V

SPECTRAL ANALYSIS OF FLUCTUATION DATA

Introduction

The analysis of fluctuation data, known as signal or spectral analysis, is primarily carried out in the frequency domain, that is, the array of phase fluctuation data vs time is transformed into the frequency domain to obtain the fluctuation frequency spectra. In this way, the amplitude of each frequency component in the spectrum can be observed, which allows the signal analysis to concentrate on the dominant fluctuations. In general, fluctuation data digitized by transient recorders with a sampling frequency f_s (typical frequencies are 256, 512, or 1000 kHz) and a specific amount of memory per signal n_T (typically 8192, 16,384, or 24,576 data points).[133] The sampling interval is then $\Delta t = 1/f_s$, and the time length of the digitized signal is $T = n_T \Delta t$. Low-pass filtering is performed at a frequency of approximately 80% of the Nyquist frequency $(f_s/2)$ to eliminate aliasing of the data. Aliasing of the data occurs when fluctuations with frequencies greater than the Nyquist frequency are present in the data. Because these fluctuations have a period shorter than the sampling interval, they are folded so as to appear as fluctuations below the Nyquist frequency. Since no low-pass filter has an infinitely sharp rolloff, the anti-aliasing filter cutoff frequency is normally set at approximately 80% of the Nyquist frequency.[134]

105

Transformation to the frequency domain for signal analysis is performed on a portion of the signal (called one realization or temporal window) of N records. Thus, the transformation results in a time averaging over $\Delta T = N\Delta t$. The frequency resolution of the transformed signal is determined by the number of intervals N over which the Fourier transform is calculated and the leakage effect associated with windowing the data. Leakage and data windowing are discussed in the next section. The minimum frequency resolution Δf is then given by the ratio of the spectrum width or sampling frequency f_s to the number of intervals used in the transform, $\Delta f = f_s/N$, and so to obtain better frequency resolution, a longer signal and so more time averaging must be used. The transformed signal can be used one temporal window at a time or $n_w = n_T/N$ windows can be averaged to obtain the average spectra, where $n_w \leq n_T/N$ and is a whole number. Overlapping windows with $n_w = 2n_T/N - 1$ (obtained by stepping $N/2$ records for each realization) can be used to increase the number of windows being averaged over to improve the statistical accuracy of the spectra.[135]

Fourier Transform

Continuous Fourier Transform

The continuous Fourier transform (CFT) can be used for characterizing linear systems and for identifying the frequency components making up a continuous waveform. The Fourier transform pair for continuous signals is[136]

$$S(f) = \int_{-\infty}^{\infty} s(t)e^{-i2\pi ft}dt \tag{5.1}$$

$$s(t) = \int_{-\infty}^{\infty} S(f)e^{i2\pi ft}df \tag{5.2}$$

where $s(t)$ is the continuous time domain signal, $S(f)$ is the continuous frequency domain signal, and f and t have the limits $-\infty < f < \infty$ and $-\infty < t < \infty$.

However, in experimental applications a continuous waveform is not obtained. The sampling of the signal results in a finite, discrete version of the Fourier transform.[136]

Discrete Fourier Transform

The discrete Fourier transform (DFT) pair that applies to sampled versions of the continuous signals $s(t)$ and $S(f)$ is[136]

$$X(f_j) = \frac{1}{N} \sum_{t_k=0}^{N-1} x(t_k) \exp \frac{-i2\pi f_j t_k}{N} \tag{5.3}$$

$$x(t_k) = \sum_{f_j=0}^{N-1} X(f_j) \exp \frac{i2\pi f_j t_k}{N} \tag{5.4}$$

for $f_j = 0, 1, \ldots, N-1$ and $t_k = 0, 1, \ldots, N-1$. $X(f_j)$ and $x(t_k)$ simply represent discrete samples of the continuous waveforms $S(f)$ and $s(t)$. Note that $X(f_j)$ and $x(t_k)$ are, in general, complex series. Although most of the properties of the CFT are retained, some differences do result from the constraint that the DFT must operate on sampled waveforms defined over finite intervals.

When $x(t_k)$ is real, the real part of $X(f_j)$ is symmetric about the folding frequency f_f where $f_f = f_s/2$, and the imaginary part is antisymmetric. This means that the Fourier coefficients between 0 and $N/2 - 1$ can be viewed as the positive frequency (real) components of the signal, while the coefficients between $N/2$ and $N - 1$ can be viewed as the negative frequency harmonics between $-N/2$ and 0. When $x(t_k)$ is real, the negative frequency harmonics are simply a mirror image of the real components; however, if $x(t_k)$ is complex, the Fourier components between $N/2$ and $N - 1$ represent the true negative frequencies in the signal.[136] Negative frequencies represent the frequency of waves traveling in the reverse direction.[44,45]

In the application of discrete Fourier analysis, two problems are often encountered: aliasing and leakage. Another more difficult problem, which is generally ignored, is finding the statistical reliability of an individual power spectral estimate

when the signal being analyzed is noise-like. This problem is generally overcome in fluctuation analysis by averaging many individual spectra together.[135,136]

Aliasing   Aliasing occurs when high-frequency components in the time domain signal impersonate low frequencies because the sampling rate is too slow. The discrete sampling of a continuous waveform with a frequency f above the folding frequency f_f (Nyquist frequency) results in a discrete waveform with an apparent frequency $f_a = f_f - (f - f_f)$ below the folding frequency. This problem is easily avoided by requiring the sampling rate to be at least twice the frequency of the highest frequency present. In practice, this requires that low-pass filters be used to attenuate frequencies above the folding frequency.[136]

Leakage   The problem of leakage is inherent in the Fourier analysis of any finite record. The record has been formed by looking at the actual signal for a period of T seconds and by neglecting everything that happened before or after this period. This is equivalent to multiplying the continuous signal by a rectangular data window. When the transformation to the frequency domain is made, the effect of the rectangular data window is a function with an amplitude of the form $(\sin x)/x$ centered at the frequency of each waveform in the signal. This amplitude function has a series of sidelobes (spurious peaks), which give false contributions to the amplitude of the waveforms at other frequencies. This sidelobe contribution is the leakage effect.[136]

The leakage problem is minimized by applying a data window, other than a rectangular window, to the time series signal, which has lower sidelobes when transformed to the frequency domain. This windowing function simply provides a smoother beginning and ending to the record to minimize the sidelobe production. A common windowing function is the Hanning window, which consists of a cosine

bell on a pedestal. The Hanning window in the time domain is defined as[135]

$$w_H(t) = \cos^2\left(\frac{\pi t}{\Delta T}\right) \tag{5.5}$$

where $\Delta T = N\Delta t$ was defined earlier and t is the data time array and is N records (data points) long. By expanding the cosine-squared term in this equation, a form suitable to numerical implementation is obtained,

$$w_H(t) = \begin{cases} \frac{1}{2}\left[1 + \cos\left(\frac{2\pi t}{\Delta T}\right)\right] & |t| \le \frac{\Delta T}{2} \\ 0 & |t| > \frac{\Delta T}{2} \end{cases} \tag{5.6}$$

Note that the Hanning window is defined in both the time and frequency domains and can be applied to the data window in either domain, i.e., before or after the application of the fast Fourier transform (FFT). The tapering of the data by the Hanning window causes a loss of amplitude in the resulting signal, which is adjusted for by multiplying by $\sqrt{8/3}$. Many windowing functions exist, each with their own pros and cons.[134,135]

Fast Fourier Transform

The FFT is the primary digital method of transforming signals from the time domain to the frequency domain.[136] The FFT rapidly computes a good approximation of the DFT for a finite-duration sampled signal. The efficient application of the FFT requires that the window length contain $N = 2^p$ records, where p is a rational number. The data signal is then divided up into n_w realizations. Each realization is multiplied by a Hanning window of length N and processed through the FFT procedure to obtain the DFT of the record. The output record is complex, having an amplitude and phase. The auto-power spectral density (APSD) or power spectrum of the original function is obtained by squaring the complex output record, $APSD = X(f_j)^2 = X(f_j) \cdot X(f_j)^*$ where $X(f_j)^*$ is the complex conjugate.

Cross-Correlation Analysis

Cross-Correlation Function

The correlation of two signals provides the similar component present in both signals as the output. The correlation integral for two signals $x(t)$ and $y(t)$ is defined as[134]

$$c_{xy}(t) = \int_{-\infty}^{\infty} x(\tau)y(t+\tau)d\tau \tag{5.7}$$

where c_{xy} is precisely the cross-correlation function representing the total correlation between $x(t)$ and $y(t)$, and t in $y(t+\tau)$ represents a time delay between the two signals. For $t = 0$, the equal-time cross-correlation function is obtained. The auto-correlation function is the special case of $x = y$. For discrete sampled signals, the cross-correlation function of $x(t_k)$ and $y(t_k)$ is defined as[134]

$$c_{xy}(t_k) = \frac{1}{N} \sum_{\tau=0}^{N-1} x(\tau)y(t_k+\tau) \tag{5.8}$$

The easiest way to obtain the cross-correlation function is via the frequency domain and the FFT. If $X(f_j)$ and $Y(f_j)$ represent the DFTs of $x(t_k)$ and $y(t_k)$, respectively, then the frequency domain cross-correlation function can be obtained from[134,136]

$$C_{xy}(f_j) = X(f_j) \cdot Y^*(f_j) \tag{5.9}$$

where $C_{xy}(f_j)$ is the DFT of $c_{xy}(t_k)$ and is called the cross-power spectral density (CPSD). If $x(t_k) = y(t_k)$, the APSD will be obtained. Since the cross-correlation function is complex, it contains the amplitude and phase of the coherent parts of the two initial signals. The amplitude is known as the cross-spectral amplitude, while the phase is known as the cross-spectral phase and represents the phase delay between the two signals for each f_j component. The phase has a range of $-\pi \rightarrow \pi$.[135]

Cross-Correlation Coefficient Function

The cross-correlation coefficient function $\rho_{xy}(t_k)$ represents the normalized total correlation between two time domain signals for a time lag of t_k and is estimated by[134]

$$\rho_{xy}(t_k) = \frac{c_{xy}(t_k)}{\sqrt{c_{xx}(0)c_{yy}(0)}} \qquad (5.10)$$

where $c_{xy}(t_k)$ is defined by Eq. (5.8) and $c_{xx}(0)$ and $c_{yy}(0)$ are simply the cross correlation functions for zero time lag, which are estimated by $\sum_j C_{xx}(f_j)$ and $\sum_j C_{yy}(f_j)$, respectively. Theoretically, Eq. (5.10) should satisfy $-1 \leq \rho_{xy}(t_k) \leq 1$.

Coherence Function

The coherence function $\gamma_{xy}(f_j)$ between the two records $x(t_k)$ and $y(t_k)$ is estimated by[134]

$$\gamma_{xy}^2(f_j) = \frac{|C_{xy}(f_j)|^2}{C_{xx}(f_j)C_{yy}(f_j)} \qquad (5.11)$$

where $C_{xy}(f_j)$ is the CPSD; $C_{xx}(f_j)$ is the APSD of $x(t_k)$ and $C_{yy}(f_j)$ is the APSD of $y(t_k)$. The coherence function is the normalized cross-correlation between the two signals and has the limits of $0 \leq \gamma_{xy}^2(f_j) \leq 1$.

Fluctuation Data Analysis

Fluctuation diagnostics measure a fluctuating plasma parameter and convert this measurement into a voltage. An analog-to-digital convertor (digitizer) is used to sample this voltage at precise intervals of time. This results in a discrete time series signal containing a discrete sample of the true fluctuations. By application of the DFT to the time series data, an estimate of the power spectrum of the fluctuating plasma parameter can be obtained. Additionally, if two or more

fluctuation measurements are made simultaneously by observing different plasma parameters and/or by making the measurements in two spatially separate locations, cross-correlation analysis can be used to estimate the power level of the coherent fluctuations, i.e., those fluctuations present in both signals. The application of discrete Fourier analysis and cross-correlation analysis of the fluctuation data is used to extract meaningful information from the time series data. In Chap. VII, the application of discrete Fourier analysis and cross-correlation analysis to reflectometer fluctuation data are discussed in detail. It is shown in this discussion that these two forms of spectral analysis are critical in obtaining quantifiable results from reflectometer fluctuation data.

CHAPTER VI

THE ATF REFLECTOMETER

Introduction

The original goals for reflectometry on ATF called for internal probing of the plasma for density fluctuation measurements in ECH and NBI-heated plasmas. During the conceptual design phase, it was quickly shown that this would not be possible with a single reflectometer but rather would require two systems. One system would need to operate below the 53 GHz ECH frequency to probe the low-density plasmas obtained with ECH only, while the second system would operate above the ECH frequency to probe the high-density plasmas obtained with NBI heating. Since this project had a limited budget, an additional restriction was to use as much existing hardware as possible. From past microwave experiments, a significant quantity of waveguide components, detectors, and sources existed for the 26.5–40 GHz band (A-band), while some waveguide components were available in the 50–75 GHz and 60–90 GHz bands (V- and E-bands, respectively).

After the conceptual design work, two reflectometers were proposed: an A-band system and a V-band system. The exact frequency ranges of the two systems were to be determined by the actual sources and hardware used. The first step in the construction of the reflectometer was to design and build the in-vacuum components and their vacuum interface. At that time, the plans called for the A- and V-band systems to be located side by side on a large external port, and so

113

the vacuum components for both systems were designed and built simultaneously. These components included the conical antennas, antenna support structure, and waveguide vacuum windows. This hardware was installed in late summer of 1989. The budget for the following year for the ATF experiment received significant cuts, and a decision was made to proceed with only the A-band system. This decision was based primarily on the fact that a complete A-band system could be built with no initial hardware acquisition, while the V-band system required a significant acquisition of hardware. Since the V-band system has not been built or operated, its initial design work and components are not discussed any further, except where they affected the design of the A-band reflectometer.

Operational Regime

The plasma regimes that can be studied are limited because of the small rf band of the reflectometer. The density range that can be studied in ATF with a 30 to 40 GHz reflectometer is limited to $(1.1-2.0) \times 10^{13}$ cm^{-3} for O-mode operation and to approximately $(1.5-8.5) \times 10^{12}$ cm^{-3} for X-mode operation at 0.95 T. Operation with the X-mode at 1.9 T is not useful because the cutoff occurs on the low-field side of the fundamental cyclotron resonance, which is located well outside the last closed flux surface. For X-mode operation, low-density ECH discharges can be studied over most of the minor radius for near-parabolic density profiles; however, since ATF often has nearly flat density profiles, the reflecting layer is often restricted to the outer third of the plasma radius. For O-mode operation, NBI plasmas are studied; however, the much higher density of these discharges limits the measurement to the edge of the plasma, i.e., outside the last closed flux surface.
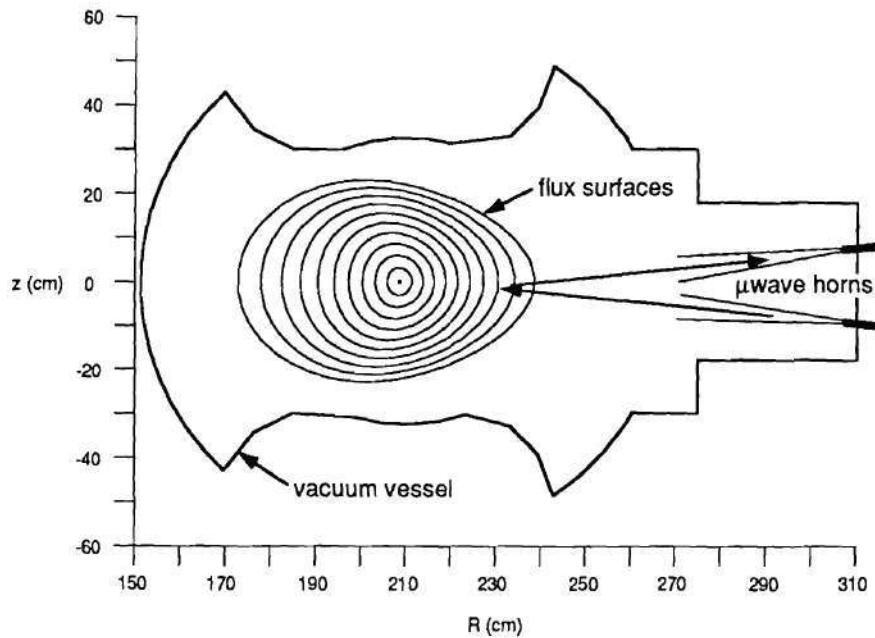
Figure 6.1: Diagram of the ATF reflectometer antennas, showing their locations in the vacuum vessel and the location where their sightlines cross in relation to the vacuum magnetic flux surfaces.

System Description

The ATF reflectometer operates two frequencies simultaneously in the same antenna system. Two tunable microwave sources allow continuous operation between 30 and 40 GHz with separation frequencies from 10 MHz to 10 GHz. The antenna system consists of two high-gain (27 dB average) conical horns with a calculated spot size at the mean reflecting layer of 6 cm at 35 GHz. The horns are located on the horizontal midplane with an angle of 12° relative to one another with their apertures located at $R = 2.70$ m ($R_0 = 2.10$ m, $a = 0.28$ m) so that their sightlines cross at $r/a \simeq 0.75$ (see Fig. 6.1). This position is defined as the mean reflecting layer.

Figure 6.2 shows the basic components and their position in the reflectometer system. The antennas are located inside the vacuum vessel with waveguide windows

115

Figure 6.2: Diagram of the ATF two-frequency correlation reflectometer, showing the major microwave components.

at the vacuum interface. The dual antenna arrangement greatly reduces the effects of internal reflections in the waveguide system as compared to a single antenna system. The waveguide vacuum windows are 0.0035-in.-thick mica disks sealed with O-rings at the vac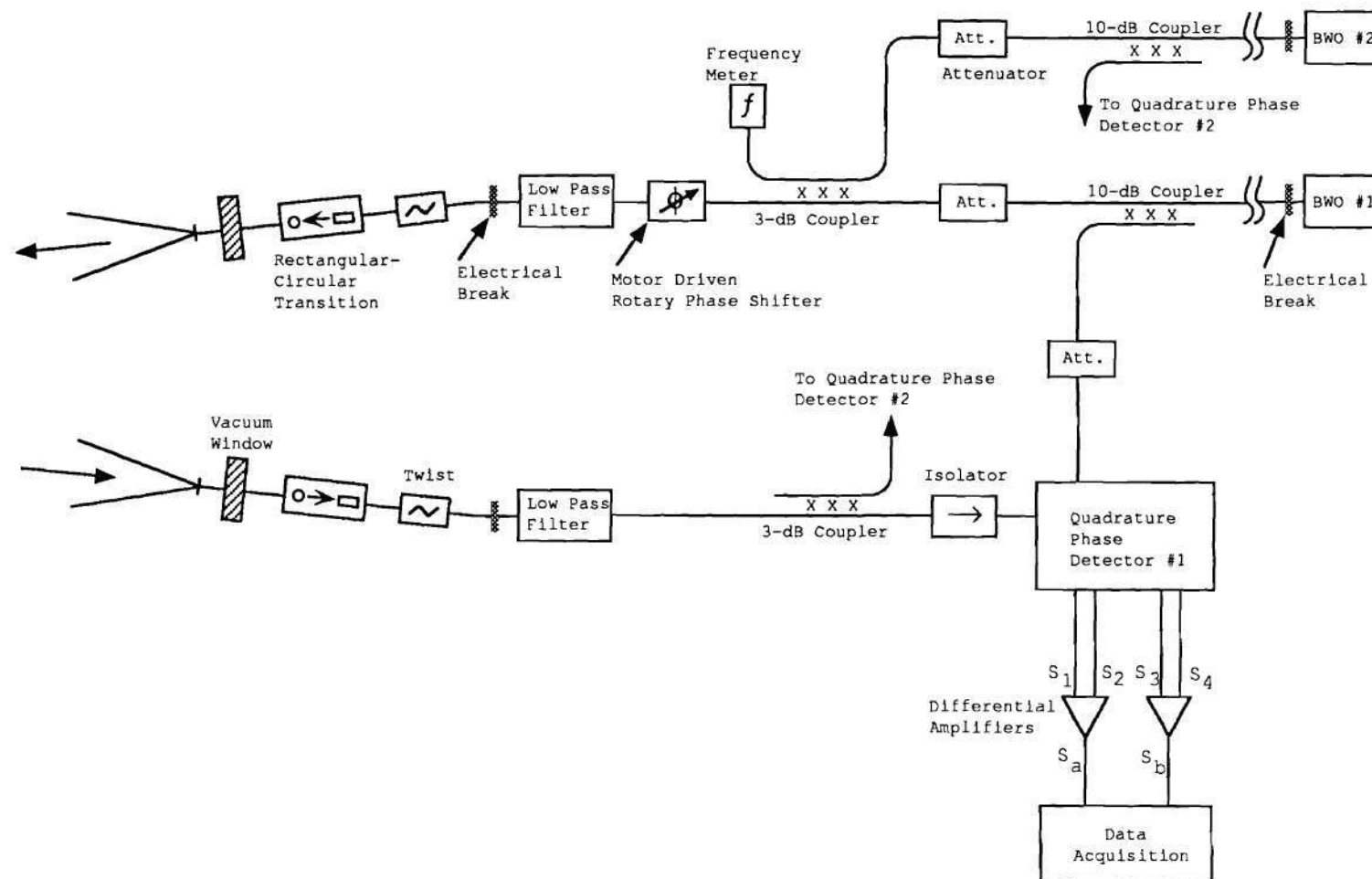uum interface waveguide joint. Transition to circular waveguide is made outside the vacuum windows to allow launching of any arbitrary orientation of wave electric field. Rectangular waveguide twists connected to the circular transitions are used to match the waveguide polarization to the desired antenna polarization for launching either the O-mode or the X-mode. Low-pass filters with >35 dB rejection above 47 GHz are used to eliminate interference from the 53 GHz ECH frequency. Two A-band BWOs are used for the microwave sources. BWOs offer the advantage of being frequency tunable over the entire waveguide band and can provide moderate power levels ($\simeq 30$ mW). The BWOs are located on the midplane 8 m from the center of the machine inside a large magnetic shielding box.

Phase detection of the reflected signal is achieved using quadrature phase detection, as discussed in Chap. III. Quadrature phase detection is obtained using two balanced detectors with a 90° phase relation as shown in Fig. 3.5. Each balanced detector is formed from two matched detectors fed into a differential amplifier. Isolators in the signal input arm (the plasma side) ensure that any reference signal which escapes from one quadrature phase detector is not reflected in the waveguide system and allowed to propagate back into the other phase detector. Table 6.1 lists the waveguide components, their relevant specifications, and their manufacturers. The ATF reflectometer is limited to a 30–40 GHz band because of the low output power of the BWOs below 30 GHz and the narrow-band characteristics of the quadrature phase detectors.

117

Table 6.1. ATF reflectometer microwave components

Component	Manufacturer and Model #	Comments
Backward-Wave Oscillators	Alfred Electronics - Model 650 Sweep Oscillator - Model 659 Plug-in Unit	power supply BWO (Varian and Watkins & Johnson)
Microwave Detectors	Hewlett Packard R422C	Planar-Doped Barrier Diodes, ± 0.6 dB freq. response, ~7.5 mV/μW sensitivity
Waveguide Low-Pass Filters	Hewlett Packard R362A	47-120 Ghz stopband, >35 dB min. rejection
Waveguide Isolators	Hewlett Packard R365A	25 dB min. isolation
Continuously Adjustable Direct Reading Phase Shifter	Alpha 528A	accuracy - 3°
Direct Reading Precision Attenuators	Alpha 510A	0 to 50 dB attenuation
Direct Reading Frequency Meter	Alpha 510A	absolute accuracy - 0.12%
Tapered Mode Transitions	Alpha 884A	converts TE10 to TE11 (WR-28 to WC-28)
Terminations	Alpha 580A	low-loss, max. VSWR - 1.05
3-dB Bidirectional Couplers	Alpha 555A	directivity ~ 30 dB, coupling accuracy ~ ± 1 dB
10-dB Bidirectional Couplers	Alpha 559A	directivity ~ 40 dB, coupling accuracy ~ ± 1 dB
3-dB Short Slot Hybrid Couplers	MDL 28HS32 (Microwave Development Laboratory)	design freq. ~ 33.5-37 GHz, directivity ~ 30 dB, coupling accuracy ~ ± 0.125 dB

Antenna Design

The conical antennas used in this reflectometer were originally used for microwave transmission experiments on the ELMO Bumpy Torus (EBT). After slight modifications to meet the requirements of the ATF reflectometer design, the length of these antenna is 17.6 in., the aperture diameter is 2.75 in., and the conical waveguide feed diameter is 0.281 in. Using the technique discussed in Chap. III, the calculated gains for these antennas range from 26 to 28 dB over the range of 30 to 40 GHz. Using this information, the 3 dB beam width for a conical horn in vacuum can be estimated using the equation[56]

$$W_3 = \left[\left(\frac{aA}{2} \right)^2 + \left(\frac{b\lambda R}{A} \right)^2 \right]^{1/2} \tag{6.1}$$

where A is the antenna aperture diameter, R is the antenna range, and a and b are correction factors that are generally very close to one. Using this equation, the predicted beam width for the above antenna parameters varies between $W_3 = 5$ cm for 40 GHz and $R = 30$ cm and $W_3 = 7$ cm for 30 GHz and $R = 40$ cm.

Antenna Mounting Structure/Shrouding

The purpose of the antenna mounting structure and shrouding is to support, aim, and protect the antenna and waveguide in the vacuum vessel. The port location for the reflectometer is centered on a major radius on the outside horizontal midplane. The criteria used in designing the antenna arrangement included the required location of the apertures to minimize plasma thermal loading on the antenna ($R = 270$ cm), the distance to the last closed flux surface (30 cm), and the expected location of the mean reflecting layer ($r/a = 0.75$). The mean reflecting layer is simply the average radial location of the cutoff layer predicted from the expected plasma conditions and the reflectometer frequency band. This information was used to calculate the required orientation of the antenna axes relative to one

119
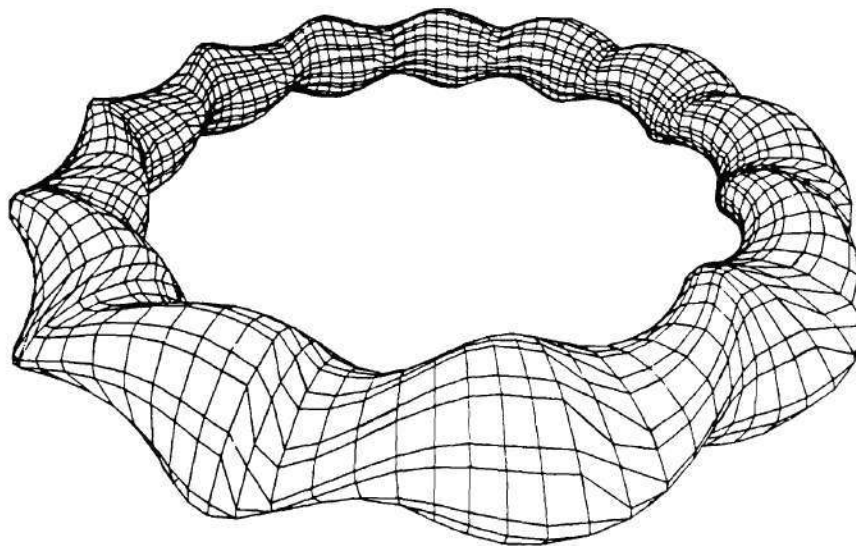
Figure 6.3: A three dimensional plot of the flux surface geometry in ATF.[137] Note that the helical field coils lead to helically convoluted flux surfaces which have a leading edge that spirals around the torus.

another so that their sightlines intersect at the mean reflecting layer. This results in specular reflection, which is reflection with the angle of incidence equal to the angle of reflection. Figure 6.1 shows the resulting antenna layout in the vacuum vessel. The antennas were mounted with an angle of 12° relative to one another. An additional constraint on the antenna layout resulted from the original plans to locate the A-band antenna and the V-band antenna side by side on the same flange. Each antenna pair was to be offset to opposite sides from the center of the flange. The A-band antenna pair is offset by 4.75 cm.

In a stellarator, the flux surfaces have an oblong shape and rotate around the vessel following the magnetic configuration of each field period, as shown in Fig. 6.3. This rotation of the flux surfaces causes the leading edge of the flux surfaces to be oriented at an angle to the horizontal midplane. To maximize the reflected
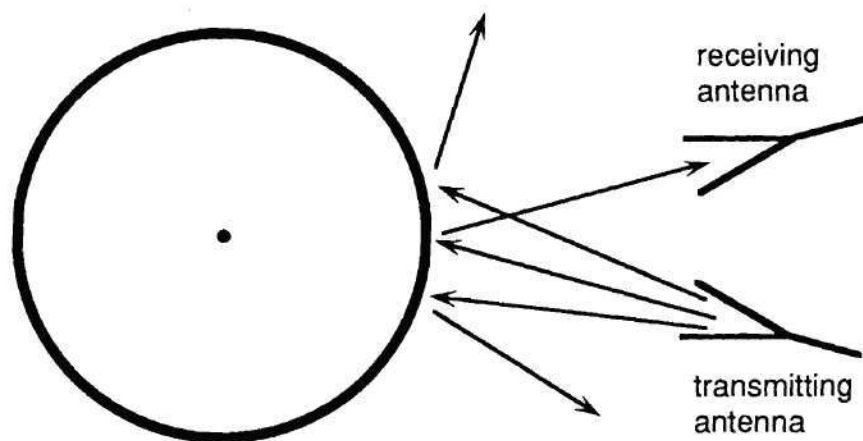
Figure 6.4: Maximizing the reflected signal. If the leading edge of a flux surface is treated as a cylinder, then the reflected microwave beam will result in a fan beam in the plane normal to the cylinder axis.

signal returning in the plane of the antennas, the sightlines of the transmitting and receiving antennas should be perpendicular to the axis of a cylinder formed from the leading edge of the flux surface located at the reflecting layer. This analogy is obtained by thinking of the plasma column as a cylinder with radius greater than the antenna beam width. For perpendicular orientation of the antennas and the cylinder, as shown in Fig. 6.4, the beam is reflected directly backward in the plane of the antennas, thus maximizing the reflected signal at the receiving antenna. For nonperpendicular orientation, the plane of the beams (antennas) is not normal to the cylinder axis. The probing beam is reflected backward normal to the cylinder axis, and so if the antenna's orientation is sufficiently off perpendicular, no signal will be reflected into the receiving antenna.

At the mean reflecting layer, the orientation of a cylinder formed by the leading edge of the flux surface viewed by the reflectometer is rotated approximately 15° from the horizontal axis. This meant that the flange containing the antennas had
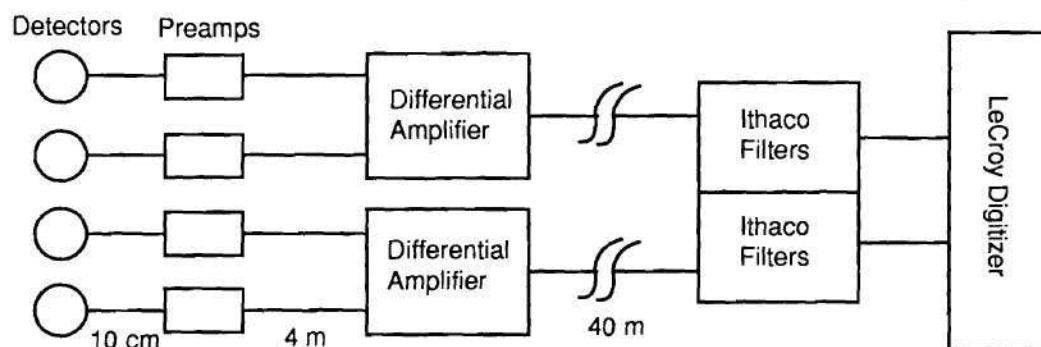
Figure 6.5: A block diagram of the detection, amplifier, and data acquisition systems used on the ATF reflectometer.

to be rotated 15° to match the flux surface orientation so that the plane containing the antenna sightlines would be perpendicular to the flux surface.

Amplifier/DAQ System

Figure 6.5 shows the basic layout of the amplifier and data acquisition (DAQ) system for the ATF reflectometer. The Hewlett Packard R422C microwave detectors have a very low capacitance in their output circuit, allowing for a large bandwidth when connected to a low impedance circuit. Since the detector signals must be carried 4 m to the differential amplifiers, each detector was connected to a preamplifier/line driver using a OP64 Op-Amp and a 3.0 kΩ input impedance.[138] The detectors are connected to the preamplifiers by 10 cm of coaxial cable. The preamplifiers have a 50 Ω output impedance with 10× gain and a 4 MHz 3 dB bandwidth and drive 4 m of a shielded twisted pair cable. The detector-preamplifier circuit 3 dB bandwidth is ∼ 2 MHz. From the preamplifiers, the signals are fed in

122
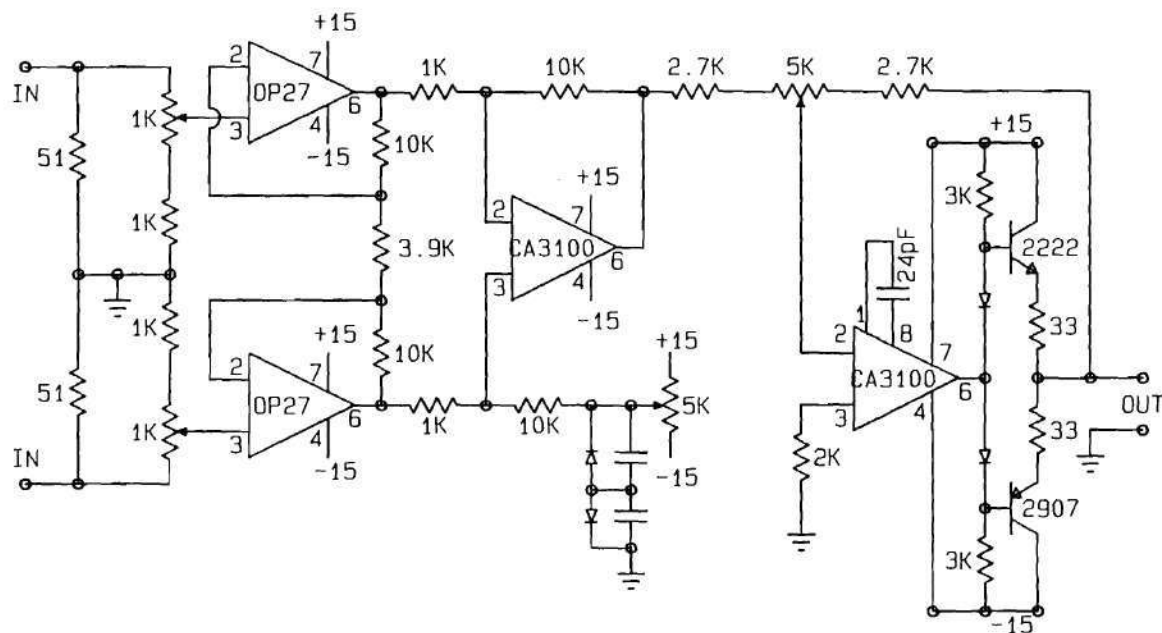
Figure 6.6: Schematic of an ATF reflectometer differential amplifier used for obtaining balanced signals.

pairs into differential amplifiers to produce balanced (dc removed) signals. Chapter III provides more discussion on how balanced detection is achieved with two microwave detectors. The differential amplifiers are a three-stage, low-noise design with a variable gain factor up to 300 and a total (detector-preamp-amplifier) 3 dB bandwidth of 1 MHz. The maximum sampling frequency of the digitizers is 1 MHz so the anti-aliasing low-pass filter cutoff frequency is never greater than half the system bandwidth. This reduces the effects of the slight differences in the frequency response of each detector-preamp-amplifier circuit. These differences include slightly different gains and phase delays for the higher frequency components. Figure 6.6 shows the schematic for one differential amplifier.[138] A resistive divider circuit at each differential amplifier input allows equalizing or balancing of the amplitudes of the two input signals to remove any dc offset remaining after differential amplification. These resistive divider circuits also provide response matching of each detector

123

pair, which results in continued balanced detection with changes in the input power to the detectors. Each quadrature phase detector uses two differential amplifiers to obtain the two balanced output signals: $\tilde{A} \sin \tilde{\zeta}$ and $\tilde{A} \cos \tilde{\zeta}$.

The data acquisition system consists of anti-aliasing filters and LeCroy 8210 digitizers. The anti-aliasing filters are Ithaco 4302 Dual 24 dB/octave multipole filters. The filter cutoff frequency is set to 60–80% of the digitizer Nyquist frequency. After the anti-aliasing filtering, the signals are digitized in the transient recorders with 16 kbytes/channel of memory. The ATF data system[139,140] writes and stores the data on magnetic or optical disk connected to the Fusion Energy Division (FED) computer system.

System Operation

To obtain the quadrature phase data, the two signals containing the sine and cosine signals had to be carefully balanced so that they had equal amplitudes that would cancel out during the fringe counting procedure; see the section "Fringe Counting" in Chap. VII for more details on fringe counting. Since the output power of the microwave sources and the response of the microwave system varied considerably over only a few tens of megahertz, a method for easily balancing the signals each time the probing frequency was changed had to be developed. However, once good quadrature signals were obtained, there were still several key issues in the operation of the ATF reflectometer that were relevant to the reliability and interpretation of the data taken. The first issue was how the launched wave polarization coupled to the desired plasma mode. Next, the spatial resolution (radially, poloidally, and toroidally) of the probing beam determined the sampling volume. The system noise generated by the microwave sources and the detection system set a lower limit on

124

the detectable signal level. Finally, the ability to operate two frequencies simultaneously in the same waveguide system required special considerations to ensure negligible cross talk.

Obtaining Quadrature Signals

The technique used to set up the ATF reflectometer to obtain the quadrature phase detection was to induce a repeating 2π phase shift at the detectors and to connect the output of the two differential amplifiers from one quadrature detector circuit to an oscilloscope operating in an x-y plot mode to obtain a polar plot. By adjusting the resistance of each resistive divider circuit at the differential amplifier inputs, the amplitudes of the two input signals could be made equal so that the resulting output signal was centered about 0 V. Next, the peak-to-peak voltage of the balanced output signal was set to the desired level by adjusting the variable gain on the third stage of the differential amplifier. By doing this to both channels of the quadrature detector, i.e., to the four inputs of the two differential amplifiers forming one quadrature detector, a circle with constant radius centered exactly about the origin of the oscilloscope screen was obtained. Since the quadrature phase detectors only provide an exact 90° phase relation between the two output signals at one frequency, at other frequencies the polar plot of the quadrature signals produces an ellipse; however, by balancing and centering the ellipse on the oscilloscope, balanced detection was still achieved. In the section "Raw Signal Analysis" in Chap. VII, the technique used to adjust the balanced signals to have a 90° phase relation is discussed.

At first, the repeating 2π phase shift was created by sweeping the BWO frequency over a narrow frequency band ($\sim$ 40 MHz). This narrow sweep resulted in a phase delay between the reference signal and the signal sent to the vacuum vessel, which was reflected off the opposite wall in the vessel. This produced a

phase shift $\Delta\zeta$ because the two signals traveled very different distances to reach the detectors; $\Delta\zeta = \Delta\ell\Delta\lambda/(\lambda_1\lambda_2)$, where $\Delta\ell$ is the path length difference between the reference arm and the plasma arm of the reflectometer, λ_1 is the guide wavelength of the starting frequency of the sweep, λ_2 is the guide wavelength of the ending frequency of the sweep, and $\Delta\lambda$ is the change in the guide wavelength resulting from the frequency sweep. The problem with this technique is that the BWO power and the waveguide system response are not constant over this small frequency sweep, resulting in inaccuracies in balancing the signal. After the first year of operations, a motor-driven rotary phase shifter was added into the launching arm of the waveguide system. By spinning this phase shifter, a continuous phase shift was obtained without the changes in the signal amplitude obtained with the frequency sweeping technique. This technique proved to be the most accurate and versatile method for obtaining the balanced quadrature signals.

Polarization

As discussed in Chap. II, the magnetic shear in ATF can lead to strong mode coupling in regions where plasma propagation is not guaranteed because of the low plasma density. In this case, it is difficult to determine the correct polarization to launch to obtain the desired plasma mode near the cutoff layer. In fact, mode coupling will cause any launched polarization to result in both O- and X-modes in the plasma. The goal in determining the launched polarization is to minimize the power of the undesired mode coupled into the plasma.

The ATF reflectometer views the plasma through the ergodic region of the plasma formed by the natural magnetic divertor.[9,141] In the initial design of the reflectometer, it was assumed that the plasma density was finite ($\simeq 1 \times 10^{11}$ cm^{-3}) all the way out to the antennas. Since the last closed flux surface is located at $R = 238$ cm, this left a region of $\simeq 40$ cm in width in which the wave mode could be

126
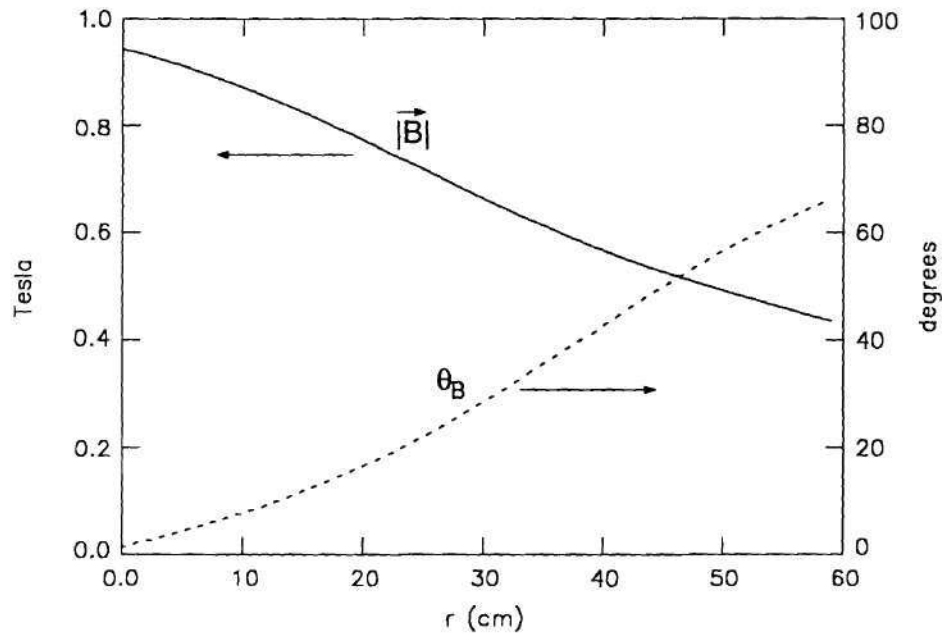
Figure 6.7: The magnetic field $|\vec{B}|$ profile and its rotation with respect to the horizontal midplane moving inward along a major radius.

determined. Figure 6.7 shows the magnetic field $|\vec{B}|$ and its rotation with respect to the horizontal midplane from the center of the plasma to the antenna aperture. Note that $B_r \simeq 0$ T, so that the wave propagation is perpendicular to the plane of the shear. In Fig. 6.8, the magnetic shear corresponding to this field polarization rotation is shown. Note that in the region of interest ($R = 240$ to 270 cm) the field polarization rotates from $30°$ to $65°$, and the local shear achieves a maximum. In choosing the polarization of the wave to be launched, an average field polarization of $\sim 45°$ was chosen. Thus, the waveguide mode was rotated $45°$ before transitioning to circular waveguide, and the resulting polarization launched from the antenna was rotated $45°$ with respect to the horizontal midplane. For the waveguide configuration of the ATF reflectometer, i.e., the wave electric field is horizontal, $45°$ polarization was used initially for launching the O-mode, but because of the high central and edge densities, this was changed to $60°$. For the X-mode, $-45°$ was used.
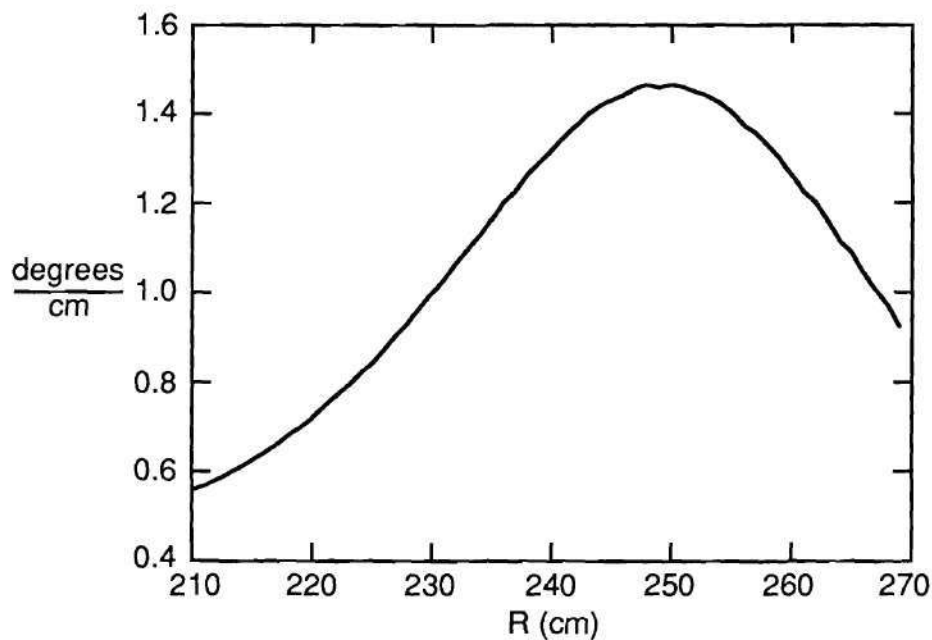
Figure 6.8: The magnetic shear in ATF resulting from the rotation of the magnetic field polarization.

It is clear that with the high shear in ATF, a pure single mode could not be coupled into the plasma. For the low-density, ECH-only plasmas studied with a probing frequency between 30 and 40 GHz only the X-mode is cut off. Thus, any O-mode that couples into the plasma will propagate through the plasma without being cut off. This transmitted O-mode wave reflects off the inner wall, propagates back through the plasma, and finally mixes with the reflected X-mode in the receiving antenna, resulting in some error in the measured signal. Figure 6.9 shows a 45° polarization (O-mode) 35 GHz raw data signal and its spectrum-integrated power plotted vs time, taken during a density ramp-up. Note that the integrated power of the fluctuations jumps by more than an order of magnitude in a very short period of time. This indicates the inception of cutoff because the phase of the reflected signal is far more sensitive to density fluctuations at the cutoff layer than to density fluctuations along its propagation path. Before cutoff, a clear 2π phase modulation

128

Figure 6.9: Top: an O-mode reflectometer raw data signal taken during a density ramp with cutoff density being achieved in the middle of the data window. Bottom: the spectrum-integrated power for this signal. Note that the integrated power increases by $\simeq 100$ when cutoff is achieved.

due to the increasing density (two-pass interferometry) is seen, while well after cutoff the reflecting layer is large enough to provide a large reflected signal. In the time from just before to just after t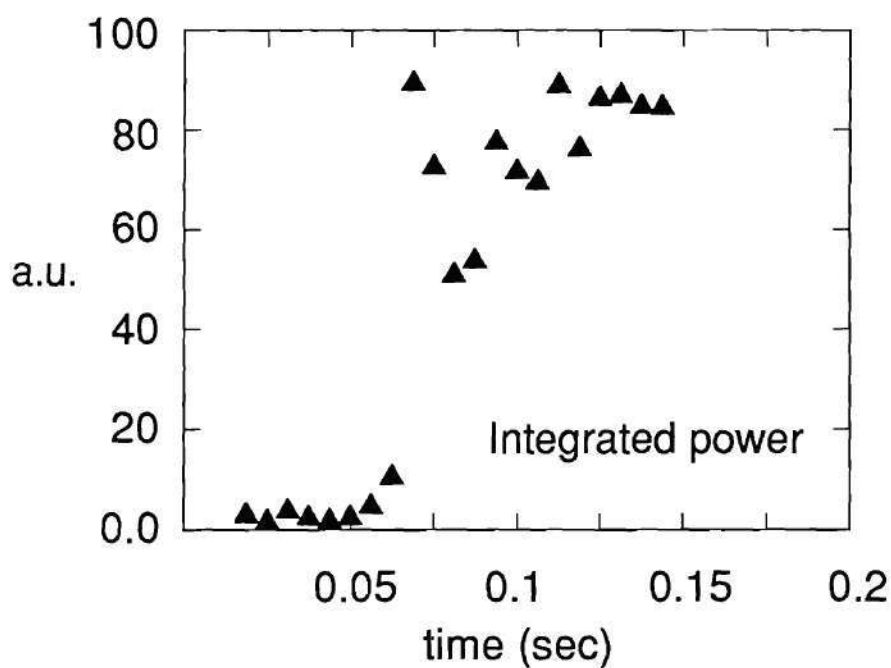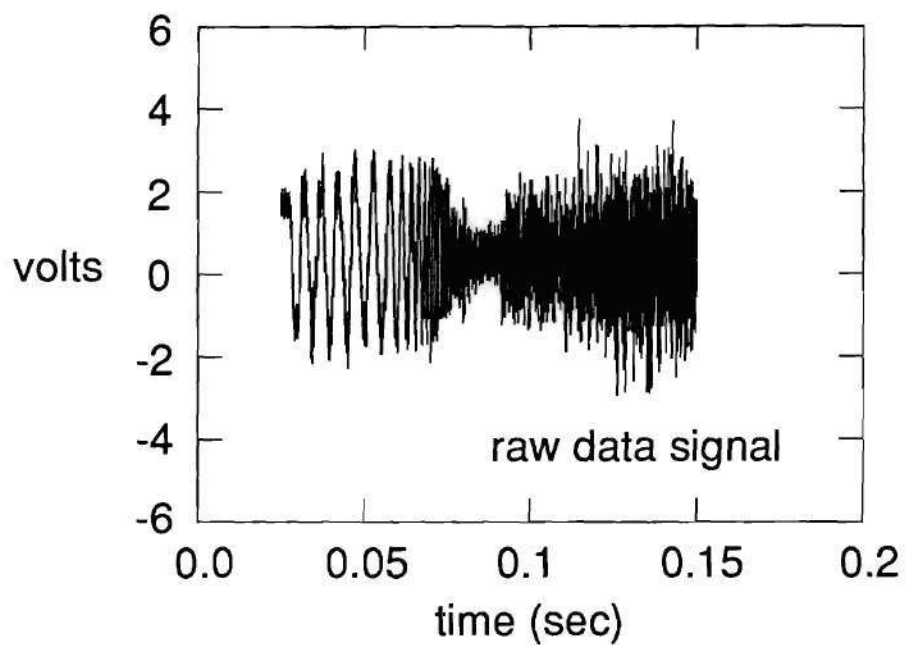he inception of the O-mode cutoff, the diffraction effects on the O-mode wave are very strong. This results in little O-mode signal being reflected back into the receiving antenna. Since the X-mode cutoff is well developed, any X-mode signal is reflected back into the receiving antenna. This signal level can then be used as an upper limit on the amount of X-mode power being reflected back into the antenna. This reflected X-mode amplitude is ~ 1.5 V, while the reflected O-mode amplitude is ~ 4 V. The percentage of power in the O- and X-modes can be estimated from the equation $\eta_n = A_n^2/(A_o^2 + A_x^2)$, where η_n is the percent power in the n mode, A_n is the amplitude of the n mode, and A_o and A_x are the O- and X-mode amplitudes, respectively. It is estimated that the reflected signal consists of $\sim 88\%$ O-mode and $\sim 12\%$ X-mode.

Reversing this argument for the low-density case of X-mode operation, if it is assumed that the amount of O-mode launched is roughly the same as the amount of X-mode launched in the case above, the maximum unwanted O-mode power can be estimated to be 10–15%. However, as shown in Fig. 6.9, the contribution to the fluctuation spectrum from the transmitted signal as measured by the integrated power before cutoff is approximately two orders of magnitude less than the contribution from the reflected signal as measured by the integrated power after cutoff. This is a significant result in justifying the validity of the X-mode data, since a considerable amount of the launched wave could couple to the O-mode. However, this argument works against the validity of the O-mode data taken during high-density discharges, in that the X-mode cutoff will occur before the O-mode cutoff and so both the O- and X-modes will be reflected back into the antenna. In this case, the integrated power of the received signal could be distorted by the undesired X-mode.

130

Modeling of the Mode Selection Problem   Due to the time schedule for the ATF reflectometer experiment, no numerical modeling of the mode problem was performed until after the completion of the experiment. As will be shown, this modeling indicates that $-45°$ is not the optimum angle for launching the X-mode in low-density plasmas. For launching the O-mode in high-density plasmas, $45°$ polarization results in $\sim 85-90\%$ of the power coupled to the plasma being O-mode. This agrees well with the estimated 88% for the data in Fig. 6.9. For $60°$ polarization, the modeling predicts that $\sim 75\%$ of the power coupled to the plasma is O-mode. The major complication in performing this modeling is that the density profile from the plasma edge to the antennas is not known, but it is expected to be nonnegligible because of the ergodic divertor region.[141,142,143] The edge density is also expected to rise significantly during the high-density NBI discharges.

Fidone and Granata[21] present a full wave model for describing wave propagation in a sheared magnetic field. Bigelow[144] has used this model to optimize the launched polarization for the 53 GHz ECH to obtain the maximum first-pass absorption in ATF, and Bell[23] has used it to model microwave transmission experiments and ECE emission on ATF. The program PTWIST, written by Bigelow,[144] has been modified for the geometry of the ATF reflectometer and used to propagate the wave up to the X-mode cutoff. At this point, the X-mode is reflected, and the O-mode continues to propagate.

The first case to study is the $45°$ polarization (O-mode) 35 GHz case discussed previously. Figure 6.10 shows the amplitudes of the O- and X-modes as the launched wave propagates from the antenna aperture located at $R = 270$ cm to the X-mode cutoff at $R \simeq 241$ cm. Note that the amplitudes plotted here are normalized by the total power, $p = p_o + p_x$, where $p_o = A_o^2$, $p_x = A_x^2$, A_x is the amplitude of the O-mode signal, and A_x is the amplitude of the X-mode signal. Thus, the plotted signals represent the amplitude of the fraction of power in each mode normalized to

131
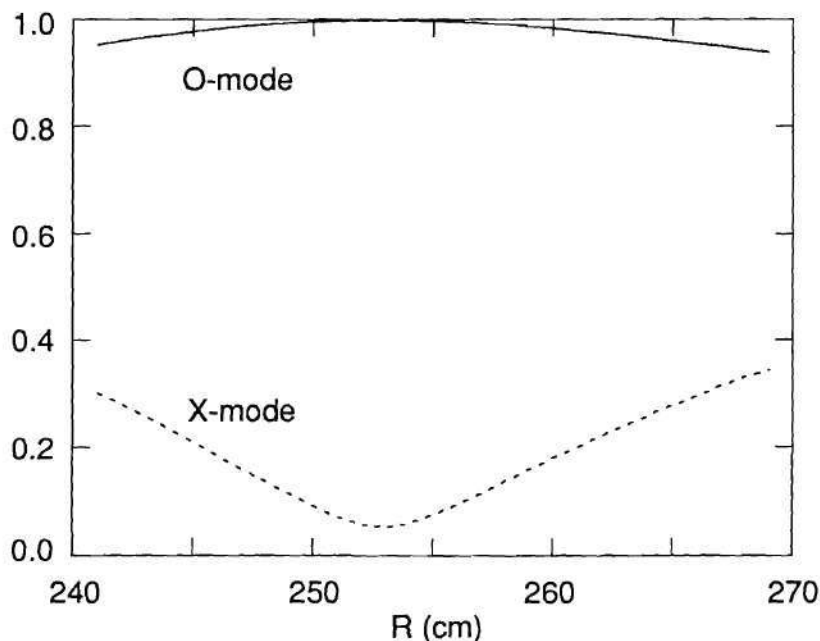
Figure 6.10: The predicted O- and X-mode amplitudes for a 35 GHz wave launched with 45° polarization. See Fig. 6.11 for the assumed density profile, and note that the antenna aperture is located at $R = 270$ cm and the last closed flux surface is located at $a = 30$ cm, with $R_0 = 210$ cm.

the total power. Figure 6.10 shows that the predicted O-mode content ($p_o = A_o^2$) is $\sim 90\%$ at the plasma edge for the assumed density profile shown in Fig. 6.11. The density at the antenna aperture is assumed to be 4×10^{11} cm^{-3}, i.e., 1/100 of the peak density. This finite density between the last closed flux surface and the antenna aperture results in a nonnegligible polarization rotation of the launched wave. This predicted O-mode power shows good agreement with that predicted from the data taken during a density ramp showing the signal amplitude before, at, and after cutoff (Fig. 6.9). Note that near $R = 253$ cm, the O-mode amplitude appears to go to 1.0 while the X-mode amplitude decreases to only ~ 0.05. This apparent incongruity is a result of the resolution of the plot, and the condition that $A_o^2 + A_x^2 = 1$ is valid in this figure. A scan of the edge density between 0.1 and 0.001 of the peak density, as shown in Fig. 6.12, indicates no significant change in

132

Figure 6.11: The assumed density profile for the O-mode polarization modeling. The central density is 4×10^{13} cm^{-3} and the density at $r = 60$ cm is 4×10^{11} cm^{-3}. The steep gradient is created using a hyperbolic tangent function and provides a fair representation of the typical edge gradients observed in ATF (see Chap. VIII).

the amount of power in the O-mode at the last closed flux surface, except at very high edge densities.

Using the same density profile, the launching of a 60° polarized wave results in $\sim 75\%$ O-mode power at the X-mode cutoff. In Fig. 6.12, the percentage of O-mode power in the launched 35 GHz wave at the X-mode cutoff is plotted vs the density at the antenna aperture for the 45° and 60° polarizations. For the 60° polarization case, this density scan shows that $\sim 96\%$ of the power at the X-mode cutoff has O-mode polarization for the highest density case, but the O-mode content is $\sim 75\%$ for the lower densities; however, the high-density case of 4×10^{12} cm^{-3} at the antenna aperture is much too high to be realistic.[143,145] Thus, a launching polarization of 45° results in a higher O-mode content than a polarization of 60°. Figure 6.13 shows the results of a scan of the launching polarization for the density
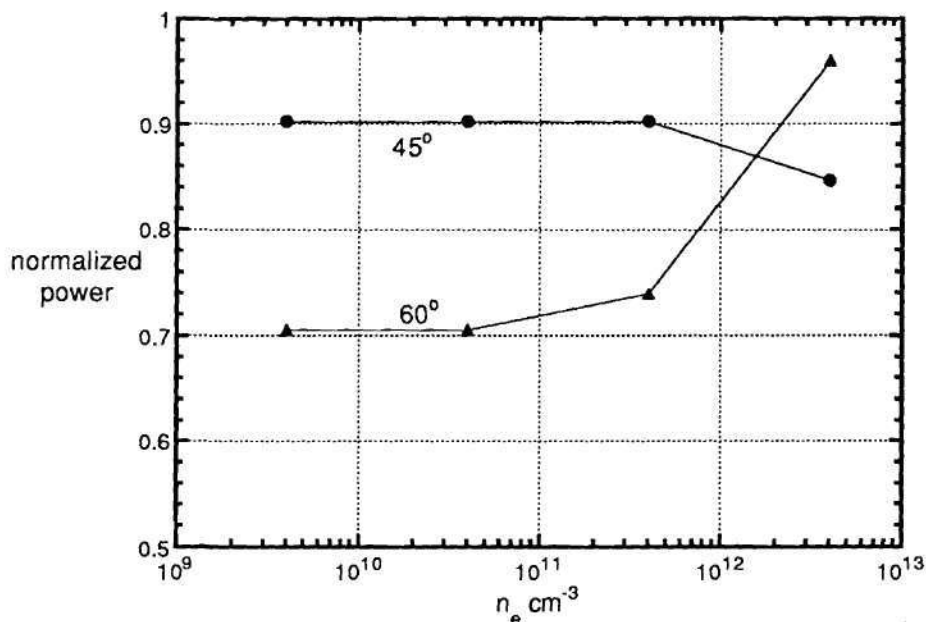
Figure 6.12: The O-mode power at the X-mode cutoff ($\sim$ plasma edge) for a 35 GHz wave vs the density at the antenna for the 45° and 60° launch polarizations.

profile in Fig. 6.11. These results predict that the optimum launching polarization for the O-mode at 35 GHz is 30°, resulting in $\sim$ 95% O-mode power at the X-mode cutoff. Note the small change in the O-mode power content for large changes in the polarization ($\sim$ ±10°). This weak dependence on the launch polarization results in a weak dependence on the assumed density profile, since most probable profile changes will result in a maximum of a ±10° change in the polarization at the plasma edge. The deviation of these results for frequencies in the range of 30 to 40 GHz will not be significant.

For the case of the low-density ECH plasmas, Fig. 6.14 shows that for the −45° polarization used in this experiment, the undesired O-mode content ($p_o = A_o^2$) is $\sim$ 20–25%. Note that the plotted signals represent the amplitudes of each mode normalized in terms of the total power, as discussed previously for Fig. 6.10. Here again, the apparent incongruity near $R = 252$ cm, where A_x appears to go to 1.0

134
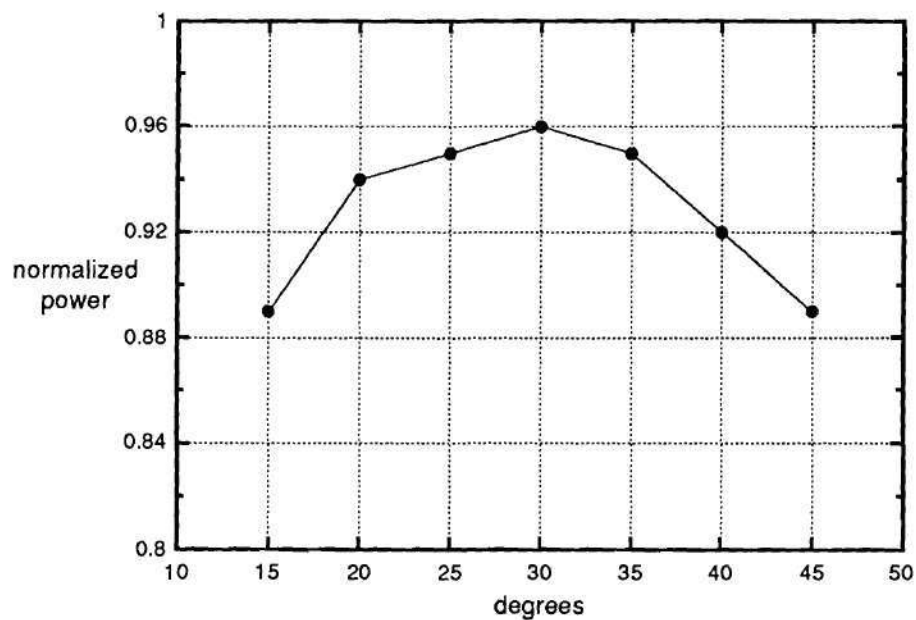
Figure 6.13: The O-mode power in a 35 GHz wave at the X-mode cutoff versus the launch polarization of the antenna.
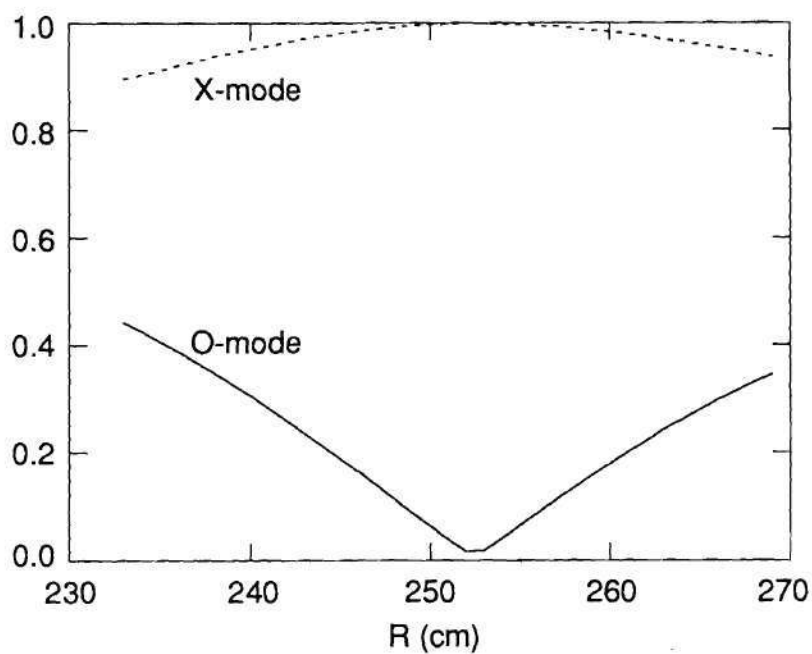
Figure 6.14: The predicted mode amplitude for a 30 GHz wave launched with $-45°$ polarization. Note: the antenna aperture is located at $R = 270$ cm and the last closed flux surface is located at $R = 240$ cm.
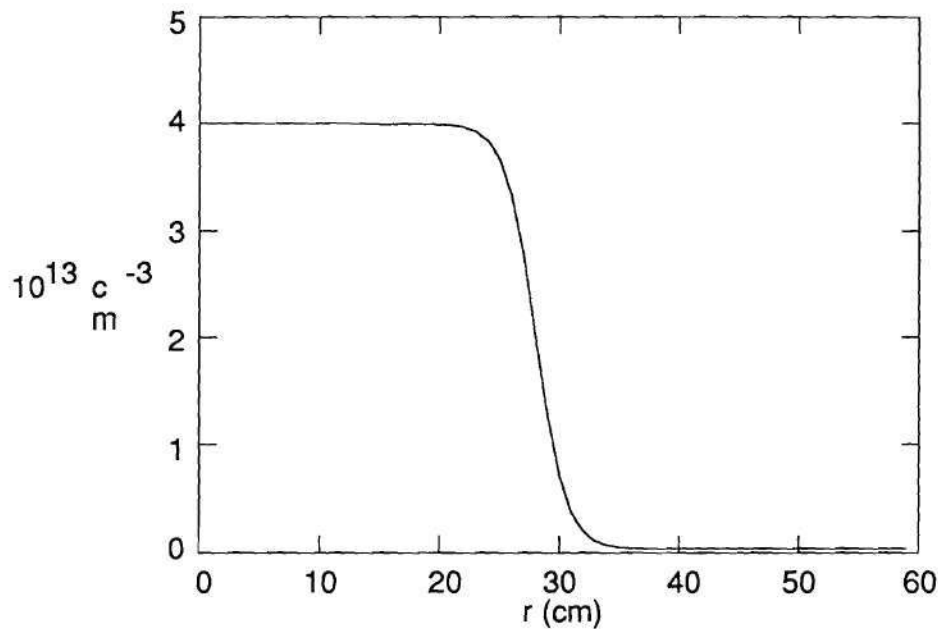
135
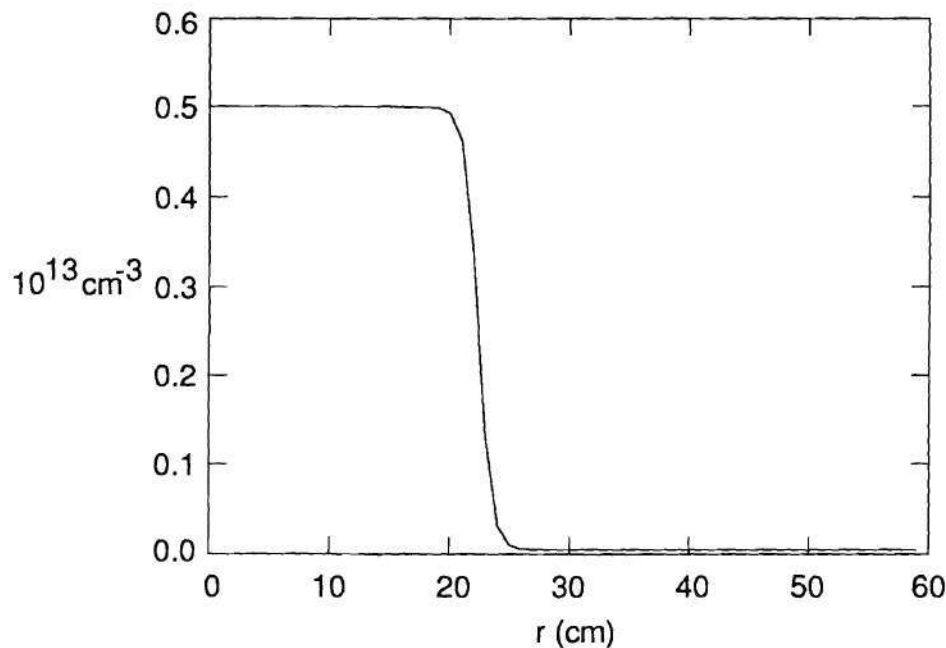
Figure 6.15: The assumed density profile for the X-mode polarization modeling. The central density is 5×10^{12} cm^{-3}, and the edge density at $r = 60$ cm is 5×10^{10} cm^{-3}. The edge gradient obtained with this profile is typical for ATF (see Chap. VIII).

while $A_o < 0$, is due to the resolution of the plot. This example uses a 30 GHz wave to maximize the affects of the edge densities. Higher frequencies will be less effected by the edge density. The density profile for this case is shown in Fig. 6.15 and has a peak density of 5×10^{12} cm^{-3} and a density of 0.01 of the peak density at 60 cm. A scan of the edge density between 0.1 and 0.001 of the peak density shows only a small change in the mode content at the reflecting layer. This weak dependence on the edge density is a result of the very low densities possible in the edge due to the low peak density.

As can be seen in Fig. 6.16, the optimum polarization to launch to maximize the X-mode content at the reflecting layer for the density profile given in Fig. 6.15 is $-70°$. This polarization results in a predicted X-mode content of $\sim 99\%$ at the X-mode cutoff. The magnetic field $|\vec{B}|$ polarization at this location is $20°$, perpen-
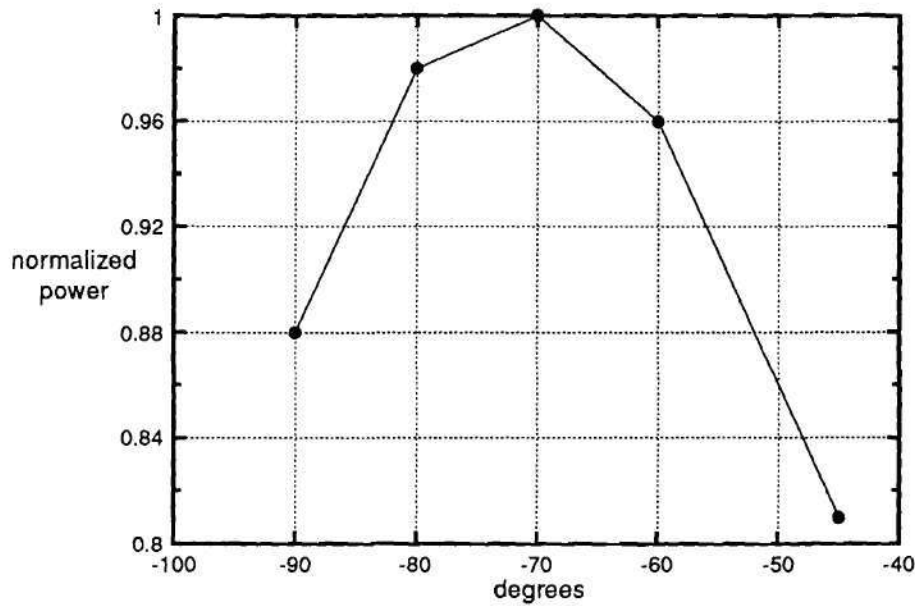
Figure 6.16: Plot of the X-mode power at the X-mode cutoff for a 30 GHz wave vs the launching polarization of the antenna.

dicular to the launching polarization. Thus, the modeling predicts no polarization rotation in the edge region outside the plasma, and so the launched wave polarization should be chosen to match the $|\vec{B}|$ field polarization at the reflecting layer. Note that the small change in the X-mode power content at the cutoff layer deviates only slightly from its maximum value for up to a $\pm 10°$ deviation from the optimal launching polarization. This indicates that these results are not sensitive to the edge density. The polarization to launch to maximize the X-mode content is sensitive to the location of the density gradient with respect to the magnetic field. Figure 8.1 in Chap. VIII shows two typical density profiles in ATF. The edge gradients in these profiles are similar to the edge gradient in the assumed profile used in these calculations; however, the location of the gradients may differ by a few centimeters. This could change the optimum polarization for maximum X-mode content by as much as $\pm 10°$, refer to Fig. 6.7; however, this would decrease the X-mode power

137

content by less than 5%.

Spatial Resolution

The spatial resolution of a reflectometer probing beam determines the spatial localization of the measurement and, to some degree, the sensitivity of the diagnostic to short-scale-length fluctuations. The poloidal and toroidal resolution is primarily determined by the probing beam width at the reflecting layer. As discussed earlier in this chapter, the beam width for the ATF reflectometer at the mean reflecting layer has a maximum value in vacuum of 7 cm. The presence of plasma will cause faster divergence of the beam, so its width at the reflecting layer may be still larger. The convex shape of the reflecting layer due to the convex flux surfaces may result in some improvement in the poloidal dimension, but this is not likely. In the case of a smooth convex reflecting surface with a radius of curvature greater than the beam width, the reflected beam fans out, and only the reflected signal from a small area is reflected back into the receiving antenna. However, in a plasma with turbulence, the reflecting layer will be like a nonuniform diffraction grating. The reflection from such a surface will be diffuse, resulting in contributions to the received signal from all parts of the incident beam.

Some researchers estimate the radial resolution of a reflectometer measurement as the depth of the reflecting layer.[69,146] As discussed in Chap. II, the radial depth of the reflecting layer is the distance the evanescent wave penetrates beyond the point where it is cut off. However, Mazzucato and Nazikian[147,148] have shown that the phase information in the reflected signal comes from a location that is localized to a region in front of the cutoff and is strongly dependent on the radial wavelength of the density fluctuations. For $k_r \ll k_0$, the fluctuation wavelength is much greater than the probing beam wavelength, and so the phase information in the reflected signal is strongly localized to the cutoff. Here, k_r is the radial wave number

of the fluctuation and k_0 is the vacuum wave number of the probing beam. Also, if $k_r \ll k_0$, the localization is strong and the magnitude of the phase fluctuations in the reflected signal should be directly proportional to the radial displacement of the cutoff layer. This conclusion comes from the observation that if $k_r \gtrsim k_0$, averaging over several fluctuation wavelengths in one probing beam wavelength would cause cancellation in the phase fluctuations; however, for $k_r \ll k_0$, less than one cycle of the density fluctuation will be observed, and so no cancellation in the reflected phase is expected. Note that the conclusion by Mazzucato and Nazikian that the phase information in the reflected signal is strongest for a fluctuation located a short distance in front of the cutoff layer indicates that the use of the cutoff position as the location of the measured fluctuations will result in a systematic error in the quoted location, since the actual location of the measured fluctuations is in front of the cutoff.

For the purposes of a simple estimate of the radial resolution, the formula given by Ginzburg[11] for the radial depth of the cutoff layer is used here. Although Mazzucato and Nazikian[148] do not directly address the estimation of the radial resolution, their conclusions would imply that a simple estimate based on k_0, like the Ginzburg equation, would only be valid for $k_r \ll k_0$. So the assumption is made here that the condition $k_r \ll k_0$ is satisfied for the fluctuations observed by the reflectometer in ATF. It is shown in Chap. IX that the mean k_r of the observed density fluctuations is $0 < k_r < 1$ cm^{-1}, while the probing beam wave number is $k_0 > 6.3$ cm^{-1}. This indicates that the assumption of $k_r \ll k_0$ is valid.

The ATF plasmas generally have density profiles with very steep edge gradients in the outer third of the plasma radius with little (flat profile) or inverted (hollow profile) density gradient in the plasma core. This restricts reflectometry measurements to the edge density gradient region. For typical density profiles, such as those shown in Chap. VIII, the density scale length in this edge gradient region
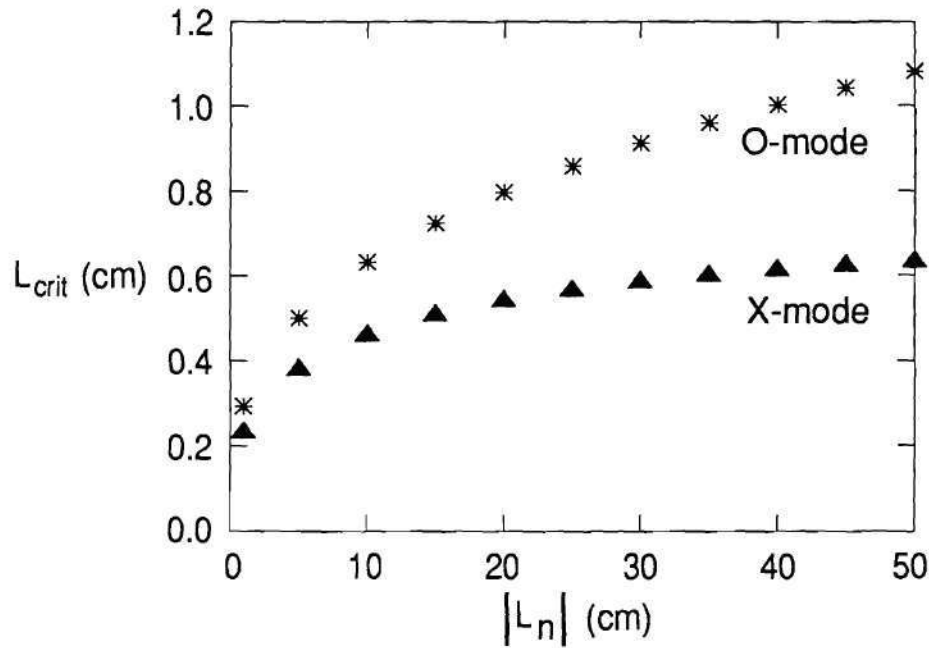
Figure 6.17: The critical layer depth for a 30 GHz wave in ATF vs the density gradient scale length. For the X-mode estimate, the magnetic field scale length $|L_B|$ is 64 cm, and the electron cyclotron and plasma frequencies are 19.7 GHz and 17.5 GHz, respectively.

is in the range 5–50 cm. The magnetic field gradient length for the magnetic field profile in Fig. 6.7 is shown in Fig. 7.11 to be in the range of 65–70 cm in the edge gradient region. Using Eq. (2.21) for the critical layer depth, Fig. 6.17 shows the predicted depth as a function of the density gradient scale length $|L_n|$ for a 30 GHz probing beam reflected at $r = 26$ cm. The X-mode estimate uses the value of the magnetic field and its scale length at $r = 26$ cm. The value of ω_{pe} is determined from Eq. (2.6) since ω_{ce} is known and ω_R is the probing beam frequency. The values assumed in producing Fig. 6.17 as given in the figure caption are typical for ATF; therefore, the typical radial resolution for the ATF reflectometer is ~ 0.4–0.6 cm for the X-mode and ~ 0.4–1.1 cm for the O-mode. As the probing frequency is increased over the 30 to 40 GHz band of the ATF reflectometer, the cutoff layer depth will decrease, and so those values shown in Fig. 6.17 are for the worst case of

30 GHz. In the section on radial coherence measurements in Chap. IX, it is shown that the measured radial correlation lengths are 2 to 4 times greater than the critical layer depth.

Two-Frequency Operation

Two-frequency operation is achieved by combining and dividing the transmitted and reflected signals in two 3 dB couplers, as shown in Fig. 6.2. Independent detection of the two signals with a frequency separation as low as 10 MHz is possible because of the homodyne detection. If two reflected signals with frequencies f_1 and f_2 are mixed with the f_1 reference signal at a square law detector (purity of the reference signal is critically important), two IF signals are possible. The first will have a zero IF, while the second will have a frequency of $|f_1 - f_2|$. Following the derivation in the section "Microwave Detectors" in Chap. III, the output voltage for this case is

$$V = k_d \left| \vec{S}_r(f_1) + \vec{S}_1(f_1) + \vec{S}_2(f_2) \right|^2 \qquad (6.2)$$

where $\vec{S}_r$ is the f_1 reference signal, $\vec{S}_1$ is the f_1 reflected signal, and $\vec{S}_2$ is the f_2 reflected signal. These signals have the form

$$
\begin{aligned}
\vec{S}_r &= A_r \left(\cos \psi_r - i \sin \psi_r \right) \\
\vec{S}_1 &= A_1 \left(\cos \psi_1 - i \sin \psi_1 \right) \\
\vec{S}_2 &= A_2 \left(\cos \psi_2 - i \sin \psi_2 \right)
\end{aligned}
\qquad (6.3)
$$

where the phase terms are defined as

$$
\begin{aligned}
\psi_r &= \omega_1 t + \phi_r \\
\psi_1 &= \omega_1 t + \phi_1 \\
\psi_2 &= \omega_2 t + \phi_2
\end{aligned}
\qquad (6.4)
$$

141

and ω_1 and ω_2 are the two frequencies. Solving Eq. (6.2) and noting that the detectors rectify and average signals at the microwave frequencies, the detector voltage can be written as

$$
\begin{aligned}
V \quad = \quad & \frac{k_d}{2} \{ p_r + p_1 + p_2 + 2\sqrt{p_r p_1} \cos(\phi_r - \phi_1) \\
+ \quad & 2\sqrt{p_r p_2} \cos [\Delta\omega\, t + (\phi_r - \phi_2)] + 2\sqrt{p_1 p_2} \cos [\Delta\omega\, t + (\phi_1 - \phi_2)] \}
\end{aligned}
\quad (6.5)
$$

where $p_r = A_r^2$, etc., and $\Delta\omega = \omega_1 - \omega_2$. Note that $\Delta\omega > 10$ MHz is always maintained for two-frequency operation of the ATF reflectometer. Since the detectors have a bandwidth of < 1 MHz, only the zero IF signal, which contains the phase and amplitude fluctuations from the f_1 reflected signal, can be detected. The terms containing $\Delta\omega\, t$ are rectified and averaged by the detector diodes. The detector voltage can now be written as

$$
V = \frac{k_d}{2} [p_o + p_2 + 2\sqrt{p_r p_1} \cos(\phi_r - \phi_1)]
\quad (6.6)
$$

where the definition $p_o = p_r + p_1$ has been used. Since the reference signal power level is at least 20 dB above the reflected signal power $(p_r \sim p_o \gg p_2)$, the f_1 detector's response to the power fluctuations of the f_2 reflected signal (the p_2 term) is negligible compared to the detector's response to the f_1 signal's phase and amplitude fluctuations; thus, the fluctuations in the f_2 signal are invisible to the f_1 detection system. This lack of sensitivity to the amplitude and frequency fluctuations in the reflected signal at other than the reference signal frequency is a direct result of the vector addition, as shown in Fig. 6.18, of the signal amplitudes. This is a result of operation in the square law regime. For example, consider two signals at the same frequency so that if $p_r = 100$ (any units), then $p_1 \leq 1$ since $p_r/p_1 \geq 20$ dB is required. By vector addition of the amplitudes, $\vec{S} = \vec{S}_r + \vec{S}_1$ where $\vec{S}_r$ and $\vec{S}_1$ are the amplitude vectors defined in Eq. (6.3), $\vec{S}$ will have a maximum range of 9 to 11. Since the power is defined as $p = \vec{S}^2$, the maximum range of the resulting signal power is 81 to 121. However, if p_r and p_1 add by addition of the signal powers

142
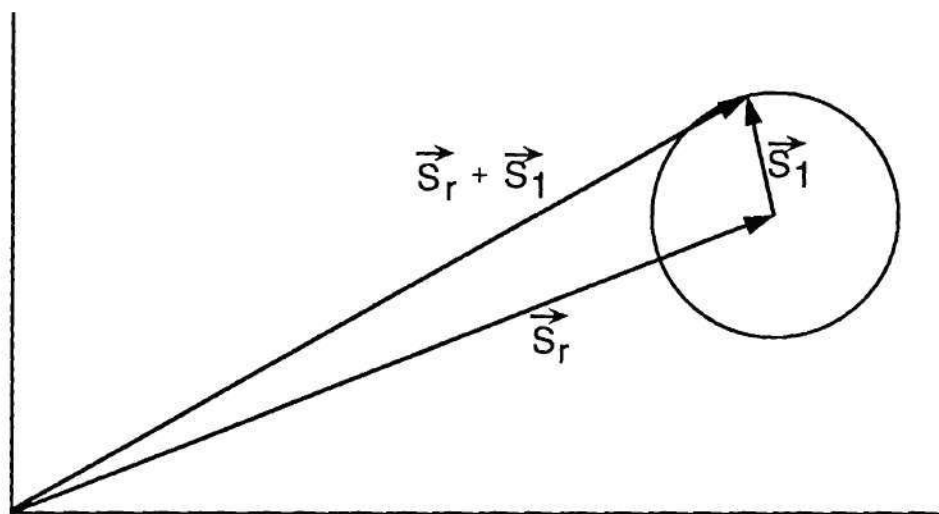
Figure 6.18: Two signals in a square law detector combine by vector addition.

only — for example, if $\vec{S}_1$ is at a different frequency — then the maximum range of $p = p_r + p_1$ is 100 to 101. Thus, the vector addition signal has a maximum of 40 times more variation in the power than the simple power addition signal. The vector addition of the reference and reflected signals also certainly increases the system sensitivity to very small phase fluctuations.

Noise Estimates

The vector addition of the amplitudes rather than the simple power addition also greatly improves the signal-to-noise ratio. The two largest noise sources are the amplifier system and the microwave sources. Since phase detection is used, the amplitude fluctuations in the microwave sources will contribute negligibly to the total noise level; however, the frequency fluctuations in the sources will result in phase fluctuations in the analyzed data. For fluctuation analysis, the noise is investigated in the frequency domain to determine its contribution to the fluctuation
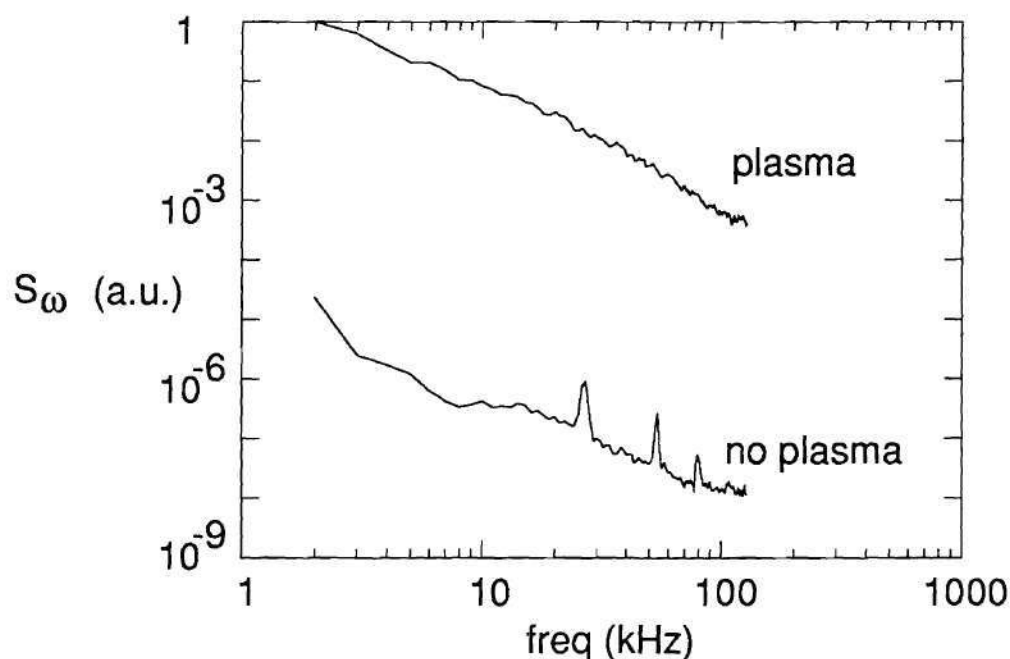
Figure 6.19: The signal amplitude levels obtained by Fourier analysis with (upper) and without (lower) plasma show the relative signal-to-noise ratio for a normal plasma signal. Note: the two spectra have units of fringes squared.

spectrum. In Fig. 6.19, typical noise and plasma spectrums are shown for fringe-counted signals. Fringe counting is discussed in detail in the following section on page 149. The use of fringe-counted signals removes any contribution from the unwanted amplitude variations and gives the true phase fluctuations in the reflected signal normalized to 2π so that they are directly comparable. The signal-to-noise ratio in this typical case is 40 dB for frequencies above 5 kHz. The noise signal is obtained by digitizing a no-plasma shot with magnetic fields where the probing beam is reflected off the far wall of the vacuum vessel. On occasion, one or both of the BWOs pickup 360 Hz bursts of 55 kHz noise from the ATF helical field power supplies. This pickup produces coherent oscillations in the BWO's output frequency, which can become large. Figure 6.20 shows a typical case where this 55 kHz noise is pronounced in the noise signal; however, note that the signal-to-noise ratio is

144
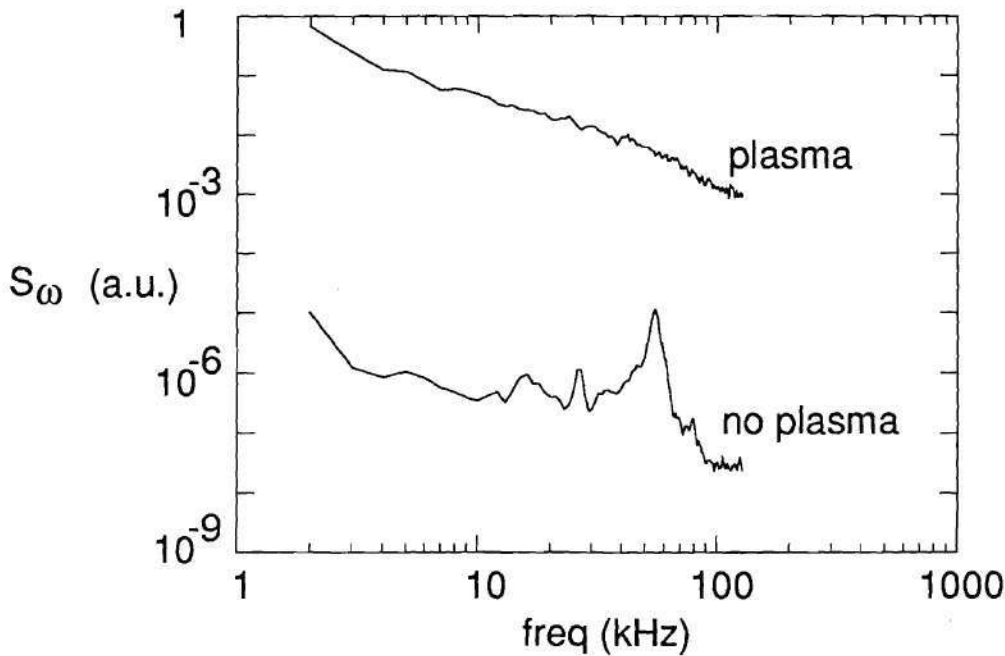
Figure 6.20: Power spectra for two signals with and without plasma, showing a strong 55 kHz fluctuation in the microwave source frequency.

still ~ 25 dB. This peak has no detectable contribution to the power spectrum for the plasma signal; thus, fluctuation analysis relying on the power spectrum and its integrated power is not typically affected by such a noise source.

System Summary

The ATF reflectometer is a tunable two-frequency reflectometer operating in the 30 to 40 GHz band using a dual antenna arrangement and quadrature phase detection. The reflectometer system is designed to allow the use of either the O-mode or the X-mode, selectable by the change of two waveguide twists. For O-mode operation, the density range that can be studied is limited to $(1.1–2.0) \times 10^{13}$ cm^{-3}. For X-mode operation at 0.95 T, the density range is approximately $(1.5–8.5) \times 10^{12}$ cm^{-3}.

X-mode operation at 1.9 T is not useful because the cutoff occurs on the low-field side of the fundamental cyclotron resonance, which is located well outside the last closed flux surface. Because of the magnetic shear in ATF, the launching of purely one mode is not possible. Modeling has shown that, under most circumstances, the proper polarization to launch should be oriented to the magnetic field polarization at the plasma edge. The spatial resolution of this reflectometer is estimated to be ~ 7 cm (the antenna beam width) in the poloidal and toroidal directions and ~ 0.5 to 1.1 cm in the radial direction. The ATF reflectometer simultaneously probes the plasma with two different microwave frequencies. Two frequencies can be independently detected in the same waveguide system by obtaining pure reference signals and using square law detectors.

An important issue for any fluctuation diagnostic is the system noise level. If the noise level is too high, the fluctuation measurements are highly suspect at best. For the ATF reflectometer, the noise level is down by at least 25 dB and often down by much more. In Chap. VII, the methods used in analyzing the data from this reflectometer are discussed. The improved techniques of quadrature phase detection and two-frequency operation play a significant role in allowing quantitative results to be obtained with this reflectometer.

CHAPTER VII

ATF REFLECTOMETER SIGNAL/DATA ANALYSIS

Introduction

The ATF reflectometer has incorporated phase detection, via the quadrature phase detectors, which has allowed quantitative measurements of the density fluctuations to be obtained by reflectometry. To obtain the phase delay due to the fluctuations in the cutoff layer, the raw data signals must be fringe counted, as discussed in the section "Raw Signal Analysis" below. Once the phase fluctuation signal is obtained, new quantitative results are possible. The density fluctuation amplitude $\tilde{n}_e/n_e$ can be calculated using the equations given in the section "Estimating $\tilde{n}_e/n_e$ From the Measured Phase Fluctuations" starting on page 158. The uncertainty in these calculations is also derived and discussed in the same section. A second quantitative result that is easier to obtain with phase detection is the measurement of the radial coherence of the density fluctuations and their radial correlation length. These measurements and their uncertainty are discussed in the section "Radial Coherence/Correlation Length Measurements" starting on page 170.
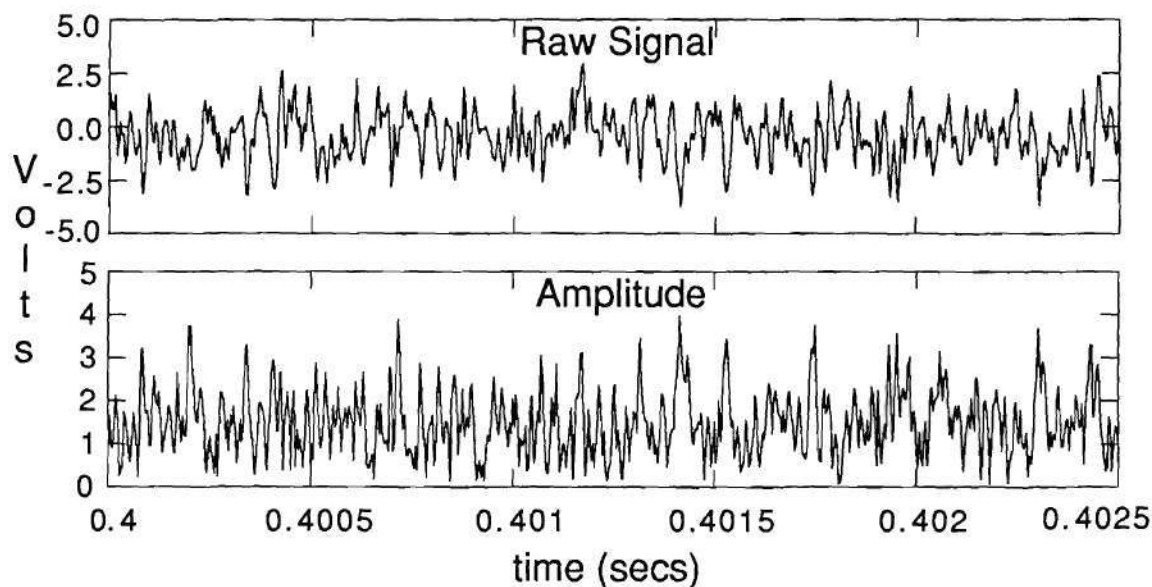
Figure 7.1: A raw data signal and the calculated amplitude fluctuations in the raw data signal. Note: the amplitude fluctuations are of the order of the peak-to-peak raw signal voltage.

Raw Signal Analysis

Quadrature phase detection, described in detail in Chap. III, is a type of homodyne detection that is superior to simple homodyne detection because it provides the two output signals $V_a = \tilde{A} \sin \tilde{\zeta}$ and $V_b = \tilde{A} \cos \tilde{\zeta}$, where $\tilde{\zeta}$ is the phase fluctuation in the reflected signal, primarily resulting from fluctuations in the critical layer, and $\tilde{A}$ is the fluctuating amplitude of the reflected signal. The fluctuating amplitude can be calculated from $\tilde{A} = (V_a^2 + V_b^2)^{1/2}$ and removed from V_a and V_b to obtain $\sin \tilde{\zeta}$ and $\cos \tilde{\zeta}$. The removal of $\tilde{A}$ is important in analyzing the data because the amplitude modulation is of the order of the raw signal amplitude, as shown in Fig. 7.1. Amplitude fluctuations of this magnitude make analysis of the data difficult. Coherence measurements between the calculated amplitude fluctuations $\tilde{A}$

148

and the phase fluctuations $\tilde{\zeta}$ or the sine and cosine signals are inconclusive on the relationship between the phase and amplitude fluctuations. V_a and V_b can also be used in a fringe-counting program to calculate the actual phase fluctuations. The use of fringe counting is a relatively new analysis technique for these data.

A difficulty that arises when analyzing the raw data is that each quadrature phase detector is designed for a specific center frequency, and at other frequencies V_a and V_b do not have a 90° phase relation. However, the amount of phase deviation $\Delta\psi$ can be estimated or measured, and V_b can be advanced or delayed using the relationship

$$V_b' = \frac{V_b - V_a \sin(\Delta\psi)}{\cos\Delta\psi} \tag{7.1}$$

to obtain a 90° phase relation between V_a and V_b'.

Fringe Counting

The sine-cosine detection obtained with quadrature phase detection allows the determination of the actual phase fluctuation. Taking the inverse tangent of the ratio of the two signals gives the phase signal with limits of $\pm\pi$. Unfortunately, when the phase advances beyond π, the phase is reset to $-\pi$, resulting in a large discontinuity in the phase. This phase reset results in distortion to the signals' frequency spectrum. However, these phase resets can be removed numerically so that the phase can be tracked over many 2π (fringe) movements. Fringe counting also permits determination of the direction of the phase shift, which indicates the direction of motion of the cutoff layer. In fringe counting the ATF reflectometer data, an unexplained phase jump problem has been encountered. Data taking during steady-state plasmas, in which the line-averaged density is constant and so the position of the cutoff layer is expected to be constant, show many fringes of phase change during the data window (see Fig. 7.2). Closer inspection of the data shows that most of the phase shift is due to phase jumps greater than π occurring over

149
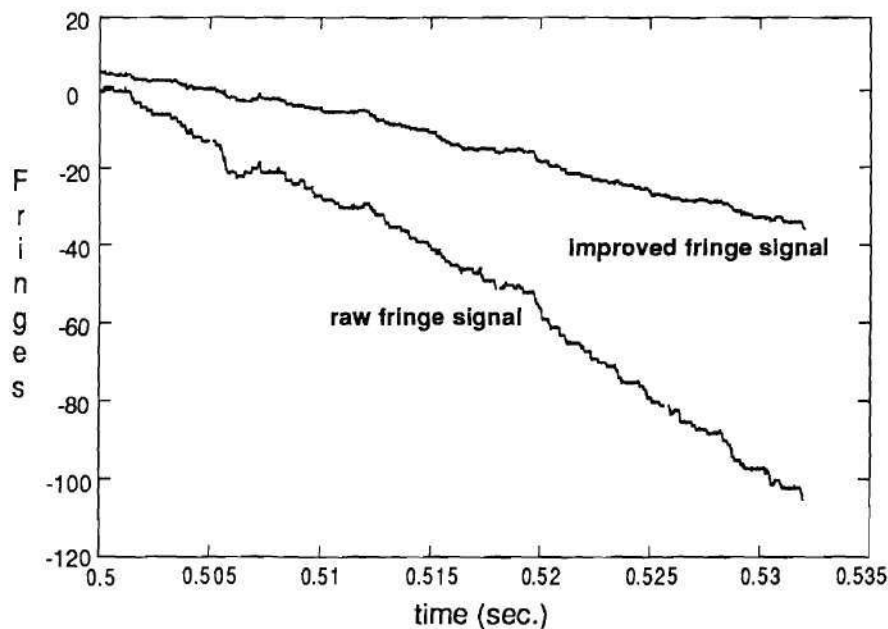
Figure 7.2: The raw and improved fringe-counted signals. Note that most of the large phase jumps in the raw signal have been removed to obtain the improved signal.

several consecutive data points. The cause of these phase jumps has not been determined, but it can clearly be assumed that they are not due to a real movement of the cutoff layer because the total phase change represents a distance greater than the plasma radius. Possible sources of these phase jumps are interference effects in the amplitude and phase of the quadrature signals due to reflection off a turbulent surface (comparable to a diffraction grating), deviations from true quadrature signals due to unbalanced amplitudes, or a non-90° phase relation between the two channels. Additionally, the phase jumps may be a result of asymmetric phase spectra resulting from Bragg scattering. If a significant portion of the received signal is Doppler shifted due to Bragg scattering, a significant asymmetry will occur between the positive and negative sides of the frequency spectrum. Refer to Chap. V for an explanation of negative frequencies.

A strong argument for the phase jump problem being caused by a strong scattered component in the received signal is the systematic trend in the fringe data. As shown in Fig. 7.2, the phase is advancing in one direction for the entire data window. Random phase scrambling and deviations from true quadrature detection would be expected to produce random phase jumps, while a significant contribution from scattering would produce a continuous phase advance superimposed upon the phase fluctuations. This is quite similar to the observed phase data. Quadrature phase detection provides the necessary information to look for Doppler shifting in the raw data. By writing the raw data in the form of a complex signal,

$$V = \cos \tilde{\zeta} + i \sin \tilde{\zeta} \tag{7.2}$$

where the amplitude fluctuations $\tilde{A}$ have been calculated and removed, the positive and negative frequencies of the fluctuation spectra can be resolved. In Fig. 7.3, the complete spectra for the signal defined in Eq. (7.2) are shown. Small differences can be seen in the amplitudes on each side of 0 kHz. Computing the percent difference between the positive and negative sides with the equation

$$\delta(\%) = \sum_i \frac{A(f_i) - A(-f_i)}{[A(f_i) + A(-f_i)]/2} \times 100 \tag{7.3}$$

where δ is simply the percent difference, $A(f_i)$ represents the amplitude of the ith positive frequency term and $A(-f_i)$ represents the amplitude of the ith negative frequency term. A difference of up to $\sim 35\%$ is indicated by Fig. 7.4. The fringe-counted data for this signal had many phase jumps, similar to the uncorrected fringe data in Fig. 7.2. Unfortunately, no data with zero phase jumps have been obtained to determine if the Doppler shift goes away; however, it does appear that the total phase shift due to the phase jumps does increase with increasing amounts of Doppler shift.

The phase jumps represent a significant problem in performing fluctuation analysis on the data because they cause a significant increase in the power spec-
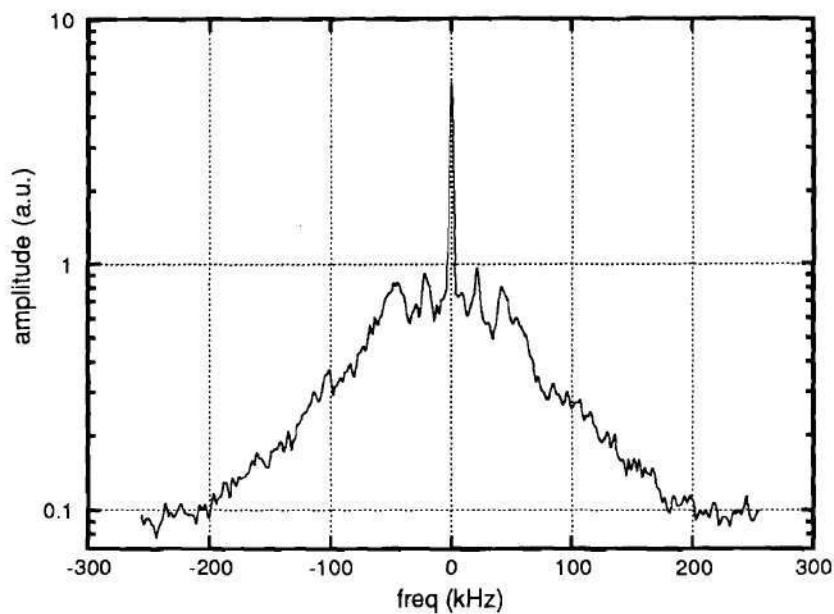
Figure 7.3: Fourier analysis of the complex signal from the reflectometer quadrature phase detector, showing the positive and negative sides of the spectrum. Note, this is the FFT of $e^{i\tilde{\zeta}}$, not the FFT of $\tilde{\zeta}$.
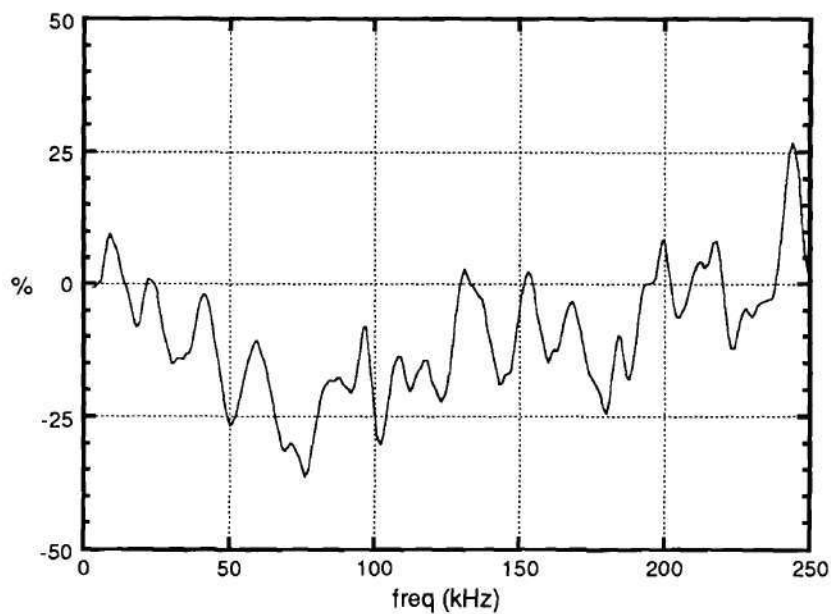
Figure 7.4: The difference between the amplitudes of the ith positive and negative frequency components of the Fourier-analyzed complex signal.

152
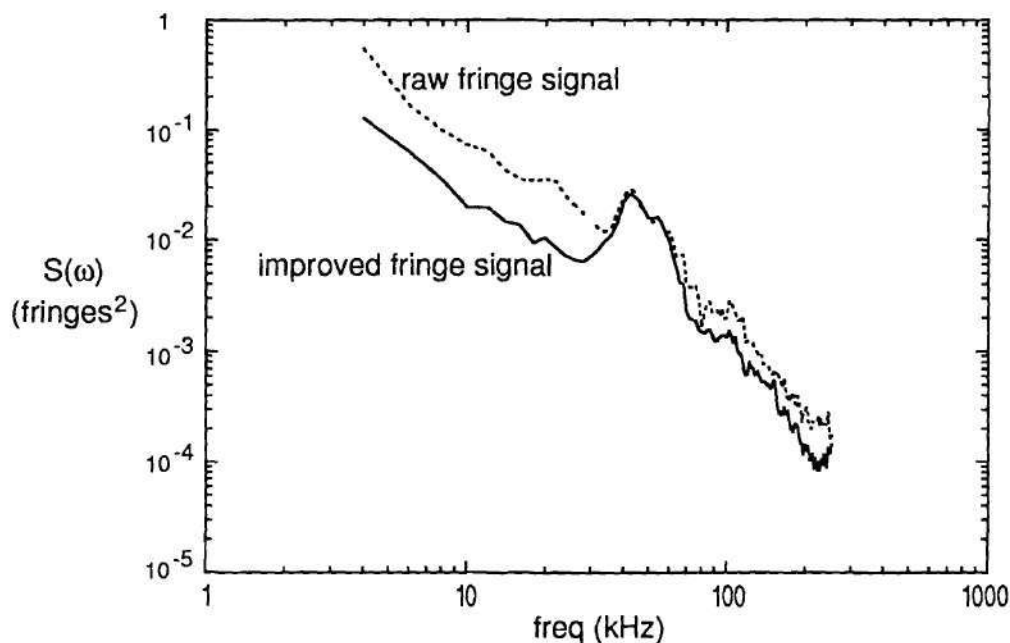
Figure 7.5: The power spectra for the raw and improved fringe-counted signals.

trum when the data are Fourier analyzed, as shown in Fig. 7.5. These phase jumps make quantifiable forms of data analysis on the signal difficult because they produce a significant noise source across the entire frequency spectrum due to their step-function-like shape. Since the phase jumps are not believed to represent a real movement of the cutoff layer, the raw fringe signals are processed through an algorithm that removes a significant number of the phase jumps. This can considerably reduce the contribution of the phase jumps to the power spectrum. The algorithm removes most phase jumps by looking at the difference between every two and three consecutive data points. If the difference between any two adjacent data points is $> 0.5\pi$, the difference is treated as an offset and removed from that data point and all the following data points in the data array. Next, if the difference between every other data point is $> 0.8\pi$, the difference is subtracted from the affected data. Generally, fewer than 5% of the data points produce these undesired phase jumps.

153

The improved fringe signal resulting from this phase jump removal is shown in Fig. 7.2, and the improvement in the power spectra is shown in Fig. 7.5. Note the significant decrease in the power spectrum for the improved fringe signal over most of the spectrum. No conclusive evidence exists to support this form of data manipulation, but the removal of the phase jumps must be done to obtain reasonable power spectra. The following observations support this manipulation: the rapid increase in the power spectra of the raw fringe signals below 30 kHz is not observed in the sine or cosine signals' spectra; the coherence between the raw data signals and any one of the sine, cosine, or improved fringe signals is good for the entire spectrum, except for the improved fringe signals where the coherence falls off sharply around 10–20 kHz; the coherence between the raw data and the raw fringe signal is not as high and falls off sharply for frequencies less than 30–40 kHz. Radial coherence measurements (see page 170) provide similar observations; primarily, the coherence between two signals obtained from two closely spaced cutoff layers is approximately the same for the sine/cosine signals and the improved fringe signals for frequencies above $\sim$ 10–20 kHz, but the coherence between two raw fringe signals or between a raw fringe signal and a sine or cosine signal falls off rapidly for frequencies below 30–40 kHz. These observations provide some support for the validity of removing the phase jumps, as well as providing an indication that the low-frequency resolution of the improved fringe data is $\gtrsim$ 10 kHz.

Uncertainty in the Measured Phase

Later in this chapter the rms phase fluctuation amplitude $\tilde{\zeta}$, which is the rms amplitude of the fringe signal, is used to calculate the density fluctuation amplitude $\tilde{n}_e/n_e$. Additionally, the uncertainty in $\tilde{n}_e/n_e$ is estimated based on the uncertainties in the parameters used in calculating $\tilde{n}_e/n_e$. One of the uncertainties that is needed is due to the error in $\tilde{\zeta}$ calculated from the spectral amplitude of the fringe signals.

154

The dominant error in $\tilde{\zeta}$ is believed to result from the phase jumps in the fringe signals. The phase jumps lead to a systematic overestimation of $\tilde{\zeta}$. Since the severity of the phase jumps varies from one signal to the next, the correction for the overestimation is believed to be 20% $\pm$ 20%; that is, the best case is no phase jumps with no biasing of $\tilde{\zeta}$ and the worst case is a 40% biasing of $\tilde{\zeta}$ due to the phase jumps. The 20% offset is removed from $\tilde{\zeta}$ when $\tilde{\zeta}$ is used in Eq. (7.11) to calculate the radial width δr_c of the fluctuations. Additionally, the uncertainty in $\tilde{\zeta}$ is estimated to be $\sigma_{\tilde{\zeta}}/\tilde{\zeta} \simeq 20\%$. Note that the rms phase is calculated as the square root of the sum of the APSD of each fringe signal for $10 \text{ kHz} \leq f_i \leq f_s/2$, where f_i is the ith frequency component of the APSD and f_s is the digitizing frequency.

There are other possible sources of error in the measured phase, but these are expected to be small or unquantifiable at this time. These sources include noise in the detected signals due to frequency modulation of the BWOs, pickup in the detectors and amplifiers, and averaging of the reflected phase due to the presence of more than one wave cycle in the sampling volume for $k_r \ll k_0$. See the section "Spatial Resolution" in Chap. VI for a discussion on the size of the sampling volume. The total system noise is discussed in the section "Noise Estimates" in Chap. VI where it is concluded that the total system noise is not significant. The possible averaging of the reflected signal over several spatial cycles of a fluctuation due to the finite measurement volume would lead to scrambling of the sum phase at the detectors. This could lead to a reduction in the measured phase. This possible error is neglected here.

Calculating the Cutoff Location r_c and Its Uncertainty

The position of the cutoff layer is easily calculated from the O- or X-mode cutoff conditions, $\omega = \omega_{pe}$ or $\omega = \omega_R$, respectively, where ω_{pe} and ω_R were previously defined in Chap. II. Simply, the density profile and magnetic field profile for the X-mode are used to calculate the cutoff frequency profile. Then a numerical interpolation is done to obtain the radius at which $\omega = \omega_{pe}$ or $\omega = \omega_R$, where ω is the probing beam frequency. To estimate the random uncertainty in the calculated cutoff position, propagation of errors is used in the equation for the cutoff frequency to calculate the standard deviation of the cutoff frequency profile. The cutoff location is then calculated for the original profile plus one standard deviation and again for the original profile minus one standard deviation. For the O-mode, the standard deviation of the cutoff frequency is simply given by the uncertainty in the plasma frequency,

$$\frac{\sigma_{\omega_{pe}}}{\omega_{pe}} = \frac{1}{2}\frac{\sigma_{n_e}}{n_e} \tag{7.4}$$

where σ_{n_e}/n_e is the uncertainty in the electron density. For the X-mode, the standard deviation of ω_R (or variance, here) is obtained from Eq. (2.6) as

$$\sigma_{\omega_R}^2 = \frac{\sigma_{\omega_{ce}}^2}{4\omega_{ce}^2}\left(\omega_{ce} + \frac{\omega_{ce}^2}{\sqrt{\omega_{ce}^2 + 4\omega_{pe}^2}}\right)^2 + \frac{\sigma_{n_e}^2}{n_e^2}\left(\frac{\omega_{pe}^2}{\sqrt{\omega_{ce}^2 + 4\omega_{pe}^2}}\right)^2 \tag{7.5}$$

where $\sigma_{\omega_{ce}}/\omega_{ce}$ simply translates to the uncertainty in the magnetic field $\sigma_B/|\vec{B}|$.

The ATF magnetic field is determined completely by the currents applied to the helical and vertical field coils and is calculated to a high degree of accuracy using the Biot-Savart law solution.[149,150] For the typical ECH discharges studied with the ATF reflectometer, the density profiles are characterized by a steep edge gradient occurring over the outer one-third of the minor radius, see Fig. 8.1 in Chap. VIII. The uncertainty in $|\vec{B}|$ at any known position may be very small, but because of the

156
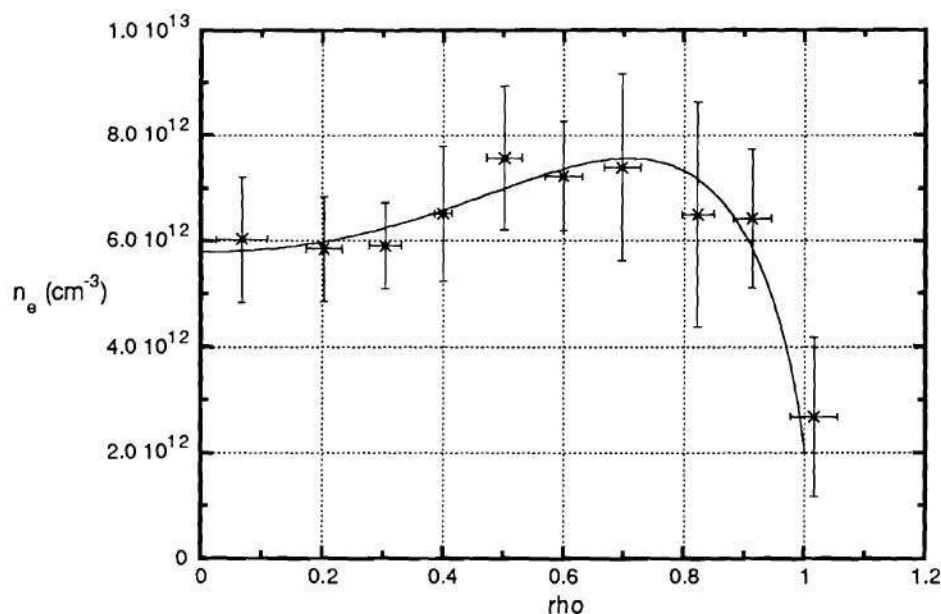
Figure 7.6: Thomson scattering density data points from 16 shots and 8 laser positions[152] with error bars. The best fit density profile is also shown.

uncertainty in the location of the cutoff layer some uncertainty in determining $|\vec{B}|$ is introduced. This uncertainty is estimated here as the average change in $|\vec{B}|$ over the density gradient region, i.e., from $\rho = 0.75$ to 1.0 or $r = 22$ cm to 30 cm. As can be seen in Fig. 6.7, the magnetic field in this region is ~ 0.72 T $\pm 7\%$; therefore, for the purposes of estimating the uncertainties in the reflectometer data, $\sigma_{\omega_{ce}}/\omega_{ce} = 7\%$ will be assumed.

The density profiles (e.g. see Fig. 8.1) used in analyzing the ATF reflectometer data are obtained from Thomson scattering measurements.[151,152] Figure 7.6 shows a typical set of Thomson scattering data with the fitted profile.[152] The data points shown were obtained by averaging the data from 16 shots during which the laser was scanned over 8 different radial positions.[153] The error bars represent the experimental standard deviation in the raw data. From Fig. 7.6, the uncertainty

in the density in the edge gradient region is typically 25%. For the purposes of estimating the uncertainty in the reflectometer data, $\sigma_{n_e}/n_e = 25\%$ is assumed from here on.

For typical low-density ECH discharges, $\sigma_{\omega_R}/\omega_R \approx 5\%$ to 10%, which corresponds to an uncertainty in the location of the cutoff position of $\sigma_{r_c}/r_c \approx 5\%$ to 10% in the edge gradient region of the plasma. As discussed in the section "Spatial Resolution" in Chap. VI, the phase information in the reflected signal is most sensitive to fluctuations occurring a short distance in front of the cutoff layer; therefore, quoting the location of the cutoff layer as the location of the fluctuation measurement introduces a systematic error in the quoted location of the measured fluctuations. This systematic error is neglected here; the cutoff position is used as the location of the measured fluctuation information. The systematic error is probably of order 1 to 3 times λ_0 of the probing beam; thus, the position of the measured fluctuations is moved outward $\sim$ 1–3 cm from the cutoff position.

Estimating $\tilde{n}_e/n_e$ From the Measured Phase Fluctuations

Most fluctuation reflectometers have not been used to quantify the density fluctuation level $\tilde{n}_e/n_e$ because the signal they measure is $\tilde{A}\cos\tilde{\zeta}$. With quadrature phase detection, the ATF reflectometer can measure $\tilde{\zeta}$, which is necessary for fluctuation amplitude estimates. In the following section, the equations for estimating $\tilde{n}_e/n_e$ is developed, and an equation for the uncertainty in this $\tilde{n}_e/n_e$ estimate is derived.
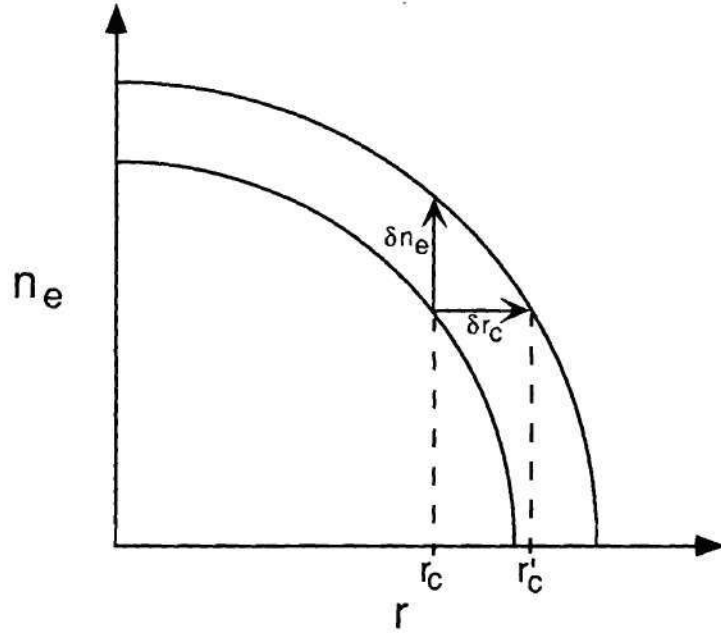
Figure 7.7: The initial cutoff condition $n_e(r_c)$ becomes $n_e(r'_c) + \delta n_e$ when the initial density is perturbed by δn_e and the cutoff position r_c becomes r'_c.

Density Perturbation Expansion

For a fixed probing beam frequency ω, the cutoff is located at a position r_c, and the density at this location is $n_e(r_c)$. Now, a perturbation δn_e moves the cutoff location to r'_c and the density at r_c is now given by $n_e(r_c) \rightarrow n_e(r'_c) + \delta n_e$, as shown in Fig. 7.7. The new cutoff density $n_e(r'_c)$ is now rewritten using the standard Taylor series expansion as

$$n_e(r'_c) = n_e(r_c) + \left. \frac{dn_e}{dr} \right|_{r_c} \delta r_c \tag{7.6}$$

where the derivative dn_e/dr is evaluated at the initial cutoff location r_c and $\delta r_c = r'_c - r_c$. Now noting that the derivative of the density at r_c can be written as $n_e(r_c)/L_n$, where $L_n = n_e(dn_e/dr)^{-1}$ is the density gradient scale length and will be negative under most conditions, Eq. (7.6) becomes

$$n_e(r'_c) = n_e(r_c) \left[1 + \frac{\delta r_c}{L_n} \right]_{r_c} \tag{7.7}$$

159

O-mode Solution The initial equation for the O-mode cutoff is given by

$$\omega^2 = \omega_{pe}^2(r_c) = \frac{e^2 n_e(r_c)}{\epsilon_0 m_e} \tag{7.8}$$

Applying the density perturbation shown in Fig. 7.7, the equation for the cutoff becomes

$$\omega^2 = \frac{e^2}{\epsilon_0 m_e} \left[n_e(r_c') + \delta n_e \right] \tag{7.9}$$

Substituting in Eq. (7.7) for $n_e(r_c')$, applying the initial condition $\omega^2 = \omega_{pe}^2(r_c)$, and solving, an equation for the density fluctuation amplitude is obtained,

$$\frac{\delta n_e}{n_e} = \frac{\delta r_c}{L_n} \tag{7.10}$$

Here, δr_c is the radial width or amplitude of the density fluctuations and can be inferred from the reflectometer phase as

$$\delta r_c = \frac{\tilde{\zeta} \lambda}{2} \tag{7.11}$$

where $\tilde{\zeta}$ is the phase fluctuation amplitude in fringes corrected for the bias resulting from the phase jumps, as discussed in the section "Uncertainty in the Measured Phase" on page 154, normalized to 2π radians (fringes), and λ is the probing beam wavelength. The factor of $1/2$ results from the wave traversing δr_c on arrival and after reflection.

Finally, the density fluctuation amplitude is

$$\frac{\tilde{n}_e}{n_e} = \frac{\tilde{\zeta} \lambda}{2 L_n} \tag{7.12}$$

where δn_e has been replaced with the more standard $\tilde{n}_e$. If $\tilde{\zeta}$ is the amplitude of one frequency component from the amplitude spectrum obtained by Fourier analysis of a fringe signal, then $\tilde{n}_e/n_e$ is the fluctuation amplitude for the ith frequency component, but if $\tilde{\zeta}$ is the rms phase amplitude obtained by taking the square root of the sum over frequency of the APSD, the density fluctuation level or rms density fluctuation amplitude is obtained. For more details on the Fourier analysis and the definition of the APSD, see Chap. V.

160
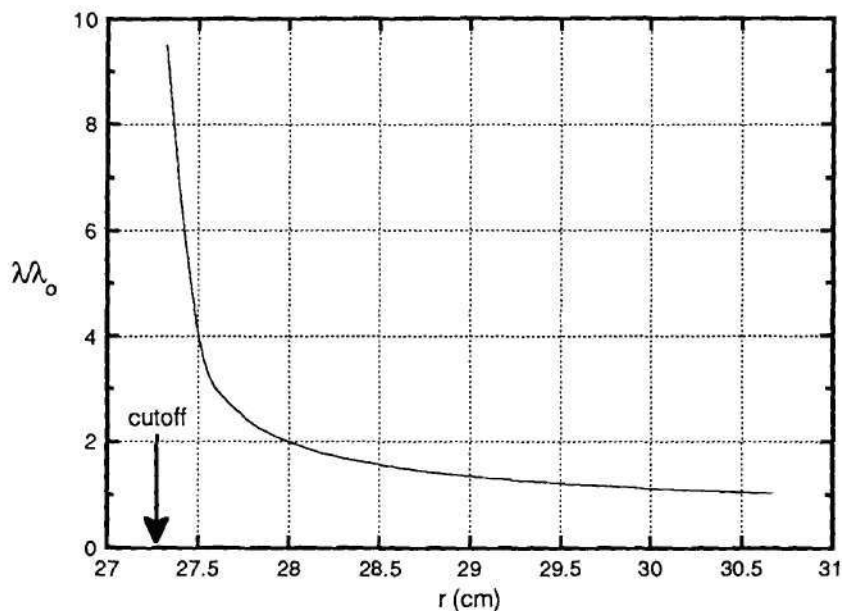
Figure 7.8: The probing beam wavelength, normalized to the vacuum wavelength, as a function of the distance in front of the cutoff layer.

Discussion on Choosing λ   The appropriate value of λ to use in Eq. (7.11) for calculating δr_c is not well defined. The wavelength in the plasma is greater than the vacuum wavelength and sweeps to infinity as cutoff is approached, as shown in Fig. 7.8; however, the appropriate value of the wavelength is certainly not infinity because the density fluctuations would then produce no phase shift in the reflected signal. The vacuum wavelength λ_0 could be used, but this would clearly lead to an underestimate since $\lambda > \lambda_0$ in the plasma and since the density fluctuations at the cutoff layer do not cause the entire plasma to move in unison. Now consider the case where the vacuum wavelength of the probing beam is less than the radial correlation length of the fluctuations $\lambda_0 < L_c$. The density fluctuations at the cutoff layer are coherent over some radial width, causing the electrons to move in unison within the distance L_c of the cutoff layer. Thus, even though the cutoff layer is moving, the probing beam sees the same density profile within the coherent region.

161

Outside the coherent region, the density fluctuations at the cutoff layer do not affect the electrons, and so the probing beam sees a changing density or path length as the cutoff layer moves. Thus, the phase information in the reflected probing beam will be determined by the radial displacement of the cutoff layer and the probing beam wavelength just outside the region of the coherent density fluctuations.

It is shown in Chap. IX that the radial correlation lengths of the density fluctuations in the edge density region of ATF are of order 1–3 cm. From the argument above, this would imply that the wavelength to use in determining δr_c from $\tilde{\zeta}$ is the wavelength 1–3 cm in front of the cutoff layer. From Fig. 7.8, λ is seen to vary roughly between 1.5 and 3.5 times λ_0 in this region. For the purposes of the data discussed in this dissertation, the average value of $\lambda = 2.5\lambda_0$ is used. This simple approximation assumes that the phase information in the reflected signal is localized to a small region just in front of the cutoff layer. As discussed in the section "Spatial Resolution" in Chap. VI, Mazzucato and Nazikian[147,148] have shown that this is true only for $k_r \ll k_0$, where k_r is the radial wave number of the fluctuations and k_0 is the probing beam wave number. For the case of $k_r \gtrsim k_0$, the phase information in the reflected signal will be reduced by averaging of the reflected signal over multiple spatial cycles of the fluctuation. In this case, the systematic underestimation of δr_c will be much larger, requiring a larger correction factor. It is shown in Chap. IX that the mean k_r observed by reflectometry in ATF, as determined by radial coherence measurements, is $k_r < 1$ cm^{-1}, while for the 30–40 GHz probing beam, the minimum k_0 is 6.1 cm^{-1}. Thus, the ATF reflectometer operates in a regime where $k_r \ll k_0$, and so the simple approximation $\lambda \simeq 2.5\lambda_0$ is sufficiently valid for the results shown in this dissertation. Radial coherence measurements and radial wave number estimations are discussed later in this chapter.

The choice of $\lambda = 2.5\lambda_0$, as discussed above, is an attempt to estimate and correct for the systematic uncertainty represented by the unknown value of

162

the wavelength producing the largest contribution to the phase of the reflected signal. This estimated value of λ can lead to systematic errors in δr_c and $\tilde{n}_e/n_e$ since it does not address the possible change in sensitivity due to changes in the radial wavelength or correlation length of the fluctuations between measurements. Additionally, the appropriate value of λ is probably dependent on the ratio of the radial wave number of the density fluctuations to the vacuum wave number of the probing beam. This ratio may vary between measurements, leading to an error in λ. For purposes of estimating the uncertainty in $\tilde{n}_e/n_e$, the random error in λ is estimated to be $\sigma_\lambda/\lambda \simeq 20\%$, based on the assumption that it is half of the range $(1.5\lambda_0$ and $3.5\lambda_0)$ used to estimate λ.

X-mode Solution   The unperturbed condition for the right-hand (upper) X-mode cutoff can be written as $\omega^2 - \omega\omega_{ce}(r_c) - \omega_{pe}^2(r_c) = 0$. Applying the density perturbation shown in Fig. 7.7, the equation for the cutoff becomes

$$\omega^2 - \omega\frac{eB(r_c')}{m_e} - \frac{e^2}{\epsilon_0 m_e}\left[n_e(r_c') + \delta n_e\right] = 0 \tag{7.13}$$

where $B(r_c')$ can be written in the form of Eq. (7.7), e.g.,

$$B(r_c') = B(r_c)\left[1 + \frac{\delta r_c}{L_B}\right]_{r_c} \tag{7.14}$$

where L_B is the magnetic field gradient length at r_c. Substituting in these expansions for $n_e(r_c')$ and $B(r_c')$, the equation for the cutoff becomes

$$\omega^2 - \omega\frac{e}{m_e}B(r_c)\left[1 + \frac{\delta r_c}{L_B}\right]_{r_c} - \frac{e^2}{\epsilon_0 m_e}n_e(r_c)\left[1 + \frac{\delta r_c}{L_n} + \frac{\delta n_e}{n_e}\right]_{r_c} = 0 \tag{7.15}$$

Applying the unperturbed equation for the cutoff and solving, the density fluctuation amplitude can be written as

$$\frac{\delta n_e}{n_e} = -\left[\frac{\omega\omega_{ce}}{\omega_{pe}^2}\frac{\delta r_c}{L_B} + \frac{\delta r_c}{L_n}\right]_{r_c} \tag{7.16}$$

Substituting in Eq. (7.11) for δr_c, the density fluctuation amplitude in terms of the measured phase fluctuation is obtained:

$$\frac{\tilde{n}_e}{n_e} = -\left[\left(\frac{\omega^2}{\omega_{pe}^2} - 1\right)\frac{1}{L_B} + \frac{1}{L_n}\right]_{r_c} \frac{\tilde{\zeta}\lambda}{2} \qquad (7.17)$$

Note that the X-mode equation for $\tilde{n}_e/n_e$ contains the equation for the O-mode estimate plus a correction for the effect of the magnetic field in the cutoff equation.

Uncertainty in $\tilde{n}_e/n_e$ Estimates

The random uncertainty in calculating $\tilde{n}_e/n_e$ from Eq. (7.12) or Eq. (7.17) is obtained by applying the technique of propagation of errors.[154] The uncertainty estimates derived here neglect systematic uncertainties that lead to biasing of the final results. These systematic uncertainties are discussed in the previous sections. The biasing resulting from these systematic uncertainties was estimated and corrected for in the data. The two biases considered in this experiment are the $\sim$ 20% overestimation of $\tilde{\zeta}$ due to the phase jumps, as discussed in the section "Uncertainty in the Measured Phase" on page 154, and the underestimation of δr_c due to the probing beam wavelength being greater than the vacuum wavelength in the plasma, as discussed in the section "Discussion on Choosing λ" on page 161.

For the O-mode case [Eq. (7.12)], the equation for the uncertainty $\sigma_{\tilde{n}_e}/\tilde{n}_e$ is immediately found to be

$$\frac{\sigma_{\tilde{n}_e}}{\tilde{n}_e} = \left(\frac{\sigma_{\delta r_c}^2}{\delta r_c^{\,2}} + \frac{\sigma_{L_n}^2}{L_n^2}\right)^{1/2} \qquad (7.18)$$

where σ is the standard deviation and the covariance between δr_c and L_n is assumed to be zero. The uncertainty in L_n is estimated in the section "Estimate of $\sigma_{\tilde{n}_e}/\tilde{n}_e$ for the X-mode" on page 166, where it is shown that a reasonable estimate for this uncertainty is $\sigma_{L_n}/L_n \approx 0.5$. The uncertainty in δr_c is given by the application of propagation of errors in Eq. (7.11) and the estimated uncertainties in $\tilde{\zeta}$ and λ. The uncertainties in $\tilde{\zeta}$ and λ were estimated previously to be $\sigma_{\tilde{\zeta}}/\tilde{\zeta} \simeq 20\%$ and

$\sigma_\lambda/\lambda \simeq 20\%$, leading to an estimated uncertainty in δr_c of $\sigma_{\delta r_c}/\delta r_c \approx 0.28$. For these values, the uncertainty in the density fluctuation amplitude is 57%. Clearly, if better density profile measurements were available on ATF, the uncertainty in $\tilde{n}_e/n_e$ could be significantly reduced.

X-mode Uncertainty   For the X-mode, $\sigma_{\tilde{n}_e}/\tilde{n}_e$ is not as straightforward as that for the O-mode and is written in terms of the partial derivatives of Eq. (7.17).[154] First, the variance is given by

$$
\begin{aligned}
\sigma_{\tilde{n}/n}^2 &= \sigma_\omega^2 \left(\frac{\partial \frac{\tilde{n}_e}{n_e}}{\partial \omega} \right)^2 + \sigma_{\omega_{pe}}^2 \left(\frac{\partial \frac{\tilde{n}_e}{n_e}}{\partial \omega_{pe}} \right)^2 + \sigma_{L_B}^2 \left(\frac{\partial \frac{\tilde{n}_e}{n_e}}{\partial L_B} \right)^2 \\
&+ \sigma_{L_n}^2 \left(\frac{\partial \frac{\tilde{n}_e}{n_e}}{\partial L_n} \right)^2 + \sigma_{\delta r_c}^2 \left(\frac{\partial \frac{\tilde{n}_e}{n_e}}{\partial \delta r_c} \right)^2 + \sigma_{L_n \omega_{pe}}^2 \left(\frac{\partial \frac{\tilde{n}_e}{n_e}}{\partial \omega_{pe}} \right) \left(\frac{\partial \frac{\tilde{n}_e}{n_e}}{\partial L_n} \right) \quad (7.19)
\end{aligned}
$$

where $\sigma_{L_n \omega_{pe}}^2$ is the covariance between the density gradient and the plasma frequency and all other covariances are assumed to be zero. The covariance between any two terms is zero if the two terms are independent of one another, and here $\sigma_{L_n \omega_{pe}}^2$ is approximated as $\sigma_{L_n} \sigma_{\omega_{pe}}$. Evaluating the partial derivatives in Eq. 7.19 and substituting back in, the variance can be written as

$$
\begin{aligned}
\sigma_{\tilde{n}/n}^2 &= \sigma_\omega^2 \left(-\frac{2\omega}{\omega_{pe}^2} \frac{\delta r_c}{L_B} \right)^2 + \sigma_{\omega_{pe}}^2 \left(\frac{2\omega^2}{\omega_{pe}^3} \frac{\delta r_c}{L_B} \right)^2 + \sigma_{L_B}^2 \left[\left(\frac{\omega^2}{\omega_{pe}^2} - 1 \right) \frac{\delta r_c}{L_B^2} \right]^2 + \sigma_{L_n}^2 \left(\frac{\delta r_c}{L_n^2} \right)^2 \\
&+ \sigma_{\delta r_c}^2 \left[-\left(\frac{\omega^2}{\omega_{pe}^2} - 1 \right) \frac{1}{L_B} - \frac{1}{L_n} \right]^2 + \sigma_{L_n} \sigma_{\omega_{pe}} \left(\frac{\delta r_c}{L_n^2} \right) \left(\frac{2\omega^2}{\omega_{pe}^3} \frac{\delta r_c}{L_B} \right) \quad (7.20)
\end{aligned}
$$

On the ATF reflectometer, the probing beam frequency ω can be measured to an accuracy of at least 0.1%, and so its uncertainty is neglected from here on. The uncertainty in $\tilde{n}_e/n_e$ is now estimated by

$$
\begin{aligned}
\left(\frac{\sigma_{\tilde{n}_e}}{\tilde{n}_e} \right)^2 &= \frac{\sigma_{\omega_{pe}}^2}{\omega_{pe}^2} \left(\frac{2\omega^2}{\omega_{pe}^2} \frac{\delta r_c}{L_B} \right)^2 + \frac{\sigma_{L_B}^2}{L_B^2} \left[\left(\frac{\omega^2}{\omega_{pe}^2} - 1 \right) \frac{\delta r_c}{L_B} \right]^2 + \frac{\sigma_{L_n}^2}{L_n^2} \left(\frac{\delta r_c}{L_n} \right)^2 \\
&+ \frac{\sigma_{\delta r_c}^2}{\delta r_c^{\,2}} \left[-\left(\frac{\omega^2}{\omega_{pe}^2} - 1 \right) \frac{\delta r_c}{L_B} - \frac{\delta r_c}{L_n} \right]^2 + \frac{\sigma_{L_n}}{L_n} \frac{\sigma_{\omega_{pe}}}{\omega_{pe}} \left(\frac{\delta r_c}{L_n} \right) \left(\frac{2\omega^2}{\omega_{pe}^2} \frac{\delta r_c}{L_B} \right) (7.21)
\end{aligned}
$$

where n_e has dropped out.
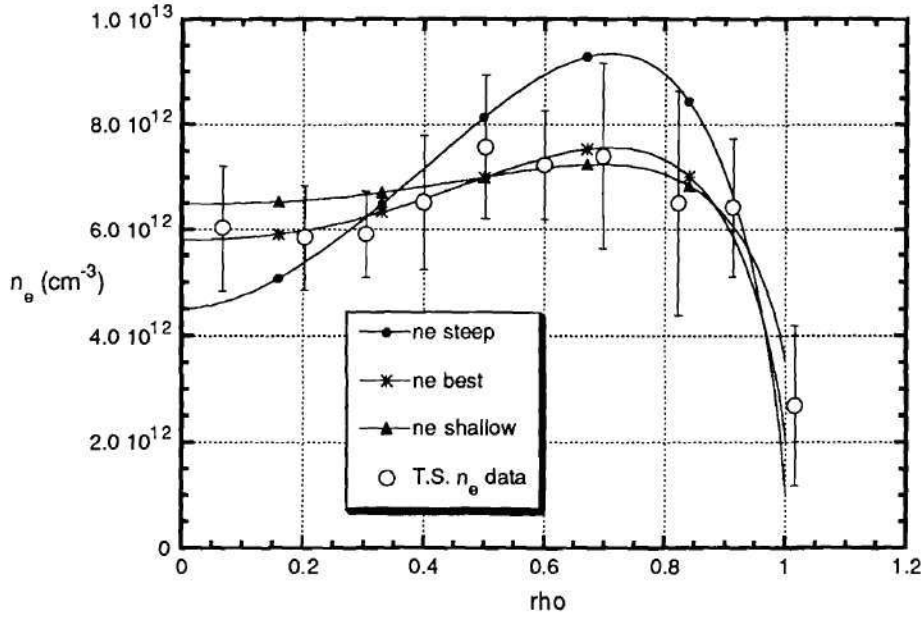
Figure 7.9: Two extreme density profile fits to the Thomson scattering data and the best fit. Note: these are extreme variations in the fitted profile under the restriction that the same fitting function is used.

Estimate of $\sigma_{\bar{n}_e}/\bar{n}_e$ for the X-mode The uncertainty in

$$\omega_{pe} = \left(\frac{e^2 n_e}{\epsilon_0 m_e} \right)^{1/2} \tag{7.22}$$

is dependent on the uncertainty in the electron density σ_{n_e}/n_e and by propagation of errors is given by $\sigma_{\omega_{pe}}/\omega_{pe} = \frac{1}{2}\sigma_{n_e}/n_e$ where $\sigma_{n_e}/n_e \approx 0.25$ for the Thomson scattering measurements on ATF, as discussed previously in this chapter in the section "Calculating the Cutoff Location and Its Uncertainty." By changing the profile fit to the Thomson scattering data points shown in Fig. 7.6, two realistic extremes on the density profile can be obtained, as shown in Fig. 7.9. A limitation in making these extreme fits is that the same fitting function, defined in Eq. (8.1), was used for all three fits. Note that the profiles shown have not been scaled using the line-integrated density measured by the 2 mm interferometer. Before any Thomson scattering density profile is used for further calculations, the line-integrated density

166
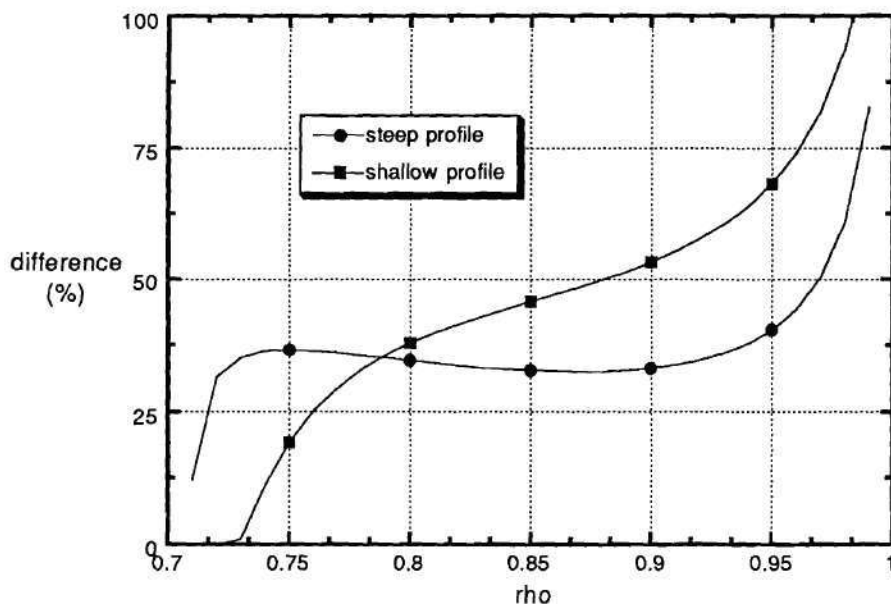
Figure 7.10: The difference between the calculated values of L_n for the best fit density profile in Fig. 7.9 and the two extreme fits. Since the reflectometer data come from the edge gradient region, only this region is shown here.

for the fitted profile is calculated and compared with that measured by the 2 mm interferometer. In this case, the ratio of the sequence-averaged line-integrated density from the 2 mm interferometer and the calculated line-integrated density for the fitted profile would be used to scale the fitted density profile. In Fig. 7.10, the normalized differences, e.g., for the steep profile $(L_n^{best} - L_n^{steep})/L_n^{best}$ and similarly for the shallow profile, between the calculated values of L_n for the best fit density profile and the two extreme profile fits are shown. Note that, for these three fitted profiles, the radial location of the maximum density was fixed, and the profiles were scaled to match the measured line integrated density measured. If this location of the maximum density was allowed to change, very large differences between the best fit profiles' gradient length and the two extreme fit profile's gradient lengths occur as the peaks are approached. This is due to the rollover in the density pro-

167

file. Since the uncertainty in L_n at the location of the X-mode cutoff is desired, the comparison of the calculated values of L_n for the three fitted density profiles would have to be adjusted in radius so that the values were aligned so that they correspond to the same cutoff frequency. To simply estimate typical uncertainties in L_n, the location of the maximum density was held fixed and the comparison of the gradient lengths was made with respect to the radial location. Using Fig. 7.10, an average uncertainty in L_n can be estimated as the average of the differences in the calculated density gradient lengths. Thus, the uncertainty in L_n can be estimated to be $\sigma_{L_n}/L_n \approx 0.5$.

Also discussed in the section "Calculating the Cutoff Location and Its Uncertainty" of this chapter is the estimation of the uncertainty in the magnetic field. The magnetic field is calculated to a high degree of accuracy using the Biot-Savart law[149,150] since the magnetic field in ATF is determined completely by the currents applied to the field coils. Therefore, the uncertainty in the magnetic field and in its gradient length at any known location is negligible, but the uncertainty of these values at the cutoff layer has some uncertainty because of the imprecise knowledge of the location of the cutoff layer. As shown in Fig. 7.11, the magnetic field gradient length changes slowly over the outer one-third of the minor radius ($20 \leq r \leq 30$ cm), where most reflectometer data are obtained. The magnetic field gradient length in this region is ~ 65 cm $\pm 7\%$, and so the uncertainty in the gradient length is estimated to be $\sigma_{L_B}/L_B \approx 0.07$.

Finally, the uncertainty in the measured signal $\delta r_c = \tilde{\zeta}\lambda/2$ is estimated to be 0.28, as discussed on page 164. Typical X-mode reflectometer data in low-density ATF plasmas are obtained from a region of the plasma with the following typical parameter values: $\omega_{pe} = 17.5$ GHz, $\omega_{ce} = 19.7$ GHz, $\omega = 30$ GHz, $L_B = -64$ cm, and $L_n = -25$ cm. A typical measured value for δr_c is 0.2 cm, and the resulting fluctuation amplitude [calculated from Eq. (7.17)] is $\tilde{n}_e/n_e = 0.014$ with

168
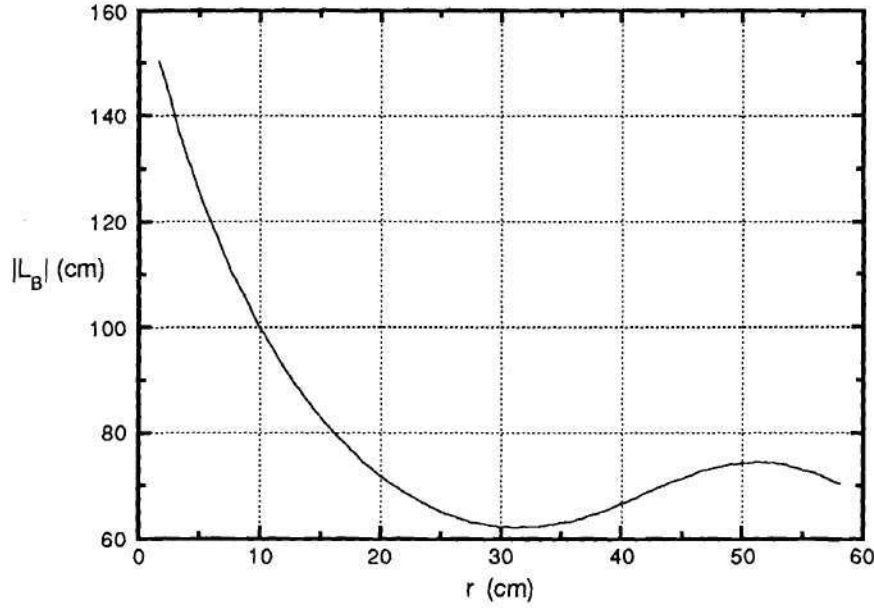
Figure 7.11: The magnetic field gradient length $|L_B|$ for the geometry of the ATF reflectometer.

an uncertainty of $\sim 48\%$.

Using the values of the plasma parameters and uncertainties defined above, the sensitivity of $\sigma_{\tilde{n}_e}/n_e$ was tested by varying each of the individual uncertainties, $\sigma_{\omega_{pe}}/\omega_{pe}$, σ_{L_B}/L_B, σ_{L_n}/L_n, and $\sigma_{\delta r_c}/\delta r_c$, from 0 to 1.0 while holding all other parameters constant. The results of this scan are shown in Fig. 7.12. Note in Fig. 7.12 that the uncertainty in the density profile via the uncertainty in ω_{pe} can quickly dominate $\sigma_{\tilde{n}_e}/\tilde{n}_e$. Unfortunately, the 25% uncertainty estimated for $n_e(r)$ can lead to relatively large uncertainties in L_n, especially with the steep edge gradients present in the flat or hollow density profiles obtained in ATF. Figure 7.12 shows that increasing σ_{L_n}/L_n to 100% increases $\sigma_{\tilde{n}_e}/\tilde{n}_e$ to $\sim 70\%$, while decreasing σ_{L_n}/L_n to 0 decreases $\sigma_{\tilde{n}_e}/\tilde{n}_e$ to $\sim 30\%$ for the assumed parameters. The uncertainty in the magnetic field gradient length is sufficiently small that it contributes negligibly to $\sigma_{\tilde{n}_e}/\tilde{n}_e$. Finally, the uncertainty in the measured radial displacement of the fluctuation $\sigma_{\delta r_c}/\delta r_c$ is

169
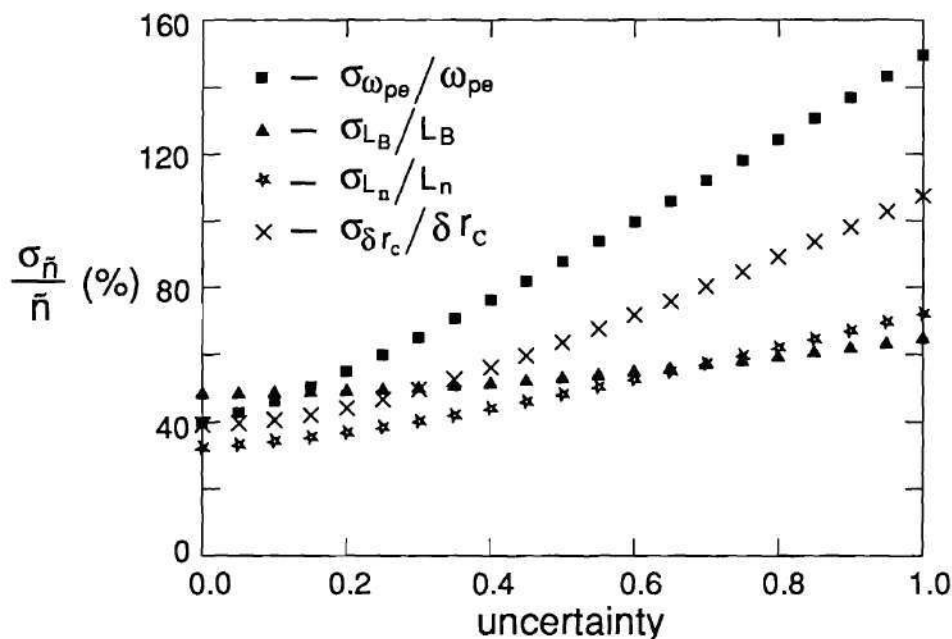
Figure 7.12: Individual scans of the uncertainties in ω_{pe}, L_B, L_n and δr_c and the resulting values of $\sigma_{\tilde{n}_e}/n_e$.

the most likely parameter to increase $\sigma_{\tilde{n}_e}/\tilde{n}_e$ significantly. As can be seen in Fig. 7.12 if $\sigma_{\delta r_c}/\delta r_c$ is increased by a factor of two to 56%, $\sigma_{\tilde{n}_e}/\tilde{n}_e$ increases by almost a factor of two to $\sim 70\%$.

Radial Coherence/Correlation Length Measurements

The capability of the ATF reflectometer to operate two frequencies simultaneously along the same radial chord with a frequency separation as low as 10 MHz with quadrature phase detection provides a simple means of making radial coherence measurements of the density fluctuations. The frequency-resolved coherence $\gamma(f)$ between the phase of the signals reflected at the two critical layers is calculated using standard cross-correlation analysis techniques, as discussed in Chap. V,

170

and is determined as a function of the frequency separation between the two signals. Conversion of the frequency separation to a radial distance is dependent upon knowing the density gradient at the critical layers. The ability to obtain the phase fluctuation $\tilde{\zeta}$ from the quadrature phase detectors greatly improves the ability to perform radial coherence measurements.

Correlation Length Determination

The normalized coherence, defined in Eq. (5.11), between two signals is modeled as

$$\gamma = \gamma_0 e^{-\Delta r / L_c} \tag{7.23}$$

where γ_0 is the coherence for zero radial separation and may be less than one due to uncorrelated noise in the two signals, Δr is the radial separation between the critical layers associated with the two signals (probing beams), and L_c is the radial correlation length of the density fluctuations. If multiple radial separations are obtained by scanning the probing beam frequency, then the radial correlation length can be determined. Take the natural logarithm of γ to obtain

$$\ln \gamma = \ln \gamma_0 - \frac{\Delta r}{L_c} \tag{7.24}$$

where this equation is now in the form of an equation for a line, $y = sx + b$, where $y = \ln \gamma$, $x = \Delta r$. Since x and y can be obtained from the coherence analysis, the slope ($s = -1/L_c$) and y-intercept ($b = \ln \gamma_0$) can be calculated by performing a least-squares fit to Δr vs $\ln \gamma$. Since $\gamma(f)$ is determined as a function of each frequency component, the calculated correlation length will also be a function of frequency and indicates the wavelength spread at that fluctuation frequency, assuming the relation $L_c \approx \lambda^2 / \delta\lambda$, where λ is the fluctuation wavelength.

Uncertainty in the Measured Correlation Length

A simple approach to estimating the uncertainty in the measured radial correlation length, i.e., the fitted slope, is to assume that the only uncertainties in the data are due to statistical fluctuations in $\gamma(f)$. In this case, the uncertainty in the fitted slope is easily derivable, as shown by Bevington.[154] However, the uncertainties in the data are not only statistical, but rather a combination of statistical and random uncertainties. Following the technique outlined by Bevington[154] for the calculation of the uncertainties in a least-squares fit, the first step is to identify the uncertainties contributing to the total uncertainty. The independent variable for the least-squares fit is Δr and the dependent variable is $\ln \gamma$. Bendat and Piersol[134] show that the variance resulting from statistical uncertainties in γ^2 estimated by DFT analysis, described in Chap. V, for two white noise signals (a good representation of fluctuation data) is given by

$$\sigma_{\gamma_i^2}^2 \simeq \frac{\sqrt{2}\,(1 - \gamma_i^2)}{\gamma_i \sqrt{n_w - 1}} \tag{7.25}$$

where n_w is the number of realizations or windows averaged over in calculating the average spectra and coherence, the subscript i indicates the ith frequency component, and σ_{γ_i} is given by

$$\frac{\sigma_{\gamma_i}}{\gamma_i} = \frac{1}{2}\frac{\sigma_{\gamma_i^2}}{\gamma_i^2} = \frac{1}{\sqrt{2}\gamma_i}\frac{1 - \gamma_i^2}{\sqrt{n_w - 1}} \tag{7.26}$$

When 50% overlapping windows are used, as is the case for the ATF signal analysis code, the number of windows averaged over is $n_w = 2n_T/N - 1$, where n_T is the total number of data points and N is the number of data points in a single window. The overlapping of the windows decreases the variance in the estimated coherence or spectra because information that is lost at the ends of the window because of the windowing function (e.g., a Hanning window) is now included in an overlapping window; however, since some information is used in both windows,

172

the effective decrease in the variance is not simply that from the apparent increase in the number of windows. Welch[155] derives an estimate of the effective decrease in the uncertainty due to the use of overlapping windows vs no overlap. For the analysis of the reflectometer signals, for which $n_T = 16384$ and $N = 512$ for 512 kHz and 1 MHz sampling rates, or $n_T = 8192$ and $N = 256$ for a 256 kHz sampling rate, the standard deviation calculated for $n_w = 2n_T/N - 1$ windows is expected to underestimate the real standard deviation by a small amount, estimated from Welch's equations[155] to be $\sim 5\%$. The underestimation of σ_{γ_i} is neglected from here on. The variance in the dependent variable $\ln \gamma_i$ is, by applying propagation of errors to Eq. (7.26), found to be

$$\sigma^2_{\ln \gamma_i} = \left(\frac{\sigma_{\gamma_i}}{\gamma_i} \right)^2 \simeq \frac{(1 - \gamma_i^2)^2}{2\gamma_i^2(n_w - 1)} \tag{7.27}$$

Note that, this calculation is repeated for the ℓ independent pairs of signals, each pair having an independent value of the radial separation Δr_ℓ. Thus, the subscript ℓ is implicit in the above equations indicating the ℓth radial separation.

Next, the uncertainty in the independent variable Δr_ℓ must be transformed into an effective uncertainty in the dependent variable. This effective uncertainty is estimated as

$$\sigma^2_{\Delta r_{i\ell}} \simeq \left(\sigma_{\Delta r_\ell} \frac{\ln \gamma_i}{\Delta r_\ell} \right)^2 \tag{7.28}$$

where $\sigma_{\Delta r_\ell}/\Delta r_\ell$ is the uncertainty in Δr_ℓ due to the uncertainty in the measured density profile obtained from Thomson scattering on ATF. Note that for large values of $\sigma_{\Delta r_\ell}/\Delta r_\ell$, this method of accounting for the uncertainty in Δr_ℓ will underestimate the uncertainty. The total uncertainty in the ℓth value of the dependent variable $\ln \gamma_i$ is the root sum square of the contributing uncertainties,

$$\sigma^2_{i\ell} \simeq \sigma^2_{\ln \gamma_i} + \sigma^2_{\Delta r_{i\ell}} \simeq \frac{(1 - \gamma_i^2)^2}{2\gamma_i^2(n_w - 1)} + (\ln \gamma_i)^2 \left(\frac{\sigma_{\Delta r_\ell}}{\Delta r_\ell} \right)^2 \tag{7.29}$$

where the subscript ℓ is implicit in $\sigma_{\ln \gamma_i}$ and γ_i.

173

As given by Bevington,[154] the uncertainty in the fitted slope s_ℓ for a least-squares fit is given in terms of its variance as

$$\sigma_{s_i}^2 \simeq \frac{1}{\Delta_i} \sum_\ell \frac{1}{\sigma_{i\ell}^2} \qquad (7.30)$$

where Δ_i is given by

$$\Delta_i = \sum_\ell \frac{1}{\sigma_{i\ell}^2} \sum_\ell \frac{\Delta r_{i\ell}^2}{\sigma_{i\ell}^2} - \left(\sum_\ell \frac{\Delta r_{i\ell}}{\sigma_{i\ell}^2} \right)^2 \qquad (7.31)$$

and the uncertainty in $L_{c_i} = -1/s_i$ is simply $\sigma_{L_{c_i}}^2/L_{c_i}^2 = \sigma_{s_i}^2/s_i^2$. In estimating $\sigma_{L_{c_i}}^2$, the uncertainty in the radial separation $\sigma_{\Delta r_\ell}/\Delta r_\ell$ is approximated as the uncertainty in the density gradient scale length. Note that for the case of simple homodyne detection, the problem of coherence between two nonlinear signals, $\sin \tilde{\zeta}_1$ and $\sin(\tilde{\zeta}_2 + \varphi)$ where φ is the phase between the two signals, produces an additional uncertainty in γ_i that must be included in the definition of σ_{γ_i}. This is not the case when the true phase fluctuations in the reflected microwave beam are obtained via fringe counting of quadrature phase data.

Total Correlation Length

Another parameter that can be calculated from the radial coherence data is the cross-correlation coefficient function defined by Eq. (5.10) and repeated here,[134]

$$\rho_{xy}(t_k) = \frac{c_{xy}(t_k)}{\sqrt{c_{xx}(0)c_{yy}(0)}} \qquad (7.32)$$

where c_{xy} is the cross-correlation function defined in Eq. (5.8), and $c_{xx}(0)$ and $c_{yy}(0)$ are the auto-correlation functions for zero time lag. This function, $\rho_{xy}(t_k)$, is basically a time domain normalized coherence similar to the frequency domain coherence function γ. For zero time delay ($t_k = 0$), the cross-correlation function represents the total correlation for all frequency components between the two signals $x(t)$ and $y(t)$ and can be used like γ in the previous section "Correlation Length Determination"

starting with Eq. (7.23), to estimate the total correlation length for all frequencies between the two signals. Since the cross-correlation provides only one value of $\rho_{xy}(t_k)$, as opposed to the i frequency components of γ_i, the subscript i can be neglected for this case. Note that, for this zero time delay case, the cross-correlation function is simply given by $c_{xy}(0) = \sum_f C_{xy}(f_j)$, and the auto-correlation functions are given by $c_{xx}(0) = \sum_f C_{xx}(f_j)$ and $c_{yy}(0) = \sum_f C_{yy}(f_j)$.

The uncertainty in the total correlation length is estimated using the same procedure given in the previous section for the uncertainty in the frequency domain correlation length calculated from γ_i, but the uncertainty in $\rho_{xy}(0)$ is used in place of $\sigma_{\gamma i}/\gamma_i$ in Eq. (7.26). By propagation of errors, the uncertainty in $\rho_{xy}(t_k)$ is found to be

$$\frac{\sigma_{\rho_{xy}}^2(t_k)}{\rho_{xy}^2(t_k)} \simeq \frac{\sigma_{c_{xy}}^2(t_k)}{c_{xy}^2(t_k)} + \frac{\sigma_{c_{xx}}^2(0)}{4c_{xx}^2(0)} + \frac{\sigma_{c_{yy}}^2(0)}{4c_{yy}^2(0)} \tag{7.33}$$

where the statistical uncertainty in $c_{xy}(t_k)$ for two white noise–like signals is given by Bendat and Piersol as[134]

$$\frac{\sigma_{c_{xy}}^2(t_k)}{c_{xy}^2(t_k)} \approx \frac{1}{2BTn_w} \left[1 + \rho_{xy}^{-2}(t_k) \right] \tag{7.34}$$

where B is the bandwidth of the signals, T is time length of each data window, and n_w is the total number of windows averaged over, as discussed in the previous section. Bendat and Piersol give the statistical uncertainties in $c_{xx}(0)$ and $c_{yy}(0)$ as

$$\frac{\sigma_{c_{xx}}^2(0)}{c_{xx}^2(0)} = \frac{\sigma_{c_{yy}}^2(0)}{c_{yy}^2(0)} \approx \frac{1}{2BTn_w} \tag{7.35}$$

Now using Eq. (7.34) with $t_k = 0$ and Eq. (7.35) in Eq. (7.33), the uncertainty in $\rho_{xy}(t_k)$ can be obtained and used in Eq. (7.27) in place of $\sigma_{\gamma i}^2/\gamma_i^2$ to calculate the uncertainty in the total correlation length. Note that, $\ln \gamma_i$ in Eqs. (7.28) and (7.29) must be replaced by $\ln \rho_{xy}(0)$.

Radial Wave Number Estimation

The radial wave number k_r of the coherent fluctuations can be estimated from the phase between the coherent parts of the two reflected signals. This technique, often used to determine k_θ from two-tip Langmuir probes and HIBP,[28] simply takes the measured phase delay of the propagating wave between the two measurement points and divides it by the distance between the two points. For the radial coherence data obtained with the ATF reflectometer, k_r is obtained from

$$k_r = \frac{\phi_r}{\Delta r} \tag{7.36}$$

where k_r has units of radians per cm, ϕ_r is the cross-spectral phase and is obtained from the imaginary part of the CPSD, and Δr is the radial separation between the two critical layers. See Chap. V for the definition of the CPSD. The cross-spectral phase ϕ_r is obtained as a function of frequency from the cross-correlation analysis. In practice, the mean radial wave number $\bar{k}_r$ is calculated for the ATF reflectometer data. The quantity $\bar{k}_r$ is obtained by replacing ϕ_r with the weighted mean phase $\bar{\phi}_r$ in Eq. (7.36), where $\bar{\phi}_r$ is given by

$$\bar{\phi}_r = \frac{\sum_i \phi_{ri} A_i}{\sum_i A_i} \quad \text{for} \quad \gamma_i \geq 0.4 \tag{7.37}$$

The subscript i indicates the ith frequency component, A_i is the magnitude of the CPSD, and γ_i is the normalized coherence function. This technique for determining $\bar{k}_r$ only works for fluctuations that are coherent, so the condition that the normalized coherence be at least 0.4 is used. The minimum value of γ_i was set at 0.4 to ensure that the phase information being summed over represented the true coherent fluctuations. As the coherence decreases below this value (for example, see Fig. 9.6 in Chap. IX), the cross-spectral phase shows significant scatter resulting from the dominance of the noncoherent fluctuations in the two signals. It should be noted, therefore, that the measured $\bar{k}_r$ is thus the wave number of the coherent spectrum.

176

Another parameter often used to describe the wave number spectrum is the turbulent broadening factor σ_k, which is basically the width of the measured k spectrum. Here, σ_{kr} is obtained from

$$\sigma_{kr} = \frac{\sigma_{\phi r}}{\Delta r} \tag{7.38}$$

where $\sigma_{\phi r}$ is the width (standard deviation) of the measured phase and is given by

$$\sigma_{\phi r} = \left(\frac{\sum_i (\phi_i - \bar{\phi}_r)^2 A_i}{\sum_i A_i} \right)^{1/2} \qquad \text{for } \gamma \geq 0.4 \tag{7.39}$$

where σ_{kr} has the same units as $\bar{k}_r$. Again, σ_{kr} approximates the width of the coherent spectrum at the specified Δr.

Uncertainty in the Measured Radial Wave Number

The uncertainty in $\bar{k}_r$ is easily shown to be given by

$$\left(\frac{s_{k_r}}{k_r} \right)^2 = \left(\frac{\sigma_{\bar{\phi}r}}{\bar{\phi}_r} \right)^2 + \left(\frac{\sigma_{\Delta r}}{\Delta r} \right)^2 \tag{7.40}$$

where $\sigma_{\bar{\phi}r}/\bar{\phi}_r$ is the uncertainty in the measured mean phase and $\sigma_{\Delta r}/\Delta r$ is the uncertainty in the radial separation, as discussed in the radial correlation length section above. The variance in the weighted mean phase is, as obtained by application of propagation of errors[154] to Eq. (7.37),

$$\sigma_{\bar{\phi}r}^2 = \frac{1}{(\sum_i A_i)^2} \sum_i \left[(A_i \sigma_{\phi_i})^2 + \sigma_{A_i}^2 \left(\phi_i - \bar{\phi}_r \right)^2 \right] \tag{7.41}$$

where σ_{ϕ_i} is the variance in each $\phi(f_i)$ and for statistical errors only is given by Bendat and Piersol[134] for white noise–like signals as

$$\sigma_{\phi_i}^2 = \frac{1 - \gamma_i^2}{2\gamma_i^2 (n_w - 1)} \tag{7.42}$$

where γ_i is the normalized coherence for each $f(i)$ and n_w is the number of data windows averaged over in the Fourier analysis. The variance in the magnitude of

177

the CPSD, σ_{A_i}, for each frequency component f_i is estimated as the sum of the statistical variance given by Bendat and Piersol[134] and the estimated uncertainty due to the variation in the fringe counting, as discussed in the section "Uncertainty in the Measured Phase" on page 154. Thus, the variance in A_i is estimated as

$$\sigma_{A_i}^2 = A_i^2 \left[\frac{1}{n_w} + \left(\frac{\sigma_A}{A} \right)^2 \right] \tag{7.43}$$

where the second term in the brackets represents the estimated uncertainty due to the phase jumps in the fringe data and, for the calculations in this dissertation, $\sigma_A/A = 20\%$ is used.

The uncertainty in the width of the k_r spectrum, σ_{kr}, is given by

$$\left(\frac{s_{\sigma_{kr}}}{\sigma_{kr}} \right)^2 = \left(\frac{s_{\sigma_{\phi r}}}{\sigma_{\phi r}} \right)^2 + \left(\frac{\sigma_{\Delta r}}{\Delta r} \right)^2 \tag{7.44}$$

where $s_{\sigma_{\phi r}}^2$ is the variance in $\sigma_{\phi r}$ and is obtained by the application of propagation of errors to Eq. (7.39). This variance is then estimated to be

$$s_{\sigma_{\phi r}}^2 = \frac{1}{\sigma_{\phi r}^2 (\sum_i A_i)^2} \sum_i \left\{ \left(\phi_i - \bar{\phi}_r \right)^2 A_i^2 \left(\sigma_{\phi_i}^2 + \sigma_{\phi r}^2 \right) + \left[\frac{\sigma_{A_i}}{2} \left((\phi_i - \bar{\phi}_r)^2 - \sigma_{\phi r}^2 \right) \right]^2 \right\} \tag{7.45}$$

where all the parameters have been previously defined. Results of k_r calculations with the uncertainties are shown in Chap. IX.

Poloidal Wave Number Estimation

In Chap. IV, the diamagnetic drift frequency was defined as $\omega_{*e} = k_\theta v_D$, where $k_\theta = m/r$ is the poloidal wave number and v_D is the local electron drift velocity. If it is assumed that the poloidal group velocity of the fluctuations can be approximated by the electron drift velocity and that ω_{*e} can be approximated by the mean frequency $\bar{\omega}$ of the measured fluctuation spectra, then the mean poloidal wave

178

number can be estimated by $\bar{k}_\theta = \bar{\omega}/v_D$. Here, $\bar{\omega}$ is the weighted mean frequency of the measured spectra and is obtained from

$$\bar{\omega} = \frac{\sum_i \omega_i A_i}{\sum_i A_i} \qquad (7.46)$$

where ω_i is the ith frequency component obtained from the Fourier analysis of the time data and A_i is the magnitude of the APSD. The definition for the APSD is given in Chap. V. As with the $\bar{k}_r$ calculations above, the width or turbulent broadening of the k_θ spectrum is estimated by the width or standard deviation in the measured spectrum, i.e., $\sigma_{k\theta} = \sigma_\omega/v_D$, where σ_ω is given by

$$\sigma_\omega = \left(\frac{\sum_i (\omega_i - \bar{\omega})^2 A_i}{\sum_i A_i} \right)^{1/2} \qquad (7.47)$$

Of course, these estimates are based on knowing v_D, which is not measured directly but rather inferred from other data. The diamagnetic drift velocity is given by

$$v_D = \frac{1}{L_p}\frac{T_e}{eB} + \frac{E_r}{B} \qquad (7.48)$$

where the first term is the gradient drift velocity v_∇, with L_p being the pressure gradient length, and the second term is the $\vec{E} \times \vec{B}$ drift velocity ($v_{E\times B}$). Here, E_r is the radial electric field, and it is estimated from the radial potential profiles obtained with the HIBP.[156]

Uncertainty in the Estimated Poloidal Wave Number

The techniques used in the previous section for estimating the uncertainty in the measured radial wave number are used to provide the necessary equations for estimating the uncertainty in the poloidal wave number due to random errors. These estimates neglect all systematic uncertainties, such as contributions to the spectra from Doppler shifting, the functional dependence of the amplitude of the reflected signal on the radial wavelength of the fluctuations, and the assumptions that $\omega_{*e} \simeq \bar{\omega}$

179

and that the fluctuation group velocity equals v_D. First, the uncertainty in $\bar{k}_\theta$ is given by

$$\left(\frac{\sigma_{k_\theta}}{\bar{k}_\theta}\right)^2 = \left(\frac{\sigma_{\bar{\omega}}}{\bar{\omega}}\right)^2 + \left(\frac{\sigma_{v_D}}{v_D}\right)^2 \tag{7.49}$$

where $\sigma_{\bar{\omega}}^2$ is the variance in the measured mean frequency and $\sigma_{v_D}^2$ is the variance in the calculated drift velocity. The uncertainty in the mean frequency $\bar{\omega}$ is obtained by propagation of errors and is given by

$$\sigma_{\bar{\omega}}^2 = \frac{1}{\left(\sum_i A_i\right)^2} \sum_i \left[(A_i \sigma_{\omega_i})^2 + \sigma_{A_i}^2 (\omega_i - \bar{\omega})^2\right] \tag{7.50}$$

where σ_{ω_i} is estimated for statistical uncertainties as f_s/N with f_s being the digitization frequency and N being the number of data points in each data window, as defined in Chap. V.[134] All other parameters in this equation have been previously defined.

The variance in the calculated drift velocity is estimated by

$$\sigma_{v_D}^2 = \left(\frac{\sigma_{L_p}}{L_p}\right)^2 v_\nabla^2 + \left(\frac{\sigma_{T_e}}{T_e}\right)^2 v_\nabla^2 + \left(\frac{\sigma_B}{B}\right)^2 v_D^2 + \left(\frac{\sigma_E}{E}\right)^2 v_{E \times B}^2 \tag{7.51}$$

where the potential covariance between the pressure gradient length and the electron temperature has been neglected. σ_{L_p}/L_p is estimated as the rms value of σ_{L_n}/L_n and σ_{L_T}/L_T where L_n and L_T, the density and temperature gradient lengths, respectively, are calculated from the profiles fitted to the Thomson scattering data, as discussed previously in this chapter, and have been estimated to have a typical uncertainty of 50% each. Thus, σ_{L_p}/L_p is estimated as 71%. T_e is also determined from the profiles fitted to the Thomson scattering data and has an estimated typical uncertainty of 25%. The uncertainty in the magnetic field value B has been previously estimated in this chapter to be 7%. Finally, the electric field is obtained from the derivative of the potential measured by the HIBP and is given an estimated typical uncertainty of 100% due to the preliminary nature of the measurements and the assumption that the profile measured in one shot in the sequence will be the same for all shots in the sequence.[157]

The uncertainty in the width of the k_θ spectrum $s_{\sigma_{k\theta}}$ is estimated similarly to $\sigma_{k\theta}$ above. First, $s_{\sigma_{k\theta}}$ is given by

$$\left(\frac{s_{\sigma_{k\theta}}}{\sigma_{k\theta}}\right)^2 = \left(\frac{s_{\sigma_\omega}}{\sigma_\omega}\right)^2 + \left(\frac{\sigma_{v_D}}{v_D}\right)^2 \tag{7.52}$$

where σ_{v_D} has been previously defined and $s_{\sigma_\omega}^2$ is the variance in the width of the frequency spectra and is estimated as

$$s_{\sigma_\omega}^2 = \frac{1}{\sigma_\omega^2 (\sum_i A_i)^2} \sum_i \left\{ (\omega_i - \bar\omega)^2 A_i^2 \left(\sigma_{\omega_i}^2 + \sigma_{\bar\omega}^2\right) + \left[\frac{\sigma_{A_i}}{2}\left((\omega_i - \bar\omega)^2 - \sigma_\omega^2\right)\right]^2 \right\} \tag{7.53}$$

Again, all parameters have been previously defined, and results of these error estimates are shown with measured data in Chap. IX.

Summary

The use of quadrature phase detection has allowed the measurement of the actual phase delay of the reflected probing beam via fringe counting of the sine/cosine signals obtained from the quadrature detector. This phase detection method suffers from rapid phase jumps, which are too large to be caused by a real movement of the cutoff layer and which artificially increase the spectral amplitude when Fourier transformed into the frequency domain. Since these phase jumps are not believed to represent real fluctuations in the plasma at the cutoff layer, a significant number of the phase jumps are removed numerically. This results in a significant reduction in the noise contribution to the spectral amplitude resulting from the phase jumps; however, the first 10 kHz of data are still strongly biased by the phase jumps and so are neglected in all data analysis techniques. Once the phase fluctuations in the probing beam have been obtained, the density fluctuation amplitude can be determined from the phase fluctuation amplitude and the wavelength of the probing beam. To determine both the location of the probing beam's

181

cutoff and the density fluctuation amplitude, a density profile is required. In ATF, these profiles are obtained from the Thomson scattering system. The equations for estimating the density fluctuation amplitude for both the O-mode and the X-mode are derived in this chapter, as is the uncertainty associated with their estimated values.

The tunable two-frequency operation of the ATF reflectometer allows radial coherence measurements of the density fluctuations to be made, and by tuning the frequencies to different values, the coherence measurements can be made for several different radial separations. This allows the radial correlation lengths of the density fluctuations to be estimated from the change in the normalized coherence between the two cutoff layers as their separation is increased. Radial coherence measurements can also be used to infer the radial wave number k_r of the coherent part of the fluctuation spectrum using the two-point coherence technique often used by Langmuir probes. Finally, the mean poloidal wave number $\bar{k}_\theta$ can be estimated from the mean frequency of the density fluctuations and the diamagnetic drift velocity calculated from the Thomson scattering pressure profiles and the HIBP electric field profiles. The determination of the poloidal wave number allows the measured density fluctuation amplitudes to be compared with theoretical models for the fluctuations, since the models require $\bar{k}_\theta$ in their estimates. In Chap. VIII, reflectometer data from two sequences in ATF are presented and discussed. Then in Chap. IX, the analysis techniques developed in this chapter are applied to the reflectometer data to quantify and describe the observed density fluctuations as completely as possible. Finally, at the end of Chap. IX, the measured fluctuation amplitudes are compared with the values predicted by theory to identify the source of the fluctuations.

182

CHAPTER VIII

EXPERIMENTAL RESULTS

Introduction

Although the ATF reflectometer has operated in a variety of plasma regimes, including 0.95 T ECH, and 0.63, 0.95, and 1.9 T NBI, the 0.95 T ECH discharges have been found to be the most interesting because with X-mode operation internal probing of the plasma is possible and because reproducible steady-state conditions can be obtained. With NBI discharges, the typical densities obtained are sufficiently high to prevent internal probing of the plasma with either the X-mode or the O-mode; that is, cutoff is generally achieved outside the last closed flux surface. Reviews of the results obtained in ATF are given by Murakami et al.,[158,159] Colchin et al.,[160] and Harris et al.[161] Some reflectometer results are also presented in these papers. In this chapter, two ECH sequences with similar magnetic and plasma conditions are described. Additionally, reflectometer time and frequency (Fourier-transformed time series) data are presented and discussed. Then in Chap. IX, the detailed analysis of the reflectometer data and its interpretation are given for the two sequences discussed in this chapter.

Magnetic Configuration and Plasma Conditions

Since ATF is a torsatron, its magnetic configuration and operation are much different from those of a tokamak. The unique features of the ATF magnetic configuration are discussed in Chap. I. The two sequences of discharges in ATF to be discussed here are 90030801 and 90092804 occurring on 8 March 1990 and 28 September 1990, respectively. The shot numbers included in sequence 90030801 are 11265–11289 (excluding 11273 and 11286), while for sequence 90092804, the shots included are 16872–16897 (excluding 16882–16889). These sequences are for the standard magnetic configuration, i.e., $B_0 = 0.94$ T, major radius of 2.05 m, and vacuum magnetic axis at 2.08 m. The magnetic configuration is generally described in terms of the ratio of the trim coils' current-turns to the helical coil's current-turns. ATF has three vertical field VF trim coils, the inner, outer and mid. For these two sequences, the ratio of the inner to the helical was ≈ 0.15, the ratio of the outer to the helical was ≈ 0.075, and the ratio of the mid to the helical was 0. The ATF Thomson scattering system was used to obtain the average density, temperature, and pressure profiles for each sequence.[151,152] Figure 8.1 shows the fitted density profiles for both sequences. These hollow density profiles are obtained from the fitting function

$$n_e(\rho) = (n_b - n_o)\frac{1}{\gamma}\left[(1 - \rho^\alpha) - (1 - \gamma)(1 - \rho^\alpha)^\beta\right] + n_o \qquad (8.1)$$

where n_b is the central density, n_o is the edge density, γ is given by

$$\gamma = 1 - 1/\left[\beta(1 - \rho_m^\alpha)^{\beta-1}\right] \qquad (8.2)$$

and ρ_m is the radial location of the maximum density. The profile is then specified by the parameter set $(n_b, n_o, \alpha, \beta, \rho_m)$ where the limits $\alpha \leq 1.0$ and $\beta \geq 1.1$ are used. Figures 8.2 and 8.3 show the temperature and pressure profiles for the same sequences. Note that the errors bar shown here for the density and temperature
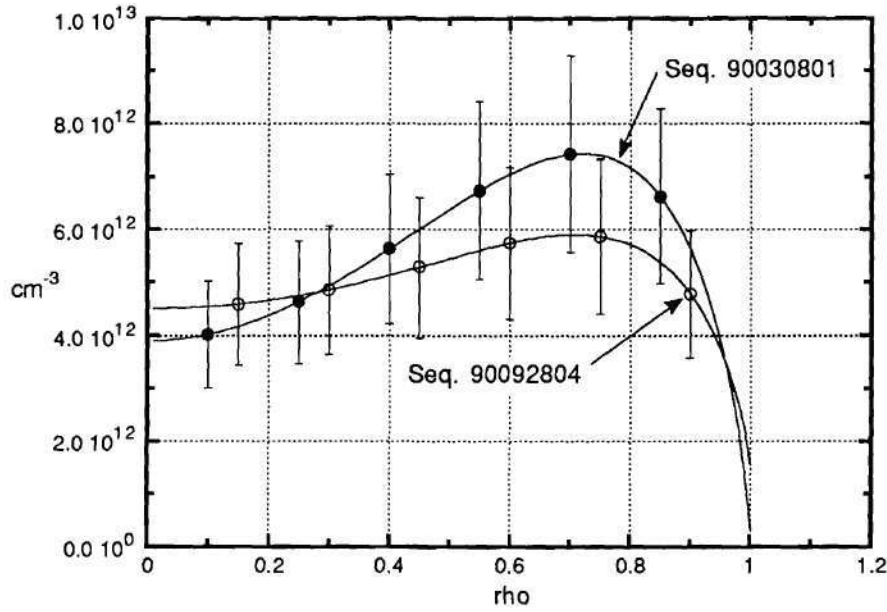
184

Figure 8.1: The density profiles for sequences 90030801 and 90092804. The profile for sequence 90030801 is specified by $n_b = 3.9 \times 10^{12}$ cm^{-3}, $n_e = 0.325 \times 10^{12}$ cm^{-3}, $\alpha = 2$, $\beta = 1.1$ and $\rho_m = 0.72$, while that for sequence 90092804 is specified by $n_b = 4.52 \times 10^{12}$ cm^{-3}, $n_e = 1.56 \times 10^{12}$ cm^{-3}, $\alpha = 2.274$, $\beta = 1.1$ and $\rho_m = 0.701$.

represent an estimate of the typical uncertainty for Thomson scattering measurements in the low-density ECH plasmas in ATF.[153] The error bars on the pressure profile are obtained by a simple propagation of errors.

In Fig. 8.4, the time history of the line integrated density (NEL), the saddle loop stored energy (SL_ENRGY),[162] diamagnetic stored energy (ST_ENRGY),[162] and the ECH power (ECHPOWER)[144] for these discharges are shown. These plots were obtained by averaging over the shots in each sequence. The Thomson scattering profiles for sequence 90030801 were obtained at 500 ms, and the reflectometer data window started at this time. In sequence 90092804, the Thomson scattering profiles were obtained at 300 ms, and again, the reflectometer data window started at this time. Note, in sequence 90030801 the reflectometer digitization frequency was 512 kHz so that a 32 ms data window was obtained, while for sequence 90092804 the
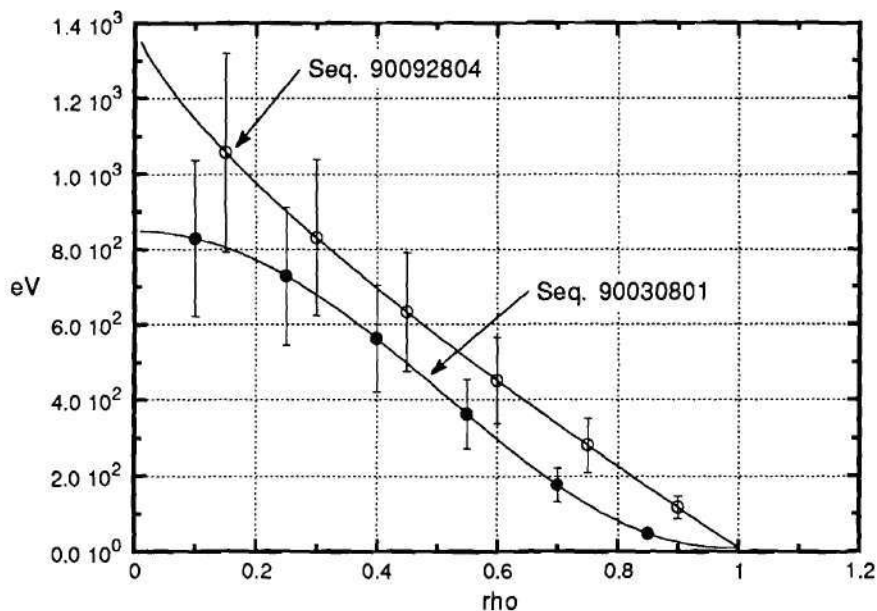
Figure 8.2: The temperature profiles are specified by the standard parabolic profile parameters $(T_0, T_{edge}, \alpha, \beta)$. For 90030801, $T_0 = 850$ eV, $T_{edge} = 10$ eV, $\alpha = 2$ and $\beta = 2.4$, while for 90092804, $T_0 = 1400$ eV, $T_{edge} = 10$ eV, $\alpha = 0.73$ and $\beta = 0.98$. Note, the central peak in the fitted temperature profile for sequence 90092804 is not physical, but rather a result of the curve fitting program.

Figure 8.3: The pressure profiles for sequences 90030801 and 90092804. The pressure profiles are obtained from the product of the density and temperature profiles.

186

digitization frequency was 1 MHz with a 16 ms data window.

In Table 8.1, the parameters describing both the reflectometer operating conditions and the plasma conditions for each shot in sequence 90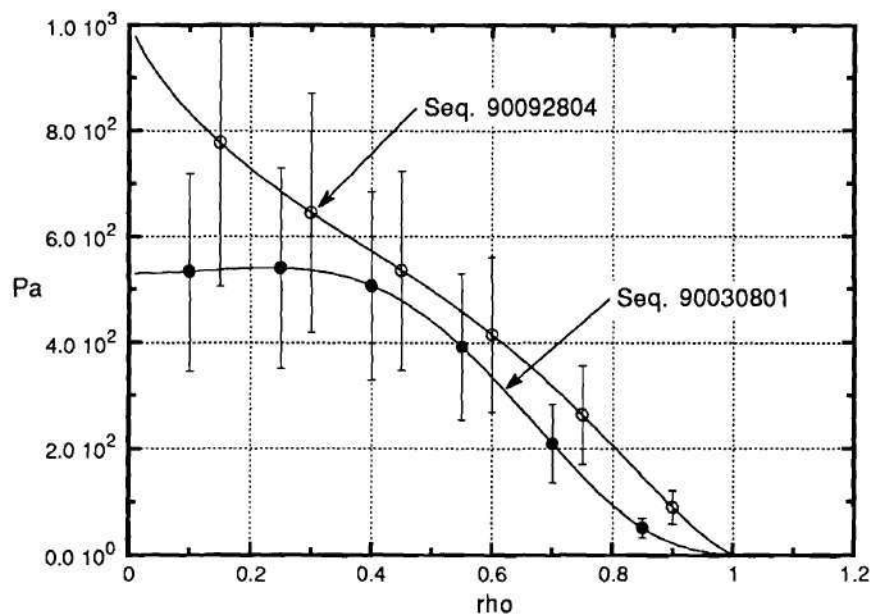030801 are listed. RF1 and RF2 are the two probing frequencies of the reflectometer, and R_1, R_2 and ρ_1, ρ_2 are the major radii and the flux-surface-normalized radii of the cutoff positions, respectively. Also shown are the average (over the reflectometer data window) NEL, SL_ENRGY, ST_ENRGY, and ECHPOWER. The cutoff locations are obtained from the upper X-mode cutoff frequency profile calculated from the sequence average density profile scaled by the line-averaged density $\bar{n}_e$ for each shot; that is, $\bar{n}_e$ for each shot is multiplied by the central peaking factor calculated from the fitted profile to obtain a new central density for each shot. This scales the profile for each shot to account for small shot to shot variations in the density. The central peaking factor for the Thomson scattering density profile is obtained from the ratio of the central density to the calculated $\bar{n}_e$ for the profile. Table 8.2 presents this information for sequence 90092804. Note the much larger spread in NEL in this sequence.

Reflectometer Data

For these two sequences, the reflectometer was operated with one probing beam frequency fixed near the top of the edge density gradient, while the other probing beam was scanned down the gradient by changing the frequency between discharges. This method of operation allows radial coherence measurements to be made for several different radial separations with one end of the measurement range approximately fixed in location. This method also provides a radial profile of the density fluctuations since one probing beam is scanned across the density gradient.
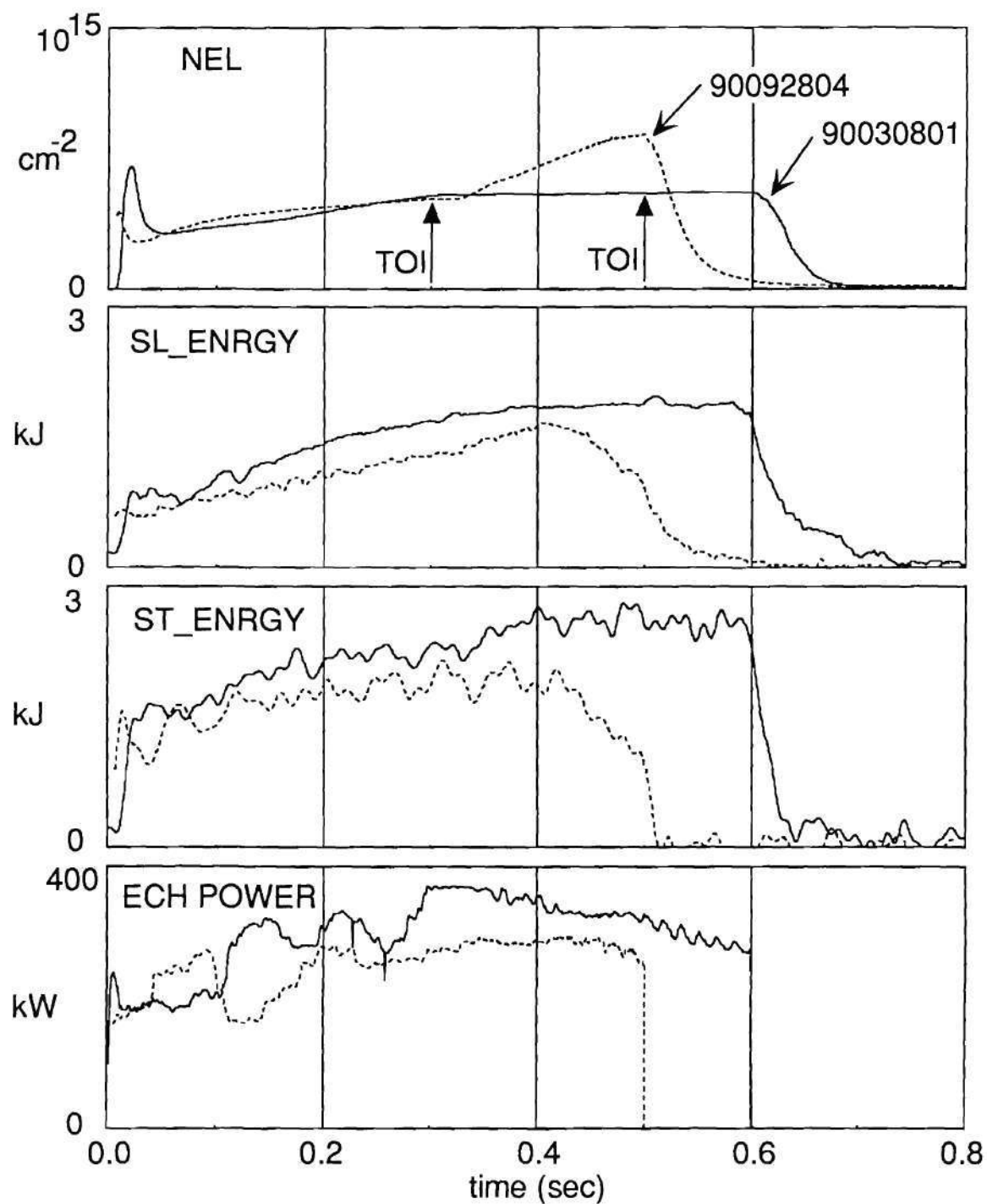
187

Figure 8.4: The time history of sequences 90030801 and 90092804 in terms of their line-integrated densities, stored energies, and ECH power. The reflectometer data windows are 500–532 ms and 300–316 ms, respectively. TOI is the time at which the Thomson scattering data is obtained.

188

Table 8.1. Reflectometer and plasma paramaters for sequence 90030801

Shot #	RF1	R1	ρ1	RF2	R2	ρ2	NEL	ST_ENRGY	SL_ENRGY	ECH Power
11265	37.02	231.03	0.781	36.32	232.32	0.818	3.63E+14	2.02	1.90	303
11266	36.64	231.45	0.794	36.34	232.00	0.809	3.58E+14	2.65	1.93	289
11267	36.64	231.52	0.796	36.34	232.06	0.811	3.57E+14	2.54	1.95	312
11268	36.42	232.14	0.813	36.34	232.27	0.817	3.63E+14	0.00	0.00	312
11269	36.42	231.91	0.807	36.34	232.05	0.811	3.58E+14	0.00	0.00	299
11270	36.42	231.70	0.801	35.75	232.78	0.831	3.55E+14	2.86	1.81	307
11271	36.42	232.13	0.813	35.75	233.11	0.840	3.63E+14	2.68	2.09	307
11272	36.42	232.13	0.813	35.75	233.10	0.840	3.63E+14	2.51	2.02	306
11274	36.42	232.20	0.815	35.07	233.94	0.862	3.64E+14	2.72	1.93	309
11275	36.42	232.14	0.813	35.07	233.90	0.861	3.63E+14	2.33	1.89	316
11276	36.42	232.17	0.814	34.38	234.60	0.880	3.63E+14	2.75	1.84	315
11277	36.42	232.04	0.810	34.38	234.53	0.878	3.61E+14	2.26	1.85	304
11278	36.42	232.20	0.815	34.38	234.62	0.880	3.64E+14	2.23	1.82	316
11279	36.42	232.21	0.815	33.59	235.28	0.897	3.64E+14	2.75	1.91	325
11280	36.42	232.27	0.817	33.59	235.31	0.898	3.66E+14	2.50	1.87	313
11281	36.42	232.22	0.816	32.41	236.11	0.917	3.64E+14	2.19	1.89	305
11282	36.42	232.27	0.817	32.41	236.13	0.918	3.66E+14	2.72	1.82	331
11283	36.42	232.30	0.818	31.41	236.72	0.932	3.65E+14	2.83	1.95	327
11284	36.42	232.40	0.821	31.41	236.75	0.933	3.68E+14	2.54	1.92	316
11285	36.42	232.33	0.819	31.41	236.73	0.932	3.66E+14	2.57	1.87	323
11287	36.42	232.36	0.819	31.41	236.74	0.932	3.67E+14	2.69	1.92	334
11288	36.42	232.73	0.830	31.41	236.84	0.935	3.74E+14	2.50	1.90	312
11289	36.42	232.50	0.823	31.41	236.78	0.933	3.70E+14	2.83	1.88	319

Table 8.2. Reflectometer and plasma paramaters for sequence 90092804

Shot #	RF1	R1	ρ1	RF2	R2	ρ2	NEL	ST_ENRGY	SL_ENRGY	ECH Power
16872	32.8	235.35	0.867	32.22	236.07	0.886	3.38E+14	2.04	1.28	310
16873	32.8	235.37	0.867	32.22	236.09	0.887	3.36E+14	2.04	1.37	297
16874	32.8	236.70	0.903	32.22	237.21	0.915	3.78E+14	2.30	1.37	296
16875	32.8	234.36	0.839	32.22	235.27	0.865	3.17E+14	2.02	1.29	289
16876	32.8	234.51	0.843	32.67	234.72	0.849	3.19E+14	1.94	1.23	289
16877	32.8	236.25	0.891	32.67	236.38	0.894	3.66E+14	1.80	1.40	254
16878	32.8	236.02	0.885	32.67	236.17	0.889	3.56E+14	1.90	1.37	308
16879	32.8	234.94	0.856	32.67	235.13	0.861	3.30E+14	1.98	1.21	299
16880	32.8	236.06	0.886	32.67	236.21	0.890	3.59E+14	2.02	1.35	292
16881	32.8	238.12	0.938	32.67	238.20	0.940	3.93E+14	1.81	1.52	254
16890	32.8	234.96	0.856	29.24	238.52	0.947	3.29E+14	1.77	1.28	264
16891	32.8	235.33	0.866	29.24	238.64	0.950	3.38E+14	1.77	1.31	259
16892	32.8	234.82	0.852	30.6	237.40	0.920	3.26E+14	1.73	1.19	253
16893	32.8	234.65	0.848	30.6	237.32	0.918	3.20E+14	2.04	1.31	248
16894	32.8	236.12	0.887	30.6	238.05	0.936	3.61E+14	2.13	1.35	252
16895	32.8	235.45	0.870	31.47	236.94	0.909	3.41E+14	2.04	1.32	239
16896	32.8	236.12	0.887	31.47	237.38	0.920	3.61E+14	2.03	1.38	257
16897	32.8	236.50	0.897	31.47	237.64	0.926	3.75E+14	2.25	1.37	254

Unfortunately, the reflectometer cannot make measurements inside or over the top of these hollow-density profile plasmas. Tables 8.1 and 8.2 show that the cutoff locations ρ_c for these two sequences are limited to the edge gradient region of the density profile, $0.75 < \rho_c < 1.0$. This exemplifies the primary limitation of the reflectometer for density fluctuation measurements in these hollow-density discharges. The reflectometer can only obtain information in regions where a sufficient density gradient exists to provide a radially localized cutoff position.

The reflectometer time series data provide little or no useful information until they are processed. Figure 7.1 shows an example of a short section of time series data. The raw data are processed through a fringe-counting code, as discussed in Chap. VII, to obtain the actual phase shift in the reflected signal resulting from the movement of the cutoff layer. These time series phase data still provide little or no insight into the density fluctuations in the plasma until they are Fourier transformed to the frequency domain. In Fig. 8.5 and 8.6, the amplitude spectra from three radially separated positions in the plasma are shown for sequences 90030801 and 90092804, respectively. In both sequences, a fairly large amplitude peak is observed around 50 kHz with a width of $\sim$ 20 kHz. It is shown in Chap. IX that this bump or feature has a long radial correlation length and is globally coherent across this edge gradient region. Note that in both figures the spectra broaden as the cutoff position is moved outward in the plasma. The spatial separations between the spectra shown in Fig. 8.5 and in Fig. 8.6 are probably larger than that suggested by the cutoff positions indicated on the figures. The typical uncertainties in the cutoff locations can be estimated from the error bars shown in Fig. 9.2. From Fig. 9.2, the uncertainty in the location of the inner cutoff positions (those near the peak in the edge gradient) is large, while the uncertainty in the outer cutoff positions is small. For sequence 90030801, the radial error bars on the inner data points extend to $\rho = 0$. This is an artifact of the technique used to estimate these uncertainties,
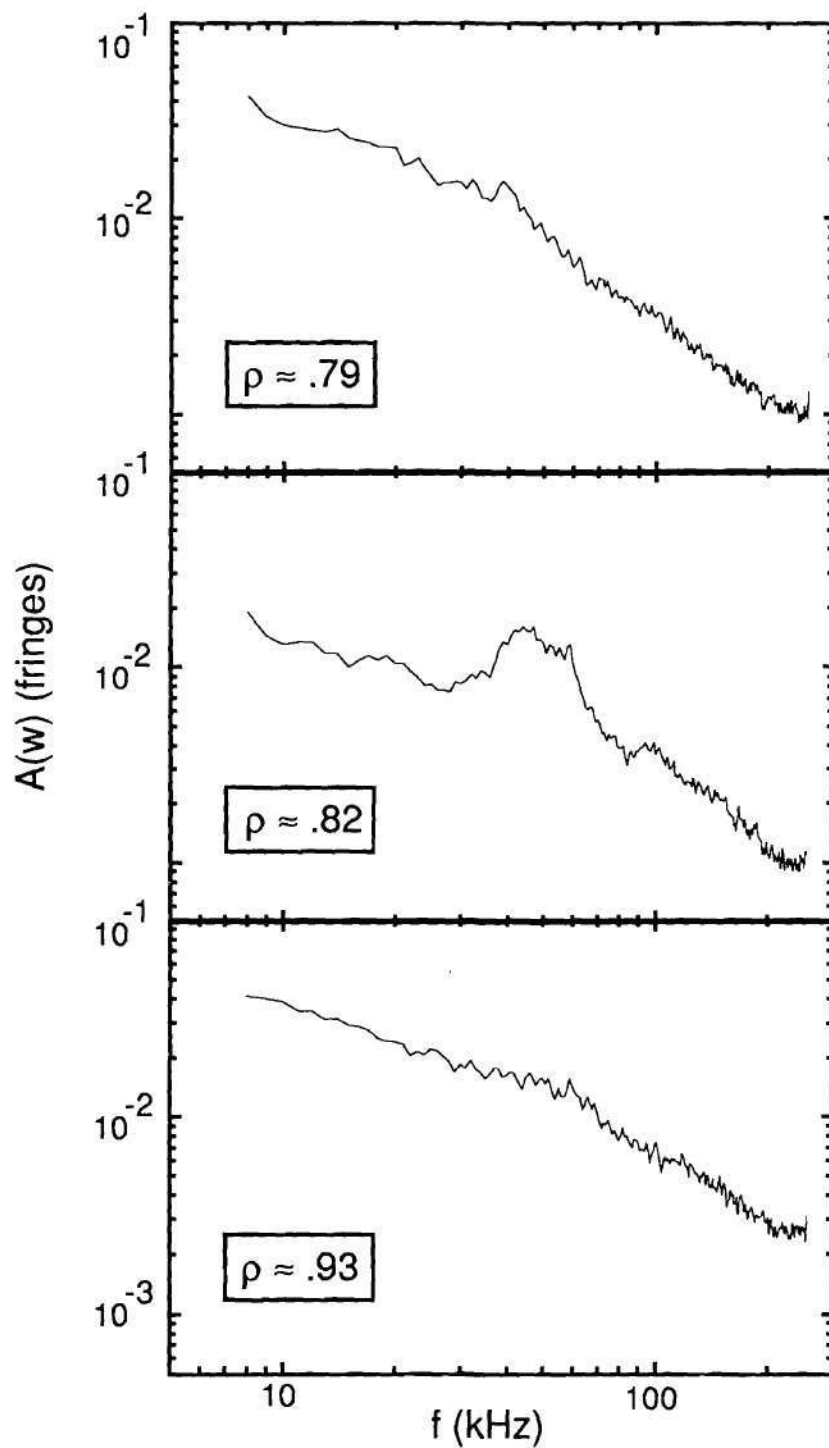
Figure 8.5: Three density fluctuation spectra from three radially separated cutoff layers for sequence 90030801. Note the large peak in the center spectrum and the lack of such a peak in the other spectra. This is an indication of a localized measurement.
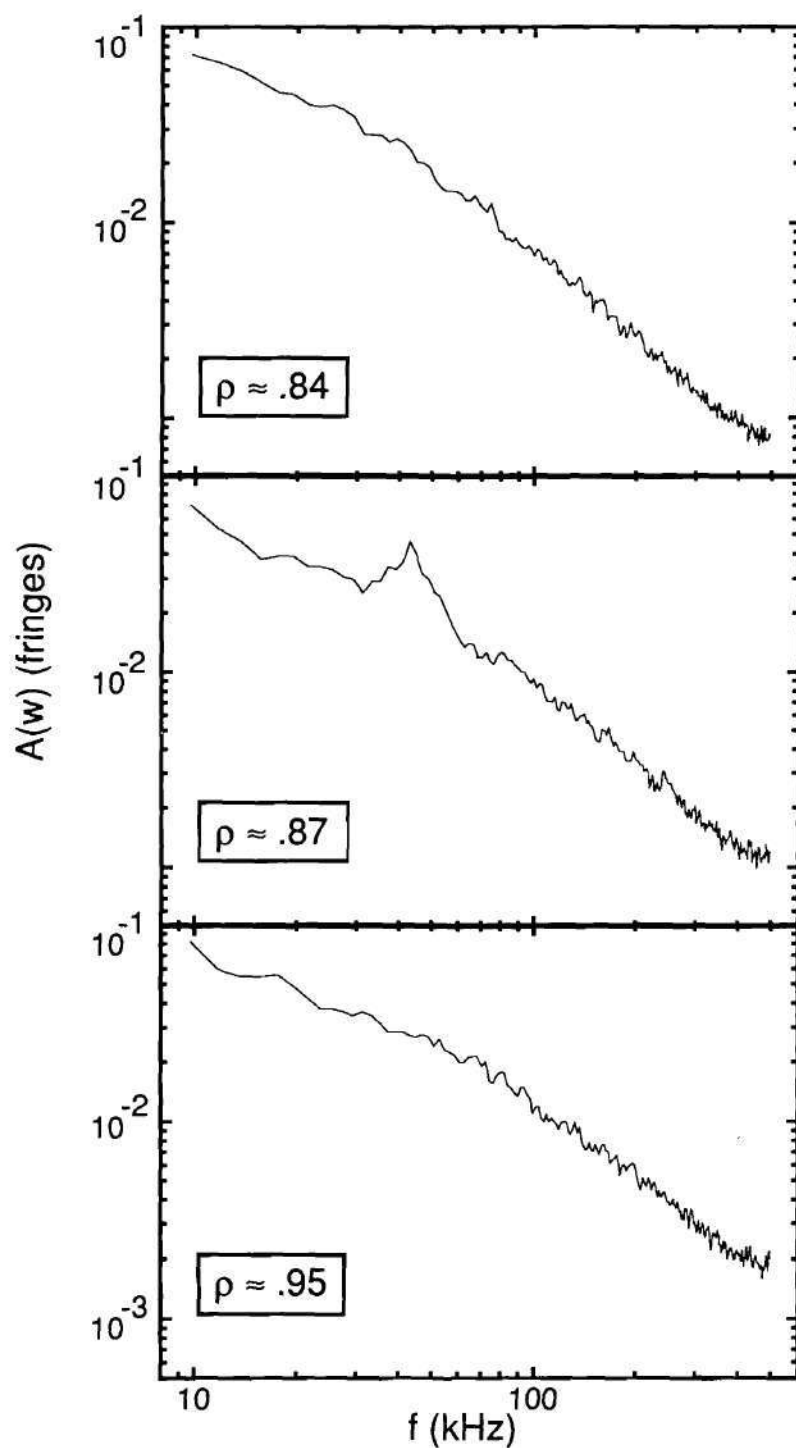
192

Figure 8.6: Three density fluctuation spectra from three radially separated cutoff layers for sequence 90092804. Note the similarities with Fig. 8.5; i.e., the large peak in the center spectrum and the broadening of the spectra with increasing ρ.
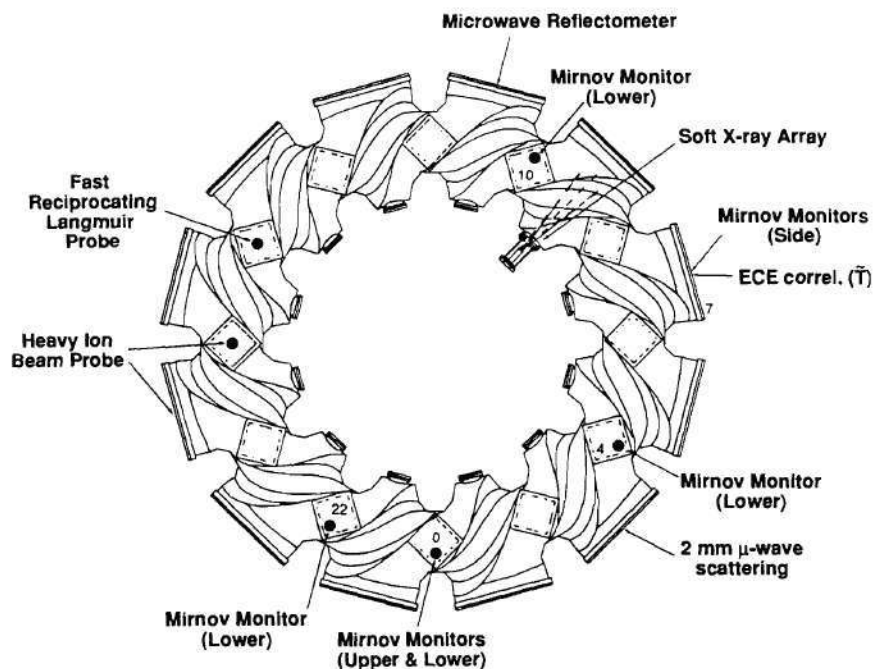
Figure 8.7: Locations of the ATF fluctuation diagnostics. The 2 mm microwave scattering diagnostic is planned for installation in the summer of 1991.[170]

as discussed in Chap. IX. Since cutoff was obtained and the density profiles were hollow, the cutoff had to occur somewhere near the peak in the edge density gradient. Therefore, the uncertainty in the given cutoff positions is estimated to be $\sim 25\%$. Thus the very small spatial separation suggested by the cutoff positions indicated on the figures is most likely much larger.

Comparison With Other Fluctuation Data

In sequence 90092804, the reflectometer was operated simultaneously with the FRLP[145,163,164,165] and the HIBP[166,167,168] in an attempt to verify of the the reflectometer measurements. In Fig. 8.7, a schematic of the ATF vacuum vessel showing the location of the fluctuation diagnostics is shown.[169] The Mirnov monitors are used
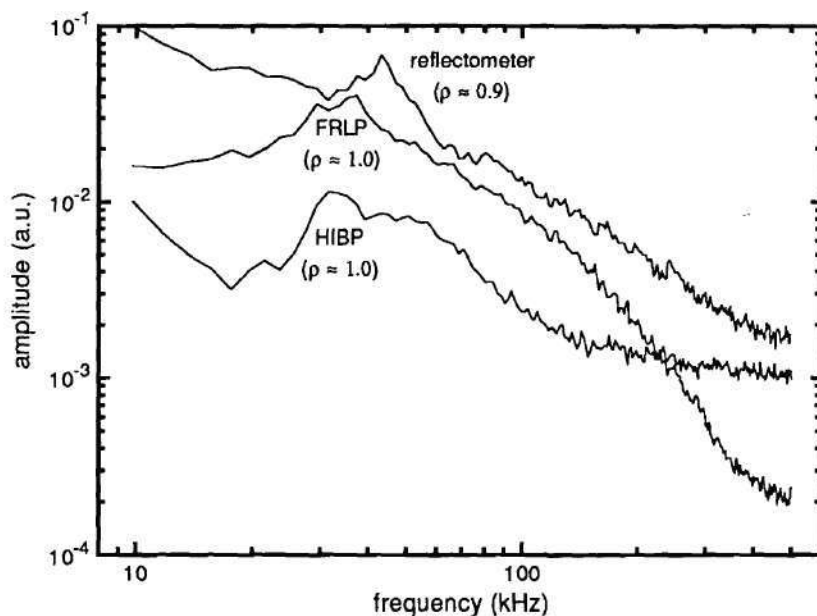
194

Figure 8.8: These spectra ($\propto \bar{n}_e/n_e$) were measured by the reflectometer, FRLP, and HIBP during sequence 90092804. Note the similar peaks in these spectra at 30–50 kHz.

to measure magnetic fluctuations in the plasma, which are generally produced by MHD modes.[133,171] Unfortunately, these monitors obtain no signal above their noise level in the low-density ECH plasmas being studied here. Their primary use is in the high-density NBI-heated plasmas and some higher density ECH plasmas when pellet injection is used. For more information on FRLP measurements in ATF, see the work by Hidalgo et al.,[164] Uckan et al.,[145,163,165] and Harris et al.[98] This sequence was the initial operational run of the HIBP, and so the accuracy of the measurements, in both their radial position and amplitude, is not quantified. Information on the ATF HIBP may be obtained from Aceto et al.[156,166,168] and Zielinski et al.[167]

Figure 8.8 shows the amplitude spectra for the density fluctuations measured by the FRLP and HIBP at $\rho \simeq 1.0$ and the reflectometer at $\rho \simeq 0.9$ during sequence 90092804. The spectra shown here are proportional to the density fluctuations but

have arbitrary units so the relative amplitude differences are not meaningful. The spectra obtained by all three diagnostics clearly show a similar peak between 30 and 50 kHz. The HIBP measurement is near its minimum signal level, as indicated by the bottoming out of the spectra for frequencies above ~ 150 kHz. Two differences between the reflectometer measurements and the HIBP and FRLP measurements can be seen. First, the ~ 10 kHz offset between the reflectometer-measured peak and the peak measured by the HIBP and the FRLP may be an indication of Doppler shifting between the spectra observed by all three diagnostics. Doppler shifting of the reflectometer probing beam was discussed in the section "Fringe Counting" in Chap. VII.

The second difference between the reflectometer spectra and the spectra from the HIBP and the FRLP is the difference in the measured radial location of the peak. The reflectometer measurements show the peak to be at $\rho \simeq 0.9$, while the HIBP and FRLP observe a peak in their spectra at $\rho \simeq 1.0$. This contradiction may be due to the fact that the phase fluctuations in the reflectometer signal are primarily caused by fluctuations in front of the cutoff layer. As stated in the section "Discussion on Choosing λ" in Chap. VII, the phase information is estimated to be coming from 1 to 3 vacuum wavelengths in front of the cutoff layer. This corresponds to a difference of $\Delta \rho \sim 0.04$–0.1 between the location of the cutoff layer and the location of the fluctuations. If this offset is corrected for in the quoted location of the measured reflectometer spectra, then the spectra from the three diagnostics show better agreement. This potential systematic offset in the location of the measured fluctuations is neglected when quoting the location of the reflectometer measurements, which are simply quoted to be the cutoff location. Other possible sources of this contradiction are the variation in the plasma conditions from shot to shot since the spectra shown are not all from the same shot, very large errors in the Thomson scattering profiles used to calculate the cutoff location, or variations

in the spectra due to the different toroidal and poloidal locations of each diagnostic. A comparison of the reflectometer-measured rms fluctuation amplitude $\tilde{n}_e/n_e$ with the FRLP and HIBP measurements is shown in Fig. 9.5 in Chap. IX.

Since the reflectometer and the FRLP operate with the same DAQ system,[133] cross-correlation analysis between the two signals is possible and in fact easy to perform, while the HIBP uses a different DAQ system with a separate clock and start/stop (trigger) signal, making cross-correlation analysis difficult. The purpose of looking for coherence via the cross-correlation of the signals from these different diagnostics is to further verify the measurements being made and to look at the localization or globality of the instability. Figure 8.9 shows the cross-correlation of the reflectometer phase signal reflected at $\rho \simeq 0.92$ and the FRLP current signal obtained at $\rho = 1.0$. There is clearly a strong coherence between 40 and 70 kHz, corresponding to the peak seen in the previously shown spectra. It is not clear at this time whether the cross-phase between these two signals has a meaning or is simply a result of systematic effects in the diagnostics. The FRLP floating potential signals, which are a measurement of the potential fluctuations in the plasma, show a similar peak in their spectra at 50 kHz, and similar cross-correlation analysis shows coherency at a lower level between the reflectometer-measured density fluctuations and these potential fluctuations. Clearly, any coherence between the reflectometer signals and the FRLP signals indicate a globally coherent instability, since the two diagnostics are located 90° poloidally and 75° toroidally apart. This corresponds to 2.5 field periods in ATF. Relative to the field lines, the two measurements are from radially separated flux surfaces, and for the last closed flux surface ($t = 1.0$), the two measurements are for field lines with a $\sim 30°$ poloidal separation. In Chap. IX, it is shown that this feature has strong radial coherence and a long radial correlation length. The significance of these measurements and observations is discussed further in Chap. IX.
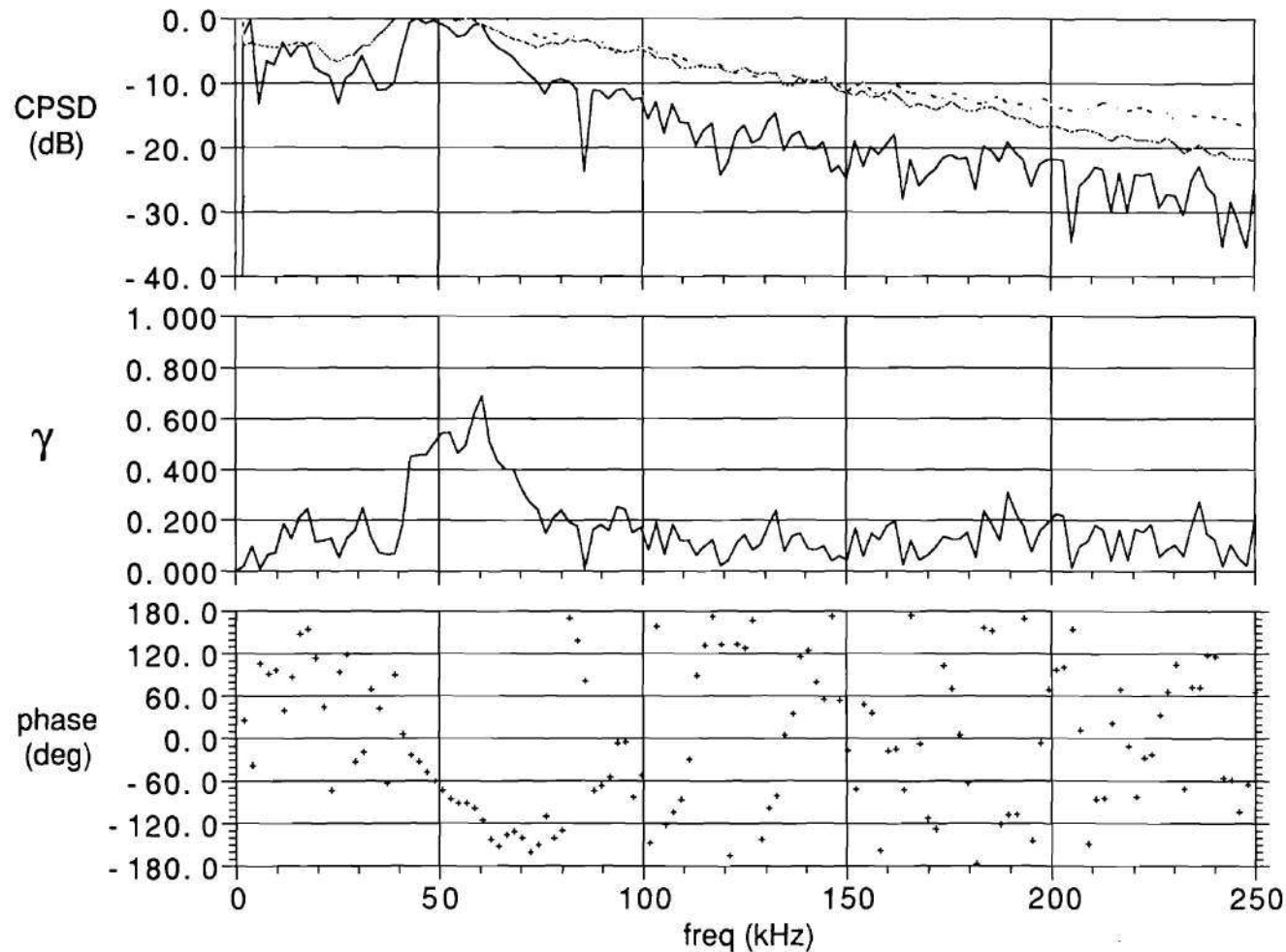
Figure 8.9: Cross-correlation of the reflectometer phase signal and the FRLP current signal to obtain the coherence between the two signals. Note the strong coherence for the ~ 50 kHz peak. The two dashed lines in the upper graph are the APSDs for the two signals.

The HIBP measurement is obtained in a region between the beam entrance position at the upper port shown in Fig. 8.7 and the exit position in the large outer port.[156,166] This position is approximately 105° toroidally and 60° poloidally away from the reflectometer, and approximately 45° toroidally and 30° poloidally away from the FRLP. Coherence measurements between the HIBP and the reflectometer and FRLP were possible with careful alignment in time of the signals to account for the slightly different triggering times. These measurements (not shown here) found coherence with both the reflectometer signals and the FRLP signals.[157,172] This observation provides additional support to the global nature of the instability.

Discussion

The two 0.94 T ECH sequences, 90030801 and 90092804, provide similar operating conditions for the analysis and comparison of reflectometer data. In sequence 90030801, a reflectometer radial coherence scan was performed by fixing one frequency so that its cutoff position was near the top of the edge density gradient and varying the second frequency so that its cutoff layer was scanned radially outward down the density gradient. The reproducible plasma conditions in this sequence provide an excellent set of data for radial coherence and correlation length analysis, as well as density fluctuation amplitude calculations. Sequence 90092804 was performed in conjunction with the FRLP and the initial operation of the HIBP. In this sequence, the plasma conditions were not as reproducible or constant. This resulted in poor radial coherence measurements for the correlation length calculations. However, this sequence is important because the FRLP and HIBP obtained density fluctuation amplitude measurements in the same discharges. This allowed the comparison of the fluctuation spectra observed by all three diagnostics.

CHAPTER IX

ANALYSIS OF EXPERIMENTAL RESULTS

Introduction

In Chap. VIII, the experimental and plasma conditions for two sequences of discharges in the ATF torsatron were presented and discussed. The reflectometer data for these two sequences were discussed, and some frequency spectra were shown. In this chapter, a detailed analysis of the reflectometer data is performed using the analysis techniques described in Chap. VII. First, the density fluctuation amplitudes are calculated from the reflectometer data and compared with similar data obtained from the FRLP and the HIBP. Next, coherence analysis techniques are used to calculate the radial correlation lengths and the mean radial wave numbers $\bar{k}_r$ of the density fluctuations. Finally, estimates of the mean poloidal wave number $\bar{k}_\theta$ are made on the basis of the mean frequency of the spectra. With $\bar{k}_\theta$, the measured density fluctuation amplitudes can be compared with theoretical models for the turbulence in the edge gradient region of the plasma.

Density Fluctuation Amplitude

Using the analysis technique discussed in the section "Estimating $\tilde{n}_e/n_e$ From the Measured Phase Fluctuations" in Chap. VII, the rms density fluctuation
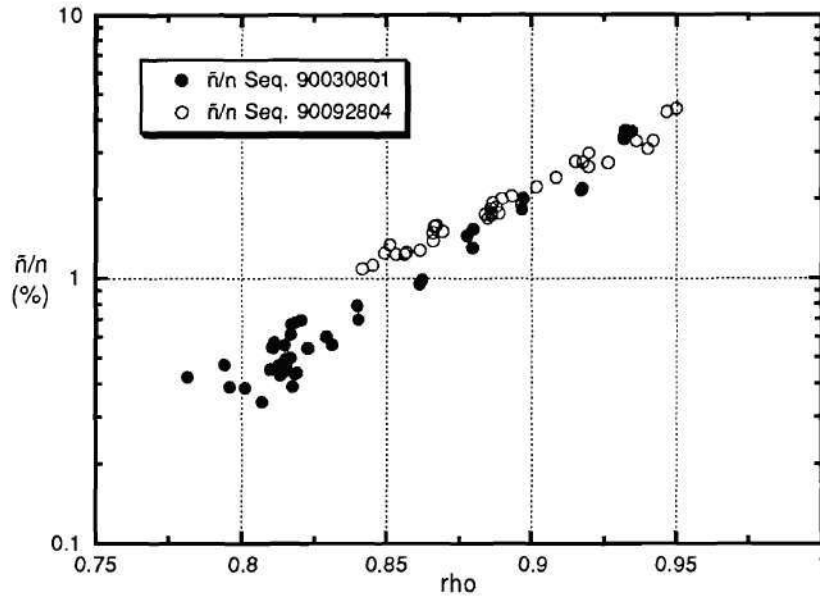
Figure 9.1: The density fluctuation amplitude $\tilde{n}_e/n_e$ as a function of radius for sequences 90030801 and 90092804. Refer to Fig. 9.2 for the uncertainties in this data. Error bars are left out for clarity.

amplitudes for sequences 90030801 and 90092804 are calculated and plotted as a function of radius in Fig. 9.1. Note that for both sequences, the data points are between $\rho \simeq 0.8$ and 0.95, which is the region of the edge electron density gradient, and the value of $\tilde{n}_e/n_e$ varies by approximately one order of magnitude in this region. Using Eqs. (7.21) and (7.5), the uncertainty in the amplitude and radial location of each data point shown in Fig. 9.1 is calculated and plotted in Fig. 9.2. The values of the individual uncertainties used in calculating the overall uncertainties are discussed in Chap. VII. As discussed in Chap. VII, the uncertainty in the radial cutoff location is estimated from the uncertainty in the cutoff frequency profile. Two perturbed cutoff frequency profiles are calculated by adding and subtracting one standard deviation of the cutoff frequency profile to the original cutoff frequency profile. The uncertainty in the radial position of the probing beam cutoff is then assumed to be
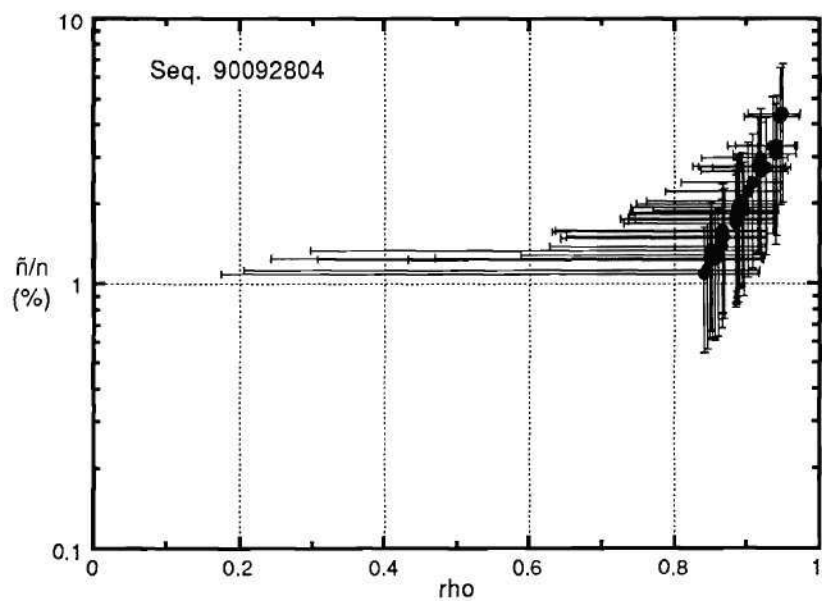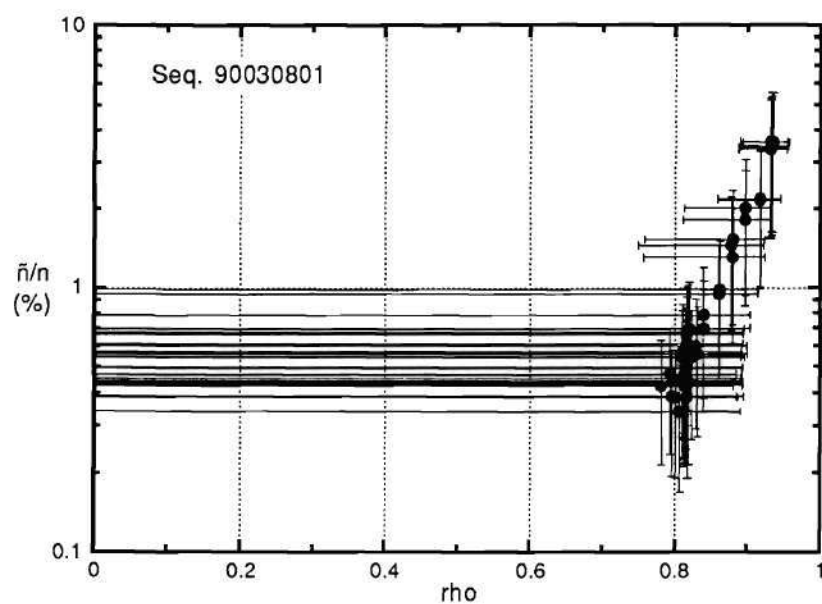
Figure 9.2: $\tilde{n}_e/n_e$ with the estimated uncertainty in each data point for sequences 90030801 (top) and 90092804 (bottom). Note: the very large horizontal error bars associated with the inner points result from the rolling over or peaking of the density gradient in the edge region.

203

the change in the cutoff location calculated for these two perturbed profiles. When calculating the cutoff position for the case of the original cutoff frequency profile minus one standard deviation, it is often found that the probing beam is no longer cut off; however, the raw data show clearly that cutoff was obtained. The horizontal error bars going to $\rho = 0$ in Fig. 9.2 represent such a case. Since the probing beam was cut off, these large error bars are not accurate. For the hollow density profiles shown in Fig. 8.1, the probing beam can only be cut off in the edge gradient, and so these large radial uncertainties, indicated by the large horizontal error bars going to $\rho = 0$, are an artifact of the calculation technique and are ignored from here on.

In determining $\tilde{n}_e/n_e$, the rms phase delay of the reflectometer probing beam is converted to a radial width and then divided by L_n to obtain the fluctuation amplitude. In Fig. 9.3, the radial width δr_c and $\tilde{n}_e/n_e$ of the fluctuations is plotted vs the radius, while in Fig. 9.4 δr_c and $\tilde{n}_e/n_e$ are plotted vs the density gradient length. Note how $\tilde{n}_e/n_e$ is very dependent on L_n for its radial trend, while δr_c does not clearly show this same dependence. From Fig. 8.1, it is apparent that the density gradient lengths for both sequences vary considerably over the edge gradient region, and so on first glance the validity of the measured values of $\tilde{n}_e/n_e$ and its radial trend was highly suspect. However, simultaneous operation of the reflectometer with the FRLP and the HIBP was performed during sequence 90092804 in an attempt to obtain verification of the measured fluctuation amplitudes. The results of these measurements are shown in Fig. 9.5. The reflectometer and FRLP measurements do not overlap, but they do show good agreement. The HIBP measurements are the first obtained by the ATF beam probe and so are considered preliminary. Fair agreement is obtained in the region where the measurements overlap. Note that the HIBP measurements for values near $\tilde{n}_e/n_e \sim 1\%$ are an upper-bound estimate (limited by noise).

Thus, the evidence for the validity of the reflectometer-measured values of
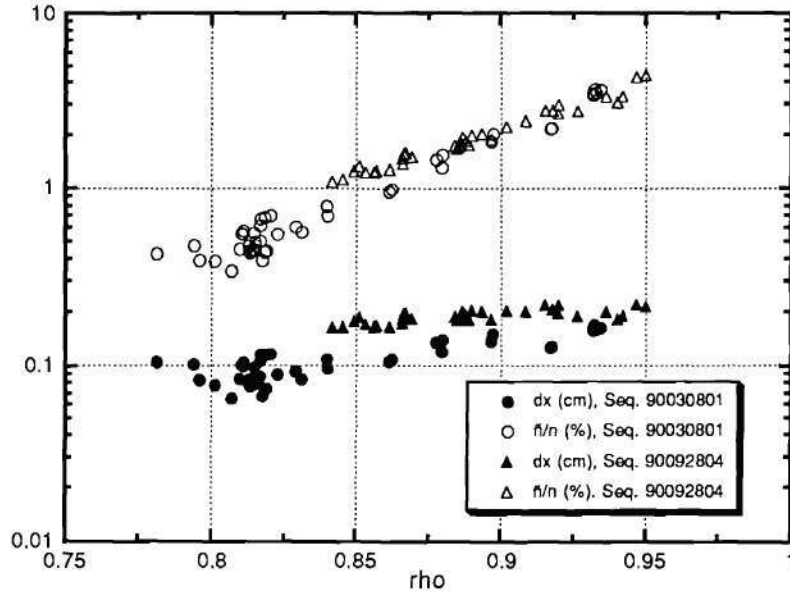
204

Figure 9.3: The rms radial width δr_c of the density fluctuations and their corresponding $\tilde{n}_e/n_e$ values, showing their variation with radius. As discussed in Chap. VII, the estimated uncertainty in dx is 28%. See Fig. 9.2 for error bars for $\tilde{n}_e/n_e$.
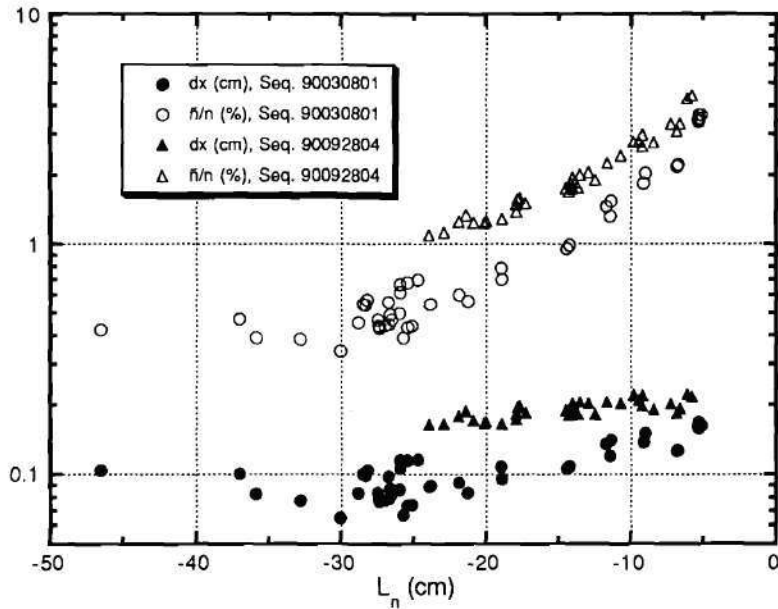

Figure 9.4: The rms radial width δr_c and $\tilde{n}_e/n_e \sim \delta r_c/L_n$ vs L_n showing the strong dependence of $\tilde{n}_e/n_e$ on L_n. Note that δr_c also shows some dependence on L_n. See the caption of Fig. 9.2 for information on the uncertainties.
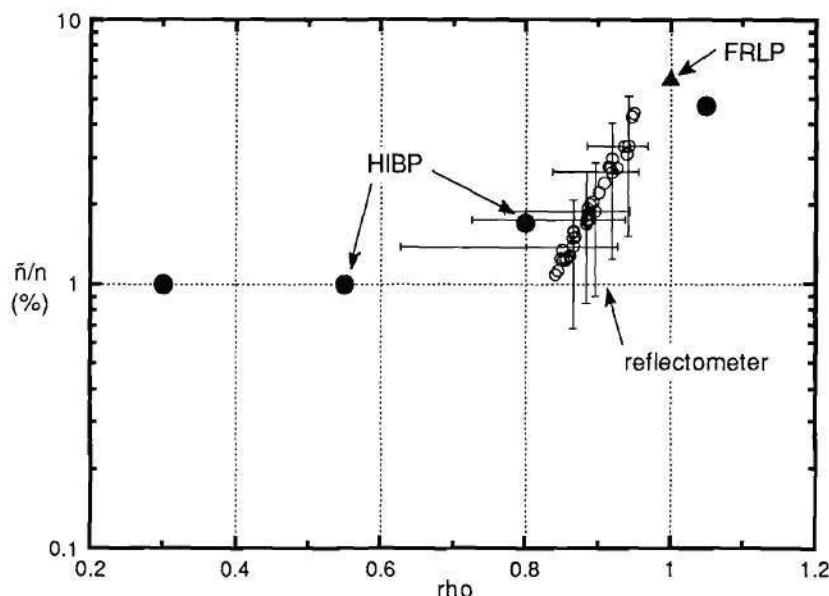
Figure 9.5: Comparison of $\tilde{n}_e/n_e$ from the reflectometer, the FRLP, and the HIBP, operated simultaneously.

$\tilde{n}_e/n_e$ is strong, but it is not conclusive. The strong dependence of $\tilde{n}_e/n_e$ on L_n is still disconcerting; however, the theoretical predictions for $\tilde{n}_e/n_e$ discussed in Chap. IV were based on the calculation of a radial width or mixing length divided by the density gradient length. This will cause the theoretical predictions to show a similar strong dependence on L_n. Later in this chapter, it will be shown that there is good agreement between the measured values of $\tilde{n}_e/n_e$ and the theoretically estimated values of $\tilde{n}_e/n_e$ for the MHD resistive interchange instability.

Radial Coherence Measurements

The ATF reflectometer simultaneously probes the plasma with two beams at different frequencies launched and received in the same antenna/microwave system.

This two-frequency technique allows the radial coherence and correlation length of the density fluctuations to be measured. Refer to Chap. V and VII for a discussion of cross-correlation or coherence analysis of fluctuation signals and its application to two-frequency reflectometry. For example, in Fig. 9.6 the cross-correlation between two fringe-counted reflectometer signals is shown. Note the large peak in the spectrum at ~ 50 kHz. This peak is radially coherent over most of the edge density gradient and has a nearly constant phase of $0°$. The correlation length and the interpretation of the phase are discussed in more detail in the following sections. A similar peak is observed in the spectra from sequence 90092804. The density fluctuation spectra are often dominated by a peak near 50 kHz, but analysis of the rms $\tilde{n}_e/n_e$ for the whole spectrum or just for the frequencies encompassing the peak shows a similar trend in radius.

Radial Correlation Length

Using the analysis techniques discussed in the section titled "Radial Coherence/Correlation Length Measurements" in Chap. VII, the radial correlation lengths and their uncertainties for sequences 90030801 and 90092804 are calculated and plotted in Fig. 9.7. The error bars represent one standard deviation and are calculated using the equations derived in Chap. VII. Note the extremely long (~ 4–5 cm) correlation length for the peak near 50 kHz for sequence 90030801. The estimated width of the reflecting layer in this region of the plasma is between 0.5 and 1.5 cm. The background correlation length for the remainder of the spectrum is ~ 2 cm, and the apparent increase above 100 kHz cannot be taken with confidence because of the corresponding increase in the uncertainty. In the plot for sequence 90092804, the apparent basic coherence is again ~ 2 cm, but the long correlation peak is not as clear. The peak near 60 kHz is not as pronounced or as wide as the peak in the upper plot, but a large peak is present in many of the individual spectra from many

207
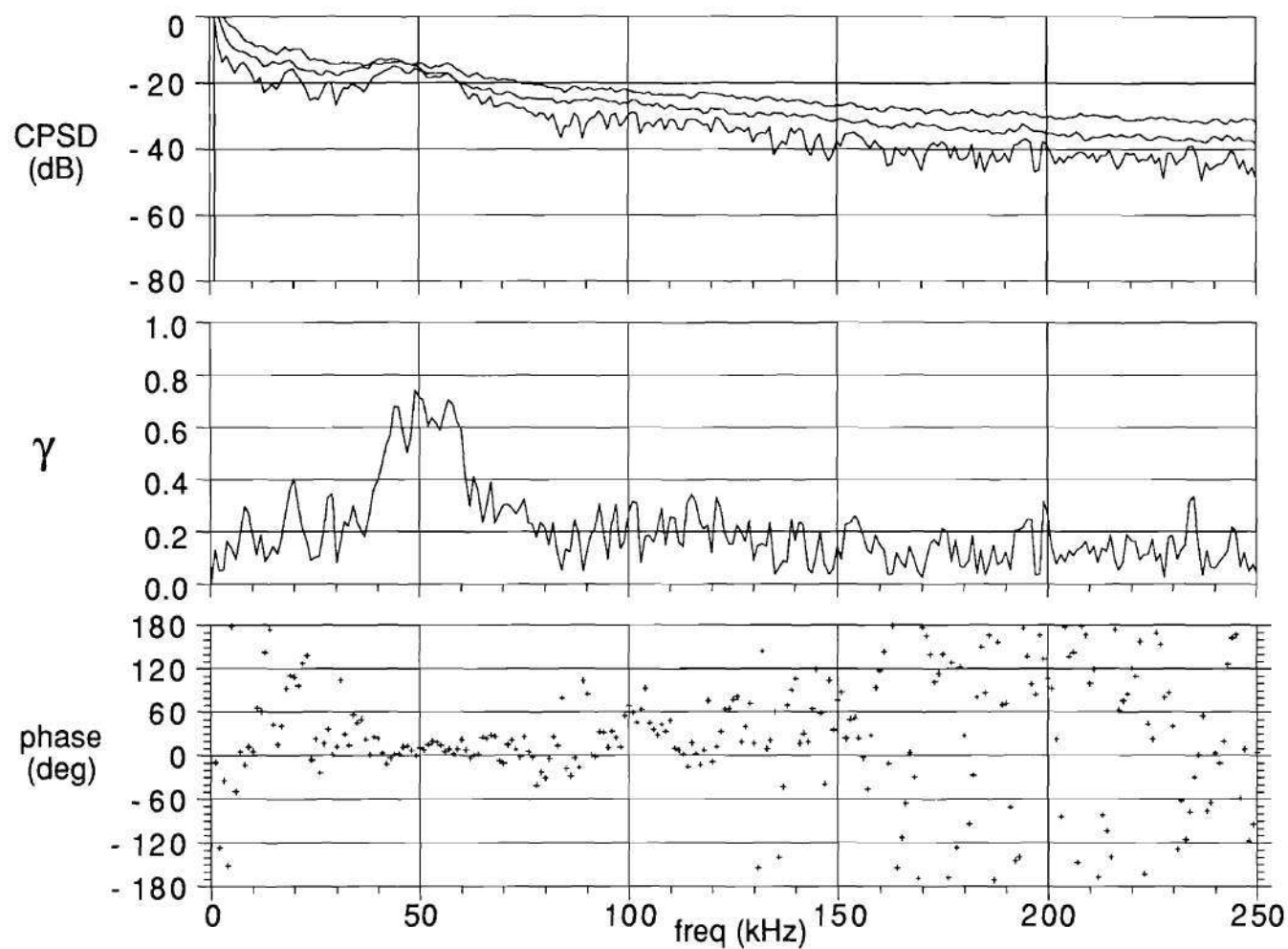
Figure 9.6: The CPSD, normalized coherence γ, and cross-phase of the cross-correlation of the two reflectometer probing beams from shot 11281 in sequence 90030801 for $\Delta r_c \simeq 4$ cm. Note the coherence peak at ~ 50 kHz and its nearly zero phase value. The two upper lines in the top graph are the APSDs for the two signals.

Figure 9.7: The radial correlation lengths and their uncertainties for sequences 90030801 (top) and 90092804 (bottom), calculated from the coherence between the two radially separated probing beams for many radial separations.

Figure 9.8: The cross-correlation coefficient function $\rho_{12}(0)$ for sequences 90030801 and 90092804 vs Δr_c. The time domain or mean correlation length is obtained from the slope of the fi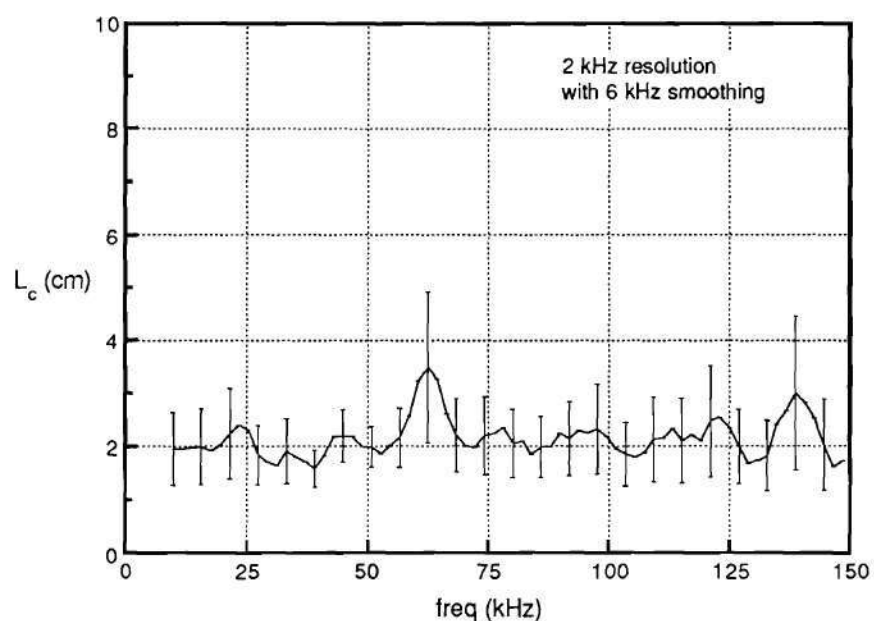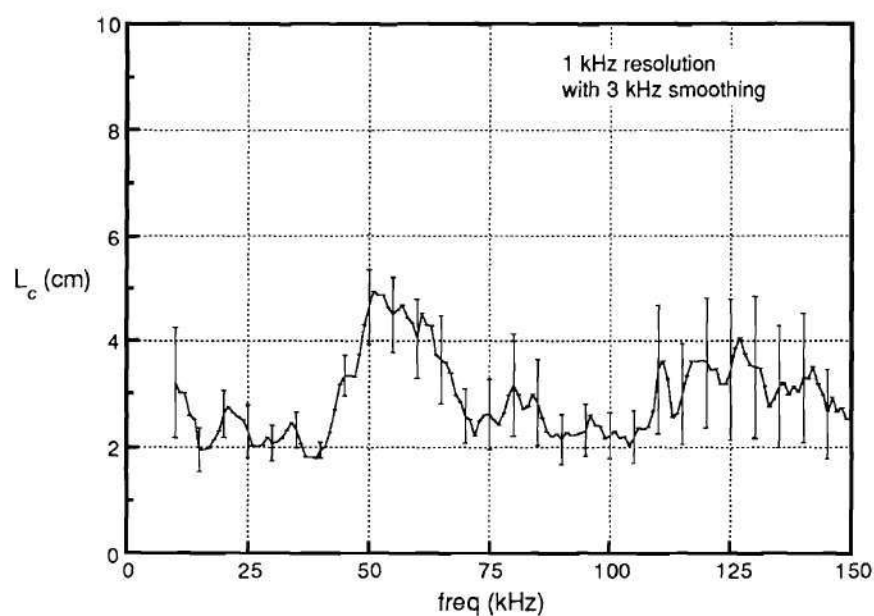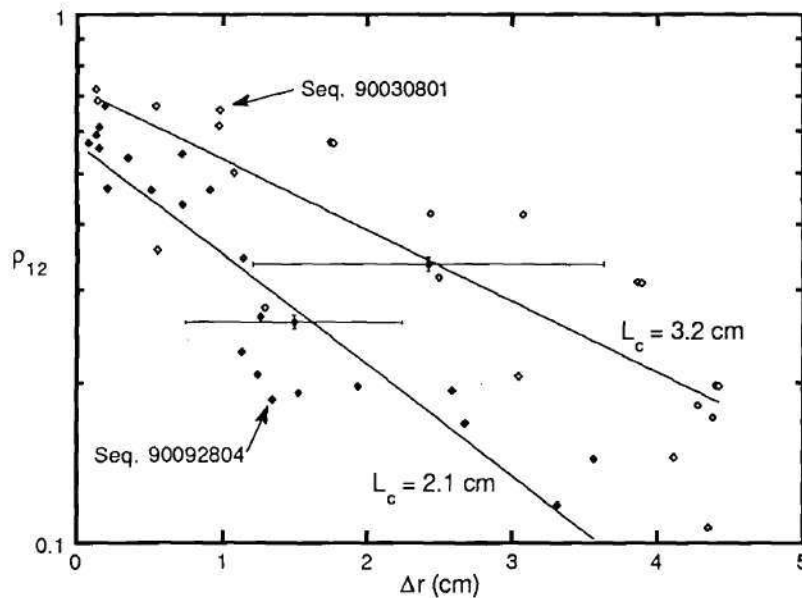tted lines. The error bars represent the typical uncertainties, e.g., statistical uncertainties in $\rho_{12}(0)$ of $\sim 3\%$ and the uncertainty in Δr of $\sim 50\%$.

shots. The reproducibility of the plasmas was poor during this sequence and caused the coherence to vary significantly between shots even though the calculated radial separations were similar.

As discussed in section "Total Correlation Length" in Chap. VII, the time domain cross-correlation coefficient function can be used to calculate the total correlation length for all frequency components. Here, the cross-correlation coefficient function for zero time lag is calculated and used to estimate the total radial correlation length of the density fluctuations at all frequencies below the Nyquist frequency. In Fig. 9.8, the cross-correlation coefficient function estimates for zero time lag for sequences 90030801 and 90092804 are shown as a function of the radial separation between the two reflectometer probing beams.

The total correlation length is then calculated similarly to the frequency

domain correlation length, i.e., the slope of the line fitted to the natural logarithm of the cross-correlation coefficient function. Note, typical error bars for the cross-correlation coefficient function and the radial separation are shown for one data point from each sequence. This time domain total correlation length may represent an estimate of the radial mixing length of the density fluctuations. For sequence 90030801, this total radial correlation length is ~ 3.2 cm $\pm 20\%$, while for sequence 90092804 it is ~ 2 cm $\pm 28\%$.

Radial Wave Number $\bar{k}_r$ Measurements

The mean radial wave number $\bar{k}_r$ can be determined from the radial coherence measurements, as discussed in Chap. VII. The radial coherence measurements can provide the relative phase or cross-phase between the coherent parts of the two input signals, as discussed in Chap. V. Basically, the cross-phase is the phase change due to the fluctuation's radial propagation from one measurement point (cutoff layer) to the next measurement point (second cutoff layer). Dividing this phase by the radial separation Δr_c between the two measurement points gives an estimate of k_r. In Fig. 9.9, the mean radial wave number $\bar{k}_r$ is plotted as a function of the radial separation between the reflectometer cutoff layers. Error bars are included with the plotted k_r data and were calculated using the equations given in Chap. VII. The error bars are $\sim 50\%$ of the data value and are primarily determined by the uncertainty in the radial separation of the two cutoff layers. The mean wave number $\bar{k}_r$ is plotted vs Δr_c because the measurement technique used was to fix the frequency of one probing beam and step the other frequency between discharges. Thus, one measurement point was approximately fixed on the density gradient and the other point was scanned down the gradient. The mean wave number $\bar{k}_r$ is then determined over a portion of the gradient and not at one location on the gradient. These measured values of $\bar{k}_r$ are very close to zero regardless of the
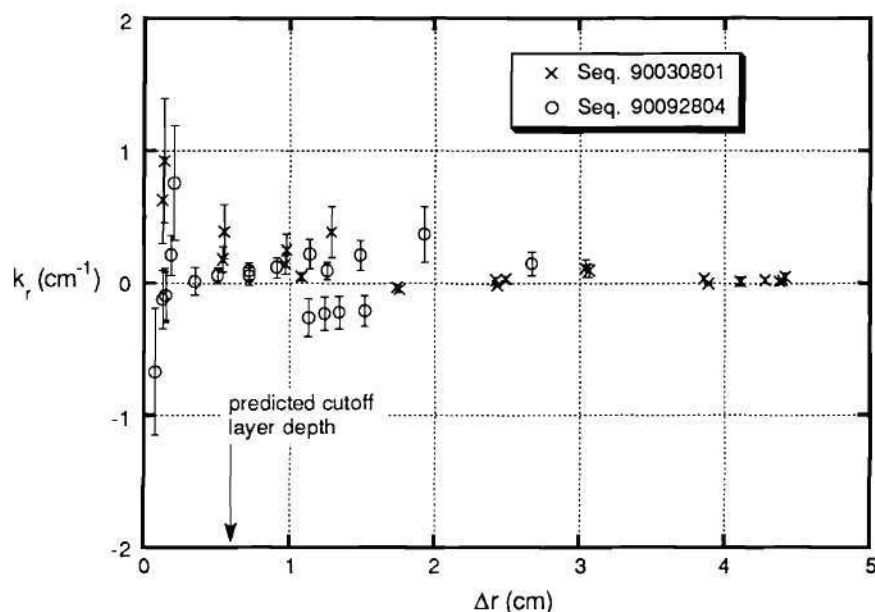
211

Figure 9.9: The measured values of $\bar{k}_r$ determined from the reflectometer radial coherence data. $\bar{k}_r$ is basically ~ 0 except near zero radial separation, where the cutoff layers are overlapping.

radial separation, except for very small separations where $\bar{k}_r$ can approach 1 cm^{-1}. The fact that $\bar{k}_r \sim 0$ cm^{-1} indicates that the fluctuations being observed have a very long radial wavelength. The increase in $\bar{k}_r$ for very small Δr_c is due to the small values of Δr_c and not to an increase in the phase. Since $\bar{k}_r$ is calculated from the CPSD weighted phase (mean phase), the values shown here will be dominated by the radially coherent peak at ~ 50 kHz, especially for larger values of Δr_c where the only coherent signal is this peak.

The width of the k_r spectrum, σ_{kr} (as defined in Chap. VII), is very similar to that shown here for $\bar{k}_r$, that is, $\sigma_{kr}/|\bar{k}_r| \sim 1$ as shown in Fig. 9.10. There is considerable variation in the ratio $\sigma_{kr}/|\bar{k}_r|$, but in general, the ratio is of order 1. This ratio is actually determined by the values of the mean phase $\bar{\phi}_r$ and its width or standard deviation $\sigma_{\phi r}$ obtained from the cross-correlation of the two radially

212
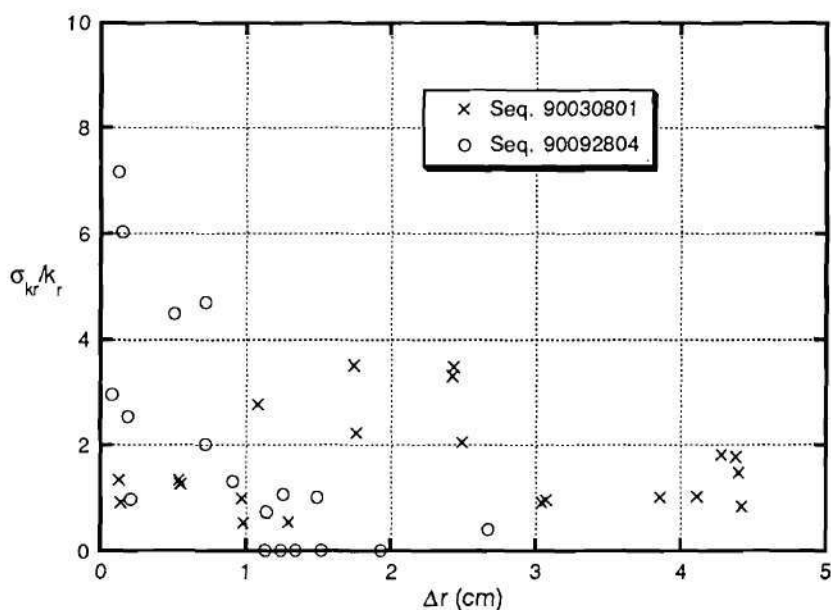
Figure 9.10: The measured values of $\sigma_{kr}/|\bar{k}_r|$ vs the radial separation of the cutoff layers. Note that there is considerable spread in the values of $\sigma_{kr}/|\bar{k}_r|$, but the mean value is ~ 1.

separated signals. In Fig. 9.11, the mean phase $\bar{\phi}_r$ used in calculating $\bar{k}_r$ is shown along with the width $\sigma_{\phi r}$ of the phase spectrum. The error bars are calculated using the equations given in Chap. VII. The phase values shown here are $\sim 10°$ for all separations, but they do show up to a factor of two variation. For these small phase angles, this factor of two variation has only a minor impact on $\bar{k}_r$. To illustrate the effect of the peak in the spectrum, Figs. 9.12 and 9.6 show the radial coherence for $\Delta r_c \simeq 0.5$ cm and 4 cm, respectively. Figure 9.12 shows that the entire spectrum, at least for $\gamma \geq 0.4$, has an approximately constant radial phase that is very near zero ($\sim 10°$). Figure 9.6 shows that for a much greater radial separation, the only coherent signal ($\gamma \geq 0.4$) remaining is the peak at ~ 50 kHz and that this peak still has a roughly constant phase near zero.
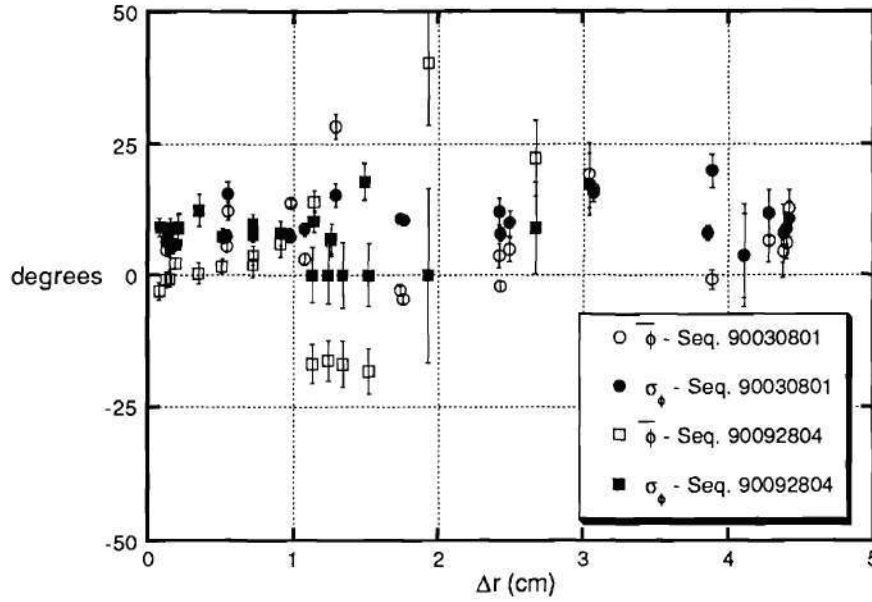
Figure 9.11: The measured values of $\bar{\phi}_r$ and $\sigma_{\phi r}$ used in calculating $\bar{k}_r$.

Poloidal Wave Number k_θ Estimates

As shown in Chap. IV, the various instability models used to predict the density fluctuation levels require the poloidal wave number k_θ to be known. The technique applied here to estimate k_θ from the reflectometer data is discussed in Chap. VII. This technique is based on the relation $\omega_{*e} = k_\theta v_D$, where ω_{*e} is the diamagnetic drift frequency and v_D is the electron drift velocity [Eq. (7.48)]. Assuming that the poloidal group velocity of the fluctuations is to first order v_D and that ω_{*e} can be approximated by the mean frequency $\bar{\omega}$ of the measured spectra, the mean poloidal wave number $\bar{k}_\theta$ is simply obtained from $\bar{k}_\theta = \bar{\omega}/v_D$. In Fig. 9.13, the reflectometer-estimated values of $\bar{k}_\theta$ with the estimated error bars are plotted vs the drift velocity. Also shown are a large number of $\bar{k}_\theta$ values measured by the FRLP for a wide range of ECH plasma conditions.[164] The error bars are determined

214

Figure 9.12: The results from cross-correlation analysis of the two reflectometer signals from shot 11267 are shown. The radial separation between the two cutoff layers is 0.5 cm. The two dashed lines in the top graph are the APSDs for the two signals.
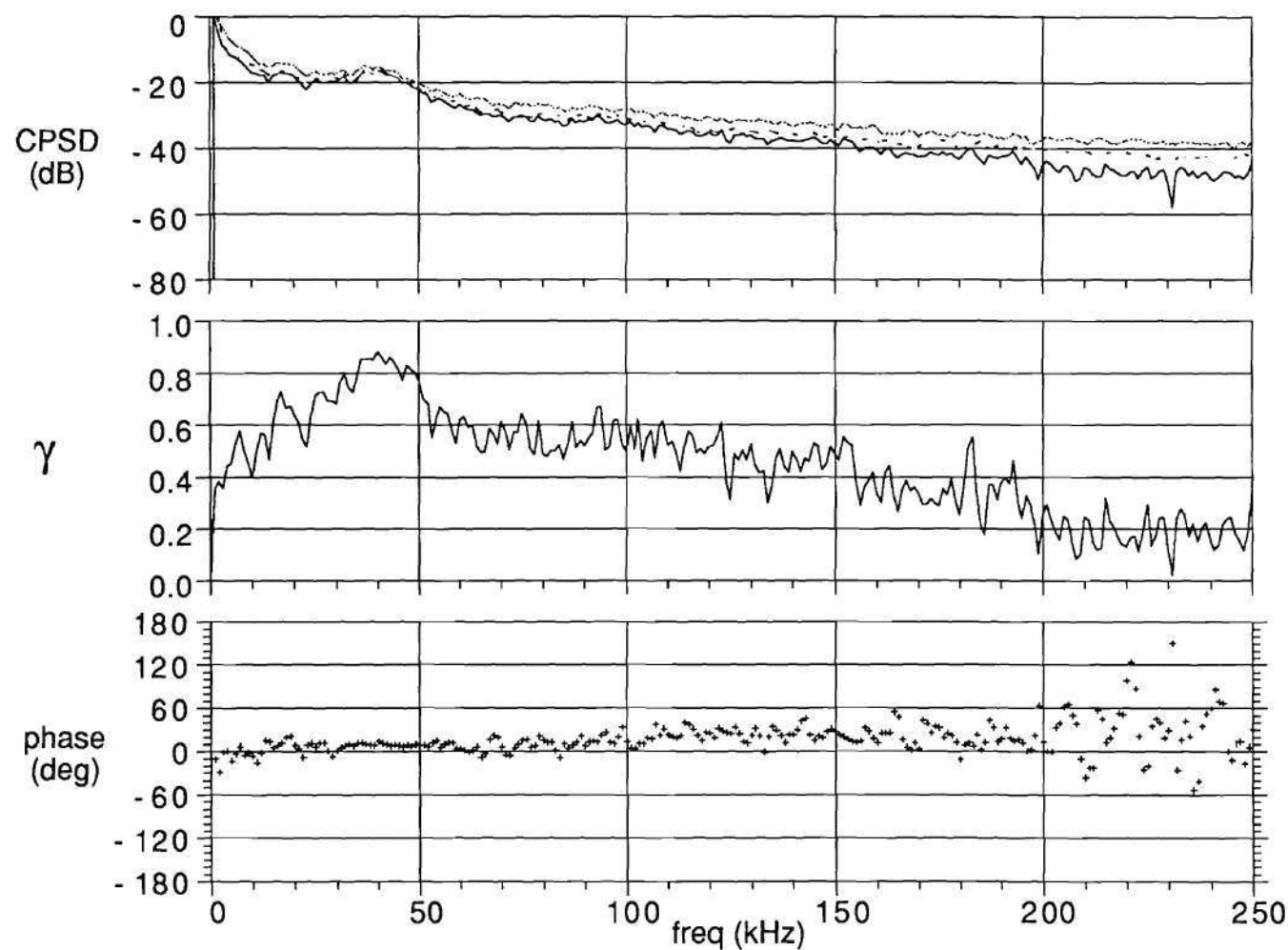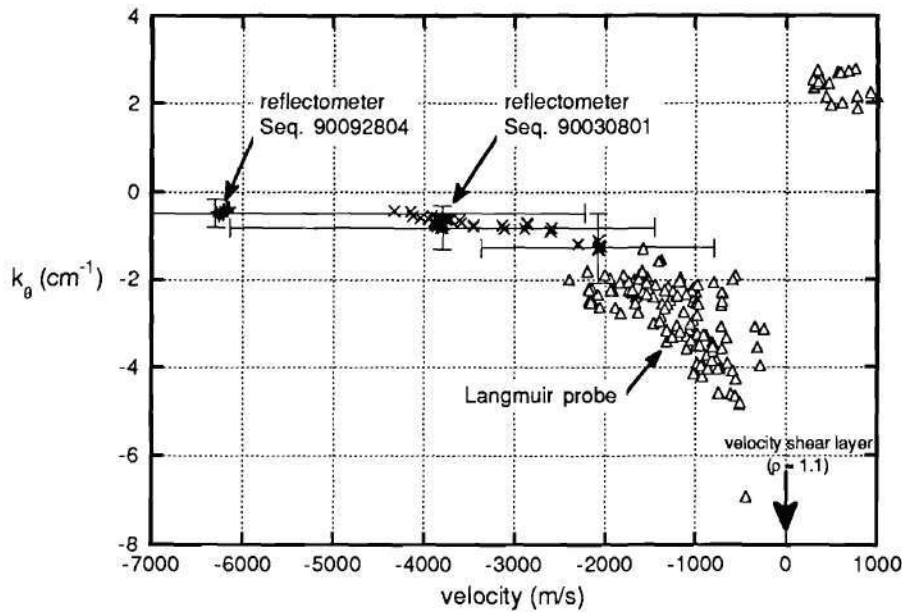
Figure 9.13: The values of $\bar{k}_\theta$ estimated from the reflectometer fluctuation spectra and measured by the FRLP.[164]

by the uncertainty in the mean frequency $\bar{\omega}$ of the spectra and the uncertainty in the diamagnetic drift velocity v_D. The uncertainty in $\bar{k}_\theta$ is about a factor of 2 and is dominated by the uncertainty in v_D. The outermost reflectometer data points and the innermost FRLP data points come from roughly the same region in the plasma, i.e., $\rho \simeq 0.95$, and so agreement between the two diagnostics is expected. For sequence 90030801, good agreement between the reflectometer and the FRLP is seen within the range of the error bars on the reflectometer data. Sequence 90092804 does not show as good agreement because of the much higher calculated diamagnetic drift velocity and its large uncertainty. The velocity shear layer, i.e., where the velocity changes direction, shown in this figure is located outside the last closed flux surface and is discussed in more detail by Hidalgo et al.[164]

The turbulent broadening $\sigma_{k\theta}$ of the $\bar{k}_\theta$ spectra is often of as much interest

216
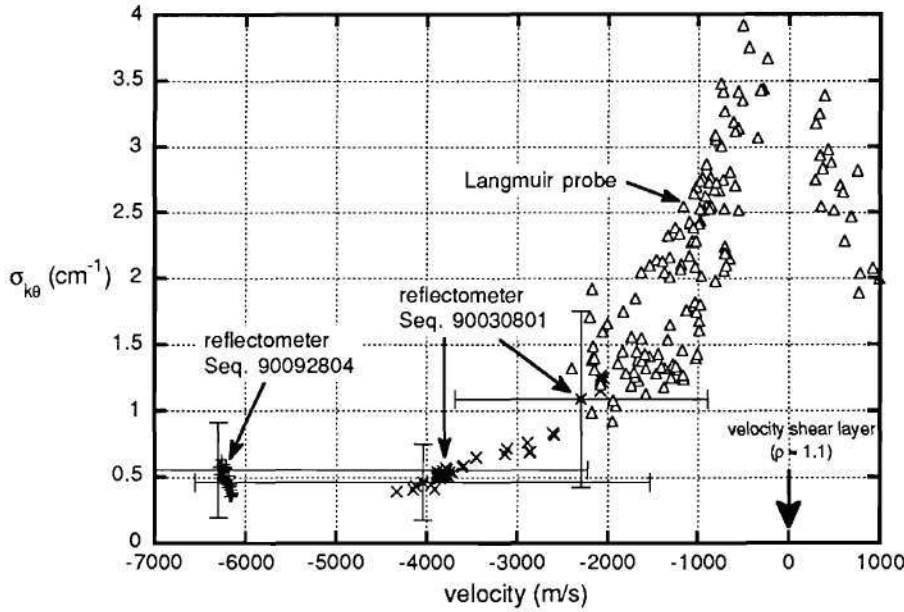
Figure 9.14: The values of $\sigma_{k\theta}$ estimated from the reflectometer fluctuation spectra and measured by the FRLP.[164]

as $\bar{k}_\theta$ itself. $\sigma_{k\theta}$ is estimated here by calculating the width or standard deviation σ_ω of the measured spectra and dividing by v_D. Figure 9.14 shows the reflectometer-estimated values of $\sigma_{k\theta}$ plotted as a function of the drift velocity, as well as the FRLP-measured values of $\sigma_{k\theta}$.[164] Here again, error bars have been estimated and plotted for the reflectometer data. For both the reflectometer and FRLP measurements, the ratio of the turbulent broadening of the k_θ spectra to $\bar{k}_\theta$ is found to be ~ 1.

In calculating $\bar{k}_\theta$ and $\sigma_{k\theta}$, Eq. (7.48) must be used to estimate the fluctuation drift velocity. The first part of Eq. (7.48) is the gradient drift term and is calculated from the electron density and temperature profiles, while the second term is the $\vec{E} \times \vec{B}$ drift term. The radial component of the electric field is required to calculate $\vec{E} \times \vec{B}$ drift velocity and is obtained from the plasma potential measurements made by the HIBP.[156] The radial electric field is then estimated from this potential profile

217

as $E_r = -d\phi/dr$. In the region of interest ($0.8 \leq \rho \leq 0.95$), the typical values of the electric field measured by the HIBP for this type of low density ECH discharge with this magnetic configuration have been estimated as $E_r = -7$ V/cm ± 7 V/cm.[157]

Comparison With Theory

In Chap. IV, the primary instabilities potentially present in ATF were reviewed. From this review, it was concluded that in the edge gradient region of the plasma ($0.8 \leq \rho \leq 1.0$), the most likely sources of density fluctuations are the resistive interchange instability and the DTEM. The resistive ballooning instability is not expected to be important in this region because the toroidal curvature term driving the ballooning instability is much smaller than the helical curvature term that drives the interchange instability, as shown in Fig. 4.1. Although the DTEM could drive the turbulence at the levels observed in these experiments, as discussed in Chap. IV, it is expected to be localized to a single field period, or at most, have coupling between 2 or 3 adjacent field periods. The observed turbulence has a strong globally coherent feature. This global feature suggests that the DTEM is not the source of the observed turbulence. Additionally, Harris et al.[161] have shown a connection (coherence) between the density fluctuations and the magnetic fluctuations in the edge region of some high-stored energy NBI-heated plasmas in ATF. The presence of the globally coherent feature and a magnetic component in the turbulence strongly suggests an MHD-driven instability.

Using Eq. (4.14), the theoretically predicted rms density fluctuation amplitudes for the resistive interchange instability are estimated using the data for the two ATF sequences discussed in this chapter. Additionally, Eq. (4.16) is used with Eq. (4.15) to estimate the nonlinear enhancement factor to obtain an estimate for

218

the nonlinear resistive interchange instability. The results of these calculations are shown in Fig. 9.15 for both sequences. The density and temperature profiles were continued out to $\rho = 1.2$ using FRLP profiles in the region of $1.0 \leq \rho \leq 1.2$.[164] The HIBP values were obtained in sequence 90092804 but are assumed to be similar for both sequences because of the similarities in the profiles. The FRLP values shown in both plots are typical values obtained from measurements in many ECH plasmas.[98,164] The agreement between the measured values of $\tilde{n}_e/n_e$ and the theoretically predicted values for the resistive interchange instability is quite good in the region of $\rho \sim 0.8$ to 1.05. Outside $\rho \simeq 1.05$, the fluctuation amplitude continues to rise, while the amplitude of the resistive interchange fluctuations falls. In this region, it is believed that ionization- or radiation-driven thermal drift instabilities are driving the fluctuations, causing the continued rise in $\tilde{n}_e/n_e$.[173]

The amplitude and trend of $\tilde{n}_e/n_e$ measured by the reflectometer are quite similar to the amplitudes predicted for the linear resistive interchange instability; however, the possibility of systematic uncertainties in the reflectometer data is substantial and not included in the error bars. These systematic errors could substantially increase (or decrease) the values of $\tilde{n}_e/n_e$ shown here, so that the measured values could agree with either the linear or nonlinear theories.

Discussion

In this chapter, the results of density fluctuation measurements in two ATF sequences of ECH plasmas were presented. Using the advanced features of the ATF reflectometer, i.e., quadrature phase detection and two-frequency operation, the measured fluctuations were quantified as completely as possible. First, the density fluctuation amplitudes $\tilde{n}_e/n_e$ were calculated for the measured probing beam
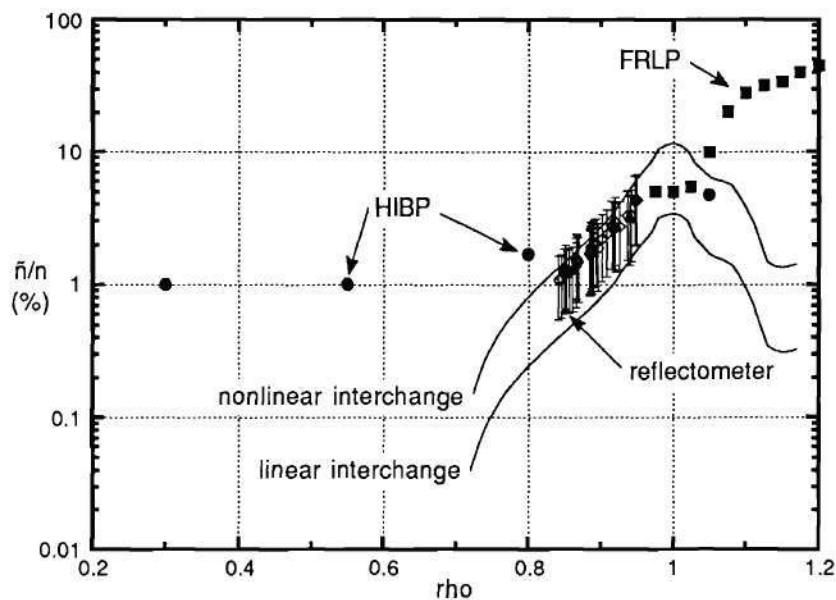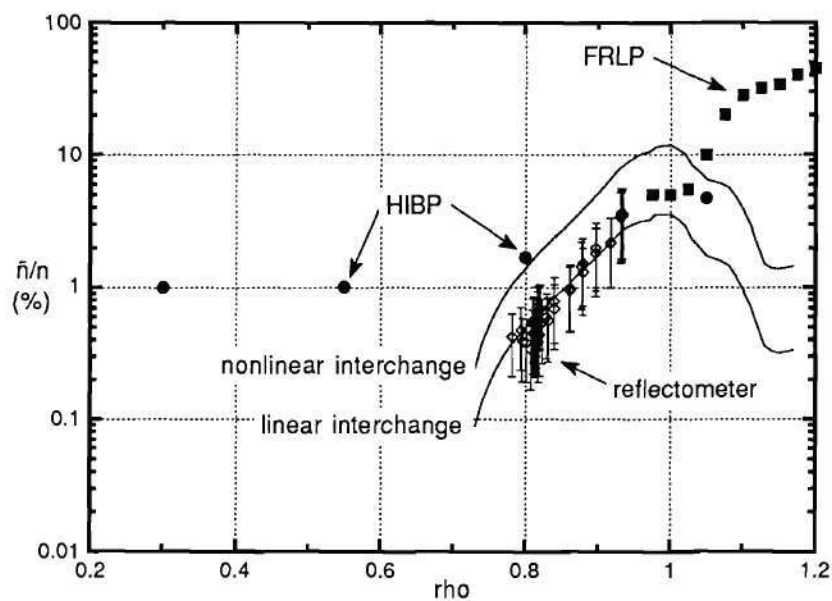
Figure 9.15: The theoretically predicted values of $\tilde{n}_e/n_e$ and the experimentally measured values for sequences 90030801 (top) and 90092804 (bottom).

phase fluctuations, and the uncertainties in these values of $\tilde{n}_e/n_e$ were calculated. Next, the radial coherence measurements made between two radially separated cut-off layers were used to estimate the radial correlation lengths. These measurements showed that a large peak around 50 kHz dominated the fluctuation spectrum in these plasmas and that this peak had a correlation length up to ~ 4 cm, while the correlation length for the rest of the spectrum was ~ 2 cm. Using the phase from the cross-correlation of the two radially separated signals, the mean radial wave number $\bar{k}_r$ was estimated and found to be $\ll 1$ cm^{-1} and $\sigma_{kr}/\bar{k}_r$ was found to be ~ 1. This is a significant finding as it implies that the fluctuations have a very large radial wavelength. Using the relationship $\omega_{*e} = k_\theta v_D$, the mean poloidal wave number $\bar{k}_\theta$ was estimated from the mean frequency of the reflectometer-measured fluctuation spectra and the calculated drift velocity. These calculations found $\bar{k}_\theta \sim 1$ cm^{-1}, in fair agreement with the FRLP measurements. It was also found that the turbulent broadening $\sigma_{k\theta}$ divided by the mean wave number $\bar{k}_\theta$ was of order 1 cm^{-1}, $\sigma_{k\theta}/\bar{k}_\theta \sim 1$. An important observation here is that $\bar{k}_r$ is apparently much less than $\bar{k}_\theta$ ($\bar{k}_r \ll \bar{k}_\theta$), although this statement cannot be conclusively made with the uncertainties in the measured values of $\bar{k}_r$ and $\bar{k}_\theta$.

The theoretical model for the resistive interchange instability was applied to the data for sequences 90030801 and 90092804, and good agreement between the predicted values of $\tilde{n}_e/n_e$ and the measured values was found in the edge density gradient region of the plasma, i.e., $0.8 \leq \rho \leq 1.0$; however, they diverge for $\rho > 1.0$, where an ionization- or radiation-driven thermal instability is believed to be driving the turbulence. Although the reflectometer cannot measure the $\vec{E} \times \vec{B}$ particle transport because of the fluctuations that it observes, the Langmuir probe can. In Fig. 9.16, the particle flux measured by the FRLP at $\rho \simeq 1$ in an ECH plasma is shown. Note that the peak in the power spectrum occurs near ~ 40 kHz, similar to the reflectometer observations, but that the peak in the particle flux occurs
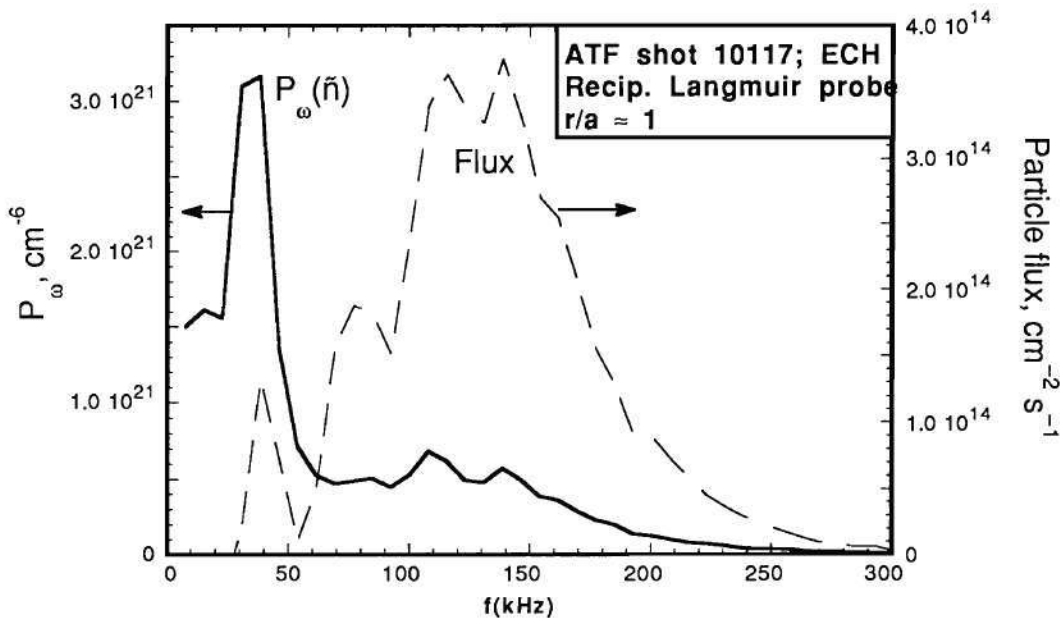
Figure 9.16: The FRLP-measured density fluctuation spectrum and its associated $\vec{E} \times \vec{B}$ particle transport are shown. Note that the dominant fluctuations in the power spectrum cause little of the $\vec{E} \times \vec{B}$ transport.

between 100 and 150 kHz. In fact, the flux due to fluctuations below 100 kHz is down by a factor of two or more from the peak flux. This means that the large fluctuations below 100 kHz produce no significant $\vec{E} \times \vec{B}$ particle transport, but they still could drive other forms of transport. Since the resistive interchange instability forms small magnetic islands by the interchanging of magnetic field lines, energy and particle transport occurs nearly instantaneously since particles traveling along one of these field lines will be rapidly carried to a cooler region of the plasma. The physical picture generated for the observed turbulence is a series of $m = \bar{k}_\theta r \sim 25$ magnetic islands rotating around the plasma poloidally with a radial wave number of ~ 0. The measured value of $\bar{k}_r$ could imply either solid rotating islands or radial wavelengths of the order of the minor radius. These islands apparently extend globally around the machine on a flux surface since coherence was observed between

the reflectometer, HIBP, and FRLP measured signals at toroidally and poloidally separated locations. The presence of these magnetic islands (the strong coherent feature in the fluctuation spectra) could be defining the location of the edge density gradient in ATF.

CHAPTER X

CONCLUSION

Summary

The goal of measuring density fluctuations with reflectometry is to better describe the physical characteristics of the fluctuations in the plasma so that the source of the fluctuations may be determined and ways to control them found. Various theoretical models have been developed to predict the instabilities in plasmas. The information from a reflectometer diagnostic in conjunction with other diagnostics can be compared with these various theoretical models in the attempt to identify the source of the instability. In Chap. IV, various instabilities are discussed in terms of their existence in the ATF torsatron and the ability of a reflectometer diagnostic to measure them. It is found that in the steep edge gradient region of the ECH discharges in ATF, the most likely sources of turbulence that a microwave reflectometer can measure are the MHD pressure-gradient-driven resistive interchange instability[91] and the DTEM.[80]

The ATF reflectometer used a dual-horn antenna design to minimize the effects of internal reflections in the waveguide system (the bane of single-antenna systems) and allow the use of quadrature phase detection. Fringe counting of the sine and cosine information obtained from the quadrature phase detector provides the phase fluctuations in the reflected signal resulting from the density fluctuations in the plasma. Using the rms amplitude of the phase fluctuations, the density fluc-

tuation level can be estimated based on the conversion of the phase fluctuations to a radial displacement of the cutoff layer. As discussed in Chap. VII, the technique used for the ATF reflectometer data requires $k_r \ll k_0$. To allow for better quantification of the density fluctuations, two microwave signals are launched simultaneously from the same antenna system. This allows fluctuation measurements to be made simultaneously at two radially separate positions. By performing cross-correlations between these two radially separated measurements, the radial coherence of the fluctuations can be determined.

In Chap. VIII, the results from two ECH-only sequences in ATF are presented. The reflectometer spectra from these sequences show a large peak near 50 kHz, which is observed to be localized in radius. The FRLP and the HIBP also see a similar peak in their spectra obtained during one of these two sequences. Cross-correlation analysis of the signals from all three diagnostics showed this peak to be globally coherent. In Chap. IX, the density fluctuation amplitudes and their uncertainties are estimated. These values of $\tilde{n}_e/n_e$ are then compared to the values measured by the FRLP and the HIBP. Good agreement between all three diagnostics is seen. Next, the radial correlation lengths are calculated and found to be on average ~ 2 cm with a much longer (~ 5 cm) feature around 50 kHz. It is also shown in Chap. IX that the mean radial wave number is ~ 0 cm^{-1}. This implies that the fluctuations have the physical characteristics of a solid rotating body.

The mean poloidal wave number $\bar{k}_\theta$ of the fluctuations was estimated from the reflectometer data using the technique discussed in Chap. VII and found to be ~ 1 cm^{-1}. This is in fair agreement with the FRLP measurements of $\bar{k}_\theta$, $\bar{k}_\theta \sim 2$ cm^{-1} just inside the last closed flux surface for similar ECH discharges. Using this value of $\bar{k}_\theta$, the measured values of $\tilde{n}_e/n_e$ are compared to the calculated theoretical values for the MHD resistive interchange instability. Good agreement between the measured values and the predicted values is found inside the last closed flux surface

in the edge density gradient, but outside, the measured data continue to rise while the theoretical values fall off. It is believed that thermal instabilities are driving the fluctuations outside the last closed flux surface, while the interchange instability is the most likely single instability driving the fluctuations in the edge density gradient. Other possible sources of the fluctuations are the DTEM and the resistive ballooning instability; however, the resistive ballooning instability is driven by the toroidal bad curvature, which is much less than the interchange-driving helical bad curvature in this region of the plasma. The DTEM is not believed to be the source either, because the observed turbulence is seen to have a globally coherent feature. The DTEM would be localized to the magnetic well in each field period with possibly weak coupling between adjacent field periods and so is not likely to produce the observed globally coherent fluctuations.

Review of the Key Points of Reflectometry on ATF

In the design and operation of the ATF reflectometer, several improvements over previous reflectometers have been made which has allowed new measurements to be made and new analysis techniques to be applied to the data. Below is a summary of these improvements, new measurements, and new analysis techniques.

- The use of quadrature phase detection allowed easy determination of the phase fluctuations in the reflected signal, permitting estimation of the density fluctuation amplitudes.

- Two-frequency operation using two tunable microwave sources that use the same antenna system, but with separate quadrature phase detectors, allowed detailed studies of the radial coherence of the fluctuations.

227

- The phase detection and two-frequency operation allowed localized measurements of the density fluctuations and cross-correlation analysis of these fluctuations at two radially separated cutoff layers. These new measurements required the development of new data analysis techniques, described in Chap. VII, to extract the desired information and estimate the uncertainty in this information.

- With the improved measurement techniques and the new data analysis techniques developed for the ATF reflectometer data, the density fluctuation amplitudes, radial correlation lengths, and radial wave numbers were all measured simultaneously.

The ATF reflectometer was used to study the density fluctuations in the edge electron density gradient region of the low-density ECH plasmas in ATF. Substantial new information was provided by this study on the characteristics of the fluctuations in this region of the plasma. Below is a summary of the observed fluctuation characteristics and conclusions drawn from these characteristics.

- The observed characteristics of the density fluctuations are:

  - a radial correlation length of 2–5 cm,

  - a radial wave number $k_r \sim 0$ cm^{-1},

  - $\tilde{n}_e/n_e$ ranging from $\sim 5\%$ at the plasma edge and decreasing to $\lesssim 1\%$ as the cutoff layer is scanned radially inward up the edge density gradient,

  - global coherence as indicated by coherence measurements between the reflectometer, the FRLP, and the HIBP in the vicinity of 30–50 kHz.

228

- Comparison of the measured values of $\tilde{n}_e/n_e$ with theoretical estimates for the MHD resistive interchange instability has shown good agreement in the edge gradient region in both the amplitude and radial trend.

- The MHD resistive ballooning instability is not expected to be important in this region of the plasma because of the small value of the ballooning instability driving toroidal curvature as opposed to the interchange instability driving helical curvature.

- The DTEM could drive fluctuations in this region of the plasma, but the DTEM is a localized mode. The observed fluctuations have a globally coherent feature, indicating that the DTEM is probably not the dominate source of the turbulence.

If one insists on ascribing the observed fluctuations to a single instability, the characteristics of the observed fluctuations are most like those expected for the MHD resistive interchange instability. However, the $\vec{E} \times \vec{B}$ particle transport measured by the FRLP at the plasma edge indicates that these fluctuations are not the dominant source of particle transport at the plasma edge ($\rho \sim 1.0$).

Future Experiments on ATF

The results shown in Chap. IX were obtained by the ATF reflectometer in ECH-only plasmas in the standard magnetic configuration. Magnetic configuration scans are planned in order to study the relationship between the observed fluctuations and the magnetic configuration. By varying the magnetic configuration, the shear, the magnetic well size and depth, and the elongation of the plasma can be changed. These parameters affect the growth of the instabilities significantly. The

229

reflectometer will be used in conjunction with the HIBP, FRLP, and the new 2 mm microwave scattering diagnostic to study the fluctuations in the plasma during magnetic configuration scans. One goal of these experiments is to assess the role of the DTEM in ATF. By varying the magnetic configuration, the population of helically trapped particles can be varied by almost an order of magnitude. If the DTEM is present, a trapped particle scan should provide a means of observing its existence.

Proposed Improvements and Experiments

Several improvements have been proposed for the ATF reflectometer. First, the antenna mounting structure for the present 30 to 40 GHz system could be modified to allow alignment of the antenna with the reflecting surface. This should minimize or prevent the asymmetric spectra resulting from significant Doppler shifting of the reflected probing beam by minimizing the asymmetric scattering back into the receiving antenna. This has been done on the TFTR reflectometer.[147] The next step for reflectometry on ATF would be to build a high-frequency system to study internal fluctuations in NBI-heated plasmas. This system would also be designed to use either the X- or O-modes with a dual antenna arrangement and quadrature phase detection. Finally, by using the present reflectometer system but moving one set of microwave source and quadrature phase detector to a different poloidal or toroidal location, the ability of the system to measure the m or n numbers of the fluctuations could be tested. In this technique, two separate reflectometers would be used with either a poloidal (for m) or toroidal (for n) separation between them. With the reflectometers operating at or near the same frequency, the phase of the coherent signals could be used to determine the mode numbers of the fluctuations.

REFERENCES

[1] P. C. Liewer, "Measurements of microturbulence in tokamaks and comparisons with theories of turbulence and anomalous transport," *Nucl. Fusion* **25**, 543–621 (1985).

[2] TFR Group, "Local density fluctuations measurements by microwave reflectometry on TFR," *Plasma Phys. Controlled Fusion* **27**, 1299–1306 (1985).

[3] J. Sanchez, H. J. Hartfuss, W VII-AS Team, NBI Team, E. Anabitarte, A. P. Navarro, and ECRH Group, "Reflectometry observations of density fluctuations in WENDELSTEIN VII-AS stellarator," in *Proceedings of the 17th European Conference on Controlled Fusion and Plasma Physics, Amsterdam, 1990* (European Physical Society, Geneva, Switzerland), pp. 1572–1574, Vol. 14B, Part IV.

[4] E. Mazzucato, *Density Fluctuations in the Adiabatic Toroidal Compressor*, Technical Report MATT-1151, Princeton Plasma Physics Laboratory, September 1975.

[5] J. H. Harris, *Low-Frequency Coherent Fluctuations in the Proto-Cleo Torsatron*, Ph.D. thesis, University of Wisconsin–Madison, 1981.

[6] J. Sanchez, H. J. Hartfuss, W VII-AS Team, NBI Team, Pellet Injection Team, E. Anabitarte, A. P. Navarro, and ECRH Group, "Observations of density fluctuations associated with the resonant $q = 2$ surface in the WENDELSTEIN VII-AS stellarator," *Nucl. Fusion* **30**, 2383–2391 (1990).

[7] G. Bateman, *MHD Instabilities*, 2nd ed. (MIT Press, Cambridge, 1980).

[8] K. Miyamoto, *Plasma Physics for Nuclear Fusion* (MIT Press, Cambridge, 1980).

[9] J. F. Lyon, B. A. Carreras, K. K. Chipley, M. J. Cole, J. H. Harris, T. C. Jernigan, R. L. Johnson, V. E. Lynch, B. E. Nelson, J. A. Rome, J. Sheffield, and P. B. Thompson, "The Advanced Toroidal Facility," *Fusion Technol.* **10**, 179–226 (1986).

[10] W. M. Stacey, *Fusion: An Introduction to the Physics and Technology of Magnetic Confinement Fusion* (Wiley-Interscience, New York, 1984).

231

11 V. L. Ginzburg, *The Propagation of Electromagnetic Waves in Plasmas*, 2nd ed. (Pergamon Press, Oxford, 1970).

12 K. G. Budden, *Radio Waves in the Ionosphere* (Cambridge University Press, Cambridge, 1961).

13 M. Abramowitz and I. A. Stegun, editors, *Handbook of Mathematical Functions*, 5th ed. (Dover, New York, 1968).

14 A. E. Hubbard, *Measurement of Electron Density on JET by Microwave Reflectometry*, Ph.D. thesis, University of London, Imperial College of Science and Technology, May 1987.

15 M. Brambilla and M. Moresco, "The influence of mode mixing on reflectometry density measurements in a reversed field pinch," *Plasma Phys. Controlled Fusion* **29**, 381–393 (1987).

16 M. Bornatici, R. Cano, O. De Barbieri, and F. Engelmann, "Electron cyclotron emission and absorption in fusion plasmas," *Nucl. Fusion* **23**, 1153–1257 (1983).

17 G. Bekefi, *Radiation Processes in Plasmas* (John Wiley and Sons, New York, 1966).

18 Private communications with C. Hidalgo, CIEMAT (1990).

19 T. Lehner, J. M. Rax, and X. L. Zou, "Linear mode conversion by magnetic fluctuations in inhomogeneous magnetized plasmas," *Europhys. Lett.* **8**, 759–764 (1989).

20 M. Brambilla and M. Moresco, *Numerical Simulation of Reflectometry Density Measurements in a Reversed Field Pinch*, Technical Report IPP 5/11, Max-Planck Institute for Plasma Physics, September 1986.

21 I. Fidone and G. Granata, "Propagation of electromagnetic waves in a plasma with a sheared magnetic field," *Nucl. Fusion* **11**, 133–139 (1971).

22 D. A. Boyd, "What is the limiting polarization of electron cyclotron emission leaving a fusion plasma?," in *EC-5: Fifth International Workshop on Electron Cyclotron Emission and Electron Cyclotron Heating, November 1985, San Diego, 1986* (General Atomics, San Diego, Calif.), pp. 77–87.

23 G. L. Bell, *Third-Harmonic Electron Cyclotron Emission Studies on the Advanced Toroidal Facility*, Ph.D. thesis, Auburn University, 1990.

[24] C. A. J. Hugenholtz, *Microwave Interferometer and Reflectometer Techniques for Thermonuclear Plasmas*, Technical Report 90-192, FOM-Instituut voor Plasmafysica Rijnhuizen, Nieuwegein, the Netherlands, 1990.

[25] A. E. Hubbard, A. E. Costley, and C. W. Gowers, "A simple fixed-frequency reflectometer for plasma density profile measurements on JET," *J. Phys. E: Sci. Instrum.* **20**, 423–427 (1987).

[26] I. H. Hutchinson, *Principles of Plasma Diagnostics* (Cambridge University Press, Cambridge, 1987).

[27] Ch. P. Ritz, H. Y. W. Tsui, T. L. Rhodes, R. D. Bengtson, H. Lin, and A. J. Wootton, "Portable probe system for edge turbulence and transport measurements," *Rev. Sci. Instrum.* **61**, 2998–3000 (1990).

[28] T. P. Crowley, S. C. Aceto, K. A. Connor, J. W. Heard, R. L. Hickok, J. F. Lewis, P. E. Mclaren, A. Ouroua, J. G. Schatz, P. M. Schoch, J. Schwelberger, V. J. Simcic, and J. J. Zielinski, "Recent advances in heavy ion beam probe diagnostics," *Rev. Sci. Instrum.* **61**, 2989–2994 (1990).

[29] R. E. Slusher and C. M. Surko, "Study of density fluctuations in plasmas by small-angle CO_2 laser scattering," *Phys. Fluids* **23**, 472–490 (1980).

[30] T. Tetsuka, *Measurement of Density Fluctuations on the JIPP T-II Tokamak Plasma by Millimeter and Sub-Millimeter Wave Scattering*, Technical Report IPPJ-766, Institute of Plasma Physics, Nagoya University, 1986.

[31] G. R. Hanson, J. B. Wilgen, E. Anabitarte, J. D. Bell, J. H. Harris, J. L. Dunlap, and C. E. Thomas, "ATF two-frequency correlation reflectometer," *Rev. Sci. Instrum.* **61**, 3049–3051 (1990).

[32] T. Lehecka, W. A. Peebles, N. C. Luhmann, Jr., S. R. Burns, and E. Olsen, "Reflectometry systems for the DIII-D tokamak," *Rev. Sci. Instrum.* **59**, 1620–1622 (1988).

[33] E. Anabitarte, E. G. Bustamante, M. A. G. Calderón, and J. Senties, "Characterization of a Q-band microwave reflectometer for plasma diagnosis in the tokamak TJ-1," *Int. J. Infrared Millim. Waves* **8**, 733–751 (1987).

[34] E. Anabitarte, E. G. Bustamante, M. A. G. Calderón, J. Senties, A. P. Navarro, and J. Sánchez, "Determination of the electron density profile and its fluctuations by broadband microwave reflectometry in the TJ-1 tokamak," *J. Phys. D: Appl. Phys.* **21**, 1384–1390 (1988).

233

[35] R. J. Colchin, "Density profiles by swept frequency microwaves," January 1973, ORMAK-TM-93, Unpublished Internal Report, ORNL.

[36] A. Cavallo and R. Cano, *Proposal for Density Profile Measurements By Reflectometry in Large Tokamaks*, Technical Report EUR-CEA-FC-1137, Association EURATOM-CEA sur la Fusion, January 1982.

[37] M. A. G. Calderon and F. Simonet, "Experimental study of a swept reflectometer with a single antenna for plasma density profile measurement," *Int. J. Infrared Millim. Waves* **6**, 605–628 (1985).

[38] G. Arfken, *Mathematical Methods for Physicists*, 3rd ed. (Academic Press, Orlando, FL, 1985).

[39] F. Simonet, "Measurement of electron density profile by microwave reflectometry on tokamaks," *Rev. Sci. Instrum.* **56**, 664–669 (1985).

[40] H. Bottollier and G. Ichtchenko, "Microwave reflectometry with the extraordinary mode om tokamaks: Determination of the electron density profile of Petula-B," *Rev. Sci. Instrum.* **58**, 539–546 (1987).

[41] E. J. Doyle, T. Lehecka, S. Burns, E. Olson, N. C. Luhmann, Jr., W. A. Peebles, and the DIII-D Group, "X-mode broadband reflectometry results from the DIII-D tokamak," *Bull. Am. Phys. Soc.* **34** (9) (1989).

[42] R. J. Colchin, "An underground ORMAK experiment – The Microwave Reflectometer," May 1973, ORMAK-TM-105, Unpublished Internal Report, ORNL.

[43] V. A. Vershkov and V. A. Zhuravlev, "Plasma diagnostics experiments on the T-10 tokamak by means of a reflected signal," *Sov. Phys.-Tech. Phys.* **32**, 523–526 (1987).

[44] D. L. Brower, Jr. N. C. Luhmann, W. A. Peebles, Ch. P. Ritz, and E. J. Powers, "The application of homodyne spectroscopy to the study of low-frequency microturbulence in the TEXT tokamak," *Int. J. Infrared Millim. Waves* **7**, 447–457 (1986).

[45] T. Tsukishima, I. Nishida, M. Nagatsu, H. Inuzuka, and K. Mizuno, "Dual homodyne detection system for measuring asymmetric spectra in the far-infrared regime," *Rev. Sci. Instrum.* **57**, 560–565 (1986).

[46] T. Lehecka, E. J. Doyle, R. Philipona, N. C. Luhmann, Jr., W. A. Peebles, C. L. Hsieh, T. N. Carlstrom, R. P. Seraydarian, and the DIII-D Group, "Results from the DIII-D millimeter-wave reflectometer," in *Proceedings of the 16th European Conference on Controlled Fusion and Plasma Physics, Venice, 1989* (European Physical Society, Geneva, Switzerland), pp. 123–126, Vol. 13B, Part I.

[47] J. L. Doane, E. Mazzucato, and G. L. Schmidt, "Plasma density measurements using FM-CW millimeter wave radar techniques," *Rev. Sci. Instrum.* **52**, 12–15 (1981).

[48] G. Ichtchenko, H. Bottollier-Curtet, M. Goniche, and the PETULA Group, "Density profile microwave reflectometry and confinement properties of a lower hybrid current drive sustained tokamak discharge," in *Proceedings of the 13th European Conference on Controlled Fusion and Plasma Heating, Schiersee, 1986* (European Physical Society, Geneva, Switzerland), pp. 419–422, Vol. 10C, Part I.

[49] P. Millot and F. Simonet, *A Broadband Microwave Reflectometer for Tore Supra*, Technical Report CEA-CONF-9184, Association EURATOM-CEA sur la Fusion, June 1987.

[50] J. M. Senties, E. G. Bustamante, M. A. G. Calderón, E. Anabitarte, A. P. Navarro, P. Riodas, and J. Sánchez, "Radial profile of electron density fluctuations in the TJ-1 tokamak from microwave reflectometry measurements," in *Proceedings of the 16th European Conference on Controlled Fusion and Plasma Physics, Venice, 1989* (European Physical Society, Geneva, Switzerland), pp. 51–54, Vol. 13B, Part I.

[51] Om P. Gandhi, *Microwave Engineering and Applications* (Pergamon Press, New York, 1986).

[52] Private communications with D. Dixson, Millitech Corp., South Deerfield, MA (1990).

[53] S. F. Adam and Hewlett Packard, *Microwave Theory and Applications*, 2nd ed. (Prentice Hall, England Cliffs, NJ, 1969).

[54] G. R. Hanson, E. Anabitarte, J. H. Harris, C. E. Thomas, and J. B. Wilgen, "Microwave reflectometry system for ATF," *Bull. Am. Phys. Soc.* **34** (9) (1989).

[55] O. Asada, A. Inoue, and T. Tsukishima, "Homodyne method for detecting asymmetric spectra," *Rev. Sci. Instrum.* **51**, 1308–1313 (1980).

[56] M. A. Heald and C. B. Wharton, *Plasma Diagnostics with Microwaves* (Krieger, Huntington, New York, 1978).

[57] R. C. Johnson and H. Jasik, *Antenna Engineering Handbook* (Wiley, New York, 1984).

[58] *Millimeter Wave Components & Subsystems Catalog*, Alpha Industries, Inc., 1990.

[59] A. I. Anisimov, "Method of investigating electron spatial distribution in a plasma," *Sov. Phys.-Tech. Phys.* **5**, 939-948 (1961).

[60] V. A. Anoshkin, V. E. Golant, B. P. Konstantinov, B. P. Poloskin, and O. N. Shcherbinin, "Microwave investigations of plasma on the 'Alpha' device," *Sov. Phys.-Tech. Phys.* **5**, 1370-1377 (1961).

[61] Private communications with J. B. Wilgen, ORNL (1991).

[62] S. M. Hamberger, L. E. Sharp, J. B. Lister, and S. Mrowka, "Experimental study of enhanced diffusion by electrostatic fluctuations in an ohmically heated toroidal plasma," *Phys. Rev. Lett.* **37**, 1345-1348 (1976).

[63] TFR Group, presented by F. Simonet, "Measurements of electron density profile and local density fluctuations by microwave reflectometry on TFR," in *Proceedings of the 11th European Conference on Controlled Fusion and Plasma Physics, Aachen, 1983* (European Physical Society, Geneva, Switzerland), pp. 85-88, Vol. 7D, Part I.

[64] Private communications with A. Costley, JET (1990).

[65] A. E. Hubbard, D. Campbell, and T. E. Stringer, "Direct measurement of the electron diffusion coefficient on JET using a microwave reflectometer," in *Proceedings of the 13th European Conference on Controlled Fusion and Plasma Heating, Schliersee, 1986* (European Physical Society, Geneva, Switzerland), pp. 232-235, Vol. 10C, Part I.

[66] M. Malacarne, P. Cripwell, P. A. Duperrex, A. W. Edwards, R. D. Gill, R. S. Granetz, F. Simonet, J. Snipes, and A. Weller, "Fluctuations during the JET discharges with H-mode," *Plasma Phys. Controlled Fusion* **29**, 1675-1686 (1987).

[67] M. E. Manso, F. M. Serra, and J. T. Mendonca, "A reflectometric system for studying lower hybrid energy deposition in a tokamak plasma," in *Energy Independence Conference on Fusion Energy and Plasma Physics, August 1987*, edited by P. H. Sakanaka (World Scientific, Singapore), pp. 3-12.

236

[68] R. Prentice, P. Cripwell, H. E. Clarke, A. E. Costley, J. A. Fessey, A. E. Hubbard, C. A. J. Hugenholtz, T. Oyevaar, M. Paume, A. J. Putter, A. C. Sips, and K. Slavin, "Results from JET reflectometry systems," *Bull. Am. Phys. Soc.* **33** (9) (1988).

[69] T. Lehecka, *Millimeter-Wave Reflectometry Diagnostics on the DIII-D Tokamak*, Ph.D. thesis, University of California, Los Angeles, 1989.

[70] T. Lehecka, R. Philipona, E. J. Doyle, N. C. Luhmann, Jr., W. A. Peebles, H. Matsumoto, E. J. Strait, T. S. Taylor, K. H. Burrell, and the D-III-D Group, "Characterization of density fluctuations in DIII-D," *Bull. Am. Phys. Soc.* **34** (9) (1989).

[71] A. C. C. Sips, A. E. Costley, J. C. M. de Haas, and R. Prentice, "Measurements of the electron particle diffusion coefficient with the JET multichannel reflectometer," in *Proceedings of the 16th European Conference on Controlled Fusion and Plasma Physics, Venice, 1989* (European Physical Society, Geneva, Switzerland), pp. 99–102, Vol. 13B, Part I.

[72] A. C. C. Sips, J. C. M. de Haas, A. E. Costley, G. M. D. Hogeweij, N. J. Lopes Cardozo, J. O'Rourke, and R. Prentice, "Simultaneous measurements of thermal conductivity and particle diffusivity in JET and their interpretation," *Bull. Am. Phys. Soc.* **34** (9) (1989).

[73] P. Cripwell, A. E. Costley, and A. E. Hubbard, "Correlation reflectometry," in *Proceedings of the 16th European Conference on Controlled Fusion and Plasma Physics, Venice, 1989* (European Physical Society, Geneva, Switzerland), pp. 75–78, Vol. 13B, Part I.

[74] Equipe TFR, "Tokamak plasma diagnostics," *Nucl. Fusion* **18**, 647–731 (1978).

[75] E. J. Doyle, T. Lehecka, N. C. Luhmann, Jr., W. A. Peebles, and the DIII-D Group, "X-mode broadband reflectometric density profile measurements on DIII-D," *Rev. Sci. Instrum.* **61**, 2896–2899 (1990).

[76] L. A. Artsimovich, "Tokamak devices," *Nucl. Fusion* **12**, 215–252 (1972).

[77] W. M. Stacey, *Fusion Plasma Analysis* (Wiley-Interscience, New York, 1981).

[78] S. Ichimaru, *Basic Principles of Plasma Physics* (Benjamin/Cummings Publishing Company, Reading, MA, 1973).

[79] J. W. Connor, "Micro-instabilities and anomalous transport," Lectures at the II Workshop on Magnetic Confinement Fusion: Transport and Confinement in Toroidal Devices, Santander, Spain, 1990.

[80] N. Dominguez, B. A. Carreras, V. E. Lynch, and P. H. Diamond, "Linear study of high-n dissipative trapped electron modes in $l = 2$ torsatrons," unpublished, ORNL, 1990.

[81] Private communications with N. Dominguez, ORNL (1990).

[82] J. P. Freidberg, *Ideal Magnetohydrodynamics* (Plenum Press, New York, 1987).

[83] B. A. Carreras and P. H. Diamond, "Thermal diffusivity induced by resistive pressure-gradient driven turbulence," *Phys. Fluids B* **1**, 1011–1017 (1989).

[84] B. A. Carreras, L. Garcia, and P. H. Diamond, "Theory of resistive pressure-gradient driven turbulence," *Phys. Fluids* **30**, 1388–1400 (1987).

[85] O. J. Kwon, P. H. Diamond, and H. Biglari, "Theory of neoclassical pressure-gradient-driven turbulence," *Phys. Fluids B* **2**, 291–301 (1990).

[86] L. A. Charlton and B. A. Carreras, "The effect of compressibility on magnetohydrodynamic instabilities in toroidal tokamak geometry," *Phys. Fluids B* **2**, 539–546 (1990).

[87] W. M. Manheimer and C. N. Lashmore-Davies, *MHD and Microinstabilities in Confined Plasma* (IOP Publishing Ltd., Bristol, England, 1989).

[88] V. D. Shafranov, "Magnetohydrodynamic theory of plasma equilibrium and stability in stellarators: Survey of results," *Phys. Fluids* **26**, 357–364 (1983).

[89] L. A. Charlton, J. N. Leboeuf, and V. E. Lynch, "Resistive MHD stability of stellarators with increasing plasma pressure," unpublished, ORNL, 1990.

[90] J. H. Harris et al., "Second stability in the ATF torsatron," *Phys. Rev. Lett.* **63**, 1249–1252 (1989).

[91] B. A. Carreras, N. Dominguez, J. N. Leboeuf, V. E. Lynch, and L. A. Charlton, *A First Glance at the Initial ATF Experimental Results*, Technical Report ORNL/TM-11102, Oak Ridge National Laboratory, May 1989.

[92] J. H. Harris, O. Motojima, H. Kaneko, S. Besshou, H. Zushi, M. Wakatani, F. Sano, S. Sudo, A. Sasaki, K. Kondo, M. Sato, T. Mutoh, T. Mizuuchi, M. Iima, T. Obiki, A Iiyoshi, and K. Uo, "Magnetohydrodynamic activity in high-β, currentless plasmas in Heliotron-E," *Phys. Rev. Lett.* **53**, 2242–2245 (1984).

93 J. H. Harris, J. N. Talmadge, T. D. Mantel, and J. L. Shohet, "Low-frequency coherent fluctuations in the Proto-Cleo torsatron," *Nucl. Fusion* **24**, 159–168 (1984).

94 L. Garcia, P. H. Diamond, B. A. Carreras, and J. D. Callen, "Theory of resistivity-gradient-driven turbulence," *Phys. Fluids* **28**, 2147–2158 (1985).

95 B. A. Carreras, H. R. Hicks, J. A. Holmes, V. E. Lynch, L. Garcia, J. H. Harris, T. C. Hender, and B. F. Masden, "Equilibrium and stability properties of high-beta torsatrons," *Phys. Fluids* **26**, 3569–3579 (1983).

96 B. A. Carreras, N. Dominguez, L. Garcia, V. E. Lynch, J. F. Lyon, J. R. Cary, J. D. Hanson, and A. P. Navarro, "Low-aspect ratio torsatron configurations," *Nucl. Fusion* **28**, 1195–1207 (1988).

97 T. C. Hender, B. A. Carreras, L. A. Charlton, L. Garcia, H. R. Hicks, J. A. Holmes, and V. E. Lynch, "Torsatron equilibrium and stability studies," *Nucl. Fusion* **25**, 1463–1473 (1985).

98 J. H. Harris et al., "Fluctuations and stability in the ATF torsatron," in *Proceedings of the 13th International Conference on Plasma Physics and Controlled Nuclear Fusion Research, Washington, DC, 1990* (IAEA, Vienna, in press).

99 G. S. Lee and B. A. Carreras, "Fluctuation spectrum of resistive pressure-gradient-driven turbulence," *Phys. Fluids B* **1**, 119–133 (1989).

100 K. C. Shaing and B. A. Carreras, "Nonlinear resistive g mode and electron heat conductivity in torsatron/heliotron plasmas," *Phys. Fluids* **28**, 2027–2029 (1985).

101 J. Kim and D. Choi, "Numerical study of resistive magnetohydrodynamic modes in high-temperature plasma of general toroidal geometry," *Phys. Fluids B* **1**, 1026–1033 (1989).

102 Private communications with B. A. Carreras, ORNL (1990).

103 P. H. Diamond, P. L. Similon, T. C. Hender, and B. A. Carreras, "Kinetic theory of resistive ballooning modes," *Phys. Fluids* **28**, 1116–1125 (1985).

104 T. C. Hender, B. A. Carreras, W. A. Cooper, J. A. Holmes, P. H. Diamond, and P. L. Similon, "The effects of compressibility of the resistive ballooning mode," *Phys. Fluids* **27**, 1439–1448 (1984).

239

[105] B. A. Carreras et al., "MHD activity and neutral-beam-driven transport effects in ISX-B tokamak," in *Proceedings of the 9th International Conference on Plasma Physics and Controlled Nuclear Fusion Research, Baltimore, 1982*, Vol. 3 (IAEA, Vienna, 1983), pp. 77–90.

[106] K. C. Shaing, B. A. Carreras, N. Dominguez, V. E. Lynch, and J. S. Tolliver, "Bootstrap current control in stellarators," *Phys. Fluids B* 1, 1663–1670 (1989).

[107] P. H. Diamond, R. D. Hazeltine, Z. G. An, B. A. Carreras, and H. R. Hicks, "Theory of resistive pressure-gradient driven turbulence," *Phys. Fluids* 27, 1449–1462 (1984).

[108] K. T. Tsang, J. D. Callen, and G. Vahala, "Turbulence theory for the dissipative trapped electron instability," *Phys. Fluids* 21, 1172–1180 (1978).

[109] D. F. Duchs, D. E. Post, and P. H. Rutherford, "A computer model of the radial transport in tokamaks," *Nucl. Fusion* 17, 565–609 (1977).

[110] T. E. Stringer, *Experimental Evidence on Fluctuations and Transport in Tokamaks*, Technical Report JET-P(90)15, JET Joint Undertaking, April 1990.

[111] C. S. Liu, M. N. Rosenbluth, and W. M. Tang, "Dissipative universal instability due to trapped electrons in toroidal systems and anomalous diffusion," *Phys. Fluids* 19, 1040–1044 (1976).

[112] P. H. Diamond, University of California at San Diego, "Trapped electron modes in tokamaks and stellarators: Basic concepts and key issues," Lecture given at ORNL, May 1989.

[113] J. C. Adam, W. M. Tang, and P. H. Rutherford, "Destabilization of the trapped-electron mode by magnetic curvature drift resonances," *Phys. Fluids* 19, 561–566 (1976).

[114] B. B. Kadomtsev and O. P. Pogutse, "Trapped particles in toroidal magnetic systems," *Nucl. Fusion* 11, 67–92 (1971).

[115] W. M. Tang, "Microinstability theory in tokamaks," *Nucl. Fusion* 18, 1089–1160 (1978).

[116] Liu Chen, R. L. Berger, J. G. Lominadze, M. N. Rosenbluth, and P. H. Rutherford, "Nonlinear saturation of the dissipative trapped-electron instability," *Phys. Rev. Lett.* 39, 754–757 (1977).

[117] K. T. Tsang and P. J. Catto, "Analytic solutions of the two-dimensional eigenvalue problem for the trapped-electron instability in tokamaks," *Phys. Rev. Lett.* **39**, 1664–1667 (1977).

[118] K. R. Chu and W. M. Manheimer, "Numerical study of the dissipative trapped-electron instability in tokamaks," *Nucl. Fusion* **18**, 29–33 (1978).

[119] X-H. Shi, B. D. Blackwell, and S. M. Hamberger, *Studies of Drift Waves in a Toroidal Heliac*, Technical Report ANU-PRL PP-89/1, Plasma Research Laboratory, Research School of Physical Sciences, The Australian National University, Canberra, Australia, 1989.

[120] G. M. Batanov, L. V. Kolik, A. V. Sapozhnikov, K. A. Sarksyan, Yu. V. Khol'nov, and M. G. Shats, "Low-frequency plasma density fluctuations in the L-2 stellarator," *Sov. J. Plasma Phys.* **15**, 305–308 (1989).

[121] H. Biglari, P. H. Diamond, and M. N. Rosenbluth, "Toroidal ion-pressure-gradient-driven drift instabilities and transport revisited," *Phys. Fluids B* **1**, 109–118 (1989).

[122] A. B. Hassam, T. M. Antonsen, Jr., J. F. Drake, and P. N. Guzdar, "Theory of ion temperature gradient instabilities: Thresholds and transport," *Phys. Fluids B* **2**, 1822–1832 (1990).

[123] W. Horton, Jr., D. Choi, and W. M. Tang, "Toroidal drift modes driven by ion pressure gradients," *Phys. Fluids* **24**, 1077–1084 (1981).

[124] G. S. Lee and P. H. Diamond, "Theory of ion-temperature-gradient-driven turbulence in tokamaks," *Phys. Fluids* **29**, 3291–3313 (1986).

[125] N. Mattor and P. H. Diamond, "Ion temperature gradient-driven turbulence in tokamaks with flat density profiles," *Phys. Fluids B* **1**, 1993–1997 (1989).

[126] N. Mattor and P. H. Diamond, "Theory of weak ion temperature gradient-driven turbulence near the threshold of instability," *Phys. Fluids B* **1**, 1980–1992 (1989).

[127] R. R. Dominguez and R. E. Waltz, "Ion temperature gradient mode and H-mode confinement," *Nucl. Fusion* **29**, 885–892 (1989).

[128] F. Romanelli, "Ion temperature-gradient-driven modes and anomalous ion transport in tokamaks," *Phys. Fluids B* **1**, 1018–1025 (1989).

241

[129] T. S. Hahm and W. M. Tang, "Properties of ion temperature gradient drift instabilities in H-mode plasmas," *Phys. Fluids B* **1**, 1185–1192 (1989).

[130] T. S. Hahm and W. M. Tang, "Weak turbulence theory of ion temperature gradient modes for inverted density plasmas," *Phys. Fluids B* **2**, 1815–1821 (1990).

[131] G. Rewoldt and W. M. Tang, "Toroidal microinstability studies of high-temperature tokamaks," *Phys. Fluids B* **2**, 318–323 (1990).

[132] S. Hamaguchi and W. Horton, "Fluctuation spectrum and transport from ion temperature gradient driven modes in sheared magnetic fields," *Phys. Fluids B* **2**, 1833–1851 (1990).

[133] J. D. Bell, J. H. Harris, V. K. Paré, N. A. Crocker, and J. L. Dunlap, "Signal processing and analysis of fluctuations in toroidal fusion plasmas," unpublished, ORNL, 1990.

[134] J. S. Bendat and A. G. Piersol, *Random Data: Analysis and Measurement Procedures*, 2nd ed. (Wiley-Interscience, New York, 1986).

[135] E. O. Brigham, *The Fast Fourier Transform and Its Applications* (Prentice-Hall, Englewood Cliffs, NJ, 1988).

[136] G. D. Bergland, "A guided tour of the fast Fourier transform," *IEEE Spectrum* 41–52 (July 1969).

[137] J. Sheffield, "Advanced Toroidal Facility: Improving fusions's chances," *ORNL Review* **17**, 14–23 (1984).

[138] The preamplifier and differential amplifier electronics were designed and built by G. R. Dyer, ORNL.

[139] W. R. Wing et al., "The ATF data system," *Bull. Am. Phys. Soc.* **33** (9) (1988).

[140] K. A. Stewart et al., "The data acquisition and control systems for ATF: An overview," *IEEE Trans. Nucl. Sci.* **NS-34**, 739 (1987).

[141] P. K. Mioduszewski, T. Uckan, D. L. Hillis, J. A. Rome, R. H. Fowler, J. C. Glowienka, M. Murakami, and G. H. Neilson, "Edge plasma and divertor studies in the ATF torsatron," in *Proceedings of the 16th European Conference on Controlled Fusion and Plasma Physics, Venice, 1989* (European Physical Society, Geneva, Switzerland), pp. 623–626, Vol. 13B, Part II.

[142] P. K. Mioduszewski et al., "Initial operation and edge plasma studies in ATF," *J. Nucl. Mater.* **162–164**, 825–830 (1989).

[143] T. Uckan, P. K. Mioduszewski, D. L. Hillis, C. L. Hahs, J. W. Halliwell, D. L. Million, W. R. Devan, and ATF Operations, "ATF scrape-off layer studies using an instrumented limiter system," *Bull. Am. Phys. Soc.* **33** (9) (1988).

[144] T. S. Bigelow, *A High Power Microwave Transmission and Launching System for Plasma Heating on the ATF Experiment*, Ph.D. thesis, University of Tennessee, Knoxville, 1990.

[145] T. Uckan, C. Hidalgo, J. D. Bell, J. H. Harris, J. L. Dunlap, G. R. Dyer, P. K. Mioduszewski, J. B. Wilgen, Ch. P. Ritz, A. J. Wootton, T. L. Rhodes, and K. Carter, "ATF edge plasma turbulence studies using a fast reciprocating Langmuir probe," *J. Nucl. Mater.* **176 & 177**, 693–698 (1990).

[146] T. L. Rhodes, E. J. Doyle, N. C. Luhmann, Jr., R. Philipona, C. L. Rettig, W. A. Peebles, K. H. Burrell, R. J. Groebner, and the DIII-D Group, "Correlation reflectometry measurements during L- and H-mode operation om DIII-D," *Bull. Am. Phys. Soc.* **35** (9) (1990).

[147] R. Nazikian, "Coherent scattering from plasma fluctuations," *Bull. Am. Phys. Soc.* **34** (9) (1989).

[148] E. Mazzucato and R. Nazikian, "Microwave reflectometry for the study of density fluctuations in tokamak plasmas," *Plasma Phys. Controlled Fusion* **33**, 261–274 (1991).

[149] Private communications with D. K. Lee, ORNL (1991).

[150] D. K. Lee, "Magnetic field, vector potential, and their derivatives due to currents in closed polygons of wire," *Comput. Phys. Comm.* **25**, 181–191 (1982).

[151] R. R. Kindsfather, D. A. Rasmussen, M. Murakami, C. E. Thomas, S. L. Painter, P. S. Hays, and R. N. Morris, "Two-dimensional Thomson scattering system for ATF," *Rev. Sci. Instrum.* **57**, 1816–1818 (1986).

[152] A. C. England et al., "Equilibrium studies using two dimensional electron temperature and density Thomson scattering measurements in ATF," *Bull. Am. Phys. Soc.* **35** (9) (1990).

[153] Private communications with D. A. Rasmussen, ORNL (1991).

[154] P. R. Bevington, *Data Reduction and Error Analysis for the Physical Sciences* (McGraw-Hill, New York, 1969).

[155] P. D. Welch, "The use of fast Fourier transform for the estimation of power spectra: A method based on time averaging over short, modified periodograms," *IEEE Trans. Audio Electroacoust.* **AU-15**, 70–73 (June 1967).

[156] S. C. Aceto, J. G. Schwelberger, J. J. Zielinski, K. A. Connor, T. P. Crowley, J. W. Heard, R. L. Hickok, P. E. Mclaren, A. Ouroua, P. M. Schoch, V. J. Simcic, R. C. Isler, J. Harris, M. Murakami, J. C. Glowienka, T. Uckan, and H. Okada, "Heavy ion beam probe measurements of ECH heated plasma in the advanced toroidal facility," in *Proceedings of the 18th European Conference on Controlled Fusion and Plasma Physics, Berlin, 1991* (European Physical Society, Geneva, Switzerland), pp. 161–164, Vol. 15C, Part II.

[157] Private communications with S. C. Aceto, RPI on assignment to ORNL (1991).

[158] M. Murakami et al., "Energy confinement and bootstrap current studies in the advanced toroidal facility," in *Proceedings of the 13th International Conference on Plasma Physics and Controlled Nuclear Fusion Research, Washington, DC, 1990* (IAEA, Vienna, in press).

[159] M. Murakami et al., "Recent results from the ATF torsatron," *Phys. Fluids B*, accepted for publication (1990).

[160] R. J. Colchin et al., "Overview of results from the ATF torsatron," *Phys. Fluids B* **2**, 1347–1352 (1990).

[161] J. H. Harris et al., "Second stability in the ATF torsatron–Experiment and theory," *Phys. Fluids B* **2**, 1353–1358 (1990).

[162] W. R. Wing, G. R. Dyer, J. C. Glowienka, J. H. Harris, J. W. Halliwell, and G. H. Neilson, "Diamagnetic measurements on ATF," *Bull. Am. Phys. Soc.* **34** (9) (1989).

[163] T. Uckan, C. Hidalgo, J. D. Bell, J. H. Harris, J. L. Dunlap, G. R. Dyer, P. K. Mioduszewski, J. B. Wilgen, Ch. P. Ritz, A. J. Wootton, T. L. Rhodes, and K. Carter, *ATF Edge Plasma Turbulence Studies Using a Fast Reciprocating Langmuir Probe*, Technical Report ORNL/TM-11545, Oak Ridge National Laboratory, January 1991.

[164] C. Hidalgo, J. H. Harris, T. Uckan, J. D. Bell, B. A. Carreras, J. L. Dunlap, G. R. Dyer, Ch. P. Ritz, A. J. Wootton, M. A. Meier, T. L. Rhodes, and K. Carter, "Plasma fluctuations near the shear layer in the ATF torsatron," submitted to *Nucl. Fusion* (December 1990).

[165] T. Uckan, C. Hidalgo, J. D. Bell, J. H. Harris, J. L. Dunlap, J. B. Wilgen, Ch. P. Ritz, T. L. Rhodes, and A. J. Wootton, "Characteristics of edge plasma turbulence on the ATF torsatron," *Phys. Fluids B*, accepted for publication (1991).

[166] S. C. Aceto, K. A. Connor, P. E. McLaren, J. J. Zielinski, J. G. Schatz, and G. H. Henkel, "Energy analyzer for the ATF heavy ion beam probe," *Rev. Sci. Instrum.* **61**, 2958–2960 (1990).

[167] J. J. Zielinski, S. C. Aceto, K. A. Connor J. F. Lewis, J. C. Glowienka, G. H. Henkel, D. T. Fehling, W. R. Devan, K. D. St. Onge, D. K. Lee, and A. Carnevali, "ATF heavy ion beam probe: Installation and initial operation," *Rev. Sci. Instrum.* **61**, 2958–2960 (1990).

[168] S. C. Aceto, K. A. Connor, J. G. Schwelberger, and J. J. Zielinski, "Preliminary fluctuation measurements on ATF using the heavy ion beam probe," *Bull. Am. Phys. Soc.* **35** (9) (1990).

[169] G. R. Hanson, J. H. Harris, J. D. Bell, , J. B. Wilgen, E. Anabitarte, B. Branas, J. L. Dunlap, C. Hidalgo, J. Sanchez, C. E. Thomas, and T. Uckan, "Correlation reflectometry on ATF," *Bull. Am. Phys. Soc.* **35** (9) (1990).

[170] J. B. Wilgen, M. G. Shats, J. H. Harris, K. M. Likin, A. V. Sapozhnikov, K. A. Sarksyan, G. R. Hanson, and N. Dominguez, "Microwave scattering in the ATF torsatron," *Bull. Am. Phys. Soc.* **35** (9) (1990).

[171] J. D. Bell, J. H. Harris, J. L. Dunlap, N. A. Crocker, and G. R. Hanson, "Magnetic fluctuations in ATF," *Bull. Am. Phys. Soc.* **35** (9) (1990).

[172] Private communications with J. D. Bell, ORNL (1991).

[173] J.-N. Leboeuf, D. K. Lee, B. A. Carreras, N. Dominquez, J. H. Harris, C. L. Hendrick, C. Hildago, J. A. Holmes, J. Ruiter, P. H. Diamond, A. S. Ware, Ch. P. Ritz, A. J. Wootton, W. L. Rowan, and R. V. Bravenec, "TEXT edge turbulence modeling," submitted to *Phys. Fluids B* (1991).

VITA

Gregory Richard Hanson, son of Edwin R. Hanson and Rosalie A. (Taylor) Hanson, was born January 5, 1963, in Walnut Creek, California. He graduated from Chaparral High School in Las Vegas, Nevada, in 1981 and entered the United States Merchant Marine Academy in Kings Point, New York, that same year. He studied Marine Engineering and Nuclear Engineering and spent a total of one year sailing aboard U.S. flag merchant vessels as an Engineering Midshipman. In June 1985, he received a Bachelor of Science degree in Marine Engineering, graduating first in his class, and a commission into the United States Naval Reserve.

In the fall of 1985, he entered graduate school at the Georgia Institute of Technology in Atlanta, Georgia, where he studied Nuclear Engineering and Fusion Technology. He received a Master of Science degree in Nuclear Engineering in June 1987. He continued his graduate studies, and in March 1989 moved to Knoxville, Tennessee, to begin work on a reflectometry diagnostic for the Advanced Toroidal Facility (ATF) at the Oak Ridge National Laboratory. While in graduate school, he was a drilling Naval reservist, spending one weekend per month and two weeks per year with the Navy. He married Sally J. Walters on April 28, 1990.

In September 1991, he received his Doctor of Philosophy degree in Fusion Technology from the School of Mechanical Engineering, Georgia Institute of Technology. In May 1991, he was awarded a U.S. Department of Energy Fusion Energy Postdoctoral Research Program appointment at the Oak Ridge National Laboratory to begin in September 1991.